Development of superconducting nanowire single photon detectors integrated on Silicon waveguides for quantum information

Raouia Rhazi

To cite this version:

Raouia Rhazi. Development of superconducting nanowire single photon detectors integrated on Silicon waveguides for quantum information. Physics [physics]. Université Grenoble Alpes [2020-..], 2022. English. NNT : 2022GRALY076 . tel-04077609

HAL Id: tel-04077609
https://theses.hal.science/tel-04077609

Submitted on 21 Apr 2023

HAL is a multi-disciplinary open access archive for the deposit and dissemination of scientific research documents, whether they are published or not. The documents may come from teaching and research institutions in France or abroad, or from public or private research centers.

L'archive ouverte pluridisciplinaire **HAL**, est destinée au dépôt et à la diffusion de documents scientifiques de niveau recherche, publiés ou non, émanant des établissements d'enseignement et de recherche français ou étrangers, des laboratoires publics ou privés.

THÈSE

Pour obtenir le grade de

DOCTEUR DE L'UNIVERSITÉ GRENOBLE ALPES

École doctorale : PHYS - Physique
Spécialité : Physique appliquée
Unité de recherche : Laboratoire d'Electronique et de Technologie de l'Information (LETI - CEA)

Développement de détecteurs de photons uniques supraconducteurs intégrés sur guide silicium pour l'information quantique

Development of superconducting nanowire single photon detectors integrated on Silicon waveguides for quantum information

Présentée par :

Raouia RHAZI

Direction de thèse :

Jean Michel GERARD INGENIEUR HDR, Université Grenoble Alpes	Directeur de thèse
Ségolène OLIVIER Cadre scientifique des EPIC, CEA CENTRE DE GRENOBLE	Co-encadrante de thèse

Rapporteurs :

FABRICE RAINERI
Professeur des Universités, UNIVERSITE COTE D'AZUR
CHRISTOPHE COUTEAU
Maître de conférences HDR, UNIVERSITE DE TECHNOLOGIE DE TROYES

Thèse soutenue publiquement le **5 décembre 2022**, devant le jury composé de :

FABRICE RAINERI Professeur des Universités, UNIVERSITE COTE D'AZUR	Rapporteur
CHRISTOPHE COUTEAU Maître de conférences HDR, UNIVERSITE DE TECHNOLOGIE DE TROYES	Rapporteur
NADIA BELABAS Chargé de recherche, CNRS DELEGATION ILE-DE-FRANCE SUD	Examinatrice
ELISABETH BLANQUET Directeur de recherche, CNRS DELEGATION ALPES	Examinatrice
DAVID FERRAND Professeur des Universités, UNIVERSITE GRENOBLE ALPES	Président

Abstract

This work aims at developing integrated Superconducting Nanowire Single Photon Detectors (SNSPDs) on a 200 mm SOI platform. These detectors constitute a fundamental building block for the development of scalable silicon photonics chips with close to 100% detection efficiency for applications in quantum communications and quantum computing. In this thesis, we discuss the design, fabrication, and room temperature characterization of SNSPDs integrated with silicon waveguides.

In a first phase, we developed high-quality polycrystalline NbN thin films (5-11 nm) on 200 mm silicon substrates thanks to the introduction of a thin (10-20 nm) texturing AlN layer, both materials being deposited with CMOS-compatible sputtering processes. An improvement of the NbN critical temperature up to 10 K for 9 nm thick NbN was observed with the introduction of the AlN layer. In addition, we fabricated simple fiber-coupled SNSPD architectures based on NbN/AlN material stack and operating under normal incidence illumination. The SNSPDs featured a system detection efficiency in good agreement with simulated values, validating the single-photon detection properties of the NbN/AlN stack.

In a second phase, we designed waveguide-integrated SNSPDs to achieve high detection efficiencies. We demonstrated that with the incorporation of the AlN buffer layer used to enhance the superconducting properties of the NbN layer, high absorption could be achieved for a U-shaped SNSPD configuration of less than 100 µm in length. We also showed the potential of cavity-coupled SNSPDs, in particular with silicon ring resonators to reduce the detector length and improve the timing properties. We demonstrated near-unity simulated detection efficiency using waveguide-integrated SNSPDs with nanowire lengths between 1 and 10 µm. In addition, we proposed a detection scheme where integrated SNSPDs are placed in series to achieve photon number resolution, an important feature for quantum computing applications.

In a third phase, we developed a CMOS-compatible process for the fabrication of waveguide-integrated SNSPDs on a 200 mm silicon photonics platform, using the optimized NbN/AlN stack. Finally, we performed electrical and optical characterization at room temperature, providing a first level of validation of the developed designs and processes, with notably an excellent uniformity of nanowires resistance across 200 mm SOI wafers. These results are very promising for the characterization of detector features in terms of efficiency and timing performances at cryogenic temperature.

Remerciements

C'est avec beaucoup de nostalgie pour cette période que j'écris ces remerciements. Je tiens d'abord à prendre le temps de remercier mes encadrants Ségolène Olivier et Jean-Michel Gérard de m'avoir accompagnée pendant ces trois années de thèse. Je suis très reconnaissante de l'opportunité que vous m'avez offerte de travailler sur un sujet aussi passionnant et stimulant. Votre encadrement bienveillant et exigeant a été pour moi un véritable tremplin professionnel et personnel.

Je suis également très reconnaissante envers les deux laboratoires qui m'ont accueilli, LETI-LIPS et PHELIQS-NPSC, pour leur soutien constant et leur aide tout au long de ma thèse. J'ai eu la chance de travailler dans un environnement de travail collaboratif et stimulant, qui m'a permis de m'épanouir professionnellement et d'apprendre beaucoup de choses.

Je tiens également à remercier Eva Monroy et Joël Bleuse pour leur contribution précieuse à mes travaux de thèse. Même s'ils n'étaient pas mes encadrants officiels, ils ont été des mentors inspirants et des collègues de travail très impliqués. Leur soutien et leurs conseils ont été pour moi une source d'inspiration et de motivation tout au long de ma thèse.

Enfin, je voudrais remercier tous les doctorants et le personnel des deux laboratoires LETI et PHELIQS. Votre accueil chaleureux, votre bienveillance et votre amitié m'ont beaucoup touchée et ont rendu cette expérience de thèse encore plus enrichissante.

Encore une fois, merci pour tout ce que vous avez fait pour moi et pour m'avoir permis de réaliser cette thèse. Je suis fière de ce qu'on a accompli ensemble et j'espère pouvoir continuer à contribuer à notre communauté de recherche à l'avenir.

Table of contents

Chapter 1- Introduction

1.1 A little bit of history

Light has a long and remarkable history. Light has fascinated humankind from the dawn of existence. In antiquity, there were two models for describing light. The first, known as "Particles towards," presented light as multicolored particles and was employed by the Pharaohs and Greeks. The second model, "Particles from the Eyes," is based on the idea of using the eye as a radar.

Advances in engineering and technology began to appear in the Middle Ages. Lenses were used to correct sight, and their combination was used to build advanced systems like telescopes. In the 17th century, there was a period of conceptual debate. Huygens proposed a light wave theory, comparing light to the ripples that can be seen on water after a disturbance. While Newton defends a theory that is fundamentally opposed to that of Huygens. He defends a corpuscular theory in which tiny particles form the light, and each has a particular color. However, due to Newton's notoriety at the time, Huygens' wave-like theory fades from memory.

We had to wait for modern physics, two centuries after, for Young in England and Fresnel in France, to do some experiments on light. They observe phenomena that can only be understood if light is represented as a wave. Afterwards, the British scientist Maxwell developed four equations that summarized all of the knowledge on electricity and magnetism at the time. These equations allow light to be defined as an electromagnetic wave with oscillating electric and magnetic fields.

At the end of the 19th century, the idea that physics is understood was widely spread and that from now on, the role of physicists is to improve the precision of their measurements. Albert Einstein's work on relativity at the time included light traveling in a vacuum at a universally constant speed and being invariant to any observer moving in any direction at a constant speed.

The theory of Max Planck, published in 1901 on the black body radiation, was the first step toward the quantification of light, confirmed by Einstein in 1905, who explicitly introduced the concept of the photon to explain the photoelectric effect. These studies lead to consider light as a set of corpuscles called quanta, described by an elementary energy and a momentum.

In 1905, Albert Einstein had introduced the concept of wave-particle duality of light. Light is both a wave, capable of interfering, and an ensemble of particles with defined energy and momentum. Thus, the photon is a quantum object with both wave-like and particle-like properties. This concept is at the root of the first quantum revolution and has led to the understanding of the matter structure, its properties, and its interaction with light.

The comprehension of these quantum phenomena resulted in revolutionary technologies such as transistor (1947), light emitting diodes and lasers (1960), GPS (1990), etc. These inventions allowed the development of technological information and communication. Information has become one of the essential commodities in the modern world.

The need to solve complex problems has driven an exponential increase in the computational power of information technologies. This growth was reached through the high level of integration and miniaturization of different components. However, today, semiconductor-driven information technologies are facing fundamental boundaries since the transistor scaling is now at a stage where typical dimensions are in the order of nanometers where the size of a single transistor becomes comparable to the de Broglie wavelength of the electrons, and where quantum effects determine the characteristics of the device. Moreover, the abundance of data and their dissemination on the internet strongly question their safety. To overcome these problems, new technological solutions must be developed.

Quantum technologies extend the already classical platform, making it safer, more efficient, and powerful. During the last decade, significant research efforts were focused on the comprehension and development of these quantum effects, paving the way for a second quantum revolution. Today, these concepts are coming out of laboratories to be implemented in concrete applications.

Before addressing a quick overview of quantum information applications, we will first present some fundamental principles of quantum mechanics. We will start with the definition of a quantum bit, followed by an introduction of the non-classical properties of quantum states: superposition and entanglement.

1.2 Quantum information with photons

1.2.1 Introduction of quantum mechanics concepts

Information is inherently linked to and governed by the laws of physics, and the laws of quantum mechanics govern the physical world. Quantum information is a field of technological applications of quantum mechanics based on unique properties. In quantum information, information is encoded in quantum bit or qubit, which is the quantum analog of the classical bit.

A qubit is considered as a fundamental unit of information. It can be implemented in a physical system that can exist in at least two different states such as electrons (spin up and spin down), photons (vertical and horizontal polarization), and systems defined by two energy levels such as ions and atoms.

In quantum mechanics, the state of a physical system is represented by a vector in Hilbert space $\mathcal{H}$. When $\{ |\psi\rangle_i \}$ form a vector basis of $\mathcal{H}$, any state $|\psi\rangle$ can be written as a linear combination

$$|\psi\rangle = \sum_i c_i \, |\psi\rangle_i \qquad c_i \in \mathbb{C} \qquad \textbf{(1)}$$

From the information processing point of view, a qubit contains two logical states and quantum mechanics tells us that such system can exist in a superposition of states at the same time. Thus, a qubit can be described by a two-dimensional Hilbert space $\mathcal{H}$ and can be written as a linear combination of two basis vectors $|0\rangle = \binom{1}{0}$ and $|1\rangle = \binom{0}{1}$.

$$|\psi\rangle = \binom{\alpha}{\beta} = \alpha\, |0\rangle + \beta |1\rangle \qquad \textbf{(2)}$$

α and β are complex amplitudes, with $|\alpha|^2 + |\beta|^2 = 1$. If a measurement of the state is performed onto the basis $\{|0\rangle, |1\rangle\}$, the probability to be in state $|0\rangle$ is $|\alpha|^2$ and to be in state $|1\rangle$ is $|\beta|^2$. The notation $|0\rangle$ and $|1\rangle$ is chosen to make the analogy with binary digit that takes the value 0 or 1. This suggests that the qubit can be represented as a unit vector using the Bloch Sphere representation

$$|\psi\rangle = \cos\frac{\theta}{2}\, |0> + e^{i\phi} \sin\frac{\theta}{2} |1> \qquad \textbf{(3)}$$

Figure 1 illustrates the Bloch sphere where the points are defined by their polar angles $(\theta,\phi) \in \mathbb{R}^2$.

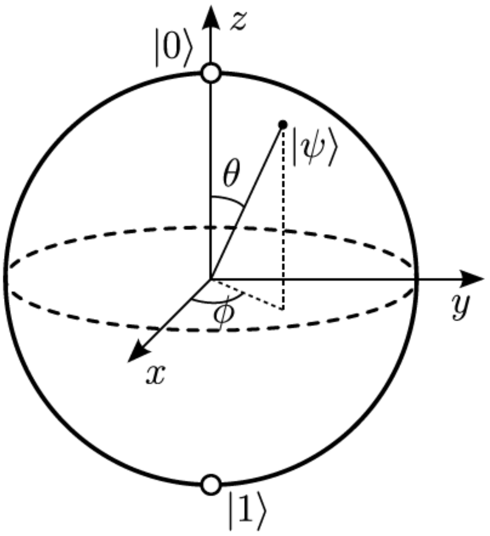

Figure 1: *Bloch Sphere representation*

The North Pole corresponds to the state $|0\rangle$ when $\theta = 0$ and $\phi = 0$ while the South Pole corresponds to the state $|1\rangle$ when $\theta = \pi$ and $\phi = 0$. All the other points of the sphere correspond to superposition states.

The principle of superposition does not only concern one qubit but also holds for states containing several qubits. One defines a system with two qubits A and B in superposition. The state of qubit A is $|\psi\rangle_A = \alpha\ |0\rangle_A + \beta|1\rangle_A$ and $|\psi\rangle_B = \gamma\ |0\rangle_B + \delta|1\rangle_B$ for qubit B. The system AB can be described by the following states $|0\rangle_A|0\rangle_B$,$|0\rangle_A|1\rangle_B$, $|1\rangle_A|0\rangle_B$ and $|1\rangle_A|1\rangle_B$, thus

$$|\psi\rangle_A|\psi\rangle_B = \alpha\gamma|0\rangle_A|0\rangle_B + \alpha\delta\ |0\rangle_A|1\rangle_B + \beta\gamma|1\rangle_A|0\rangle_B + \beta\delta\ |1\rangle_A|1\rangle_B \qquad \textbf{(4)}$$

These states constitute a basis in the Hilbert space of two-qubit states, which is of dimension 4. By concern of simplicity, the system AB can be described by

$$|\psi\rangle_{AB} = |\psi\rangle = \alpha_{00}|00\rangle + \alpha_{01}\ |01\rangle + \alpha_{10}|10\rangle + \alpha_{11}|11\rangle \qquad \textbf{(5)}$$

with

$$|\alpha_{00}|^2 + |\alpha_{01}|^2 + |\alpha_{10}|^2 + |\alpha_{11}|^2 = 1 \qquad \textbf{(6)}$$

However, there are states that cannot be written into a product of individual qubits, these states are called “entangled”. Entanglement is a non-classical correlation between at least two-quantum systems, which are described by joint properties and form a single system.

For a system composed by two qubits, there are four state maximally entangled, called the Bell’s states defined by:

$$\begin{cases} |\Psi^+\rangle = \frac{1}{\sqrt{2}}(|01\rangle + |10\rangle)\ where\ \alpha = \delta = 0, \beta = \gamma = \frac{1}{\sqrt{2}} \\ |\Psi^-\rangle = \frac{1}{\sqrt{2}}(|01\rangle - |10\rangle\ )\ where\ \alpha = \delta = 0, \beta = -\gamma = \frac{1}{\sqrt{2}} \\ |\Phi^+\rangle = \frac{1}{\sqrt{2}}(|00\rangle + |11\rangle\ )\ \ where\ \alpha = \delta = \frac{1}{\sqrt{2}}, \beta = \gamma = 0 \\ |\Phi^-\rangle = \frac{1}{\sqrt{2}}(|00\rangle - |11\rangle\ )\ \ where\ \alpha = -\delta = \frac{1}{\sqrt{2}}, \beta = \gamma = 0 \end{cases} \qquad \textbf{(7)}$$

The state of the system is revealed when performing measurements on one of the qubits. The entanglement makes that once the state of one qubit is measured, the state of the other qubit is known. To illustrate, for the state $|\phi^+\rangle$, if the first measured qubit is $|0\rangle$ (respectively $|1\rangle$) , this implies that the other qubit is also in $|0\rangle$ (respectively $|1\rangle$), without needing to measure it.

In the case of photons, information can be encoded in many different degrees of freedom such as polarization, spatial mode, time-bin, energy, and angular momentum. Moreover, several degrees of freedom of the same photons can be used simultaneously.

Single photons are a promising choice for quantum information since they are relatively easy to manipulate, transport and measure. In the following, we will only discuss the two main application of quantum information: quantum computing and quantum cryptography.

1.2.2 Quantum communication

Conventional modes of communication have transformed our society during the last decades. Today, optical fibers transfer information with low losses and at very high-speed linking the entire world. However, a strong limitation arises when it comes to transferring information securely. The wish to communicate secretly goes back to the beginning of our civilization in Ancient Greece; the Spartans (~400 JC) used the Scytale. Then, it took off during the First and Second World Wars, becoming a science of its own.

Nowadays, the development of communication networks and the explosion of information exchange are becoming a challenge for our society. Cryptography attempts to address this issue. The protocols for encrypting and decrypting messages rely on increasingly complex codes as the computers' power to crack them increases. Due to the rise of computational power, violation of information encryption becomes an issue. Another strategy is required to overcome this problem, and this is where quantum physics come into play.

A quantum key, indecipherable by classical methods, is secretly distributed between two distant counterparts in quantum cryptography. Quantum Key Distribution (QKD) ensures the absolute security of transmitted keys thanks to the laws of quantum physics. Quantum cryptography is based on Heisenberg's uncertainty principle formulated in 1927 [1] and the no-cloning theorem written by Wootters and Zurek in 1982 [2]. Werner Heisenberg formalized one of the fundamental principles of quantum physics. The characteristics of a quantum system cannot be measured without altering it, and the properties of a quantum system cannot be fully known until they are measured. Moreover, the non-cloning theorem shows that it is impossible to create a perfect copy of an unknown and arbitrary quantum state.

To prepare, transmit, or manipulate qubits, we need to define physical support and a quantum observable to encode the information. Experimental realizations of QKD devices have made significant progress over the last two decades and are based on photons transmission. Photons are naturally mobile, and their transmission at the speed of light makes them an obvious choice for quantum communication. Moreover, they are robust to ambient noise and can be transported either in free space or in optical fibers for long distances. The existing communication technologies are based on optical fibers: therefore, the implementation of QKD protocols using photons would naturally benefit from the use of already developed platforms and communication tools.

Historically, the polarization observable was the first to be used both to prove the existence of entangled states [3], as well as to perform quantum cryptography experiments[4]. To avoid going into much detail, I will simply discuss polarization here; nevertheless, other observables are used for QKD, such as time-bin, energy-time, and frequency.

Three conjugate bases are defined by the polarization states {H; V}, {D; A} and {R; L} where H, V, D, A, L, and R represent respectively the horizontal, vertical, diagonal, anti-diagonal, left circular and right circular polarization states represented in Figure 2.

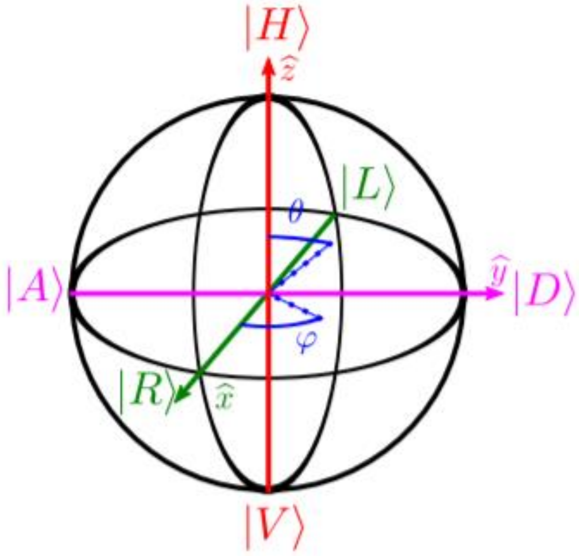

Figure 2*: Sphere of Bloch-Poincaré presenting a state of polarization.*

To encode information on the polarization state of the photon, we use polarizers and birefringent phase plates. It is possible to perform transformations on the photon's polarization state with birefringent phase plates, the most extensively utilized of which are half-wave (λ /2) and quarter-wave (λ /4) plates.

With the combination of phase plates and polarized beam splitter PBS, one can generate and analyze, for example, in the base {H; V} photonic qubits of type $\alpha|H\rangle + \beta|V\rangle$ or pairs of entangled qubits $\alpha|HH\rangle + \beta|VV\rangle$ respecting as always, the normalization rule $|\alpha|^2 + |\beta|^2 = 1$.

There are different protocols for achieving the key exchange, and these are based on either single photons based on the BB84 protocol [5] or entangled photons based on BBM92 [6,7]. BB84 is probably the most analyzed protocol, not only because it was the first protocol to be developed, but also due to its simplicity and symmetry. It has been proven that BB84 is robust against all types of attacks allowed by quantum physics, for implementations based on perfect single photon sources [8].

In order to generate the key that will be sent to Bob (the receiver), Alice (the transmitter) uses a source of polarized photons. The information is encoded in the polarization of single photons using two sets of basis of the Hilbert space. Thus, Alice can choose the polarization of each photon among the four possibilities associated with two different linear polarization basis $\{|H\rangle;|V\rangle\}$, $\{|+\rangle;|-\rangle\}$. Alice prepares in a random and equiprobable way one of the four states:

$|H\rangle$, $|V\rangle$, $|+\rangle = 1/\sqrt{2}\,(|H\rangle + |V\rangle)$, $|-\rangle = 1/\sqrt{2}\,(|H\rangle - |V\rangle)$

Then, she transmits the corresponding states to Bob. On its side, Bob receives the quantum states and needs to measure them. However, he does not know the basis used for the bit encoding used by Alice. Therefore, he selects in a random way a basis to measure each qubit. If he measures a quantum state with the wrong basis, he gets a random result while if he measures a quantum state with the good basis, he gets the correct value with a very high probability. In a second step, Bob sends to Alice the list of the basis used during the measurement. Alice indicates which are the basis that Bob has correctly chosen. Then they eliminate the bits of their raw keys corresponding to the different basis choices. This step, which eliminates the bits that cannot be correlated because they are associated with an incompatible basis is performed through a public channel and is called sifting. Afterward, Alice and Bob mutually define a part of the key that they will reveal publicly. They sacrifice a certain number of photons to ensure that they have the same value. This outcome is also used for security testing and is used to estimate the error rate. If the values do not match, depending on the calculated error rate, it may mean that the line has been intercepted. Indeed, if a spy, usually known as Eve, tries to intercept photons in order to measure the photons and send them back to Bob, she must first choose a measurement basis. If the selected basis is not the same as Alice's, the measurement result will be random like the returned photon. Therefore, Eve will introduce an error rate of 25% if she measures all the states. Because of the large error rate (25%), Alice and Bob choose to stop the protocol and start it again since the key has been compromised. When the estimated error rate is lower than 27% [9], Alice and Bob may use an error-correcting procedure, such as a quantum error-correcting code, to eliminate the differences between their outcomes without giving the adversary an advantage. Indeed, the dark counts of single photon detectors can lead to incorrect measurements, even in the absence of a spy on the channel. Therefore, BB84 is a protocol that allows one to determine whether the key has been compromised or not.

Concretely, implementing a QKD system requires some key components, including single-photon sources, quantum channels, and single photons detectors SPDs.

SPDs are required when single photons are used to transmit a quantum state. The performance of the SPDs impacts the maximum transmission distance, secure key rate R_{SK}, and quantum bit error rate R_{BE} of QKD systems. For a BB84 QKD protocol, R_{SK} and R_{BE} can be expressed as follow [10] :

$$\begin{cases} R_{sk} \propto \eta \, . \, f \, . \, u \, . \, L \\ R_{BE} \propto \frac{DCR}{R_{SK}} \end{cases} \quad \textbf{(8)}$$

where η denotes the SPD detection efficiency, f the clock frequency, u the average photon number per pulse, L the total channel loss, and DCR the SPD dark count rate.

These equations show that the performance of the BB84 QKD protocol is dependent on key SPD parameters such as η and DCR. In addition, high-speed QKD system performance will also be influenced by SPD dead time t_{dead} and timing jitter τ.

In terms of implementation, free space QKD began in 1996 in the United States on 75 meters, followed by 300 km to connect the Canary Islands of La Palma and Tenerife in 2010 [11] and in 2019 in an urban environment in Italy on 145 meters [12]. The QKD transmission on fiber has steadily improved, with only 30 cm in 1989 in IBM with Charles Bennett [13], 1100 m at the University of Geneva in 1993 [14], then 23 km in 1995 with the BB84 protocol [15]. The present record, set in China at the beginning of 2020, was 509 kilometers of transmission without a repeater [16]. Finally, the Chinese scientists have established the world’s first integrated quantum communication network, which combines over 700 optical fibers on the ground with two ground-to-satellite links to achieve quantum key distribution over a total distance of 4,600 kilometers for users across the country [17].

At the European level, the Swiss start-up IDQ[18] has linked local banks in Switzerland. In 2007, they also implemented a QKD-based election vote-counting system.

1.2.3 Quantum computing

For classical computers, information is stored in the form of binary bits that can only take two values 0 or 1, at a given time. In contrast, quantum computers replace classical bits with qubits. Therefore, quantum computers use quantum superposition to process information in parallel. Thus, the quantum computational advantage is to work in a regime where quantum algorithms can solve computational problems in a much more efficient way than classical computers.

To build quantum computers, it is necessary to develop the basic building blocks of these quantum computers, the famous qubits, capable of being in two states at the same time. Unlike quantum communication based on photons, quantum computers can be built using several different physical qubits. During the last decades, numerous candidates have been tested: atoms, ions, molecules, electrons, photons, or even superconducting circuits.

Superconducting qubits are an excellent physical mean for quantum computing and are certainly the most advanced and mature qubit solid-state technology. The leaders in this technology are Google and IBM, claiming to have reached the "quantum advantage." The first one had made a buzz with its 53 qubits on 2019 chip [19] and the second one unveiled in 2020 a 65-qubit chip [20]. Superconducting qubits have a fast operation time, and their most significant advantage is their compatibility with the microelectronic processing technology.

Photons are also good candidates for quantum computing and the quantum advantage in this platform was demonstrated in December 2020 by Chao-Yang Lu's Chinese team with 18 photonic qubits with a high level of entanglement [21]. The particularity of this demonstration is that it only requires six photons. Indeed, they managed to exploit three different quantum states (paths, polarization, and orbital angular momentum) independently and for each photon, hence the 18 qubits. More precisely, they performed the so-called Gaussian Boson Sampling (GBS) task, derived from the Boson Sampling proposed in 2011 by Scott Aaronson and Alex Arkhipov [22] as a test of quantum supremacy by an optical machine. The calculations chosen so far by the majority of the groups to test their machine has no application interest for the moment. These protocols are designed only to demonstrate the quantum advantage.

Today, several physical realization approaches are being developed in parallel, and there is no agreement on the most suitable solution to realize a quantum computer. Similarly, to quantum communication, building an optical quantum computer requires indistinguishable single photons, low-loss transmission channels, and high-performance SPDs. To this end, the development of integrated on-chip technologies is strategic for the future large-scale deployment of compact and low-cost quantum computing systems.

1.2.4 Detection of single photons

Quantum information with photons requires devices that operate at the single-photon level, and single-photon detectors are a key building block of these technologies. In addition to quantum communication and computing, there is an increasing demand for highly efficient detectors for a wide range of applications such as light detection and ranging (LIDAR) for remote sensing [23,24], picosecond imaging circuit analysis [25,26], single-molecule spectroscopy [27,28], fluorescence-lifetime measurements [29,30], medical applications such as diffuse optical tomography [31], and finally quantum metrology [32,33].

These emerging applications place high expectations on the detector performances. Single-photon detectors with near unity detection efficiencies (the probability of successfully detecting an incident photon), zero dark count rate (the rate of detector output pulses in the absence of any incident photons), with no dead time (time after a photon-detection event during which the detector is incapable of detecting a photon), short timing jitters (variation from event to event in the delay between the input of the optical signal and the output of the electrical signal), high maximum count rates, photon number resolution capabilities, and large active surfaces need to be designed for these applications.

In reality, not all these ideal characteristics are available in a single detector together at the same time. However, such level of performance in a detector is unlikely ever to be achieved. In fact, a detector is a combination of performance tradeoffs that must be established based on the requirements of a specific application.

Different systems have emerged over the last decades to detect photons with wavelengths ranging from millimeters to visible. Various approaches of single photon detectors are reviewed in the second chapter.

1.3 Quantum photonics technology

Quantum optics is both an appealing solution for photonic qubits and an indispensable transversal technology for other types of qubits. It is the only technology that allows long distance communication among qubits and between quantum computing units. Several experimental proof-of-concept demonstrations of the applications discussed above using a few qubits were performed in bulk optics bolted down to an optical bench.

However, to move beyond proofs of concept, it is necessary to manipulate several qubits. The use of bulk optics becomes more challenging as the number of circuit elements increases and as the size and coupling losses increase. The combination of photonics and quantum optics has promising potential by miniaturizing and scaling up complex laboratory setups. Hence, integrated technologies are essential for future large-scale deployment of quantum information systems. Moreover, the recent technological developments in photonic integrated chip fabrication will allow quantum photonics to take benefit of the existing semiconductor platform. Today, Silicon integrated photonics offers a high level of miniaturization, high functional stability, and mass production at an affordable cost.

Large-scale integrated quantum photonic technologies will require the integration of several building blocks. Central elements of quantum-integrated photonics are single photon sources, detectors, and reconfigurable photonic circuits. Their principal limitation is combining them into a single chip.

Today, classical photonic integrated circuits (PICs) integrating hundreds of components are already used for coherent manipulation and processing of quantum states of light [34]. However, in these experiments, a large number of fibers couple integrated output waveguides to off-chip detectors, which induces losses that are detrimental to scalability. Integrated detectors would not only offer ultra-efficient optical readout without introducing coupling losses but, they would also allow feedback and adaptive control of complex reconfigurable processing circuits, crucial for measurement-based universal quantum computing schemes [35].

1.4 Scope of the thesis

Quantum information with photons requires devices that operate at the single-photon level, and single-photon detectors are a key building block of quantum photonic systems. Among the different approaches to detect single photons, superconducting nanowire single-photon detectors (SNSPDs) outperform other single-photon detection technologies in near-infrared (NIR) due to their high efficiency, high timing accuracy, and short dead time. Their outstanding properties and compatibility with the integration of single-photon sources and passive photonic elements make SNSPDs excellent candidates for on-chip implementations. In addition, the silicon platform offers a high level of integration, high functional stability, and the perspective of affordable mass production, making it a suitable platform for this development. While efficient on-chip SNSPDs have already been demonstrated by several groups worldwide at the single device level, the scalability of quantum photonic chips requires large-scale, fully CMOS-compatible fabrication processes. As of 2018, CEA LETI, one of the European players in the field of integrated photonics on silicon chips, decided to leverage this technology to develop quantum-grade devices and quantum photonic chips.

In this context, the goal of my Ph.D. was to demonstrate for the first time integrated SNSPDs produced using a fully CMOS-compatible process on 200 mm wafers. On the way towards this objective, I had first to study and optimize, in collaboration with CEA-IRIG researchers, the superconducting properties of NbN thin films deposited in our clean-room. The quantum-grade quality of our films has been confirmed through the fabrication and study of a fiber-coupled stand-alone SNSPD. A significant part of my work consisted in designing waveguide-integrated SNSPDs in order to optimize their performances. Various configurations of SNSPDs were proposed. The dimensions of the designed structures were determined by optical simulations. Thereby, we demonstrated near-unity detection efficiency using waveguide integrated SNSPDs. In collaboration with IRIG researchers, we have also proposed a detection scheme to achieve photon number resolution PNR. For the fabrication of waveguide integrated SNSPDs, I collaborated with LETI process engineers. Together, we improved and adapted existing processes and developed new ones for the fabrication of SNSPDs. Following the fabrication, preliminary optical and electrical characterizations were conducted at room temperature on the wafer-level photonic probers of CEA-LETI. These characterizations show very encouraging results, offering a strong first validation of the technological developments. Currently, Valentin Brisson, the Ph.D. who followed up on my project, is working on low temperature characterizations in the IRIG laboratories, in order to demonstrate the maturity of the large-scale fabrication process that has been developed during this work. Such SNSPDs on waveguides are entering into the toolbox of integrated quantum photonics technologies, and will likely be used in a wide range of fields, encompassing photonic quantum computing and simulations, quantum sensing (e.g. photon number resolution) and quantum communications.

In this manuscript, the first chapter aims to give an overview of quantum information with photons. The second chapter will review the state of the art of single photon detectors. Then, we will provide a basic outline of the phenomenon of superconductivity. The main physical concepts are detailed to refine the understanding of this work. The detection mechanisms and fundamental characteristics of superconducting single-photon detectors are then described and developed. Following that, the state of the art of the SNSPDs is discussed. Then, in chapter 3, the optimization of the challenging growth of ultrathin NbN film on an AlN/Silicon substrate by sputtering technique is presented. The fabrication of a simple vertical SNSPDs to validate the detection properties of developed NbN is also addressed in chapter 3. Chapters 4 and 5 are devoted to the development of CMOS-compatible SNSPDs integrated with a photonic Silicon waveguide. Chapter 4 covers the design of integrated SNSPDs as well as the layout of the dedicated maskset. The optimized design for achieving high-efficiency waveguide-integrated SNSPDs will be shown, and the potential of cavity-coupled SNSPDs, in particular with a silicon ring resonator, will be discussed. Finally, in chapter 5, we will present the fabrication of the first integrated SNSPDs in a 200mm silicon platform and the preliminary optical and electrical characterizations of SNSPDs at room temperature.

Chapter 2 - Single Photon detection

2.1 Introduction

Single Photon Detectors (SPDs) are one of the fundamental building blocks of quantum photonic systems. Through this chapter, we will review the state of the art of single photon detectors. Then, we will provide a basic outline of the phenomenon of superconductivity. The main physical concepts are detailed to refine the understanding of this work. The detection mechanisms and fundamental characteristics of superconducting single-photon detectors are then described and developed. Finally, the state of the art of the SNSPDs is presented.

2.2 Single Photon detectors

2.2.1 State of the art of semiconductor single photon detectors

2.2.1.1 Photo-multiplier tubes PMTs

After demonstrating that the photoelectric effect was due to the absorption of single photons, this discovery paved the way for the possibility of exploiting this effect as the basis for the first single-photon detector. The latter refers to a device capable of delivering a measurable response to the absorption of a single photon. The photomultiplier tube PMT was invented in 1935, and it was the first detector able to detect single photons.

Under the action of photons, electrons are extracted from the metal by the photoelectric effect. The weak electric current generated by the photocathode is then amplified through a series of dynodes via secondary emission to obtain a high gain. The signal becomes large enough to be detected by ordinary electronics.

Photomultipliers have progressed significantly since 1935 and can be designed for diverse spectral ranges by changing the photocathode material. They are mature to detect photons of wavelengths shorter than one µm. Indeed, it is difficult to trigger the cascade process for lower energy photons (longer wavelengths). In particular, they deliver reasonable efficiency in the 300 - 720 nm range and reach up to 39 % at 550 nm [36] but only 2 % percent at 1550 nm [37]. However, because of their low efficiency at the telecommunication wavelength, they are not suitable for applications such as quantum communication. In addition, they obviously cannot be integrated due to their sizes. This disadvantage has driven the development of solid-state alternatives.

2.2.1.2 Single Photon Avalanche Diode SPAD

Avalanche photodiode is the solid-state semiconductor analog of a photomultiplier. The photo-excited electron emission and cascade amplification occur in avalanche photodiodes within a semiconductor rather than in a vacuum-like tube. The pioneer works studied photoemission processes with germanium diode in 1969 [38], and the first realization of single-photon detection in semiconductor diodes was in 1971 [39].

When a photon is absorbed, with an energy higher than the material bandgap, it creates an electron-hole pair in the depletion region of the photodiode. The carriers are then driven towards the electrodes, the p, and n region, respectively, for the hole and electron generated. When the polarization of the photodiode is large enough, other electron-hole pairs are excited during the scattering of the carriers towards the electrodes. These pairs allow amplifying the photo-induced current. Unfortunately, this amplification is not sufficient to detect single photons. In order to detect low photon flux or single photons, avalanche photodiodes are used in Geiger mode. In this mode, they are biased close to the breakdown voltage. Beyond this voltage, the diode becomes conductive. The current increases exponentially with the applied voltage until it reaches a large enough value to be measured.

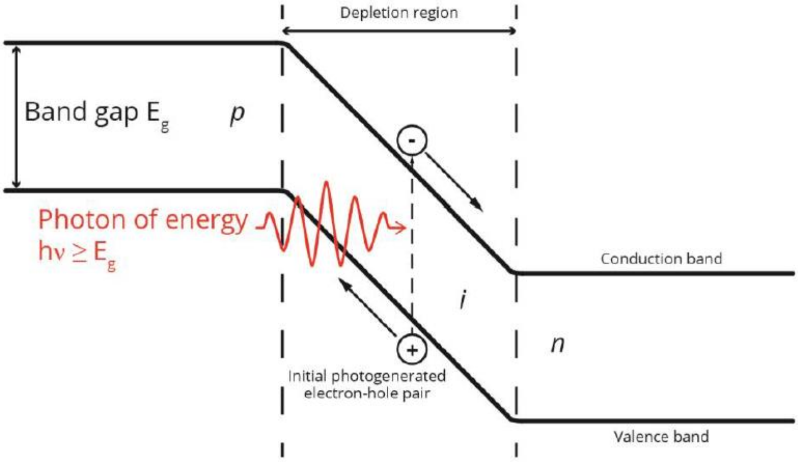

;

Figure 3: *Band diagram schematic showing the working principle of APDs*

To summarize, an Avalanche Photodiodes APDs work in linear mode and are biased below the breakdown voltage. Therefore, the current delivered is, to a first approximation, proportional to the number of incident photons on the detector, and therefore it can be used to "count" how many photons arrive. On the other hand, Single Photon Avalanche Diode SPADs have a nonlinear response; regardless of the number of incident photons (1 or more), the output is always the same because of the saturation of the generated current. Moreover, there is a "reset" time for SPADs to restore their state and allow them to be ready to detect the successive photons.

SPADs are probably the most widely used single photon detectors in quantum optics. Geiger-mode SPADs based on silicon work within the spectrum including, visible and a part of ultra-violet and near-infrared (350 - 1000 nm). They are excellent detectors in the visible, having detection efficiencies as high as 90% [40]. At wavelengths above 1100 nm, the energy of a single photon becomes smaller than the bandgap energy of Si [41]. Si-SPADs are therefore transparent, and their detection efficiency is negligible.

In the telecom band (1310 and 1550 nm), lower bandgap materials such InGaAs/InP-SPADs replace Si-SPADs [42]. Their detection efficiency is about 70% [43]. However, structures made from III-V materials suffer from high dark count rates and after pulsing due to trap states and defects. Since InGaAs has a narrow bandgap, thermally generated dark counts in the absorption region can be a significant contributor to the total dark count rate. Trap densities in III–V detectors result from epitaxial growth. As deposition technologies improve, SPADs with III-V materials will be able to achieve similar performance to their silicon counterparts. Specifically, they show a dark count rate of a few kHz and a time jitter larger than 150 ps. Hence, their detection speed is low, limiting their bandwidth [44].

Ge-Si APDs are also used for near IR detection. In such devices, light absorption takes place in Ge while the multiplication gain occurs in Si. Ge epitaxy on silicon is used to fabricate Ge–Si detectors. However, the inevitable defects at the Ge-Si interface result in a relatively high dark current that is comparable to that of their InGaAs/InP counterparts. The performance of these detectors in the future will depend on reducing the impact of the large number of defects (traps) at the Ge/Si interface [45].

The HgCdTe avalanche photodiode has also been known for a long time. However, it was not until the early 2000s that the remarkable properties of the avalanche were interpreted correctly. For APDs made with other materials, the gain is associated with significant degradation of the signal-to-noise ratio. On the other hand, APDs based on HgCdTe are based on a multiplication process initiated by a single carrier (either electrons or holes). This depends on the composition of the material, but in general, it is most often electrons. Hence, the multiplication takes place without any excess noise. Therefore, it is possible to achieve a high multiplication gain (needed to measure single photons) while maintaining a large bandwidth (~GHz or even ten GHz) to detect fast signals. For applications based on single-photon detection, it is crucial to amplify the signal without degrading it [46–48].

2.2.2 State of the art of superconductors detectors

To detect single photons, technologies based on superconducting devices have been developed in addition to photomultiplier tubes and semiconductor-based technologies presented earlier.

The energy of the superconducting gap is of the order of few meV. An incident photon has an energy a thousand times higher (1eV at 1µm), breaks a large number of Cooper pairs and creates many quasiparticles. The absorption of a photon strongly modifies the properties of the superconducting device. There are different types, and we present some examples here.

2.2.2.1 Transition-edge sensors TES

TES, also called superconducting phase-transition thermometers, are thermal detectors. These detectors operate with a constant voltage at the edge of the superconducting-normal transition. The absorption of an incident photon induces a temperature increase locally, leading to an increase of the resistance. The energy dissipated by the Joule effect is not maintained, and the detector returns to its equilibrium state by itself. The output signal results in a change of the resistance, and it is measured and amplified using a superconducting quantum-interference device (SQUID) array at cryogenic temperatures.

In the infrared, TESs have an efficiency over 90% and a low dark count rate as a result of the very low operating temperature (< 100 mK). In addition, they can be engineered to be sensitive over a wide range of wavelengths by proper selection of the superconducting material.

As a thermal device that measures the absorbed energy, its output is proportional to the number of absorbed photons. Therefore, these detectors inherently show photon-number-resolving (PNR) capability [49]. Despite these high detection efficiencies and very low dark-count rates, drawbacks generally include a slow response of ≈100 ns, maximum counting rates up to 1 MHz [50], and the requirement to operate at temperatures below 100 mK.

2.2.2.2 SNSPDs

Similarly, to TES, SNSPDs essentially exploit the unique properties of superconductors. Section 3 of chapter 2 will be dedicated to these types of detectors.

2.2.3 Conclusion

From a fabrication perspective, semiconductor technologies for single-photon detection are very advanced, and the detectors do not require cryogenic temperatures to operate. However, particularly at telecom wavelengths, they suffer from low efficiency, high dark count rates (DCRs), and long-dead times. Therefore, these detectors are not suitable for quantum information applications where these figures of merit are the key parameters.

On the other hand, Superconductor detectors have also progressed rapidly in the last decade. TES detectors inherently resolve the photon number in a given pulse while requiring a very low operating temperature (< 100 mK) and being extremely slow for high-speed applications.

All of the detectors discussed so far have several limitations. SNSPDs detectors, the subject of this thesis, are very promising technology thanks to their high efficiency, high speed, low jitter, and low achievable dark count rate. Moreover, the outstanding performance of SNSPDs combined with the possibility of integration on semiconductor substrates has motivated us to choose SNSPD as a single-photon detector.

In what follows, Section 3 first will provide a basic overview of the phenomenon of superconductivity. Afterward, the main physical concepts are detailed to refine this work's understanding. Then, the detection mechanisms and fundamental characteristics of superconducting single-photon detectors are described and developed. Finally, the state of the art of SNSPDs is discussed.

2.3 SNSPDs

SNSPDs are at the intersection of multiple physics fields, including quantum optics, nanostructure physics, materials science, and superconductivity. To fully understand the behavior of detectors and push their properties to their fundamental limits, one must first understand their material and superconducting properties.

2.3.1 Superconductivity (Meissner/BCS/Landau/types of superconductors)

Superconductivity is most often described as a phase where the electrical resistance of the material vanishes. The second remarkable property of superconducting materials is the Meissner effect. The latter corresponds to an expulsion of the magnetic field out of the volume of the material. As a result, an electric current can flow endlessly through a loop of superconducting wire without the need for an external power.

This phenomenon generally occurs at very low temperatures of the order of a few Kelvins, with a record at room temperature (about 15 degrees Celsius) of carbonaceous sulfur hydride. This record is reached at high pressure about 270 GPa and in the presence of a high external magnetic field up to 9 Teslas [51]. The temperature at which this phenomenon appears is a material fundamental characteristic, and it is known as the critical temperature T_c.

Meissner effect

In its normal state, a superconducting material can be paramagnetic or diamagnetic, but during its superconducting transition, it becomes a perfect diamagnetic, resulting in an expulsion of the magnetic field. This is known as the Meissner effect.

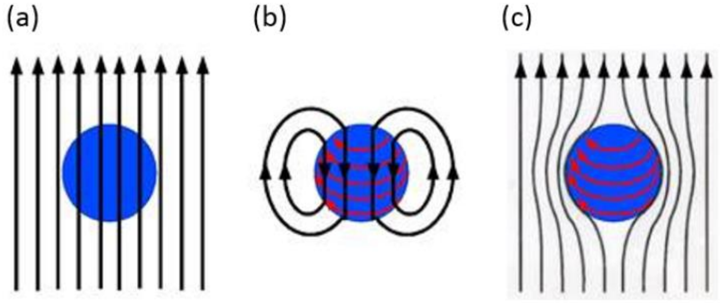

Figure 4 : *(a) normal state, with external magnetic field, (b) superconducting state, representation of the supercurrents, (c) superconducting state: expulsion of the magnetic field*

In Figure 4.a, the black arrows represent the external magnetic field applied to a sample in its normal state. When the sample becomes superconducting, currents appear on its surface, represented by red arrows. These currents create an internal magnetic field represented on Figure 4.b, here the external magnetic field is not illustrated. These supercurrents create a magnetic field that exactly compensates the external field. Therefore, the external magnetic field cannot penetrate the material, as shown in Figure 4.c.

The two fundamental theories that describe superconductivity are the BCS and the Ginzburg-Landau theories.

BCS theory

Bardeen Cooper and Schrieffer's theory (BCS) [52] established in 1957, addresses the microscopic aspect of superconductivity. This theory explains how, below the critical temperature, the electrons of a superconducting material condense into Cooper pairs of the same momentum and opposite spin, thanks to an attractive potential that overcomes the Coulomb repulsion. This condensation is achieved through interactions between the electrons and phonons of the material. The phonon is a quanta of vibration of the crystal lattice of the material. When an electron, of charge -e, passes near one of the ions of the crystal lattice, the positively charged nuclei of the lattice are attracted.

This induces a deformation of the electronic cloud, which is equivalent to a vibration, a phonon. This deformation attracts another electron toward the most positively charged region and allows it to pass through the same path as the first electron. A distant interaction between the two electrons is created, and a Cooper pair is formed.

The pairing is done at a maximum distance called coherence length and noted ξ defined in equation (1). It can be calculated using the Ginzburg Landau theory. ξ is of a few nanometers for complex compounds [53] and can reach hundreds of nanometers in some metals [54].

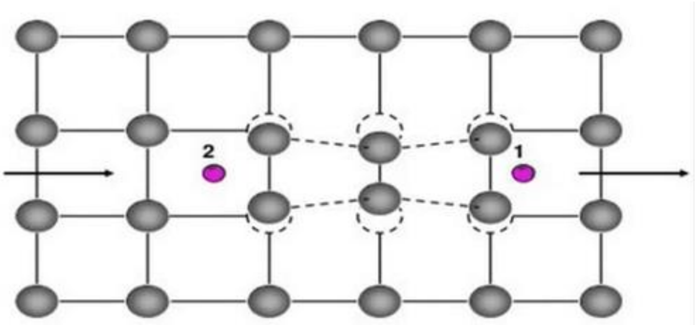

Figure 5 : *schematic explanation showing the pairing of electrons near the Fermi level into Cooper pairs via interaction with the crystal lattice [55].*

Ginzburg Landau theory

On the other hand, the Ginzburg Landau theory (1950) [56] addresses the macroscopic aspect of superconductivity. This theory describes the superconducting transition as a phase transition. Cooper pairs are described as a Bose-Einstein condensate. Due to their bosonic nature, they are not subject to the Pauli exclusion principle. Consequently, the Cooper pairs condense on the same energy level. In the theory of quantum mechanics, fermions are described by antisymmetric states. In contrast, particles with integer spin, bosons, have symmetric wave functions; unlike fermions, they share the same quantum states. Indeed, the pairing of two fermions (electron) of non-integer spin forms a quasi-particle of boson type (Cooper pair) with integer spin. Obviously, several electrons will pair up in a material, resulting in a spatial overlap of the pairs that condense into the quantum ground state. This results in an opening of a gap of 2 Δ in the excitation spectrum of the material. The parameter Δ corresponds to the binding energy of the cooper pair. Figure 6 compares the energy versus density of electronic states for a superconductor and for a normal metal.

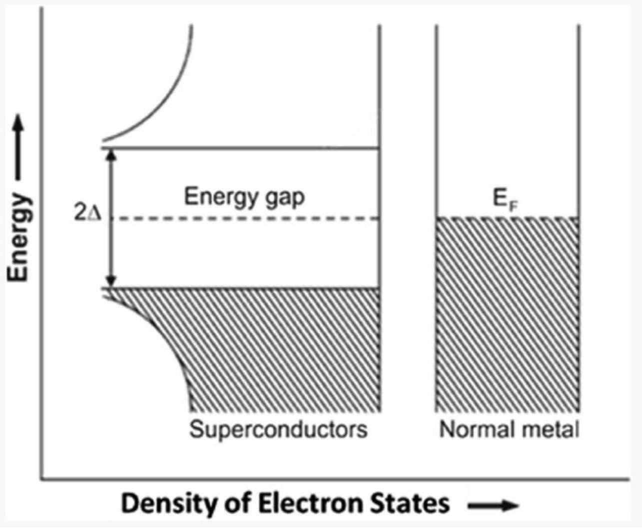

Figure 6 : *Densities of states of a metal in its normal (N) and superconducting (S) states, near the Fermi level E*$_F$ *[8].*

Unless the voltage increases to $E_g = 2\,\Delta$, no current flows at 0 K. The gap separates normal electrons from superconducting electrons. Normal electrons are above the energy gap, while superconducting electrons are below it. Because the normal electrons are thermally excited across the energy gap at nonzero temperature, a small current always flows even at a lower voltage. The energy gap reaches its maximum value at 0 K, whereas it reaches its minimum value at T_c.

Two fundamental parameters can be used to describe a superconductor: the coherence length ξ described earlier and the London penetration depth. These two characteristics are unique to each superconductor and are used to determine the Meissner effect, the superconductor's types, and the presence of vortices. These parameters are defined as the following:

$$\xi = \sqrt{\frac{\hbar}{2m|\alpha|}} \qquad \text{and} \qquad \lambda_L = \sqrt{\frac{m}{\mu_0 n q^2}} \quad \textbf{(1)}$$

Where $\hbar$ is the reduced Planck constant, m is is the mass of the charge carrier, $|\alpha|$ the wave overlap, $\mu_0$the magnetic permeability of the vacuum and n the density of charge carriers and q the carrier charge. In addition, the Ginzburg-Landau theory distinguishes between two types of superconductors according to the parameter k:

$$k = \frac{\lambda_L}{\xi} \quad \textbf{(2)}$$

The ratio of the London penetration depth λ to the superconducting coherence length ξ determines whether a superconductor is type I or type II. They differ in the way they switch from the superconducting to the normal state under the effect of a magnetic field.

Superconductor of type I

Type I superconductors are mostly pure metals (aluminum, lead, mercury, etc.) with k<$\frac{1}{\sqrt{2}}$. While most elemental superconductors are type-I, niobium, vanadium, and technetium are elemental type-II superconductors. These materials are fully described by the BCS and Ginzburg Landau theories. They show low critical temperatures between 0K and 10K.

The graph below shows the behavior of a type I superconductor as a function of temperature and magnetic field. The critical temperature of superconductivity noted T_c is the temperature at which a material becomes a superconductor without the presence of a magnetic field. The critical magnetic field of the superconductor noted H_c is the strength of the magnetic field required to make the material switch from its superconducting state to its normal state. Above it, the Meissner effect disappears, and the magnetic field can penetrate the material. Another parameter not represented here is the critical current noted I_c. It corresponds to the current needed, without a magnetic field, to make a superconductor transit to its normal state.

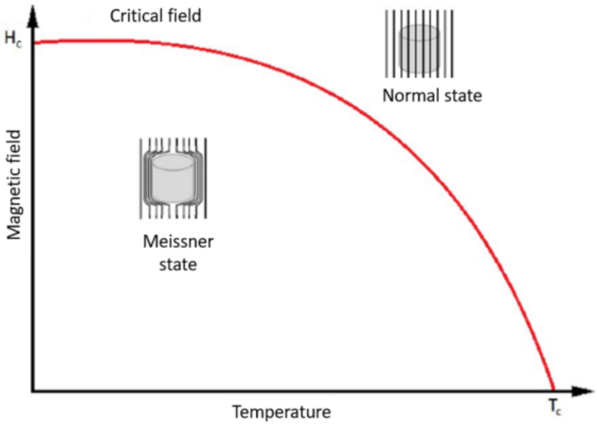

Figure 7 : *Behavior of a type I superconductor as a function of temperature and magnetic field*

Type I superconductors are also known as soft superconductors since they lose their superconductivity by low intensity magnetic field, usually up to 1T.

Superconductor of type II

Unlike type-I superconductors, type II exhibits two critical magnetic fields. The first, lower required field noted H_{c1}, occurs when magnetic flux vortices penetrate the material. The magnetic field forces the material to go from the Meissner state to a mixed state. It remains nevertheless partly superconducting outside of these microscopic vortices. Beyond the higher critical field H_{c2}, the vortex density becomes too large. As a result, the material switches from a mixed state to its normal non-superconducting state.

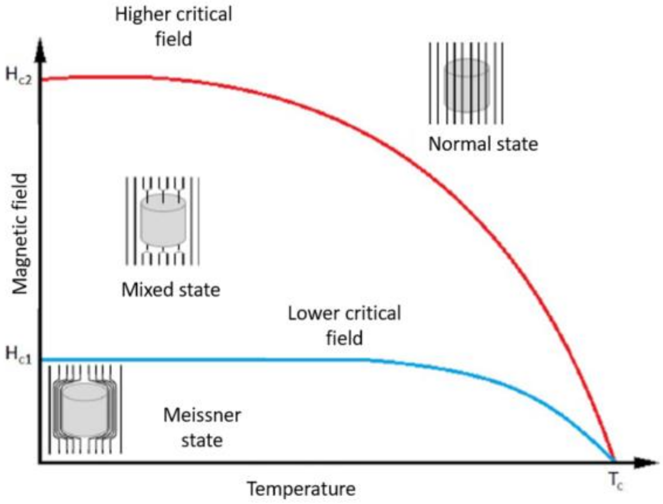

Figure 8 : *Behavior of a type II superconductor as a function of temperature and magnetic field*

Type II superconductors are complex compounds grouped by family A15 [57], cuprate [58] oxide [59]…

A vortex can be illustrated as two nested coaxial cylinders (Figure 9), whose radii are respectively, for the inner cylinder, the coherence length ξ, the outer cylinder, and the London length λ_L. This is a borderline case where the coherence length is much smaller than the London length, which corresponds to a very schematic representation of the vortex[63]. The core of the vortex is a non-superconducting zone since the superconducting electron density falls to zero. Therefore, at the core of the vortex the magnetic induction is maximum. Outside the core, currents flow without losses, acting as a screen for the induction effect on the core electrons. These screening currents, called supercurrents, develop over the thickness of the London penetration length. Over this thickness, the magnetic field does not vanish abruptly but instead decays exponentially. This decay is related to the density of superconducting electrons in the material.

The core electrons do not form pairs and interact freely with the magnetic field in which the superconductor is exposed. They are thus subjected to a Lorentz force of intensity F_L such that

$$F_L = \frac{evBsin(\vec{v};\vec{B})}{c} \quad \textbf{(3)}$$

e being the charge of the electron, v the average speed of the latter, B the intensity of the magnetic field, and c the speed of light.

The vortices are driven by the electron's motion, which dissipates energy in the superconductor and contributes to a temperature increase and if significant enough, implies a return to the material's normal state.

The existence of vortices makes the material partially permeable to the magnetic field. This allows it to reduce the constraint of the magnetic field and allows its use in high magnetic field environment. In a perfect material, the vortices are mobile, but in reality, the defects of the materials fix the vortices. The areas where the critical temperature is low are energetically favorable for vortex formation.

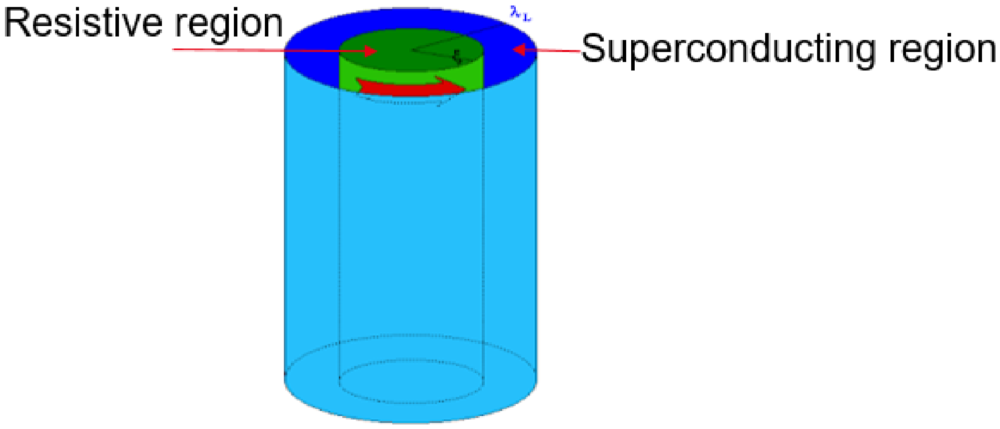

Figure 9 : *Cylindrical representation of vortices in a superconducting film*

In 2014, it was shown that vortices play a role in the detection mechanism of superconducting nanowire single-photon detectors [64], this will be discussed in the section on detection mechanisms.

2.3.2 Correlation between the electronic properties of superconducting materials and the lattice parameter

In 1950, the isotropic effect in the superconductivity of Mercury was studied [65]. The conclusions suggest that a superconductor's transition temperature is a function of nuclear mass. As the mass is lighter, the transition temperature is higher. The lattice parameter of the crystal lattice also seems to have an influence on the superconducting properties of the material. For this purpose, NbCN was studied. The idea was to modify the lattice parameter of a high T_c system, here the NbN, without modifying the mass and the quantity of valence electrons of the material. It turns out that $NbC_{1-x}N_x$ (0.15<x<0.40) has a T_c of 17.8 K [66] higher than the best values observed for NbN. In [67], the same group suggested that the phonon amplitude is larger for materials with a larger lattice parameter, resulting in an increase in the critical temperature.

2.3.3 Influence of the disorder on superconductivity

In general, a disordered material can be defined as a deviation from the ideal nature of a single crystal. It can be present on a small scale (impurities or vacancies) or a large scale (polycrystalline material, amorphous).

Superconductivity is a phenomenon that depends on the level of disorder in the material. This disorder can be structural or due to the miniaturization of superconducting structures (thin films (2D), wires (1D), or particles (0D)).

When the disorder of the material reaches a critical level, the superconducting properties are suppressed. The superconducting material then becomes an insulator; this is known as the superconducting-to-insulator transition (SIT). Superconducting nanostructures have T_c, H_c, J_c lower than those of non-disordered and bulk materials. A representation of this phenomenon is shown in Figure 10.

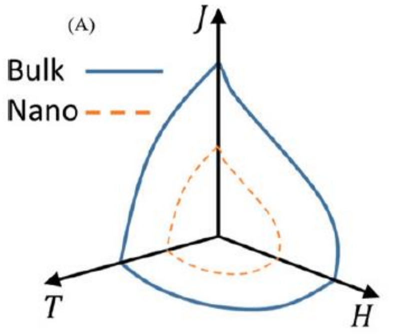

Figure 10 : *Schematic illustration that demonstrates the suppression of superconducting properties upon miniaturization. It is expected that below a certain size, the material completely loses its superconducting properties and becomes an insulator in a superconducting-to-insulator transition (SIT) [68]*

In a metal, the electric current is provided by the movement of electrons. These moving charges interact with the atoms of the lattice. A metallic "single crystal's" resistivity is determined by three factors: $\rho = \rho_T + \rho_i + \rho_{vac}$. The temperature factor ρ_T is the interaction of the electrons with the phonons formed by thermal agitation. The impurities ρ_i, on the other hand, break the network's periodicity and increase electron diffraction. The atom's vacancies ρ_{vac} correspond to a potential well, which slows down the electrons.

Single crystals have a long-range order. For polycrystalline materials, this order is broken by grain boundaries. A grain boundary can be seen as a break in the symmetry of a lattice. Either it is a void of several Angströms; in this case, the tunneling effect allows electrons to pass through it, or it is a band of amorphous material (often of the order of nanometer). In contrast, amorphous materials do not have long-range order, so the path of the electrons is disturbed, resulting in an increase in electrical resistance.

The combination of all of these factors reduces the material's conductivity and converts its metallic character to an insulating one. This particular state is known as the Mott insulator. A material with metallic behavior has a low resistance that decreases with increasing temperature. An insulating behavior exhibits the opposite. The resistivity is high, and as the temperature drops, the resistivity increases

The RRR (Residual Resistivity Ratio) is a metric that describe the electrical behavior of a material. The RRR is the slope of the resistivity curve between two temperatures. In the case of superconductors, it is the ratio between the resistivity at 300 K and at a temperature higher than the critical temperature T_c. If RRR>1 the material has a metallic behavior, if RRR<1 the material has an insulating behavior.

$$RRR = \frac{\rho_{300K}}{\rho_{20K}}$$

2.3.4 Detection mechanisms: physics of superconducting detectors

This section provides a qualitative description of the main physical models of the detection processes in SNSPDs, allowing the understanding of the basic operating principles and the device physics.

The first approach investigates the processes that lead to hotspots, resulting in a local superconductivity suppression. The second approach assumes that perturbation is caused by vortices rather than the breaking of Cooper pairs. The last approach will complete the picture by explaining the transition from a hot spot to a measurable voltage pulse. We will wrap up this section with a quick overview of the single-photon detection setup.

2.3.4.1 Microscopic picture: hotspot model

The formation of a hotspot, as introduced by Gol'tsman et al [69], can be explained by a cascade of several processes, that will be detailed in this section. In order to understand the mechanism involved in single photon detection using superconductors, we consider a thin superconducting film, of a few nanometers thick, maintained well below its critical temperature, as shown in Figure 11.

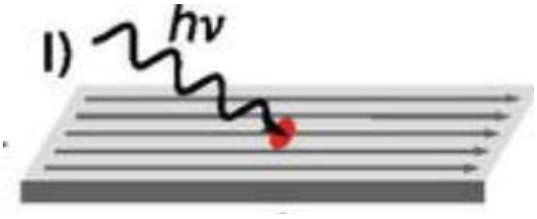

***Figure 11 :** Adapted from [70], a representation of the photon absorption process in a thin superconducting wire. The breaking of Cooper pairs occurs when a photon of energy* $\boldsymbol{h\nu}$ *is absorbed, resulting in a normal-conducting hotspot. The arrows denote a constant bias current* $\boldsymbol{I_b}$*.*

Let's first set the energy of the impinging photon

$$E_\gamma = \hbar\omega = h\nu = \frac{hc}{\lambda} \quad \textbf{(4)}$$

with $\hbar$ the Planck's constant, c the speed of light in vacuum, ω the photons angular frequency, ν the photons frequency, and the wavelength λ. The energy of a photon in the visible to near-infrared spectrum is in the range 1 to 3 eV. The absorption of such quanta can break apart a Cooper pair due to its very low binding energy $2\Delta \sim 3k_B T_C \sim 1\,meV$ with $T_c \sim 10$ K and k_B the Boltzmann constant.

As presented in Figure 12.a, the incident photon energy is absorbed by one Copper pair, resulting in one highly excited quasi-particle (energy close to the incident photon energy) and one low energy quasi-particle. Only one quasi-particle absorbs the incident photon because of the Cooper pair's large physical size (coherence length). Here, a quasi-particle refers to a single electron within the superconductor.

After absorption, very quickly, within a time of femtoseconds, this highly excited quasi-particle relaxes via electron-electron scattering (e-e), resulting in the formation of secondary quasi-particles. The emission of Debye phonons by electrons (e-ph) becomes the most efficient mechanism for energy redistribution within the electron subsystem when the average energy of the excited electrons is on the order of the Debye energy (0.1 eV).

These generated phonons excite, on their own, other electrons by breaking additional Cooper pairs. The e-ph process continues until the average energy of the system reaches the energy gap 2Δ (about 1 meV). Then, the quasi-particle avalanche process takes place by electron-electron collisions. The effective temperature of the system rises as the excited quasi-particles reach an ideal density. Because this temperature is considerably over the critical temperature, superconductivity is suppressed locally, resulting in the formation of a hot spot.

Then, as depicted in Figure 12.b, electrons with energies just above 2Δ condense into Cooper pairs and generate acoustic phonons during a time τ_R. These phonons have enough energy to break other Cooper pairs, represented in Figure 12.c, which leads to the growth of hot spots on a time scale τ_B , in the order of picoseconds. In the case of NbN $\tau_B = 7ps$ [71]. These processes continue until the substrate finally evacuates the phonons via electron-phonon interactions, and the hot spot relaxes. The wire becomes totally superconducting again, Figure 12.d [72].

Furthermore, Semenov et al. [73,74] established a direct link between the energy of the incident photon and the binding energy of the Cooper pair, setting a cutoff energy to form detectable hotspot

$$E_\gamma = h\frac{c}{\lambda} = \frac{N_0\Delta^2 wd\sqrt{\pi D\tau_{th}}}{\zeta}\left(1-\frac{I_b}{I_c}\right) \quad \textbf{(5)}$$

Here N_0, w, d, D, τ_{th} and ζ are the normal metal density of states at the fermi level, width of the nanowire, film thickness, normal state diffusivity, electron thermalization time and the multiplication efficiency of quasiparticles.

This model predicts better agreement with experimental results at a longer cut-off wavelength, but it still fails to explain the detection mechanism beyond the cut-off wavelength, as well as dark counts and their exponential behavior as a function of bias current. Vortex-related mechanisms have been proposed as explanations for these phenomena.

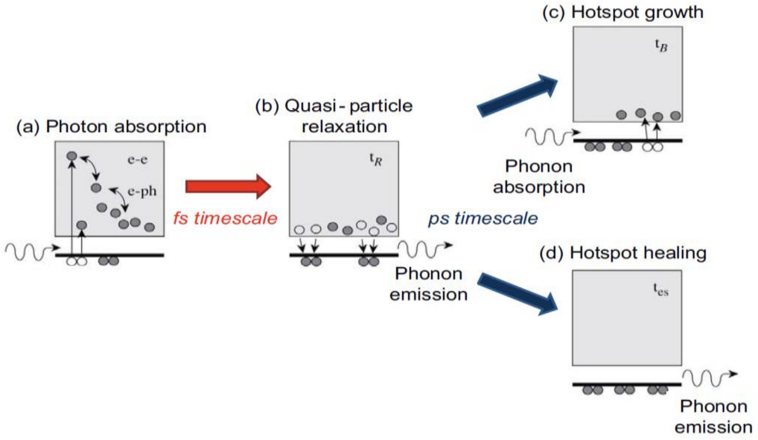

Figure 12 : *Photo-induced avalanche process in a superconductor[69]*

2.3.4.2 "Vortex-antivortex pair" model

The perturbation in the "vortex-antivortex pair" model arises from the formation of vortices rather than the breaking of Cooper pairs. Several groups have suggested that vortices could explain the origin of dark counts and low-energy photon detection.

The Berezinski-Kosterlitz-Thouless energy [75,76], $k_B T_{KBT}$, corresponds to the energy necessary to create a vortex-antivortex pair. In the absence of a magnetic field, this energy is generally too high. However, in thin films, d ~ ξ, this energy can be comparable to $k_B T$ [77,78]. As a result, the resistance does not disappear for such a superconducting thin film below T_c. On the contrary, it gradually decreases until $T = T_{BKT}$, where it reaches a second transition. This is known as the Berezinskii-Kosterlitz-Thouless (BKT) superconducting transition. Vortices are free at temperatures between T_{BKT} and T_c and become bounded below T_{BKT}. The residual resistance induced below T_c depends then on the density of the free vortices.

Vortex-assisted superconductivity destruction can be caused by one of the two following mechanisms:

- The photon's absorption locally increases the temperature of the superconductor. This temperature rise provides the system with enough energy to allow a vortex to penetrate the material. The current flow assists the vortex to cover the wire throughout its whole width, resulting in a disruption of superconductivity. After that, the wire becomes resistant.
- The photon's absorption produces a vortex-antivortex pair. In the presence of an electric current, free vortices are subject to the Lorentz force. The vortex and antivortex acquire a non-zero velocity and flow through the sample in opposite directions. The pair is broken when they are far enough apart, releasing a large amount of energy. The wire then transits from superconducting to non-superconducting

The two vortex-antivortex mechanisms generate events with identical characteristics. For the time being, neither of them has been ruled out. The validity and limits of these models have been thoroughly investigated by Engel et al.[79]. The absorption of a high-energy photon can also be explained using the hotspot model. Instead, the vortex-antivortex models explain the absorption of a low-energy photon. This means that no single model can explain all of the observations. Indeed, many processes may exist for the same detector at different photon energies, and multiple mechanisms may occur simultaneously. However, the governing mechanism may also be dictated by the device's material and geometry.

2.3.4.3 Macroscopic picture

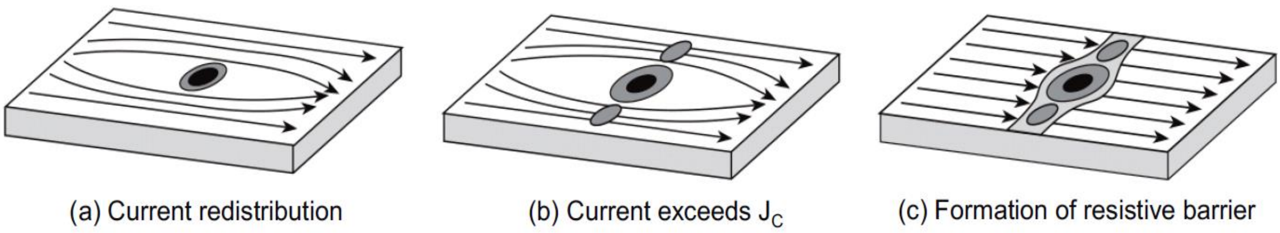
(a) Current redistribution
(b) Current exceeds J_C
(c) Formation of resistive barrier

Figure 13 : *Macroscopic explanation of the detection mechanism based on [69]*

Figure 13 depicts the SNSPD's basic operating principle schematically according to [69]. After the photon absorption and formation of the hotspot, the bias current in the superconducting nanowire is redistributed into the side channels due to the ohmic resistance of the hotspot (Figure 13.a). The current density in the side channels exceeds the critical current density J_c since the bias is close to the critical current, forcing the side channels to become resistive (Figure 13.b). The hotspot expands along the nanowire due to the Joule effect. Consequently, the wire loses its superconductivity and becomes resistive across the entire width of the nanowire; the resistance becomes in the order of several $k\Omega$ (Figure 13.c). The SNSPD is then connected in parallel to a shunt resistor (typically 50 Ω), forcing the current flowing in the nanowire to be quenched and to be redistributed in the shunt resistor's circuit (see Figure 16. A). An output circuit is used to transfer the bias current toward the readout electronics. Indeed, the current is expelled to the external load resistance and generates a voltage pulse, an equivalent electrical circuit of an SNSPDs is represented in Figure 16.A. When the heat is released through the substrate, the hotspot relaxes, superconductivity is restored, and the detector is ready to detect the next photon.

2.3.4.4 Setup description

After going over the physical models of the SNSPD detection mechanisms, we will now discuss the single photon detection setup. Figure 14 depicts this three-part configuration:

- **The optical part:** It is composed of a photon source, in this case, a continuous wave CW laser at 1550 nm, a polarizer that allows the polarization of the photons, and an attenuator that limits the photon flux to 10^6 photons per second. This photon flux is then brought to the SNSPD via an optical fiber.
- **The detector part:** The SNSPD system is composed of a superconducting device and a cryostat. It is usually cooled using a close cycled cryostat (<2.5 K). However, liquid helium is sometimes used to cool the device to 4.2 K.
- **The electronic part:** A voltage source in series with a $20\ k\Omega$ resistance was used as a quasi-constant current source for biasing the SNSPD. Then, a 50 dB low noise amplifier was used to amplify the generated voltage pulses, and a frequency photon counter was used to measure them.

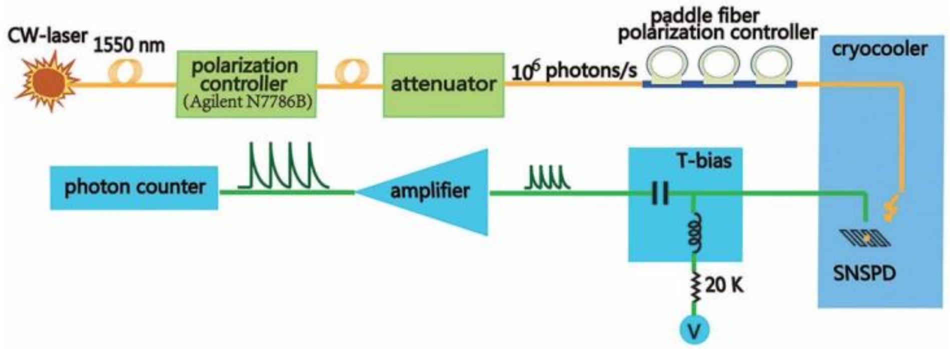

Figure 14 : *an example of system's schematic. The optical components are represented by the yellow line, while the green line represents the electric components [80].*

2.3.5 Performance parameters of an SNSPD

A good detector's key characteristics can be classified into two categories: event-related and temporal. The event-related characteristics are device efficiency DE, and the dark count rate DCR. The two temporal characteristics are the time between the arrival of the photon and the electrical signal generation, called temporal jitter, and the time required for the device to be ready to measure a new photon, defined as the reset time.

These are the characteristics that allow assessing the quality of an SNSPD. They are dependent on a variety of properties, which are categorized in this section according to their origins. The intrinsic properties are those depending on the film, from the choice of the material as well as its shape, structure, and geometry. These parameters are set for a specific device. The extrinsic parameters are related to the temperature and the optical or electronic part of the measuring bench. These factors have an extrinsic impact on the device's performance.

2.3.5.1 Detection efficiency

Detection efficiency is the probability that an incident photon will produce a measurable signal. Efficiency can be calculated by illuminating a detector with a given optical power and comparing the input photon flux to the detector count rate. The number of photons is derived by dividing the optical power P by the energy of single photon $E_{photon} = \frac{hc}{\lambda}$. For a detector operating in the single-photon counting regime, the number of photons absorbed within the detector recovery time is kept <<1 to avoid multiphoton absorption and saturation of the number of counts. Therefore, the efficiency can be expressed as

$$\eta = \frac{R}{\Phi} = \frac{Rhc}{P\lambda} \quad \textbf{(6)}$$

Where R denotes the detector's count rate in counts per second and Φ the impinging photon flux coupled to the system.

It is expressed as a percentage throughout this manuscript, with a maximum of 100%. The overall system detection efficiency SDE of a detector is governed by three independent factors and can be decomposed in the following way

$$\text{SDE} = \eta_{cpl} * \eta_{abs} * \eta_{qe} \quad \textbf{(7)}$$

Where

- $\boldsymbol{\eta_{cpl}}$

The coupling efficiency describes the coupling between the light source (input) and the detector. In other words, how many photons will arrive in the detection area. This factor η_{cpl} depends on the design of the detector and the optics of the system. For stand-alone detectors, light is delivered directly to the SNSPD chip through a fiber. Large active area [81] and fill factor [29] play an essential role in improving these devices. A nanowire meander is written typically across a 10µm×10µm [82,83] or 20µm×20µm area [84], allowing for efficient coupling to single-mode optical fibers. The losses of a fiber-coupled detection system are defined as the proportion of the photons transmitted to the input port lost before reaching the detector's active area. It is, therefore, the sum of the geometric coupling losses and any losses of the fiber within the detector system, such as tight bends or optical components like lenses.

In the case of waveguide integrated SNSPD configuration proposed by Pernice et al. [85], the coupling efficiency in this configuration takes into account the reflection at the waveguide facet in this system due to the high refractive index contrast between air and waveguide material, the mode overlap from the fiber to the waveguide, and the waveguide's loss before the photon arrives at the active detector region. This parameter can be determined by simply measuring the waveguide with no superconducting wires on top of it.

- $\boldsymbol{\eta_{abs}}$

It is the ability of the material to absorb a photon. This term does not only depend on the absorption factor of the material and its thickness but also on the design factors. By extension, it also depends on the wavelength and the polarization of the photon. In order to maximize the absorption of a film, it is recommended to select an optimal thickness. Moreover, to have the largest detection area, it is preferable to use a long wire. Besides the meander shape factors, it is important to maximize the presence of the photon in the vicinity of the detector. The presence of mirrors, antennas, and waveguides significantly improves the absorption of the detector.

- $\boldsymbol{\eta_{qe}}$

The quantum efficiency η_{qe} is the probability that the absorbed photon creates a measurable signal. A high SDE is attributed to 100% η_{qe} which is characterized by a long-range saturation of the SDE as a function of the bias current. Therefore, it is preferable to operate the device in the deterministic regime where the η_{qe} saturates at its maximum value. Saturation of detection efficiency is a desirable feature because it enables the detector to operate in a regime where small fluctuations of the bias current have a limited effect on the detector response.

Furthermore, the η_{qe} depends on the film's quality, the photon's energy as well as the parameters of the detection system such as the bias current I_b and the operating temperature T.

Film’s quality:

Because the superconducting films used for the detectors are ultrathin <6nm, inhomogeneities are likely to limit the bias current and, consequently, the efficiency. Indeed, a variation in the film thickness, crystal structure, or wire width can lower the critical current locally. The bias current is limited in this region, and the rest of the wire is biased at a lower critical current. As a result, only the wire portion with a lower I_c will be efficient at photon absorption.

Marsili et al [86] demonstrated that amorphous films are the most suitable to produce SNSPDs with high efficiencies compared to crystalline films. Amorphous films, in fact, exhibit 100% quantum efficiency, which is defined by a long-range saturation of the efficiency as a function of the bias current. Furthermore, they showed that the saturation region shrinks when the operating temperature increases. In order to better select the suitable superconducting material for a SNSPDs, a detailed review of superconducting materials will be discussed in the section “State of the art of superconducting material for SNSPDs”.

From an electrical point of view, the signal measured in an SNSPD comes from the dissipation of the current by the wire in its normal state. In order to increase the current dissipation, it is more likely to use wires with high values of normal state resistance. Higher disorder material shows high values of R_n. Amorphous materials allow for natural disorder and present high values of R_n , whereas crystalline materials can be made to exhibit purposely high disorder. Smirnov et al. [87] showed 94% system efficiency for a high normal state resistance crystalline NbN device. On the other hand, R_n should be carefully engineered because higher sheet resistance requires thinner films, which reduce optical absorption and are more subject to inhomogeneities. Moreover, the bias current I_b has a significant impact on the device efficiency. The latter increases exponentially when I_b increases due to an increase in the internal quantum efficiency until reaching the saturation. A high bias detector is more likely to click when a photon is absorbed than a low bias detector. In order to enhance the efficiency, the detector is biased as close to the maximum current as possible. The DCR, on the other hand, increases with I_b, as it will discussed in the following section. In case the saturation plateau is well defined, the measurement will be performed at the beginning of the plateau (low current). Otherwise, this problem can be solved by setting the operating temperature below 2K to maximize efficiency and reduce the number of obscurities.

<u>Photon's energy</u>

It depends on the energy brought by the photon and its ability to form the hot spot or vortex to make the wire resistive. From a hot spot point of view, the ability of a photon to produce a detectable signal is inextricably linked to its ability to break Cooper pairs to generate quasiparticles. Their concentration during the initial stage of the detection process depends on the ration between the incident photon energy and the superconducting energy gap [88,89]. The higher the energy of the photon compared to the binding energy of the pairs Δ, the greater the number of broken pairs, and it will be more likely to operate in the deterministic regime. The energy of near-infrared photons is smaller compared to the visible photons. The detector's quantum efficiency decreases as the wavelength increases. So, one option to increase the efficiency of near-infrared photons could be to reduce the width of the nanowires, which is typically around 100 nm. The only limitation of this approach is purely technological because by reducing the size of the nanowires, we increase the probability of having variation or constriction across the nanowire. Another method to increase the quantum efficiency is to use superconducting materials with a low bandgap. Since the number of quasiparticles produced by an absorbed photon depends on the ratio of the photon energy to the superconducting bandgap, decreasing the superconducting band gap produces more broken Cooper pairs for a given photon energy.

2.3.5.2 Dark counts rate

A dark count is any measurable signal that is not attributable to the intentional absorption of a photon. One can distinguish the origin from two different sources that can be classified as the intrinsic and extrinsic DCR. Thermal fluctuations cause the intrinsic DCR, which results in a switch to the resistive state without photon absorption. It is inextricably linked to the properties of the material. Materials with strong coupling (large Δ) and, therefore, high values of T_c and J_c have less spurious signals. Low energy stray photons are less likely to produce a signal since fewer Cooper pairs are broken. Furthermore, the ratio of temperature fluctuation δT to critical temperature $\frac{\delta T}{T_c}$ is smaller. As a result, temperature or current fluctuations have a lower chance of producing a signal. Crystalline materials have potentially the lowest values of DCR due to their large binding energy Δ. Unfortunately, this contradicts the requirements for a high efficiency detector. The optimization of one of two characteristics through material selection is done at the expense of the other.

On the other hand, some extrinsic parameters allow the combination of both characteristics. Engel et al. [79] suggested that if the film is narrower than 4.4 times its coherence length, it prevents the appearance of parasitic vortices, and therefore a decrease of dark counts. The use of a thin film, as stated in the previous section, leads to high efficiency.

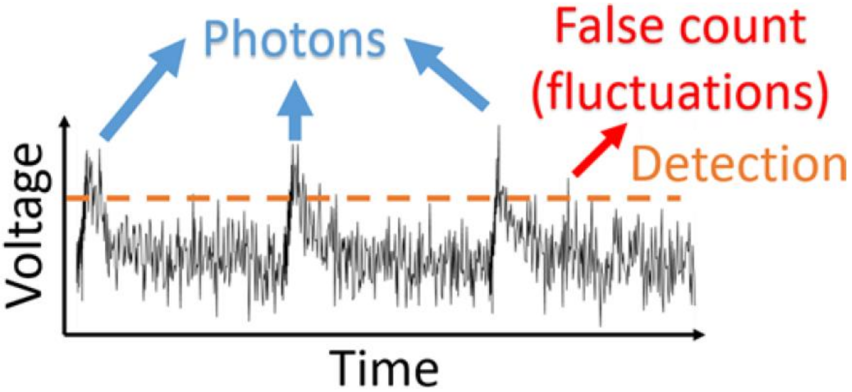

Figure 15 : *Illustration of an acquisition histogram of a SNSPD [68]*

Moreover, to reduce dark counts, short and constriction-free wires are recommended. Once the detector has been fabricated, various extrinsic factors can be adjusted. Tunable properties include temperature and bias current. While the DCR increases with the bias current, it can be reduced by lowering the detector's operating temperature. Moreover, low noise amplifiers and filters, as well as suitable thermal and optical isolation, influence the DCR. Indeed, fluctuations of the electronics measurement system can also create dark counts, but they are identifiable and can be deduced from the noise in practice. Therefore, they must be chosen carefully. For example, the optical fiber has a particular acceptance mode into which background photons can couple in fiber-coupled superconducting detectors. Furthermore, outside of the cryostat, the fiber is at room temperature. Thus, the warm end of the fiber creates blackbody photons that can couple into itself and can be detected by the device within the supported wavelength range and mode of the fiber.

Figure 15 shows a typical SNSPD acquisition histogram. Depending on the detection threshold, the noise can create more or less false signals. The background dark count rate has to be considered while measuring detector efficiency

$$R = R_{measured} - DCR \quad \textbf{(8)}$$

Finally, it is important to keep in mind that a high DCR reduces our confidence in the measured signal. Therefore, a high DCR is a limiting factor for quantum communication technologies [90]. For instance, it gives room for attacks by eavesdroppers in QKD protocols. These attacks are known as photon number splitting (PNS) [91] and beam splitting (BS) attacks [92] , in the case of systems using attenuated coherent pulses.

Concerning the state of the art of SNSPD's dark counts, several studies showed detectors with only a few counts per day .Up to date, a dark count rate as low as 10^{-4} per second has been demonstrated [93] , further studies are required to determine the origin of the remaining dark counts.

2.3.5.3 Jitter

The electrical signal is generated after the photon has been absorbed. On the other hand, this delay is not constant and can vary from one detection event to the next. This delay is known as the jitter. The mechanisms related to the jitter τ are not yet fully understood and are still a subject of current research. It is the result of the combination of two different uncertainties: the fundamental jitter of the device τ_d, which is determined by the design, geometry and the material's properties. The second contribution is the electronic jitter τ_e that comes from the electronics. Each of these factors has an equal influence according to:

$$\tau = \sqrt{\sum {\tau_i}^2} \text{ with } \tau_i \ (\tau_d, \tau_e) \quad \textbf{(9)}$$

Experimentally, the jitter is measured as a correlation between a precise synchronization signal, usually from an attenuated pulsed laser, and the SNSPD's signal. The jitter is determined by taking the full-width-half-maximum (FWHM) of a histogram of counts as a function of the time arrival of a large number of single-photon detection events. Berggren's group believes that the fundamental limit is intrinsic rather than electronic dependent [94]. While, according to Wu et al. [95], the fundamental uncertainty in photon arrival corresponds to the time it takes a vortex to cross the width of an SNSPD, which is around 1 ps. The following paragraphs will provide an overview of the elements that influence the jitter.

The parameters R_n, Δ and L_k intrinsically influence the timing jitter τ_d.The jitter is lower in materials with large binding energy Δ (high T_c & J_c values). This is due mainly to the ability to use higher bias currents. The propagation of a hot spot depends on the energy dissipated by the material. The wire becomes resistive more quickly when subjected to a high electric current [96,97]. This is also valid for films with high resistivity values R_n. A property such as J_c describes the maximum amount of current carried by a superconducting wire. However, this property does not allow us to know how fast a charge carrier is moving. The kinetic induction L_k determines the speed at which the electric signal travels through the wire from the photon absorption region to the electrodes. Indeed, photons can be absorbed in different parts of the wire. As a result, the size of the path between the electrode and the absorption area varies. Therefore, by minimizing L_k and therefore increasing the velocity of the charge carriers, the jitter can be reduced.

However, the most promising parameter to decrease the jitter is the choice of a material allowing a high critical current (large Δ). As a result, this implies that the influence of kinetic inductance comes in a subsequent stage. In other words, optimizing L_k for jitter is required only after the material has been selected, and this is achieved by device design rather than material choice. Moreover, the lowest time jitter is generally observed in crystalline detectors. This may be associated with the large values of Δ and with other properties such as the low values of L_k of crystalline films [68].

Time jitter is also affected by the heterogeneity along the nanowire in terms of cross-section and film composition [96]. Variations in the nanowire's thickness, grain size, and width can all have a local impact on the dynamics of hot spot formation, resulting in temporal jitter. Concerning the detector’s shape, narrow wires confine the hot spot and thus reduce the transition time from the superconducting to the resistive state. In addition, narrower and thinner wires increase resistance and the hot spot kinetics. Finally, reducing the length of the wire has an equivalent effect to reducing L_k. For waveguide integrated SNSPDs, the geometric jitter is believed to be relatively small due to the uniform illumination of the nanowire in the evanescent field of a waveguide, as well as the nanowire's short length when compared to meander-type SNSPDs. In this context, Calandri et al. [94], demonstrated that detection timing jitter is limited in part by the spatial variation of photon detection events along the length of the wire. To characterize the geometric jitter, they constructed a new cryogenic differential reader with less than 7 ps of electron jitter that can amplify pulses generated from both ends of an SNSPD. By differentiating the measured arrival times of the two electrical pulses, they were able to cancel the difference in propagation times partially and thus reduce the uncertainty in the photon arrival time. Thus, they achieved a 20% reduction in the overall detection time jitter of telecom wavelength photons using differential cryogenic readout.

On the other hand, Jitter τ_e is caused by electrical noise, mainly coming from the RF amplifiers, which is introduced to the amplified signal and causes uncertainty on the amplitude and timing of the readout pulse. This jitter component can be significantly reduced using cryogenic amplification due to the reduced noise temperature when operating at cryogenic temperature. So far, the systems with the lowest recorded timing jitter for all materials use cryogenic components like amplifiers, filters, and bias teas. The best recorded time jitter belongs to short straight nanowires and is lower than 3ps for NbN [98] and 4.8ps for WSi [99].

2.3.5.4 Dead time and reset time

When an SNSPD detects a single photon, it becomes resistive. SNSPDs, like all single-photon detectors, are blind for the subsequent photon for a short time after the first photon is detected. If the second photon comes before the detector is reset, it cannot be registered. This process is divided into two steps as illustrated in Figure 16.b. First, t_{dead} is the time when the detector is unable to detect a second photon. Then there is t_{reset} during which the detection efficiency gradually returns to its initial value. In practice, the reset time is defined as the time it takes for the voltage to drop from 90% to 10% of its highest intensity. Therefore, the maximum counts rate is limited by t_{reset}.

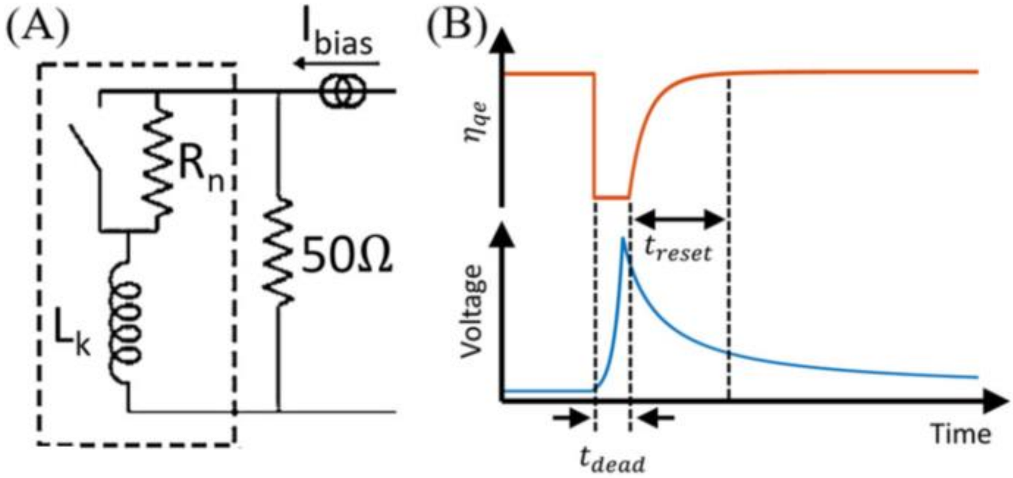

***Figure 16 :** (A)Equivalent electrical circuit of an SNSPD. (B)Representation of the evolution of the voltage and the efficiency after the detection of a photon [68]*

After the detection of a photon, the current flows through the shunt. The amount of thermal energy to be dissipated is directly proportional to the reset time. The shunt circuit is used to absorb electrical induction expressed as $\frac{1}{2}L_k I_b^2$ [100], and it enables the wire to stop dissipating energy and cool down to become superconducting again. Figure 16.A shows an equivalent electrical circuit of an SNSPD, represented by the resistance R_n in parallel with a switch (open when the photon is absorbed and closed otherwise) and a kinetic inductance L_k. Then the SNSPD is connected in parallel to a shunt resistor (here 50 Ω). In addition, Kerman et al. [101] demonstrated that

$$t_{reset} = \frac{L_k}{Z_{shunt}} \qquad \textbf{(10)}$$

This equation shows two things. To minimize t_{reset}, one must use SNSPD devices with low values of L_k. On the other hand, the impedance of the shunt circuit must be increased to maximize the energy dissipation. The impedance value of the shunt circuit must be lower than the normal resistivity R_n of the material. Therefore, if a material is highly resistive, the Z_{shunt} can be maximized and therefore t_{reset} is reduced. To this end, a material with a low kinetic value and high normal resistance has to be chosen. Crystalline materials have low values of L_k if compared with amorphous materials. This is why they are excellent choices for achieving low reset times. The nanowire shape, in turn, allows for improved reset time. As for the other characteristics, reducing the thickness and width of the wire increases the resistivity. Then, reducing the length of the wire is equivalent to decreasing L_k. Although, reducing the length of the wire is at the expense of the effective area.

However, a reduced length and a high resistance may result in latching [100]. When the current recovery in the nanowire is faster than the complete re-establishment of the superconducting state, latching occurs. As a result, the current recovers and flows back through the detector before its resistance reaches zero. Unfortunately, it cannot return to the superconducting phase due to the associated Joule heating. In order to avoid this phenomenon, these two factors must be properly engineered. Regarding the order of magnitude, in 2012, Pernice et al.[85] demonstrated 450-ps reset time with a short wire coupled to a waveguide, while in 2016, Vetter et al.[102] showed a 119-ps reset time with also a short wire embedded in an optical microcavity.

On the other hand, the implementation of superconducting single photon detectors composed of multiple pixels can improve the problem of long dead times for large active areas. Superconducting Nanowire Avalanche single Photon detectors (SNAP) devices have been developed for this purpose [103,104]. They are made of several superconducting wires in series. Since the wires are connected in parallel to each other's, the kinetic inductance of the total device is smaller than the inductance of a single wire. After the absorption of a photon, one of the wires becomes normal. The current is then shared in all the other sections. As they are already biased close to their critical current value, the addition of the current of the first wires brings all the other sections into the normal state. In this type of device, the different sections fulfill the role of the shunt. Cheng et al. [105] later reported a large-area SNAP with a 890-ps reset time but only a 20% detection efficiency at 1550 nm.

2.3.6 State of the art of superconducting material for SNSPDs

As discussed in the sections above, it is obvious that the choice of superconducting material plays a significant role in improving the detector metrics. In addition, when selecting a material, it is necessary to consider not only the material parameters but also the fabrication technological problems. Table 1 summarizes the properties required to maximize the characteristics of an SNSPD.

	Efficiency ↗	DCR ↘	Jitter ↘	Reset time ↘
Δ	low	high	high	high
T_c	low	high	high	high
I_c	high	high	high	high
R_n	high	No requirements	high	to be optimized
L_k	No requirements	No requirements	low	low
Homogeneity	amorphous	crystalline	crystalline	crystalline
Thickness	to be optimized	thick (>10nm)	thin (<10nm)	thin (<10nm)
Length	long	short	short	short
Width	narrow	narrow	narrow	narrow

***Table 1** Summary table of material trends to optimize each characteristic.*

To date, SNSPDs have been made from dozens of superconductors to date. The first SNSPD [106] was made by NbN ($T_c = 17\ K$). Furthermore, NbN is the most extensively used material because it shows high detection efficiency, low jitter, low DCR, and a high counts rate [70,84,87]. The most often used film is the polycrystalline NbN ultrathin film, deposited by DC magnetron sputtering. Several developments have resulted in an ultrathin film with low roughness, high T_c and J_c values. A more detailed review of NbN will be presented in the next chapter of this manuscript. NbTiN ($T_c = 16\ K$) is another polycrystalline material widely used for SNSPD. NbTiN can be deposited from a single alloy target of NbTi or from two different targets of Nb and Ti in a co-sputter deposition. The performance of NbTiN SNSPD generated by co-sputtering is comparable to NbN based SNSPD [70,107].

In addition, MoSi and WSi based SNSPDs have been developed for mid-infrared detection (beyond 2-3µm). WSi ($T_c = 4.9\ K$) based SNSPD showed a saturated detection efficiency of more than 90% in a wide-bias range at the telecommunication wavelength [86]. WSi is deposited by the co-sputtering of tungsten and silicon. Because WSi is amorphous, it is possible to fabricate uniform homogenous WSi nanowires without compromising their superconducting properties. The low operating temperature and significant jitter caused by the small bias current are the main limitations of WSi-SNSPD. Similarly, due to the amorphous nature of MoSi ($T_c = 7.5\ K$) films, it is possible to fabricate uniform and homogenous nanowires [108]. In addition, MoSi-SNSPD SDE reaches a record of 98% at 1550 nm in a wide-bias range [108].However, MoSi-SNSPD operate at a higher temperature than WSi-SNSPD, since MoSi has a higher T_c than WSi.

Material	T_c bulk	Deposition method	Operating temperature	Wavelength	Efficiency	jitter	reference
NbN	17 K	Sputtering ALD, MBE	0.8-2.1 K	1550-1590 nm	92-98.2 %	40-106 ps	[109,110]
NbTiN	16 K	Sputtering	2.5-2.8 K	1290-1500 nm	92-99.5 %	14.8-34 ps	[70,111]
WSi	4.9 K	Sputtering	120 mK–2.5 K*	1550 nm	93-98 %	150 ps	[86,108]
MoSi	7.5 K	Sputtering	0.8–1.5 K	1550 nm	80-87 %	26-76 ps	[112,113]
YBCO	92 K	Sputtering PLD	Photoresponse at 85K	-	-	-	[114]

Table 2 *Overview of some SNSPD leading works on different material platforms discussed in this manuscript. The detectors listed in this table are "stand-alone: normal incidence coupling" since historically, they are the ones that have been investigated the most. * Operation up to 2 K possible at the cost of higher time jitter, temperature, and jitter measurements are not mentioned.*

Several investigations on high-temperature superconductors have been conducted in the perspective of decreasing the thermal budget [115]. Because of its high T_c of 92 K, $YBa_2Cu_3O_7$ is the most extensively studied cuprate-based SNSPD material today [116–118]. However, producing a high-quality cuprate nanowire with 5 nm thickness and 100 nm width is very challenging. The majority of early cuprate studies show damaged nanowires that cannot be exploited for single-photon detection. Recent works reported an improvement in the film growth and nanofabrication processes [118–120]. Besides technological challenges, single-photon sensitivity at the telecom wavelength using cuprate superconductors has yet to be achieved since the detection wavelength is limited due to the large Δ. To conclude, Table 2, presents an overview of SNSPDs made of various superconducting materials.

2.3.7 Architectures

2.3.7.1 Stand-alone SNSPDs: Normal incidence coupling

The first device was proposed by Gol'tsman et al. in 2001 [106] and was illuminated with normal incidence. It consisted of a 1.3 µm long, 225 nm wide, and 5 nm thick straight NbN wire. Gol'tsman et al. [106] demonstrated that such device could detect visible and near-infrared single photons. In addition, the quantum efficiency of the device was estimated to be on the order of 20%.

In order to increase the optical coupling under normal incidence, it was rapidly proposed and implemented to bend the nanowire into a meander to match the optical spot size [59]. A meander with tightly packed parallel lines with a typical fill factor of 30 to 50% of the spot area was proposed [121,122] as represented in Figure 18.A. Then, an objective lens can be used to focus the light on the meander. This can be a challenging task due to the detector's low-temperature operation inside a cryostat, which requires the use of a cryo-compatible objective lens mounted inside the cryostat to achieve a narrow focus of light on the active area (meander). The other approach is to use optical fibers that directly align the fiber core over the detector. It can be achieved by manual alignment of the fiber and gluing it to the detector chip or self-alignment methods. Because of its adaptability, the second alternative is better suited. To that purpose, NIST researchers [123] suggested an etched keyhole shape on the chip substrate after being defined by electron beam or photolithography. The circular keyhole section of the chip is designed to center the detector and fit tightly into a ceramic sleeve with a slit for electrical contact. As a result, an optical fiber can be inserted into the sleeve and aligned with the detector properly. Figure 17 shows the components and completed assembly for the proposed design.

One of the main challenges of normal coupling is the short interaction length between the light and the detectors, which typically have a thickness of 4 to 10 nm. SNSPDs are therefore embedded in optical micro-cavities to increase the probability of optical absorption by allowing the photon to be reflected multiple times [81].

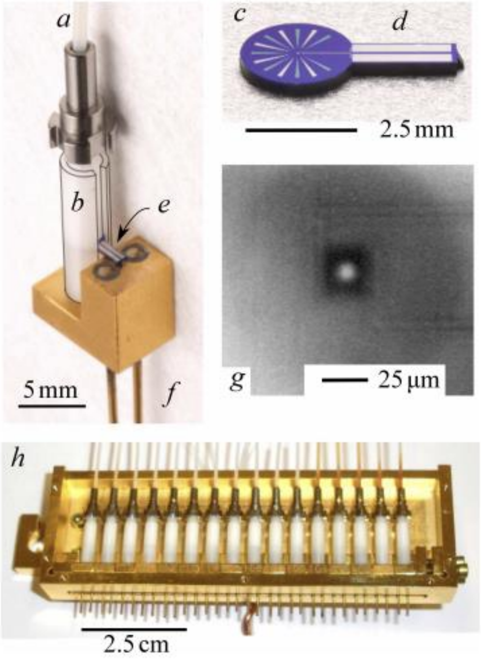

Figure 17 : *Complete fiber-to-detector assembly showing (a) single-mode fiber terminated in a stainless steel and zirconia ferrule inserted into (b) a zirconia alignment sleeve (outlined for clarity). The completed detector and substrate (c) have wiring along a silicon "tongue" (d) that extends out of the zirconia sleeve (e) and is wire bonded to pins (f) that allow electrical connection to cryogenic pre-amplifiers. A fully assembled device viewed via through-wafer infrared imaging showing (g) the laser light (bright) centered on the 25 µm×25 µm square device (dark square). A complete cryogenic assembly (h) containing 16 self-aligned, fiber coupled photon-number-resolving devices [123].*

An example of a widespread cavity consists of two layers with a difference in refractive index, commonly thermally oxidized silicon on Si wafers. Usually, the detector is above the oxide layer, which is designed so that its effective optical thickness is one-quarter of the wavelength of the light to be detected. A backside gold mirror can be deposited below to further increase the absorption, although this requires a deep backside etch of the device. For ultimate absorption efficiency, distributed Bragg reflectors (DBR) coated wafers can be exploited as substrates, allowing for better electric field confinement at the cost of the optical bandwidth. Using a simple optical cavity as depicted in Figure 18.A, Redaelli and al [122] showed an NbTiN-based detector having an overall system detection efficiency of 85% at 1310 nm. While for MoSi-based detector, a record up to 98.0% was achieved at 1550 nm [108].

However, parallel-oriented nanowires introduce an effect on the polarization sensitivity of the detector. The coupling will be better for light polarized along the nanowire, compared to light polarized perpendicularly. In many applications, the incoming photons are randomly polarized. This will result in non-optimal detection efficiency; a polarizing beam splitter and two detectors must be used to ensure maximum efficiency. Recently, a new approach was proposed by Redaelli et al.

[124] and further demonstrated by Mukhtarova et al. [125], to reduce the polarization sensitivity in normal incidence coupling. This is achieved by capping NbN-based SNSPDs with a high-index SiN dielectric layer to minimize the permittivity mismatch between NbN wires and the surrounding area.

Furthermore, the meander should be relatively long and dense to achieve high detection efficiency. This compromises the detector's speed and makes the devices more sensitive to fabrication imperfection.

From a commercial and strategic point of view, today stand-alone SNSPDs are produced by several companies. Six startups, namely ID Quantique (Switzerland), PHOTEC (China), Photon Spot (USA), Quantum Opus (USA), SCONTEL (Russia), and Single Quantum (Netherlands), are working to commercialize SNSPD technology; the oldest of these companies is SCONTEL, founded by Gol'tsman in 2004.

2.3.7.2 Integrated SNSPDs: Waveguide coupling

Manufacturing advances have enabled the development of compact, low-loss photonic integrated circuits that surpass many bulk optical systems in terms of complexity and stability. The development of an integrated quantum photonics platform with key components to generate, manipulate, and detect single photons is necessary for quantum optics progress. In particular, the integration of single-photon detectors is a key technological milestone that will enable a wide range of on-chip classical and quantum technologies.

State of the art

In 2009, Hu et al. [126] introduced the concept of integrated detectors. Two years later, in 2011, Sprengers et al. [127] presented the first experimental realization of a superconducting nanowire single-photon detector made of an NbN nanowire fabricated on top of a GaAs waveguide. Pernice et al. [85] followed up by demonstrating an NbN superconducting nanowire single-photon detectors integrated with an Si waveguides, featuring up to 91% on-chip detection efficiency at telecom wavelengths. They observed remarkably low dark counts rates and ultra-short timing jitter of 18ps. For the shortest detector of 10-µm length, they measured a reset time of 455 ps. Using short detector geometries, they could work in a sub-nanosecond pulse regime. Sub-nanosecond pulse width implies a detection rate above 2 GHz. In the same group, Schuck et al. [128] have demonstrated a low-noise NbTiN SNSPD integrated with an SiN waveguide, exhibiting a dark count rate in the milli-Hz range.

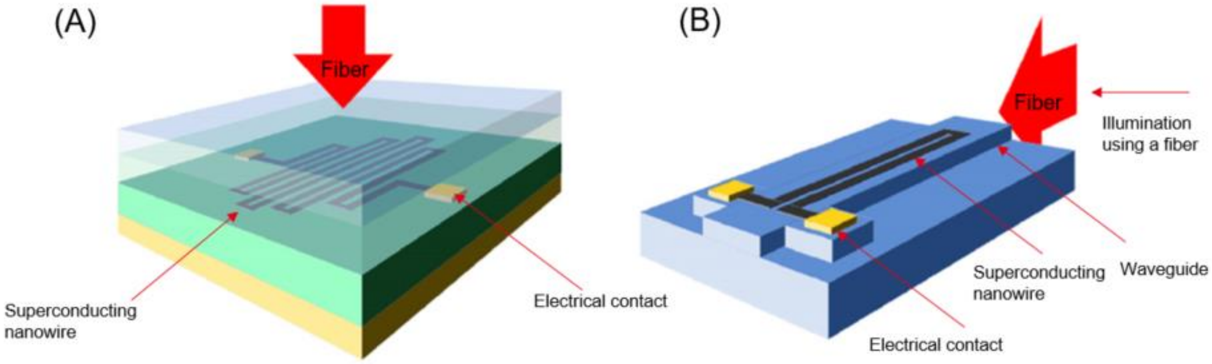

Figure 18 *: Schematic description of the devices: (A) Microcavity-enhanced detector: the nanowire meander (black) is sandwiched between two mirrors. One possible layer stack, depicted here as an example, is (starting from the bottom): a metal layer (e.g., Au, dark yellow in the figure), a transparent dielectric layer (e.g.: SiO2, green in the figure), the nanowire meander, another dielectric layer (e.g., SiO2, semitransparent-green layer) and a final layer consisting of higher-index dielectric (e.g. TiO2, top semitransparent-blue layer). (B) Waveguide-coupled detector: The material in blue is a semiconductor or a dielectric which is transparent for the injected light. In both drawings, the superconducting nanowire is contacted by two metal pads (yellow squares), and red arrows indicate the direction of incidence of light. (adapted from [124])*

Description of integrated architecture

In the waveguide configuration depicted in Figure 18.B, the SNSPD is placed atop the waveguide. The field of the waveguide mode evanescently couples to the superconducting nanowire, allowing for photon absorption in the direction of photon propagation. Photon absorption with near-unity efficiency is achieved with lengths of a few tens of micrometers [85]. This length corresponds to only a fraction of the meander structure, in vertical architectures, which is in the order of several hundred of microns (>200µm) [86] to cover the mode field diameter of the fiber. Since short nanowires have lower kinetic inductance, they are expected to feature shorter recovery times [101], which will result in higher maximum photon counting rates

Although decreasing the device length reduces the kinetic inductance and can result in GHz detection rates, this approach affects the detection efficiency due to the reduction of interaction length of the waveguide-detector. To further reduce the recovery time and increase the detection rate, photonic cavities or resonant circuits can be employed to reduce the nanowire length while keeping the same detection efficiency. However, this comes at the expense of a limited optical bandwidth [102,129,130].

Integrated platforms

Waveguide-integrated detectors have been thoroughly explored on various platforms [88]such as SOI [85,131,132], SiN [126,133–135], GaAs [136,137] and lithium niobate (LN) [138,139] and have the advantage of reducing the coupling losses, especially when all other components are integrated on the same chip. This configuration offers the advantage of reducing the coupling losses, especially when all other components are integrated on the same chip. The difference between the platforms is mainly determined by the maturity and versatility of the fabrication process, by the refractive index, which defines mode confinement, by the transparency window, which sets the optical bandwidth and by the ability to integrate several key components on the same chip, such as efficient single photon generation and detection and low-loss single photon manipulation.

Today, silicon represents one of the most widespread technological platforms for integrated photonics. Silicon has a high refractive index (n = 3.45 at 1550 nm), which allows for tight light confinement with propagation losses in the range 0.5-2 dB/cm and low bending losses, resulting in dense integrated optical structures [140,141]. Silicon nitride is an attractive alternative to silicon with a smaller refractive index than silicon (n = 1.98 at 1550 nm), limiting the confinement of the propagating light field. Nevertheless, this would allow having shorter nanowires because the coupling by evanescence will be more efficient. In addition, recently improved fabrication techniques allow obtaining extremely low surface roughness and ultra-low-loss waveguides with typically 0.05 dB/cm [142]. GaAs and related compounds, as well as lithium niobate (LN) thin films, are also being investigated for quantum photonics [139,143].

Current challenges for integrated SNSPDs

Despite the excellent detector characteristics and versatile possibilities for quantum photonics integrated circuit implementation, several challenges have to be addressed in order to build complex circuits. The yield is as the forefront of this challenges. In other words, reproducible fabrication of waveguide-integrated detectors is required in order to control characteristics such as critical current, efficiency, and temporal resolution. This holds true for normal incidence coupling architecture as well. To this aim, it is essential to better understand the correlation between the structure and chemical composition of materials at the nanoscale level, nanofabrication processes, and the resulting superconducting device properties. So far, it seems that amorphous superconductors are suitable for the high-throughput manufacturing of SNSPDs with consistent characteristics [86,108]. On the other hand, Cheng et al. [144] demonstrated that crystalline NbN detectors fabricated by plasma-enhanced atomic layer deposition exhibit good performance and reproducibility, showing promising possibilities for scaling up SNSPD by improving the material quality.

Coupling efficiency

The efficiencies mentioned in this section are measured on-chip. Waveguide-integrated SNSPDs are limited to low system detection efficiencies due to interface losses when coupling to optical fibers. Due to the high index contrast between silicon and silicon dioxide, silicon photonics waveguides have typical dimensions much smaller than standard monomode fibers (400 nm vs 8 µm). This dimension difference makes the design of fiber-to-chip interfaces challenging. This problem is usually addressed using two main approaches, in-plane (butt) edge coupling and off-plane (vertical) grating coupling [145–147].

For edge coupling, fiber is placed at the chip facet and aligned with on-chip waveguide horizontally. Edge couplers usually consist of an inverse tapered waveguide to achieve mode conversion, since a gradually varying cross-section area supports mode transformation and mode size variation. Edge couplers show high coupling efficiency, wide bandwidth, and low polarization dependent loss [145]. However, to reduce the losses, a properly cleaved and polished facet with strict smoothness requirements is required, which adds extra fabrication steps. In addition, they have a relatively large footprint and must be placed at the chip's edge. Furthermore, edge coupling solutions have a low fiber-chip alignment tolerance and limit wafer-level testing. Therefore, their high performance comes at the expense of reduced flexibility.

Grating couplers are much more flexible in terms of arbitrary coupling position on the chip, compact size, easy fabrication, and wafer-level testing capability. For grating coupling, fiber is placed above diffractive grating structures on the top of the chip. A vertical grating coupler changes the off-plane wave-vector direction of light to the in-plane waveguide direction and then couples the light into the waveguide. Although this approach has the above-mentioned advantages, it also suffers from some drawbacks. Grating couplers typically have lower coupling efficiency compared with edge couplers and are intrinsically sensitive to both wavelength and polarization. For instance, at 1550 nm, the insertion loss of silicon grating couplers is currently at 2dB [148].

Recently, efficient coupling between optical fibers and waveguide-SNSPDs nanowire detectors has been achieved using a 3D interface produced by direct laser writing that relies on total internal reflection, reaching system detection efficiencies of up to 70% over a wide spectral range in the near-infrared [149].

2.3.8 Photon number resolution

Photon number resolution (PNR) is another essential capability required for many quantum protocols and in particular for linear optical quantum computing [150]. PNR allows quantifying the number of absorbed photons during a given detection event. Transition-edge detectors (TES) inherently show photon-number-resolving (PNR) capability since their response is directly dependent on the amount of absorbed energy and therefore to the number of incident photons. Gerrits and al. [151] showed up to 5 photons resolution with a detection efficiency of 7% at 1550nm. Nonetheless, they frequently require operation at low temperatures in the 100 mK range. They have the drawbacks of slow reset times in the microsecond range and limited timing resolution. On the other hand, SNSPDs which feature much better timing performances are binary threshold detectors, and PNR is not intrinsically possible.

Arrays of interconnected detectors [152–155] or adequate engineering of the electronic readout scheme [156] can help overcoming this limitation by approaching almost-true PNR. Significant progress has been made in the development of SNSPDs with pseudo PNR, which rely on spatial multiplexing in superconducting nanowire arrays [157]. However, true PNR with SNSPDs is still missing, which is one of the key current challenges of SNSPDs. An architecture proposal for SNSPDs will be discussed later in chapter 4.

In conclusion, SNSPDs are an excellent choice for integrated single photon detectors due to their relatively simple architecture. Furthermore, integrated SNSPDs have already demonstrated excellent on-chip single-photon detection performance, revealing considerable advantages to achieve progress on a large scale.

Chapter 3- Study of NbN superconducting films on 200 mm Silicon platform

3.1 Introduction

In this chapter, we establish the fundamental building block required for SNSPDs fabrication. For our SNSPDs development, we chose NbN for its excellent superconducting properties, crystalline quality, and feedback on this material, as it has been the most studied [158–162]. NbN is an electrically conductive material with a metallic appearance that is opaque at visible wavelengths, even at thicknesses of a few tens of nanometers [163].

We start by discussing the choice of the substrate as a function of the epitaxial relationships between NbN and the substrates. Afterward, we describe the optimized deposition process to obtain high-quality thin NbN layers on a 200 mm platform, using reactive magnetron sputtering. Finally, we fabricate SNSPDs from these optimized NbN thin films, to validate their properties for single-photon detection.

3.2 Choice of the substrate

Niobium nitride (Nb_xN_y) is a non-stoichiometric and polymorphic material that exists in nine hexagonal or cubic phases. Only its face-centered cubic cfc phase exhibits excellent superconducting properties, with a critical temperature T_C for the bulk ranging between 14 and 17 K [158]. Therefore, NbN cfc is the desired crystallographic phase because of its superconducting properties.

NbN is a good candidate for SNSPDs thanks to its relatively high critical temperature and its good electrical and timing properties. However, the choice of substrate is crucial to obtain high-quality NbN material. NbN is generally deposited on amorphous or highly mismatched substrates, which leads to polycrystalline structure with degraded critical temperature and film inhomogeneities that limit the fabrication yield and reproducibility of SNSPDs. The mismatch between the lattice parameter of the substrate and the deposited layer should be chosen as small as possible because it plays a role in the residual strain of the film and the crystalline structure of the material. In order to improve the crystalline quality of NbN, low-mismatch substrates such as sapphire, TiN, MgO, SiC, GaN, or AlN [164–169] have been proposed but they are not all well-suited for large-scale implementation.

substrate	crystal family	lattice parameter Å	mismatch %
AlN	hexagonal	3.112	0.48
MgO	cubic	4.256	2.83
TiN	cubic	4.254	2.88
GaN	hexagonal	3.216	3.84
α- Al_2O_3	hexagonal	2.747	11.3
Si	cubic	5.43	23.97

Table 3 *Lattice parameter mismatch of NbN with different substrates*

The NbN lattice parameter is variable and depends on its crystallographic phase. In the following, we only consider the cfc phase of NbN whose lattice parameter is $a_{\mathrm{NbN}} = 4.38$ Å . The mismatch with the potential substrates, presented in Table 3, is calculated between the (001) substrate// (001) NbN planes for cubic substrates and between the (0001) substrate //(111) NbN planes for hexagonal substrates. The mismatch values presented in Table 3 are calculated using the formula ($\frac{b-a}{a}) * 100$, where a and b denote the NbN and substrate lattice parameters, respectively. The lattice parameter of a (111) plane of NbN is $a_{111} = \frac{a\sqrt{2}}{2} = 3.097$ Å. Based on this analysis, we can conclude that AlN has the lowest mismatch and silicon has the highest.

The choice of the substrate also depends on the targeted integration of the detector. Depending on the application and the desired operating wavelength, the substrate optical properties can be essential for designing waveguides. In addition, the technological maturity of the chosen platform should also be considered.

In this work, we intend to build SNSPDs that will operate at telecommunications wavelengths. For this purpose, we chose the 200mm silicon platform, in spite of the large lattice mismatch with NbN. In order to obtain a higher quality superconducting material, we will use AlN as a buffer layer.

3.3 NbN film growth and optimization

DC reactive magnetron sputtering is widely used to deposit NbN films. This process allows excellent control of the various growth parameters, and NbN films have been shown to be of high superconducting quality [170–172]. Although most superconducting NbN films are deposited via sputtering, chemical vapor deposition (CVD) and molecular beam epitaxy (MBE) have also been demonstrated. However, this process is carried out at high temperatures (above 1000 °C) [158,173] and currently it is not compatible with large-scale deposition.

Sputtering is a non-thermal physical vapor deposition (PVD) process suitable for atomic deposition. It can be used to deposit many materials, from dielectrics to superconductors, with thicknesses ranging from a few nanometers to the micrometer scale. The process is based on the transfer of energy and momentum from the ionized sputter gas to the solid target. Specifically, under a low-pressure gas atmosphere (Ar or N_2), a high voltage is applied between the anode and the cathode. A plasma is then created to ionize the gas atoms. The ions, attracted by the potential applied to the target, bombard the latter. Atoms extracted from the target are projected and deposited on the substrate (Figure 19). A rotating magnet mechanism behind the substrate can be used to ensure uniform deposition. The atomic weights of the ionized gas and the target are chosen to be similar for the most efficient energy transfer. Indeed, sputtering is advantageous over evaporation systems because materials with very high melting temperatures can easily be sputtered at relatively low temperatures.

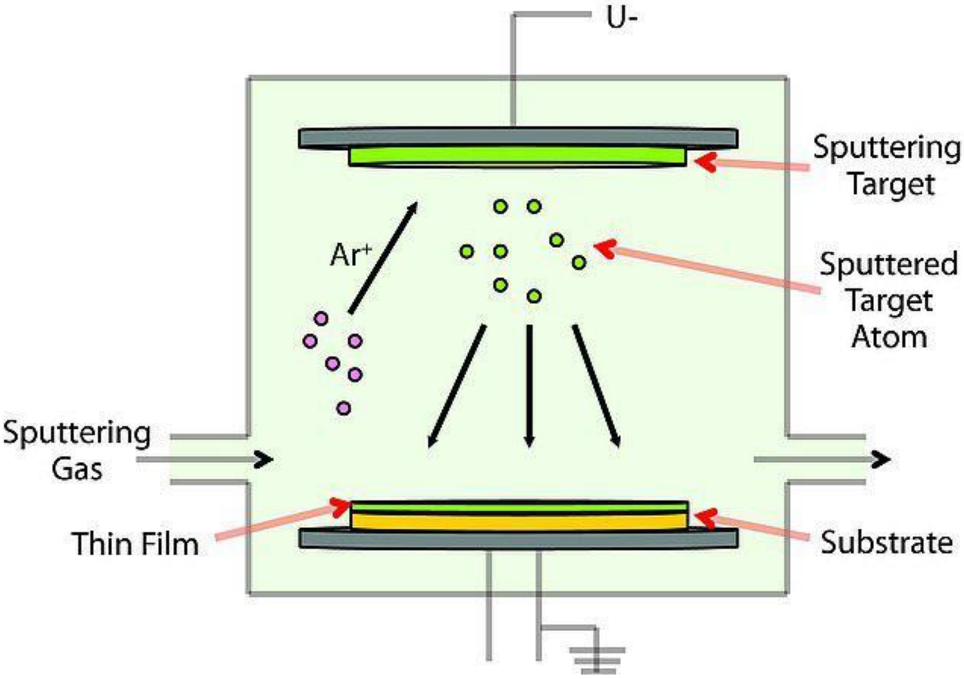

Figure 19: *Example of DC reactive magnetron sputtering system.*

NbN films with various thicknesses (5, 7, and 9 nm) were deposited on 200 mm Si (100) wafers with and without an AlN buffer layer, as summarized in Table 4. The deposition was performed using an ENDURA system by Applied Materials. Both NbN and AlN were deposited by reactive sputtering under CMOS- compatible conditions (process temperature <400°C since the back-end thermal budget for metal deposition is limited to 450°C). AlN and NbN were deposited in different sputtering chambers. Prior to deposition, the silicon wafers were cleaned in situ with Ar plasma in order to remove the native oxide. The purity of the targets was 5N (99.999%) for Nb and 5N5 (99.9995%) for Al. For both AlN and NbN deposition, the base pressure was below 5 × 10−8 mTorr and the pressure during deposition was between 2 and 10 mTorr. The process used a mixture of

$Ar:N_2$ gases with a ratio between 5:1 and 20:1 for NbN and between 1:10 and 1:5 for AlN. We used low deposition rates (<1 nm/s) to control precisely the final thickness. The thickness of NbN is determined by the weight gain method, which involves measuring the weight of the sample before and after deposition to quantify the deposited mass; this method is accurate to within 1 nm. The thickness is then calculated using the following equation 1

$$Thickness\ (\mu m) = \frac{M(g) * 10^4}{A\ (cm^2) * \rho\ (\ g\ cm^3\ )} \qquad \textbf{(1)}$$

where M is the mass of the deposited material, A is the surface, and ρ is the density of NbN (6.2 g/cm^3). The thickness of AlN is measured by ellipsometry. The thicknesses of the samples under study are summarized in Table 4 . In addition, these values were validated by comparison with transmission electron microscopy images. The thickness deviation across the 200 mm wafer remained below ±2% for NbN and below ±4% for AlN, with the deposited material slightly thicker at the edges than in the center of the wafer.

It is important to note that NbN oxidizes when exposed to air [174]. This native oxide is a self-protective layer, and the oxidation process is not linear. H.W. Chang et al. [175] investigated the oxide layer thickness on uniform high-quality NbN nanofilms (1.9 to 4.7 nm). After 200 days under standard pressure and temperature conditions, the native oxide layer does not exceed 1 nm. This sets a challenge to measure the thickness of ultra-thin NbN films with ellipsometry. Due to the presence of the oxide, the model used to calculate thickness is not accurate for nanometer-scale layers.

Sample	AlN thickness (nm)	NbN thickness (nm)	T_c (K)	ΔT (K)
S1	0	5	4.5	1.64
S2	0	7	7.0	1.94
S3	0	9	8.1	1.4
S4	11	5	9.6	2.5
S5	19	5	8.8	2.4
S6	19	7	10.0	1.45
S7	19	9	10.3	1.85
S8	26	5	8.5	2.58

Table 4 *Measurement of the superconducting critical temperature for samples with different AlN and NbN thicknesses. The relative standard deviation of* T_C *across the 200 mm wafer is ±4.5% for NbN deposited directly on Si(100) and ±7.5% for NbN deposited on AlN*

3.4 Material characterization

3.4.1 Morphology

The morphology of NbN was analyzed by atomic force microscopy (AFM) using a Bruker ICON SPM system operated in the tapping mode using TESPA-V2 probes. The AFM images in Figure 20.a and Figure 20.b compare the surface of 5 nm thick NbN layers deposited directly on Si(100) (sample S1 in Table 4) and on a 26 nm thick sputtered AlN buffer layer on Si(100) (sample S8), respectively. The images do not show significant differences in the in-plane grain size. Two-dimensional fast Fourier transform of the images point to a characteristic length of 10 ± 1 nm for NbN on AlN/Si and 14 ± 1 nm for NbN on Si. However, these numbers must be taken cautiously since they are close to the typical radius of the AFM tip (7 nm). The average root-mean-square roughness measured on different locations of the wafers is 0.24 ± 0.02 nm for 5 nm thick NbN on Si(100) and 0.27 ± 0.06 nm for 5 nm thick NbN on AlN, without a clear trend as a function of the AlN thickness (in the range of 12–26 nm).

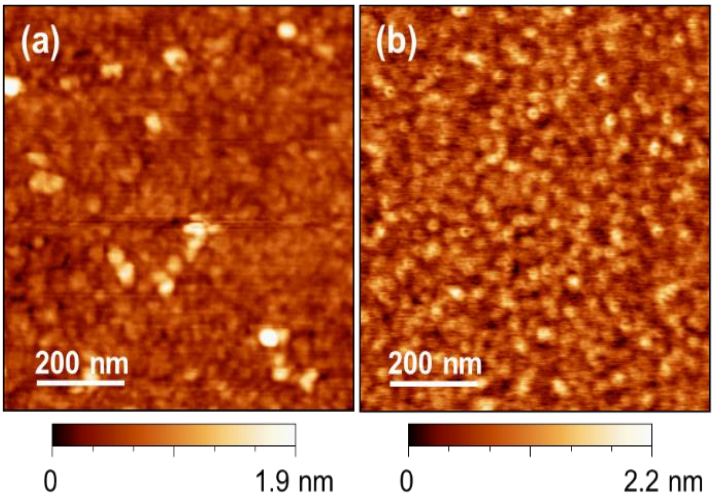

Figure 20 : *Atomic force microscopy images of (a) 5 nm of NbN on Si(100) and (b) 5 nm of NbN on 26 nm of AlN on Si(100).*

3.4.2 Superconducting-Electrical properties of NbN thin films

A Physical Property Measurement System (PPMS® Quantum design) is used to measure the electrical properties of NbN superconducting films. The PPMS is a cryostat with an integrated measurement system. It is suitable for measuring the samples' resistivity and specific heat. Each type of measurement requires a particular sample holder. For standard measurements in ^{4}He, the system operates from 1.9 K to 400 K. Considering the critical temperature of NbN, measurements were performed between 4 K and 400 K.

The sample holder used for the resistivity analyses is shown in Figure 21. The samples are fixed on the gold bottom with a resist suitable for low-temperature measurements. The samples are bonded to the measuring system by aluminum or gold wires. In addition, the sample holder is composed of three circuits measuring current and voltage. The measurement method is equivalent to the 4-point measurement. This 4-point geometry drives a constant current through the thin film via the two outer ports labeled I+ and I− while simultaneously measuring the voltage drop across the two inner points V+ and V−. This configuration allows measuring the film resistance without influencing the ohmic contact resistivity.

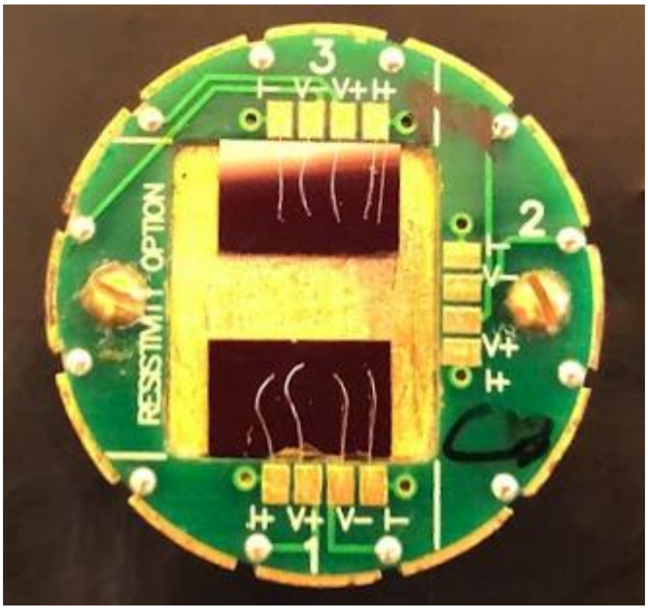

Figure 21 : *Sample holder for resistivity measurements: an example with two NbN samples*

Figure 22 depicts the evolution of the resistance of NbN layers of various thicknesses (5, 7, and 9 nm) as a function of temperature, in the case of (a) NbN deposited directly on Si (100) (samples S1, S2, and S3 in Table 4) and (b) NbN deposited on 19 nm of AlN sputtered on Si(100) (samples S5, S6, and S7). All layers show superconducting properties below a certain critical temperature, Tc, which increases with the NbN layer thickness. As reported in Table 4, the superconducting transition range ΔT (defined from 10% to 90% of the maximum value of the resistance) is sharp, between 1 and 2.5 K for all the samples under study, evidencing a clear superconducting behavior at low temperature.

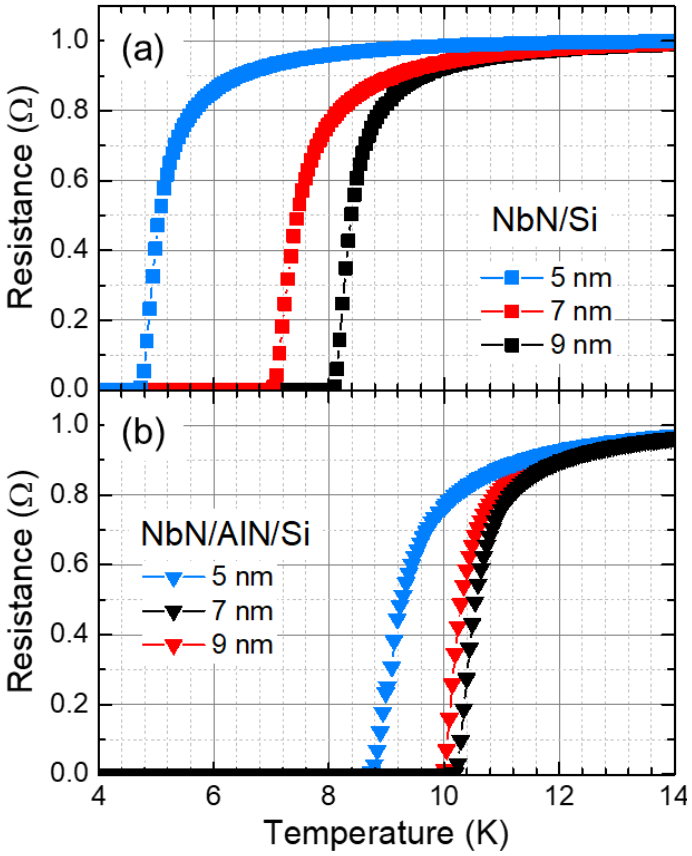

Figure 22 : *Variation of the resistance with temperature measured in NbN layers with various thicknesses as a function of temperature: (a) NbN deposited directly on Si(100) and (b) NbN deposited on 19 nm sputtered AlN on Si(100). In both graphs, the resistance of the various samples was normalized to its maximum value.*

The critical temperature ranges from 4.5 K to 8.1 K for NbN on Si, and from 8.8 K to 10.3 K for NbN on AlN/Si. This significant improvement of the T_C in the presence of an AlN buffer layer is observed for all the NbN layer thicknesses under consideration. For 5 and 9 nm thick NbN layers, the critical temperature improves by 4.3 K and 1.5 K respectively.

The beneficial effects of an epitaxial and sputtered AlN buffer layer have been already demonstrated on GaAs [176], sapphire [168] and quartz [177]. To assess the influence of the AlN thickness, 5 nm of NbN were deposited on 11 nm, 19 nm, and 26 nm of sputtered AlN.

From Figure 23, the critical temperature decreases from 9.6 K to 8.4 K with increasing AlN thickness. This degradation cannot be assigned to an increase of the roughness, since AFM measurements show comparable results for the three samples. Instead, we tentatively attribute this T_C variation to the enhanced tilt and twist of the AlN grains, as the layer grows thicker. The AlN buffer layer should therefore be kept as thin as 10 nm. The critical temperature deviation across the 200 mm wafer, derived from measurements in the center, at mid-radius and at the edge of the wafer, is

±4.5% for NbN deposited directly on Si(100) and ±7.5% for NbN deposited on AlN. Higher T_C values are systematically observed in the areas with higher NbN and AlN thickness.

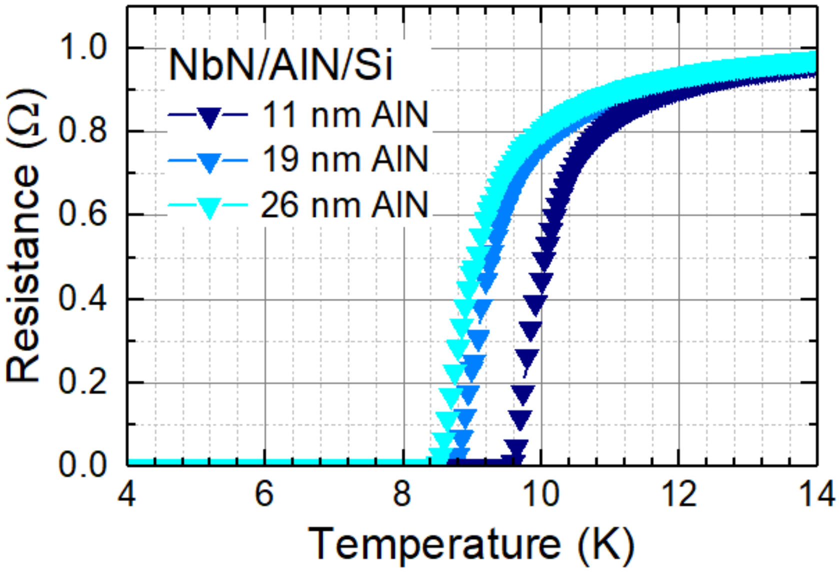

Figure 23 : *Variation of the resistance with temperature measured in 5-nm-thick NbN layers deposited on sputtered AlN with various thicknesses.*

3.4.3 Nanostructure analysis

In order to identify the crystalline nature of the NbN thin film and the impact of the substrate, the samples were analyzed by x-ray diffraction (XRD) using a Rigaku SmartLab 9 kW Cu rotating anode x-ray source ($\lambda_{K\alpha}$ = 0.15406 nm) equipped with a Ge(220) double-bounce monochromator (out-of-plane measurements) or incident Soller slits (in-plane measurements). Four kinds of experiments were carried out: **(a)** out-of-plane θ–2θ scans along the Si <l00> direction, **(b)** out-of-plane 2θ scans at grazing incidence ($\omega = 3^{\circ}$), **(c)** in-plane θ–2θ scans along Si <110> and **(iv)** in-plane 2θ scans. This combination of measurements grants a completely structural knowledge of the NbN layer. Figure 24.a and Figure 24.b show the resulting diffractograms for a 9 nm thick NbN layer on Si(100) (sample S3 in Table 4).

Both out-of-plane θ–2θ and 2θ scans display NbN-related reflections attributed to NbN(200) and NbN(111). NbN(110), NbN(200), NbN(220), and NbN(311) are detected in in-plane scans, with their intensity remaining constant when varying θ. This indicates that the NbN layer directly deposited on silicon is polycrystalline, without textured crystallites. In the case of NbN deposited on an AlN buffer layer (Figure 24.c and Figure 24.d), the out-of-plane θ–2θ and 2θ scans confirm that AlN is highly textured along [0001], with the (0002) reflection of AlN located at $\theta = 36.06^{\circ}$. Regarding NbN, only the (111) (see zoomed view in Figure 24.e) and (222) reflections are clearly resolved. The 2θ scan performed at grazing incidence does not show any peak assigned to AlN(0002), NbN(111), AlN(0004) or NbN(222), which is consistent with <0001> and <111> as preferential growth axes of AlN and NbN, respectively. However, in-plane θ–2θ scans present reflections associated to AlN(10–10) and AlN(11–20) which keep a constant intensity when varying θ. This indicates that the AlN layer is in-plane polycrystalline, even if highly <0001> textured in the out-of-plane direction. It was not possible to resolve NbN-related reflections in the in-plane measurements.

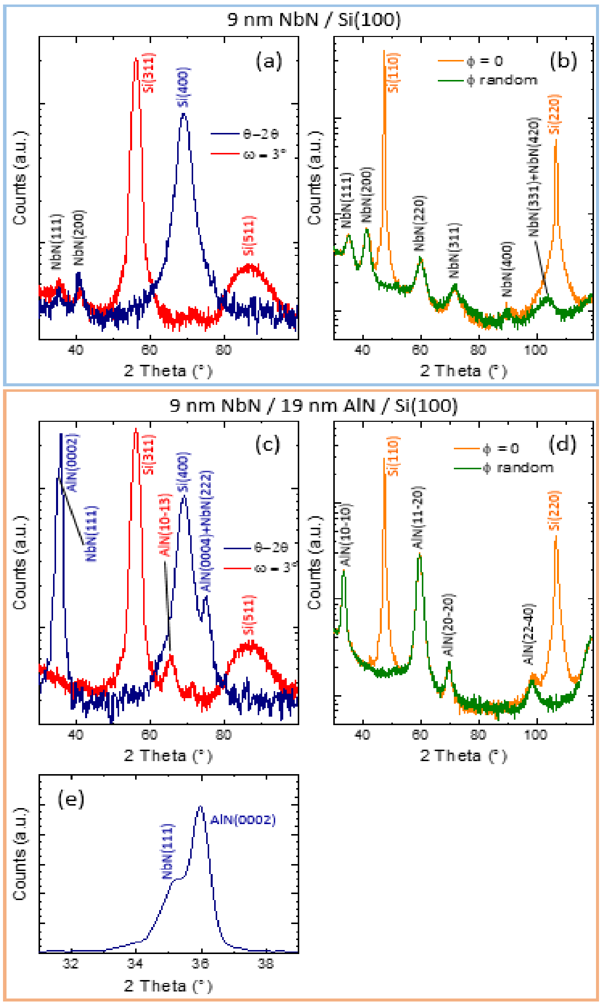

Figure 24 : *XRD analysis of (a,b) a 9-nm-thick NbN layer deposited directly on Si(100) and (c,d,e) a 9-nm-thick NbN layer deposited on 19 nm of sputtered AlN on Si(100). (a,c) XRD out-of-plane* θ–2θ *scans and* 2θ *scans at grazing incidence* ($\omega = 3°$)*. (c,d) In-plane XRD scans performed for* $\phi = 0$ *(aligned with Si<110>) and* ϕ *randomly oriented. (e) Zoomed view of the* θ–2θ *scan in (c) to outline the presence of the NbN(111) reflection.*

To get a view of the NbN/Si and NbN/AlN/Si heterointerfaces at the nanometer scale, selected samples have been studied by high-resolution transmission electron microscopy (HRTEM). For this purpose, the samples were prepared in cross-section by either mechanical polishing followed by ion milling or by focused ion beam milling and measured in a FEI-Tecnai microscope operated at 200 kV. Figure 25 compares the crystalline structure of NbN grown with and without an AlN buffer. From the HRTEM image in Figure 25.a, NbN deposited directly on Si(100) is a randomly-oriented polycrystal, consistent with XRD results. The bright contrast at the NbN/Si(100) interface (red arrow in the Figure 25.a) is a 2 nm thick amorphous layer. To identify the nature of such a layer, energy dispersive x-ray spectrometry measurements were performed in a FEI-Themis TEM equipped with super X detectors. Figure 26.a shows a high-angle annular dark-field scanning transmission electron microscopy image of the specimen and Figure 26.b presents the profile of the oxygen K, nitrogen K, silicon Kα, and niobium Lα lines when measuring along the green arrow in Figure 26.a. The peak of oxygen at the interface allows the unambiguous assignment of the amorphous layer to SiO2, which might be nitridated at the interface with NbN. Looking at the NbN layer grown on AlN, Figure 25.b reveals that the AlN/NbN interface is atomically clean and presents an epitaxial relation, with the (111) plane of NbN growing parallel to the (0001) axis of AlN, as it was previously observed using single-crystal AlN substrates [168]. Figure 25.c and Figure 25.d show a bright contrast at the AlN/Si(100) interface (red arrow in the Figure 25.c). This amorphous layer, with a thickness around 0.5 nm, is probably a native SiO_2 which was not completely removed by the Ar plasma cleaning.

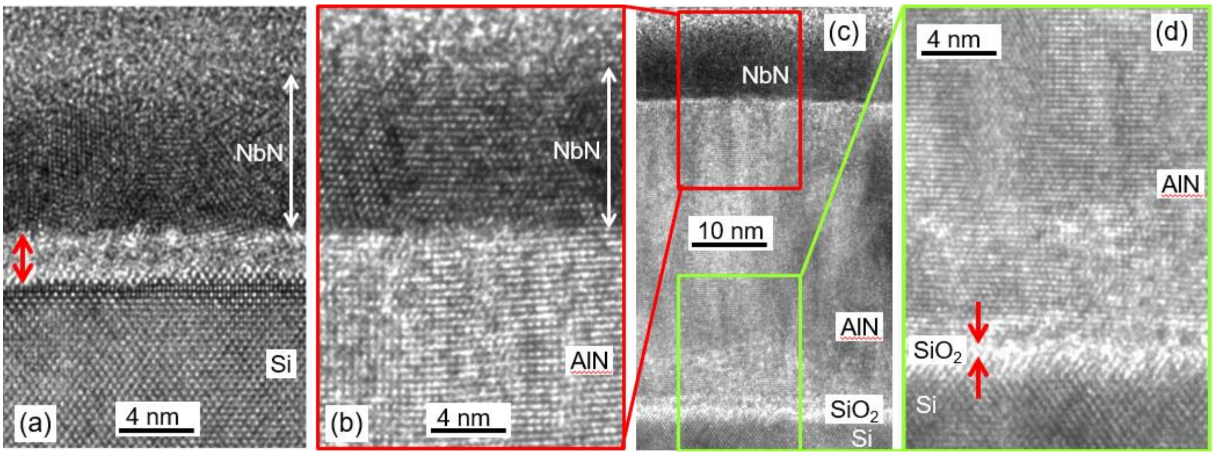

Figure 25 : *(a) HRTEM image of NbN deposited on Si(100). A 2-nm-thick amorphous layer is visible at the interface (red arrow). The NbN rock-salt layer consists of crystallites with random orientation. (b) HRTEM image of NbN deposited on sputtered AlN on Si(100). The AlN grows along the <0001> axis, and rock-salt NbN is deposited epitaxially on top following the <111> axis. (c) Full HRTEM image of the NbN/AlN/Si stack. (d) HRTEM image of the AlN/Si(100) interface showing a ≈0.5-nm-thick amorphous layer (red arrows).*

Therefore, as a summary of the structural analysis, NbN deposited directly on Si (100) is a randomly oriented polycrystal, whereas NbN deposited on sputtered AlN is textured along <111>, which points to a correlation between the crystalline structure and the improvement of the superconducting properties.

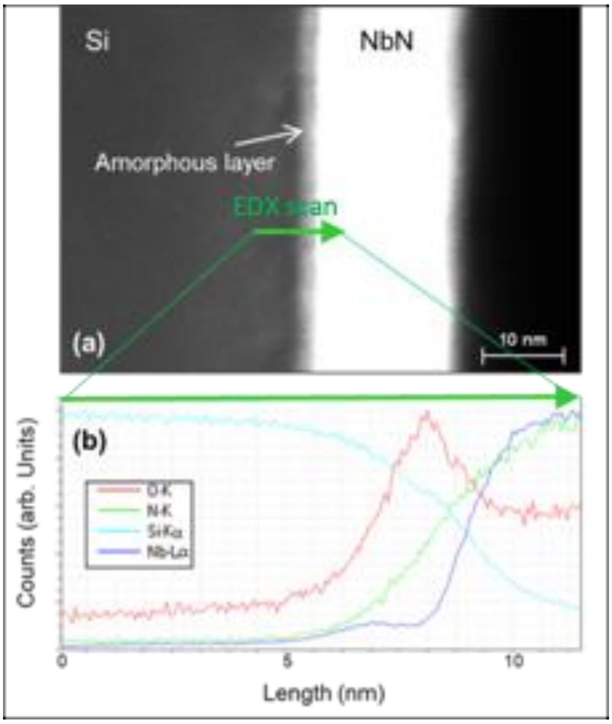

***Figure 26 :** (a) HAADF-STEM view of NbN deposited on Si(100) [same specimen as in figure 25(a)]. (b) EDX profile of the oxygen K, nitrogen K, silicon Kα, and niobium Lα lines when measuring along the green arrow in (a)*

3.4.4 NbN refractive index

In view of the design and fabrication of SNSPDs using NbN material, it is necessary to measure the optical absorption and refractive index of the material over a broad spectral range. For this purpose, a 25 nm thick NbN layer was deposited on Si(100). We assume that the thickness of the native oxide is negligible in comparison to the total layer thickness. The layer thickness was measured by x-ray reflectometry using a Bruker D8 Fabline fully-automated high-resolution diffractometer operated in the θ–θ geometry. Then, using this thickness as an input parameter, spectroscopic ellipsometry was performed using a Woollam M2000 rotating compensator ellipsometer, which features automated variable angle of incidence capability (350–1700 nm spectral range) with a spot size in the millimeter range. An oscillator-based model (Tauc-Lorentz and Drude [178,179]), Kramers–Kronig consistent, was used to describe the optical dispersion of the layer, including the position and shape of the absorption peak. The resulting values of real and imaginary refractive indices are presented in Figure 27.

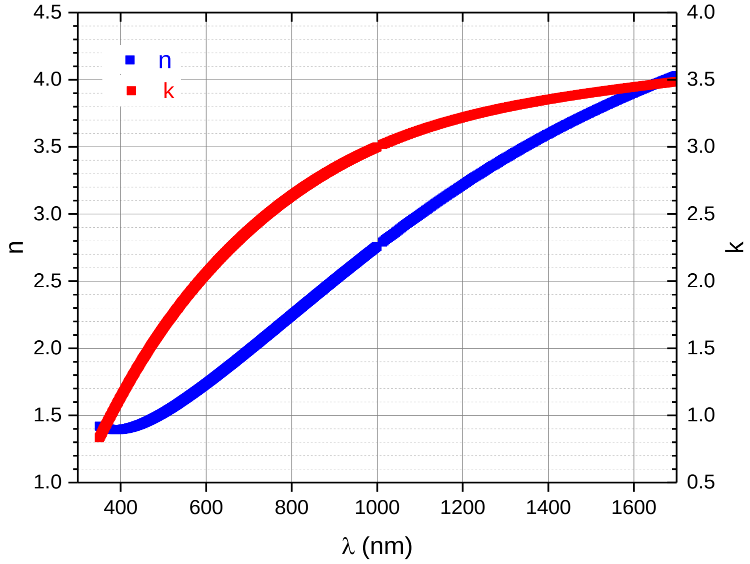

Figure 27 : *The complex refractive index of a 25-nm-thick NbN layer measured by spectroscopic ellipsometry at room temperature. The real part n, represented in blue, is the refractive index and indicates the phase velocity, while the imaginary part κ, represented in red, is called the extinction or absorption coefficient*

3.5 Stand-alone SNSPDs: Normal incidence coupling

In order to validate the properties of the deposited NbN-on-AlN films for their use in a detector device, we have fabricated and characterized SNSPDs consisting of a superconducting meander that operates under normal incidence illumination, as described in refs [168,180].

3.5.1 Simulation

To estimate the detection efficiency, we performed device simulations using finite-difference time-domain (FDTD) calculations with the Lumerical commercial software. As described in the inset of Figure 28, the NbN meander is modelled as a single grating period illuminated by a mixed polarized plane wave at normal incidence with in-plane periodic boundary conditions. Its complex refractive index was taken from the ellipsometry measurements presented in Figure 27, i.e., n = 3.83 + i 3.42 at a 1550-nm wavelength. The absorption efficiency is calculated from the difference between the input power and the amount of reflected and transmitted power, once the steady-state is reached. Figure 28 shows the simulated absorption of the device as a function of the NbN meander thickness for two AlN thicknesses of 10 and 19 nm. For the NbN thickness of 5 to 9 nm used in this study, the expected efficiency ranges from 7 to 11%, with comparable results for both values of AlN thickness.

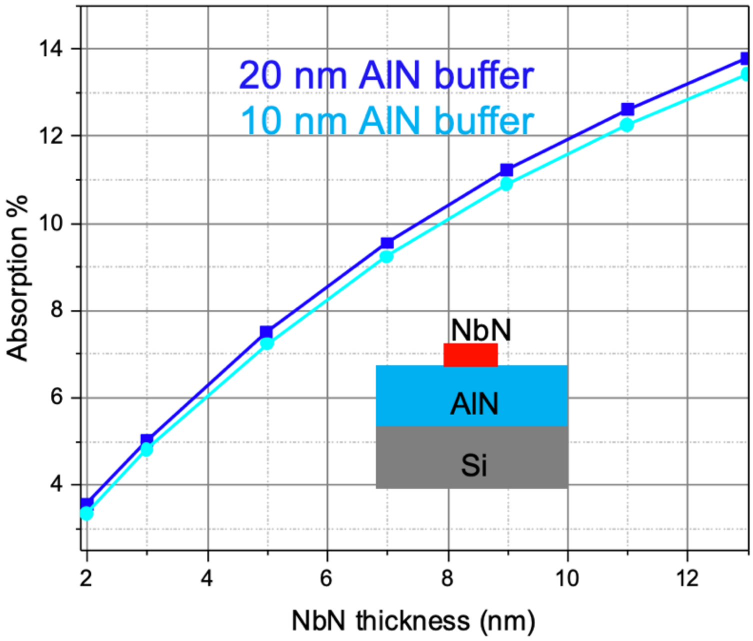

***Figure 28:** Numerical FDTD simulation of the absorption of the meander as a function of the NbN thickness for two AlN thicknesses of 10 and 20 nm*

3.5.2 Fabrication

We have fabricated SNSPDs consisting of a superconducting meander that operates under normal incidence illumination. The fabrication process of the vertical SNSPDs took place in the PTA (Plateforme de Technologie Amont) cleanroom of CEA. Luca Redaelli and Anna Mukhtarova, post-doctoral researchers at PHELIQS/NPSC, have developed this process few years ago [180]. Here, I will describe it briefly and focus on the points that I modified or developed.

After the superconducting stack deposition in the 200 mm silicon platform in LETI's cleanroom, the wafer is cut into 2 × 2 cm^2 samples. Each sample will comprise 18 SNSPDs, as represented in the right inset Figure 29. Figure 29 gives an overview of the whole fabrication process. First, ultraviolet (UV) lithography is used to establish the pattern for the metal contacts and alignment markers. After the resist exposure and development, the sample is coated in a metal evaporator with a layer of chromium (Cr) to improve adhesion, followed by gold (Au) deposition. The patterns are then transferred by means of a lift-off approach using a solution suited for resist removal. In a further phase, the SNSPD is defined by electron beam lithography due to its nanometer-scale dimensions. Alignment markers are used to align the SNSPD pattern with the metallic contact. The resist is exposed by an electron beam, and the pattern is then transferred into the NbN film via dry etching using SF_6 gas. At this point, a first quantitative measurement of the SNSPDs can be performed.

In order to perform qualitative measurements of the device efficiency, the optical coupling needs to be optimized. We used the self-aligning method developed by the NIST group [181]. This approach uses optical fibers that directly align the fiber core over the detector (meander). The circular keyhole section of the chip is designed to center the detector and fit tightly into a ceramic sleeve with a slit for electrical contact. As a result, an optical fiber can be inserted into the sleeve and aligned with the detector properly (left inset of Figure 29). In addition, the SNSPD design is slightly larger than the mode field diameter of the fiber, allowing for a misalignment tolerance of 1 to 2 µm, which is at the precision limit of UV lithography systems. Therefore, a further lithography step is performed to define the keyhole shape of the chip, which is then etched by deep dry silicon etching with the Bosch process to ensure straight and smooth sidewalls by alternating etching and passivation steps.

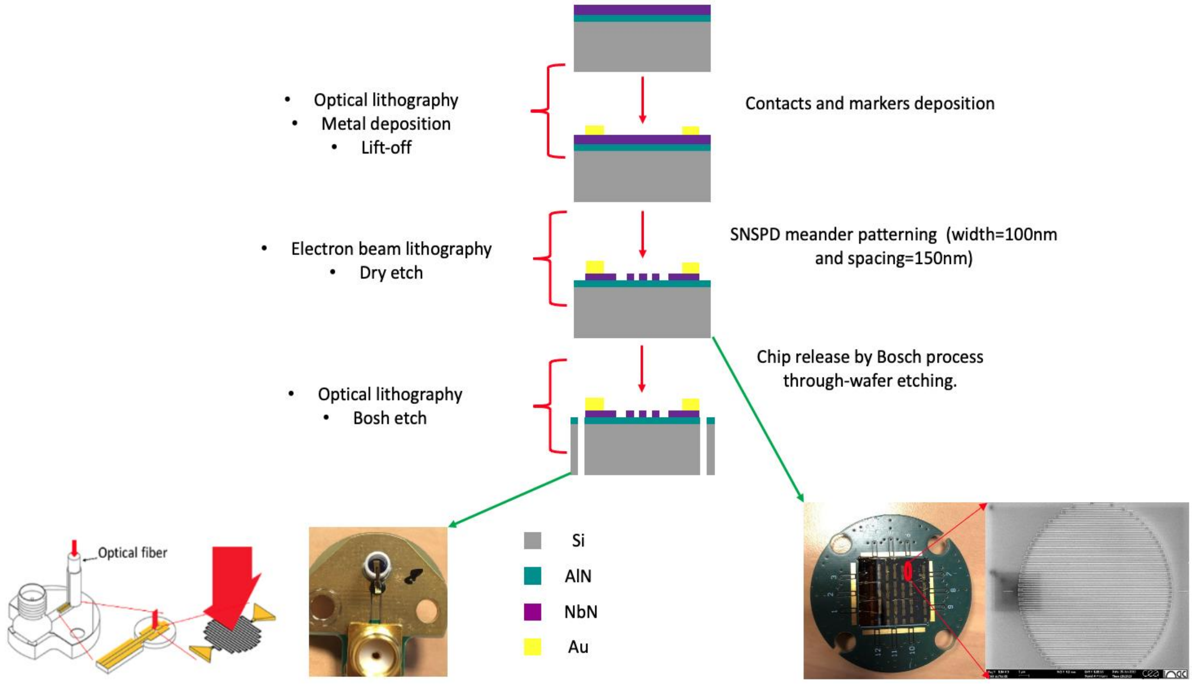

Figure 29: *Fabrication workflow for an SNSPD with normal incidence coupling. Right inset: Chip with 18 detectors with its packaging used for quantitative characterization. Left inset: SNSPD keyhole with packaging measurement.*

The existing recipes for deep dry silicon etching (laser lithography + Bosch etching) were developed for 350 µm thick substrates, whereas the substrates that we used in this study were 725 µm thick. The issue is that the resist is not thick enough to etch 725µm. To address this issue, we have investigated two approaches:

- Use of a thicker resist: Unfortunately, our attempts to use a thicker resist were inconclusive. We used AZ40XT resist with a thickness about 15 µm, but it was challenging to achieve a homogenous resist coverage on the 2×2 cm^2 sample.

- Grinding the Si substrate down to 200 µm. After the grinding process, the samples showed a variation in thickness of a few microns. As a result, laser lithography was no longer suitable for this process because the machine could not align the samples with a thickness variation of more than one micron. Therefore, a new optical mask was designed to perform the optical lithography.

For samples with an AlN layer, this layer must be etched first before the Bosch etch, since the chemistry of the Bosch process (based on SF_6) does not etch AlN. Hence, I developed a dry etching recipe based on $Cl_2/BCl_3/Ar$.

3.5.3 Characterization

The detectors were characterized at 4.2 K using a dip-stick system to immerse them in liquid helium. They were illuminated with an arbitrary polarization using a fibered continuous-wave laser diodes emitting at 1550 nm wavelength with an optical attenuator to obtain a photon flux of the order of a few nW. A light diffuser was placed in front of the detector array in order to homogenize the photon flux over the whole chip leading to mixed polarized flux (see Figure 31). The photon flux was calibrated using a reference germanium photodetector. The dip-stick incorporates cryogenic-adapted optical fibers consisting of a fiber core, fiber cladding, and coating, but no additional cladding. The SNSPDs are connected by coaxial RF lines to the electronic-readout system which is located outside the cryostat. The electronic readout system provides data on the registered counts per second.

The characterization of SNSPDs is performed in three steps. The first step is to perform an I-V measurement to determine the critical current I_C. Four detectors can be measured simultaneously, and Figure 30 shows an example of I-V characteristics. In this case, only two detectors, 2 and 3, show superconducting characteristics represented by the blue and green curves, respectively. In addition, detector 2 has a higher critical current. The variability and low reproducibility of the fabrication process can explain the lack of superconductivity observed in detectors 1 and 4.

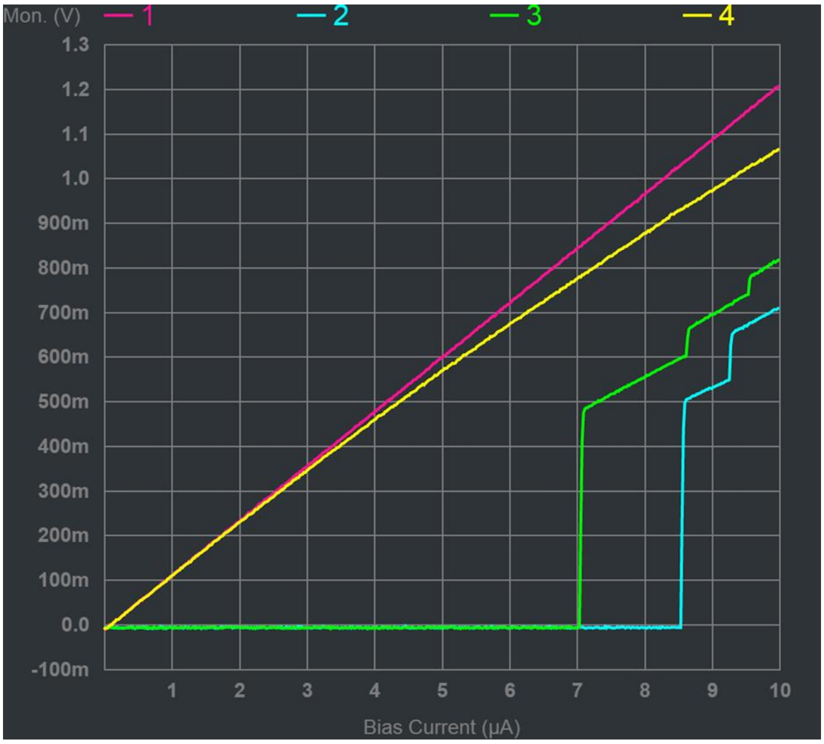

Figure 30: *example an I-V characteristics measurements of SNSPDs*

For the measurement of the photodetectors, the devices are biased at 90% of I_C. The dark counts are measured with the laser off; then, the laser is turned on to measure the signal counts.

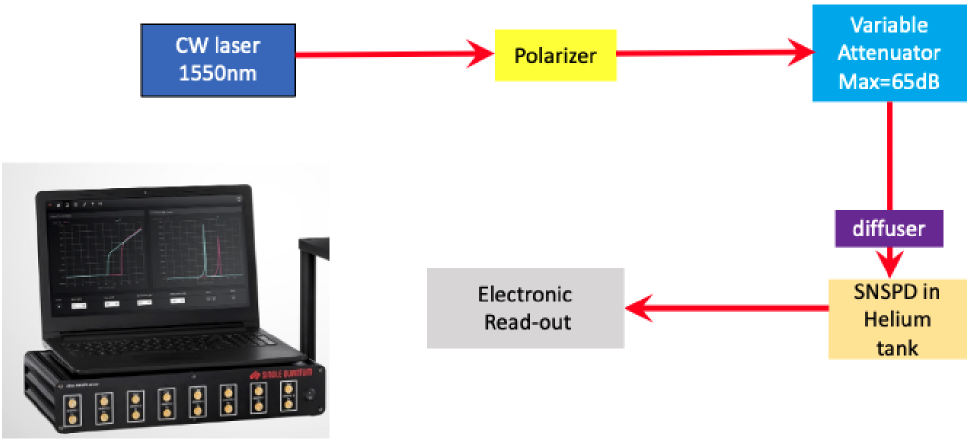

Figure 31: measurement set-up used for the electrical and optical characterization of SNSPDs

Using this configuration, the SNSPD detection efficiency η can be expressed as the ratio of the number of detected photons over the number of incident photons:

$$\eta = \frac{N_{photons\ detected}}{N_{photons\ sent}} = N_{photons\ detected} * \frac{P_{1\ photon}}{P_{system}} \qquad \textbf{(2)}$$

with

$$\mathrm{N}_{\text{photons detected}} = \frac{\text{counts (laser ON)}-\text{counts(laser OFF)}}{\text{s}} \qquad \textbf{(3)}$$

Therefore, the efficiency can be calculated using this formula:

$$\eta = \frac{\text{counts (laser ON)}-\text{counts(laser OFF)}}{\text{s}} * h * \frac{c}{\lambda} * \frac{1}{\mathrm{P}_{\text{system}}} \qquad \textbf{(4)}$$

where h is the Planck constant, c is the speed of light in vacuum, λ is the wavelength and $\mathrm{P}_{\text{system}}$ is the power measured by the germanium reference photodetector.

Figure 32 presents the efficiency of two SNSPDs with 5 nm of NbN deposited on 11 nm of AlN (S4) and 9 nm of NbN on 19 nm AlN (S7), measured at 1550 nm as a function of the bias current. The maximum recorded efficiency close to the critical current was 8% and 6% for 9 and 5 nm of NbN, respectively, which is in good agreement with the simulated values of 11 and 7%. The slightly lower experimental value can be assigned to the 1-2 nm thick surface oxidation of NbN, which was verified by X-ray reflectometry measurements.

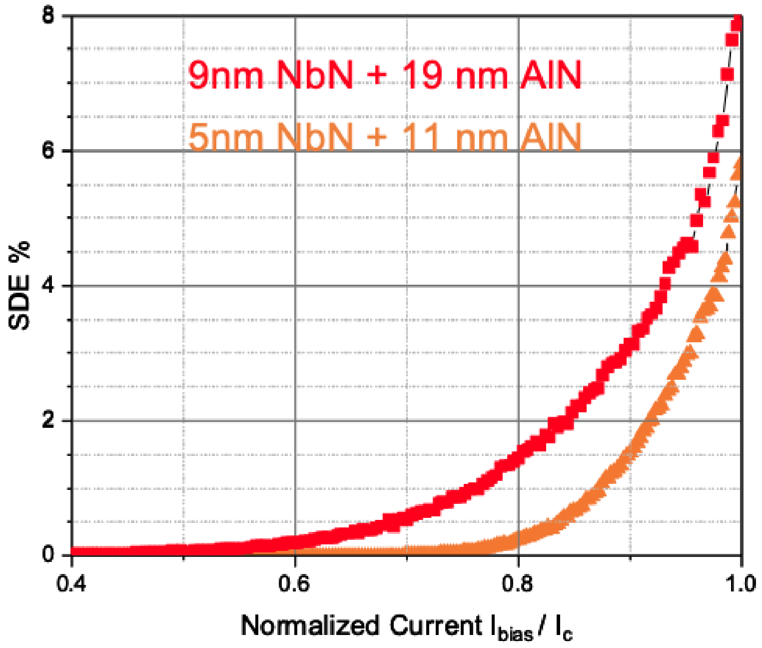

***Figure 32** : Detection efficiency as a function of the bias current/critical current ratio ($\frac{I_b}{I_c}$), measured for an SNSPD device fabricated on samples S4 and S7 and measured at 1550 nm, at 4.2 K (liquid He immersion).*

To study the saturation of SNSPDs at 4K, the characterization needs to be carried out with higher-energy photons. The saturation provides information about the maximum internal detection efficiency. Therefore, we characterized the sample S4 at λ = 808 nm. The saturation response of sample S4 is depicted in Figure 33. The maximum recorded efficiency close to the critical current was 5.8% which is in good agreement with the simulated values of 9%. Therefore, these SNSPD measurements validate the single-photon detection properties of high-quality NbN obtained using a thin buffer layer of sputtered AlN.

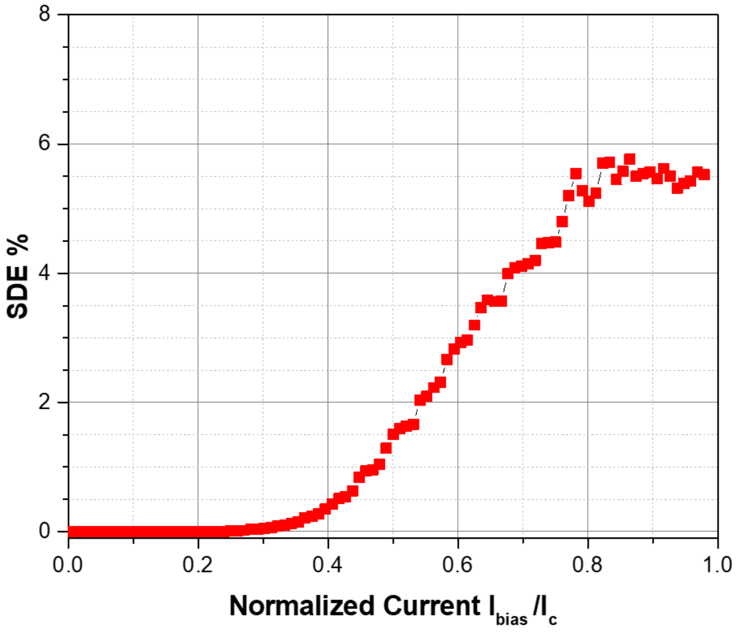

Figure 33 : *Detection efficiency as a function of the bias current/critical current ratio* ($\frac{I_b}{I_c}$)*, measured for an SNSPD device fabricated on S4 and measured at 880 nm, at 4.2 K (liquid He immersion).*

On the 2×2 cm^2 sample, it is possible to achieve relatively homogeneous illumination. However, the number of photons that reach each device cannot be evaluated precisely. Nevertheless, this configuration allows the simultaneous characterization of several detector, providing a fast validation of the superconducting properties of the meanders. Furthermore, this characterization does not require Bosh etching, which is a heavy processing step that can deteriorate the SNSPDs superconducting properties.

For a precise characterization of the SNSPD, the 2×2 cm^2 grinded chips are fully etched to obtain keyholes. Unfortunately, samples S4 and S9 were broken when inserting the keyhole in the fiber sleeve. The samples were brittle as a result of the grinding process. Therefore, I was unable to carry out these measurements.

3.6 Conclusion

We have developed high-quality polycrystalline NbN thin (5-11 nm) films on 200 mm silicon substrates thanks to the introduction of a thin (10-20 nm) AlN layer, both materials being deposited with CMOS-compatible sputtering processes. Whereas NbN directly deposited on silicon presents randomly oriented grains, NbN deposited on AlN is textured along the <111> axis, which translates into an improvement of its critical temperature up to 10 K for 9 nm thick NbN. This is important for practical applications to reduce the energy consumption, cost and footprint of cryogenic systems. In addition, we have fabricated simple fiber-coupled SNSPD architectures based on NbN/AlN and operating under normal incidence illumination. The SNSPDs feature a system detection efficiency of 6-8% for NbN thickness in the range 5-9 nm, in good agreement with simulated values. These results validate the single-photon detection properties of the NbN/AlN stack. By modifying the device design to incorporate resonant cavity effects [182], these 200 mm silicon wafers could serve as a base material for the realization of high-efficiency fiber-coupled SNSPDs, as well as arrays of SNSPDs for imaging applications in a long term perspective.

Moreover, the deposition of such NbN/AlN stack on SOI wafers can be used to fabricate waveguide-integrated detectors, which are the keystone for the development of a fully integrated quantum photonics platform able to generate, manipulate and detect a large number of photonic qubits for secure communications and quantum computing. This will be the subject of the next chapter.

Chapter 4- Superconducting Waveguide Single-Photon Detectors: Design and layout of the maskset

4.1 Introduction

This chapter is devoted to the development of SNSPDs integrated with a photonic waveguide. The final purpose is to combine them with single-photon sources and passive or active components to develop fully integrated circuits for quantum applications. We aim at developing CMOS-compatible detectors by taking advantage of advanced microelectronics and photonics platforms for future large-scale deployment, low-cost and mass manufacturing of Quantum Photonics Integrated Circuits QPICs. Through this chapter, we will cover the design of waveguide-integrated SNSPDs. First, the absorption probability of a photon by the integrated SNSPD will be studied numerically as a function of the nanowire geometry and dimensions as well as the waveguide width. In addition, a further increase in efficiency is studied by embedding the SNSPD in a ring resonator. The effect of different designs (nanowire length and ring resonator size) is simulated analytically and numerically. For both straight waveguide integrated SNSPDs and SNSPDs embedded in ring resonators, we studied the two distinct material stacks NbN on silicon and NbN/AlN on silicon. Finally, we describe the design of a maskset, called layout, including waveguide-integrated SNSPDs in various configurations.

Photonic integrated circuits are based on the manipulation of light propagating in optical waveguides. The mechanism underlying the confinement of the electromagnetic field is total internal reflection. A waveguide is typically composed of a material with a high refractive index n_1 surrounded by a material with a low refractive index n_2. If the incident angle at the surface is lower than the critical angle $\theta_c = arc\sin\frac{n_2}{n_1}$, light passing inside the high index medium will undergo an entire internal reflection at the interface of the low index material [183]. Therefore, the light is trapped inside the high index material. Light confinement can be achievable in one, two, or three dimensions depending on the structure type.

Propagation is quite simple to understand for large waveguides. However, when the dimensions of the confinement structure are reduced to the order of magnitude of the wavelength, other phenomena arise. Light reflected from the upper interface interferes with light reflected from the lower interface. As a result, the light propagates in specific modes. Waveguides with only one propagating shape are called single-mode waveguides. Most of the commonly used waveguides in photonics have finite dimensions in both axis x and y as shown in Figure 34 . The electric field is two-dimensionally confined and free to propagate along the third direction in these structures. The study of the optical modes of a wave propagating in the z-direction leads to the search for solutions to Maxwell's equation derivatives [183] :

$$\frac{\partial^2 E_z}{\partial x^2}+\frac{\partial^2 E_z}{\partial y^2} = [\beta^2 - k_0^2 n^2(x,y)]\, E_z \quad \textbf{(1)}$$

$$\frac{\partial^2 H_z}{\partial x^2}+\frac{\partial^2 H_z}{\partial y^2} = [\beta^2 - k_0^2 n^2(x,y)] H_z \quad \textbf{(2)}$$

Where n is the refractive index, $k_0 = \frac{\omega}{c}$ is the wave vector in vacuum, $\beta = n_{eff} k_0$ is the propagation constant, E_z the z component of the electric field and H_z that of the magnetic field.

Unfortunately, these equations do not have analytical solutions; in order to solve them, it is necessary to make some approximations. The two most popular methods are the Marcatili method and the effective index method. Alternatively, it is possible to use numerical methods like the Finite-Difference Eigenmode (FDE) method [184].

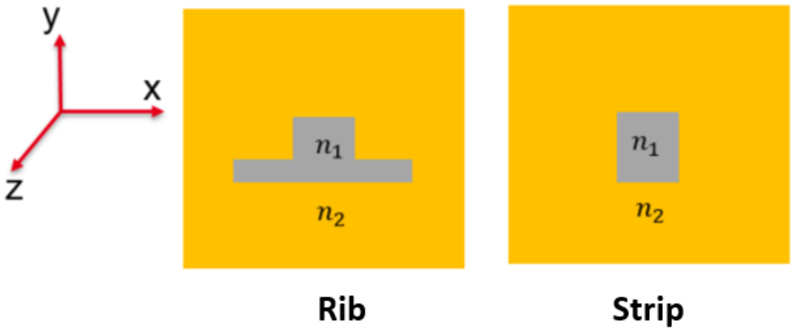

***Figure 34 :** Schematic showing a rib waveguide on the left and the strip waveguide on the right. (The oxide is represented in yellow and the silicon in grey)*

By using these different resolution methods, it has been demonstrated that the intensity of the traveling electric field does not vanish abruptly at the waveguide's boundaries but rather decreases exponentially with distance. This evanescent tail of the electric field depends on the refractive index contrast between the waveguide material and the surrounding medium. It is, therefore, possible to make the evanescent field interact with external devices, such as a superconducting nanowire single-photon detector.

4.2 Design of Waveguide Integrated SNSPDs

The proposed architecture is based on the SOI integrated SNSPD successfully built by Pernice et al. in 2012 [185]. In this configuration, the superconducting nanowire is placed atop the SOI waveguide, and evanescent coupling takes place at the interface between the nanowire and the waveguide. As a result, a fraction of the field is absorbed by the nanowire due to the exponentially decaying field outside the waveguide and inside the detector. Since the coupling is achieved through evanescence, the mode guided in the SOI waveguide should feature a significant evanescent tail into the superconducting nanowire on top to allow for maximum absorption over a short length. Therefore, it is necessary to select the appropriate waveguide geometry that meets the desired field distribution criteria.

Waveguides with strong mode confinement are obtained either by partial etching of the silicon layer, resulting in a rib geometry [186,187], or by full etching of the silicon down to the buried oxide, resulting in a strip geometry [188,189] (see Figure 34). Kahl et al. [190] showed that strip structures exhibit a higher field absorption by the SNSPDs than rib structures. This is explained by the fact that the propagation field is more distributed towards the substrate in rib waveguides and features a smaller overlap with the nanowire on top. For this reason, we opted for strip waveguide geometry in this work.

Regarding the dimensions, the height of the waveguide is determined by the silicon layer of the SOI. In the silicon photonics platform developed at LETI, the height of silicon waveguides has been selected to be 300 nm. This thickness corresponds to a historical choice made by LETI for telecom/datacom applications. It corresponds to a trade-off in the efficiency of the fiber grating couplers at the wavelengths of 1550 and 1310 nm. The objective being to develop a fabrication process for waveguide-integrated SNSPDs that is compatible with the existing mature platform, we will keep the 300 mm waveguide thickness.

The optimal width of the SOI waveguide will be determined in the following by numerical simulations to simultaneously ensure a monomode behavior in TE polarization, minimize propagation losses and maximize the evanescent part of the field on the top of the waveguide. In order to optimize the absorption efficiency, we will first investigate the photon absorption probability of an integrated SNSPD as a function of the geometry and dimensions of the nanowires and of the waveguide width on which it is placed. Then, we will explore a further improvement by embedding the SNSPD into a resonant cavity formed by a ring resonator. Finally, we propose a novel detection scheme for achieving PNR using integrated SNSPDs in series.

4.2.1 Straight waveguide-integrated SNSPDs

Figure 35 shows the NbN waveguide-integrated SNSPD schemes that will be investigated in this section. Figure 35.a consists of a straight nanowire, while Figure 35.b depicts a U-shaped nanowire expected to provide more absorption per unit length and thus lead to more compact devices. It has been shown in the material development section that the incorporation of an AlN layer improves the superconducting properties of NbN by increasing the critical temperature by a few Kelvin. Our objective is to also investigate the impact of the AlN layer on the fabrication process and the performances of SNSPD devices. In the following, we will therefore perform simulations of structures with NbN directly on silicon and with the presence of the intermediate AlN layer.

The simulations were carried out with the finite difference eigenmode solver (FDE) available with the commercial software Lumerical MODE. By solving Maxwell's equations on a transverse mesh of the waveguide, this solver calculates for each mode supported by the waveguide geometry, their spatial field profile, their effective index, their propagation losses. All simulations were performed at a wavelength of 1.55 µm. The refractive indices for the silicon waveguide, the oxide cladding and the buffer AlN layer are respectively n(Si) = 3.476, n(SiO_2) = 1.44 and n(AlN) = 2.029. Furthermore, according to the ellipsometry measurements of Niobium Nitride presented in Chapter 3, the refractive index of NbN is n (NbN) = 3.833 + 3.425 i.

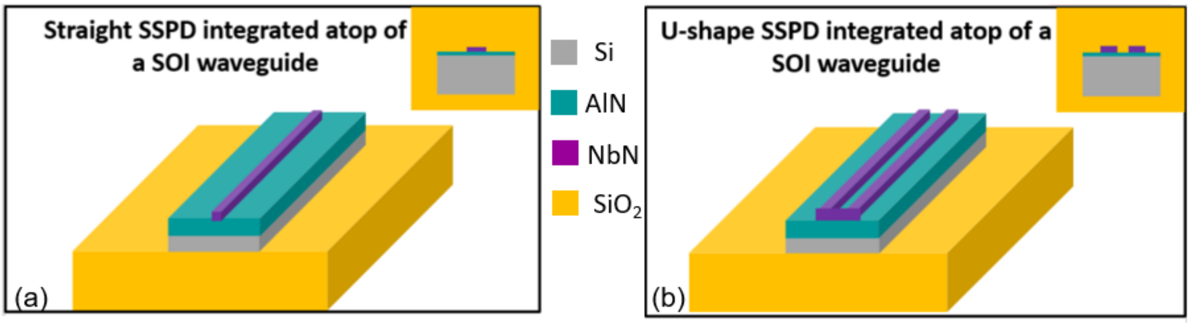

Figure 35 : *Schematics of NbN-based SNSPD integrated on (SOI). The simulations were performed with native oxide that is not represented in the figures for the sake of clarity (not to scale)*

The aim of this optical simulation is to study the absorption efficiency of field from the waveguide into the detector. Here, the evanescent field at the waveguide interface overlaps with the superconducting nanowire and gets partially absorbed. The simulations are performed by calculating the propagation loss inside a waveguide originating from absorption within the superconducting nanowire on top of it. Through these simulations, we will investigate the nanowire geometry (straight or U-shape), its length as well as the waveguide width.

4.2.1.1 Choice of nanowire geometry

The U-shape structures will be the main development of this work, while straight nanowire structures will provide a reference. In the U-shape structure, the detector is modeled as two parallel nanowires approximating a U-shaped nanowire. The curvature was not taken into account in the simulation. The dimensions chosen for the two NbN nanowires are 100 nm in width, separated by a gap of 120 nm. This choice results from several compromises. Indeed, wider nanowires would result in higher absorption. However, the nanowires need to be narrow for successful hot spot formation. Tyler [191] investigated the effect of varying the distance between the nanowires. The analysis revealed that the absorption increases as the separation decreases. That is because the nanowires get closer to the waveguide center, where light confinement is highest. Bringing the wires too close together, on the other hand, is challenging in terms of fabrication. In addition, shifting the U-shape nanowire on either side of the waveguide center while maintaining the 120 nm separation to simulate possible misalignment results in a decrease in absorption. This is because the highest mode confinement is found in the waveguide center.

4.2.1.2 Investigation of waveguide width

To achieve strong field absorption of NbN, we first need to optimize the waveguide width. Therefore, we simulated the absorption by varying the width (400 nm, 500 nm and 600 nm) for several thicknesses of NbN (5 nm, 7 nm and 9 nm). The standard nanowire dimensions (100 nm wide and 120 nm for space separation) were used. The results are presented in Figure 36.

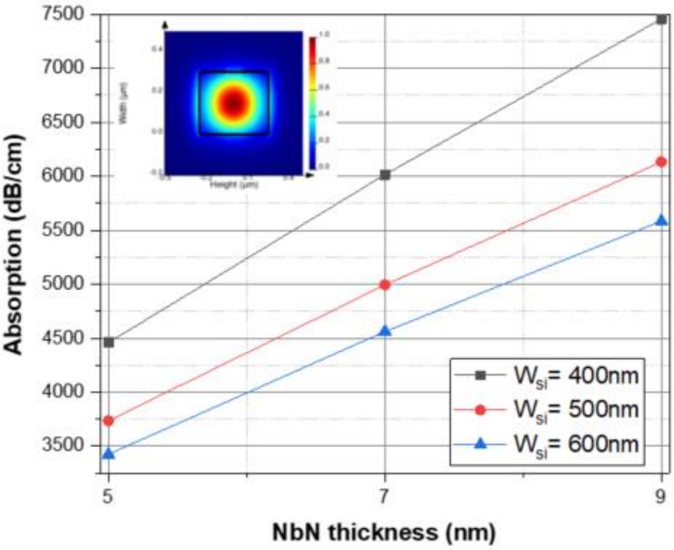

Figure 36 : *Study of the nanowire absorption in function of the NbN nanowire thickness and Si waveguide width. The absorption increases with the NbN thickness and decreases with the waveguide width.*

Since the mode is confined closer to the center, where the nanowires are positioned, narrower waveguides exhibit higher absorption. The waveguide dimensions cannot be reduced further because this would result in propagation losses due to scattering by sidewall roughness. Therefore, we set the waveguide width to 400 nm. The inset shows the intensity distribution inside the waveguide-integrated SNSPD for the fundamental TE mode. It can be seen that the waveguide mode overlaps with the nanowires, resulting in field absorption from the waveguide into the nanowires. In addition, Tyler and al. [191] performed FDTD simulations to estimate the losses due to reflections caused by connecting the two nanowires and introducing a 90 degree bend towards the edge for electrical connections. It was found that the highest expected reflections are 0.004% which are negligible.

4.2.1.3 Nanowire length

The coupling length between the detector and the propagating mode determines the absorption efficiency. As a result, higher absorption efficiency requires the use of longer or wider nanowires. On the other hand, long nanowires have a larger footprint, a higher jitter and a longer recovery time which can limit their counting rate. Figure 37 compares the configuration of a straight nanowire versus a U-shape nanowire. Figure 37.a shows that the absorption of a straight nanowire is much lower than that of a U-shape one. This is expected because there is more NbN to absorb the field propagating for the U-shape nanowire. The trend is the same for the different NbN thicknesses. Figure 37.b compares the lengths of the nanowires to achieve a given absorption for the two configurations with 5 nm of NbN. For a residual transmission of the order of 10^{-3} , a 67 µm detector is needed in the U-shape configuration versus 115 µm for a straight nanowire, making a difference of almost 50 µm. Therefore, the U-shape configuration is more advantageous because it allows designing compact detectors.

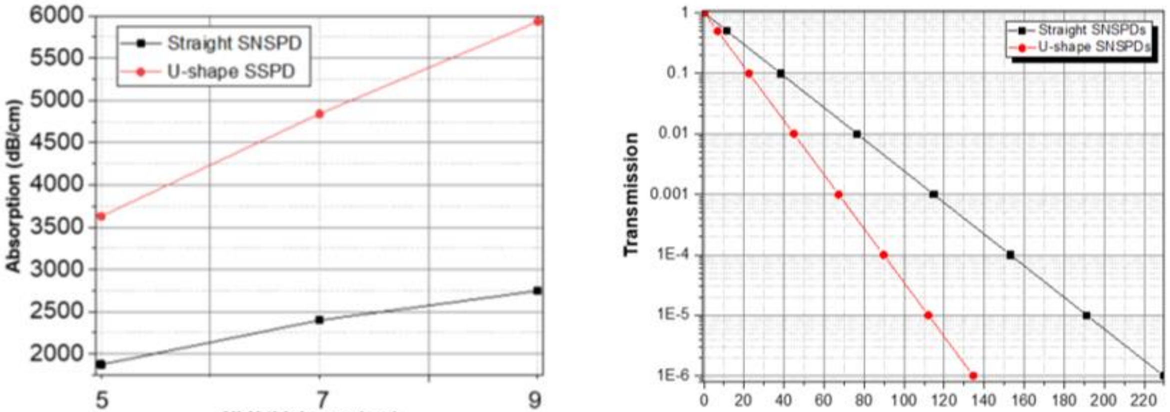

(a) (b)

Figure 37 : *(a) Absorption simulation results for U-shape and straight SNSPDs as a function of NbN thickness. (b) Transmission simulations for both configurations as a function of nanowire length.*

As already discussed in the previous chapter, to improve the superconducting properties of NbN, a buffer layer of AlN was introduced. However, this layer results in moving the NbN away from the waveguide mode. For this reason, a stack with only 10 nm AlN was developed to achieve a better evanescent coupling while improving the quality of the NbN. The impact of the 10 nm AlN layer on the transmission is shown in Figure 38. For a residual transmission of 10^{-3}, the AlN layer lengthens the detector by about 15 µm to 81 µm.

4.2.1.4 Conclusion

In conclusion, the simulations show that high absorption can be achieved for a U-shaped SNSPD configuration centered on the waveguide, leading to nanowire length of less than 100 µm, even in the presence of the AlN buffer layer developed to improve the superconducting properties of the NbN layer. Therefore, the length of nanowires of straight waveguide integrated SNSPDs is much shorter than that of meander structure (vertically coupled detectors), which is on the order of several hundred microns (>200µm).

However, it is important to keep in mind that the simulations only provide a theoretical estimation of the absorption. Due to possible fabrication imperfections or limitations, such as the difficulty to control the deposition of nanometric layers and the size of the patterns, the required length to achieve a given absorption might be slightly higher experimentally.

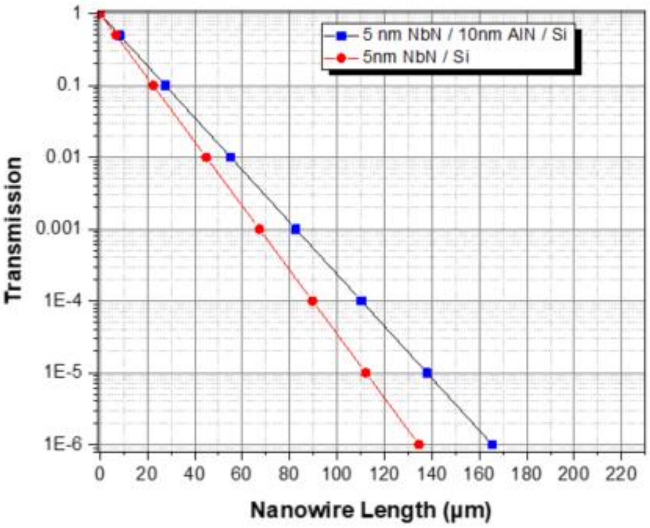

Figure 38 : *Comparison of transmission simulation results of a U-shaped detector with and without the incorporation of the AlN buffer layer.*

4.2.2 SNSPDs embedded in Ring Resonators

The previous section showed that the absorption (expressed in dB/cm) of waveguide-integrated SNSPDs is proportional to the interaction length between the propagating mode and the NbN nanowires. Long nanowires improve the absorption [192,193], but on the other hand, they also increase the inductance, resulting in slow devices [194]. The length of waveguide-integrated nanowires is already significantly shorter than those of vertically coupled detectors (typically >200 µm). There is therefore a strong interest in shortening the nanowire length while increasing the efficiency, decreasing the detector footprint and reducing the impact of possible fabrication imperfections[195]. In analogy to fiber-coupled detectors [196,197], enhancement of the absorption efficiency can be achieved by embedding the detector in a photonic cavity to benefit from multiple passes of light through the superconducting material[198–200]. Recent results on integrating SNSPDs inside a photonic-crystal cavity [198] demonstrated a highly efficient SNSPD with a length of only 8.5 µm. Furthermore, using a ring cavity has been shown to improve conventional photodiode efficiency [201,202].

However, because of the presence of the cavity, the detector functionality is limited in bandwidth. Nonetheless, the cavity filtering effect helps to reduce stray light absorption, resulting in a lower dark count rate. Additionally, the use of compact detectors reduces the dark counts induced by defects. Fast detectors with a Gcps count rate would enable a very high rate for the raw distribution of secret quantum keys. This approach breaks the recovery time vs. absorption efficiency trade-off dilemma, allowing to design and fabricate very compact devices.

In this work, the SNSPD was embedded in a waveguide racetrack cavity based on the model proposed by Tyler et al. [191]. This configuration can be tuned to achieve resonance for any SNSPD wavelength. The racetrack resonator geometry was chosen because of its compatibility with standard photonic elements and LETI's expertise in low loss, high quality factor, silicon ring resonators.

4.2.2.1 Ring resonator model

The ring resonator is one of the building blocks of PICs. Resonators are simple structures composed of a looped waveguide, allowing to create an optical cavity, forcing light to propagate multiple times in a closed path, before it is lost. The ability to confine light in a resonant structure improves the light-matter interaction, leading to short SNSPDs with high-efficiency. Ring resonators have been widely used over the past decades [203] and are exploited for many applications, such as wavelength conversion [204–206] and generation of non-classical states of light for quantum communication[207–209].

As shown in Figure 39, the resonator can be accessed evanescently through a bus waveguide (side coupling). At a given wavelength, the phase shift, after a round-trip in a ring resonator with a radius R, is:

$$\phi(\lambda) = \frac{2\pi}{\lambda}\, n_{eff}(\lambda). 2\pi R \quad \textbf{(3)}$$

where $neff$ is the effective index of the waveguide at the input wavelength. From Figure 39, the resonance condition is satisfied when there is no phase shift between the fields E1 and E2. As a result, after a round-trip, (λ) has to be equal to an integer multiple of 2π and the resonance condition can be expressed as follows:

$$m(\lambda_0) = \frac{2\pi}{\lambda_0}\, n_{eff}\,(\lambda_0). R \quad \textbf{(4)}$$

where the integer m is the resonant mode number. Therefore, after a round trip, the light interferes constructively.

Assuming that only one single clockwise mode of the resonator is excited, the attenuation of the amplitude of the electric field collected through the round-trip due to the losses is expressed by

$$A = e^{-\alpha_{nw} L_{nw}\, \pi/2} \times e^{-\alpha_{si} L_{Si}\, \pi/2} \quad \textbf{(5)}$$

Where $\boldsymbol{\alpha_{nw}}$ and $\boldsymbol{\alpha_{si}}$ represent the losses in the nanowire region $\boldsymbol{L_{nw}}$ and in the racetrack made of silicon $\boldsymbol{L_{Si}}$ as illustrated in Figure 39.

The following matrix [183,210] can express the interaction between different fields

$$\begin{matrix} E_{out} \\ E_2 \end{matrix} = \begin{bmatrix} T & iK \\ iK & T \end{bmatrix} \begin{matrix} E_{in} \\ E_1 \end{matrix} \quad \textbf{(6)}$$

T is the transmission coefficient, and K is the coupling coefficient, both of which are expressed in amplitude and are linked through the equation $|T|^2 + |K|^2 = 1$. For the abrupt phase shift in an ideal coupling regime, the imaginary i value is added [211]. At resonance, the equations of the normalized transmitted power and the normalized power circulating in the ring can be reduced to:

$$P_{transmitted}(\lambda_0) = \left|\frac{E_{out}}{E_{in}}\right|^2 = \frac{(A-T)^2}{(1-AT)^2} \quad \textbf{(7)}$$

$$P_{circulating}(\lambda_0) = \left|\frac{E_1}{E_{in}}\right|^2 = \frac{A^2(1-T^2)}{(1-AT)^2} \quad \textbf{(8)}$$

The resonant condition corresponds to the transmission minimum.

The maximum field intensity in the ring is obtained at the so-called critical coupling condition when the transmission coefficient is equal to the losses in the cavity $A = T$.

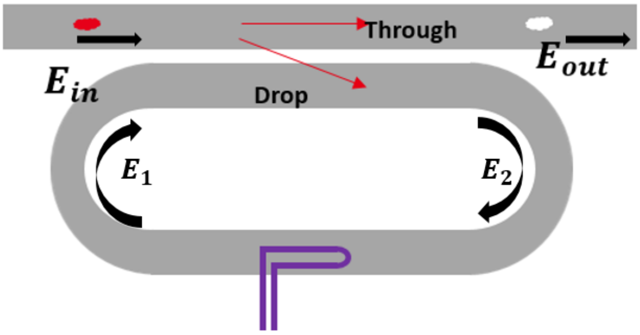

Figure 39 : *Top-view schematics of an SNSPD integrated atop a racetrack resonator. The light entering the bus waveguide is represented by* $\boldsymbol{E_{in}}$*, and the collected light is represented by* $\boldsymbol{E_{out}}$*. The drop corresponds to the transmission coefficient per unit length T, and the through corresponds to the reflectivity coefficient.*

4.2.2.2 Design and Simulation model of SNSPD integrated in a resonator

Figure 39 illustrates an SNSPD integrated with a waveguide racetrack resonator. At the resonant frequency and under critical coupling condition, i.e., when the losses inside the cavity balance the coupling losses, light is coupled in and out of the resonator in the coupling region and destructively interferes at the waveguide output. This means that the absorption of the SNSPDs reaches its maximum value. At this point, photons become trapped inside the cavity and remain there until they are absorbed by the nanowire or out-scattered at the waveguide walls. For racetrack resonators with low losses, the nanowire acts as the main dissipative medium, allowing for near-unity absorption efficiency of the detector. The losses of the racetrack must therefore be carefully minimized through an optimized etching process as they are the main limitation from achieving unitary detection efficiency.

For the simulation, two distinct racetrack resonators were considered. Racetrack lengths of just over 57 µm (configuration 1) and 67 µm (configuration 2) were chosen. The 57.1 µm length is the result of two 7.5 µm bend-radius semicircles (this is the minimum bend radius to achieve low losses) and 5 µm long straight waveguide sections. On the other hand, the 67.1 µm circuit has a 10 µm straight waveguide. The SNSPD is modeled as two parallel NbN nanowires of 5 nm thickness approximating a U-shape nanowire. The standard dimensions of the two NbN nanowires are 100 nm in width of 120 nm in separation between the nanowires. The SNSPD is placed atop a silicon waveguide with a cross-section of 400 nm by 300nm (cross-section optimized in the previous section).

This structure has been investigated both analytically and numerically and the results are complementary as explained in the following. The objective is to determine for each configuration the gap between the bus waveguide and the racetrack resonator in order to achieve critical coupling, hence maximum detection efficiency by the nanowire embedded in the cavity.

- Analytical modeling

Tyler et al. [191] provided an analytical model to investigate SNSPDs integrated with resonators, in which the transmission coefficient at critical coupling is expressed as follows

$$\boldsymbol{T = \alpha^2 = 10^{-(\alpha_{nw}L_{nw}+\alpha_{si}L_{si})/20}} \quad \textbf{(9)}$$

For the simulation, four different values of silicon waveguide losses were considered $\boldsymbol{\alpha_{si}}$= [0.5,1,1.5,2] dB/cm). As this parameter depends on the fabrication, the chosen values correspond to the range of loss values usually measured for silicon waveguides fabricated at LETI. Therefore, the transmission coefficient accounts for scattering losses in the waveguide throughout the racetrack length $\boldsymbol{L_{Si}}$ as well as the losses due to absorption of the nanowire $\boldsymbol{L_{nw}}$.

In this model, the nanowires are simulated as a waveguide section with a corresponding complex effective refractive index to take into account their effect. However, this model is only an approximation. Lumerical's finite difference eigenmode solver (FDE) is used to calculate the effective refractive index $\boldsymbol{n_{eff}}$ of the fundamental TE mode of this section and its effective absorption $\boldsymbol{\alpha_{nw}}$. Table 5 shows the values of $\boldsymbol{n_{eff}}$ and $\boldsymbol{\alpha_{nw}}$ obtained with Lumerical. Afterwards, we calculated the transmission coefficient using equation **(9)** for several nanowire lengths between 1 µm and 10 µm.

The transmission results for both racetrack configurations are shown in Table 6, Table 7, Table 8 and Table 9. It was also calculated for each considered waveguide loss $\boldsymbol{\alpha_{si}}$, nanowires length $\boldsymbol{L_{nw}}$.and for the two different stacks: 5 nm NbN/Si and 5 nm NbN/1 0 nm AlN/Si. According to these results, the considered variation of $\boldsymbol{\alpha_{si}}$ has a minor impact on the transmission, whereas the variation of the nanowire length $\boldsymbol{L_{nw}}$ has a more significant influence. Moreover, the two different stacks exhibit different transmission values, this is mainly explained by a smaller $\boldsymbol{\alpha_{nw}}$ due to the integration of an AlN buffer.

	5 nm NbN /Si	5 nm NbN/10 nm AlN /Si
$\boldsymbol{n_{eff}}$	2.46 + i0.013	2.47 + i0.01
$\boldsymbol{\alpha_{nw}}$ (dB/cm)	4459.9	3627.6

***Table 5** The effective index and the corresponding $\boldsymbol{\alpha_{nw}}$ for NbN on Si and NbN/AlN on Si*

α_{si} / L_{nw}	1 µm	2.5 µm	5 µm
0.5 dB/cm	0.9018	0.7731	0.5980
1 dB/cm	0.9012	0.7726	0.5976
1.5 dB/cm	0.9006	0.7721	0.5972
2 dB/cm	0.9000	0.7715	0.5968

Table 6 *Transmission coefficient for* $L_{Si} = 57.1$ µm *for NbN on Si*

α_{si} / L_{nw}	1 µm	2,5 µm	5 µm	10 µm
0.5 dB/cm	0.9017	0.7730	0.5980	0.3578
1 dB/cm	0.9010	0.7724	0.5975	0.3576
1.5 dB/cm	0.9003	0.7718	0.5970	0.3573
2 dB/cm	0.8996	0.7712	0.5966	0.3570

Table 7 *Transmission coefficient for* $L_{Si} = 67.1$ μm *for NbN on Si*

α_{si} / L_{NbN}	1 µm	2.5 µm	5 µm
0.5 dB/cm	0.9193	0.811	0.6582
1 dB/cm	0.9187	0.8105	0.6577
1.5 dB/cm	0.9181	0.8099	0.6573
2 dB/cm	0.9174	0.8094	0.6569

Table 8 *Transmission coefficient for* $L_{Si} = 57.1$ μm *for NbN/AlN on Si*

α_{si} / L_{NbN}	1 µm	2.5 µm	5 µm	10 µm
0.5 dB/cm	0.9192	0.8109	0.6581	0.4334
1 dB/cm	0.9184	0.8103	0.6576	0.4331
1.5 dB/cm	0.9177	0.8098	0.6571	0.4327
2 dB/cm	0. 9170	0.809	0.6566	0.4321

Table 9 *Transmission coefficient for* $L_{Si} = 67.1$ μm *for NbN/AlN on Si*

- Numerical simulation

This section describes how to calculate the transmission coefficient numerically for a given gap between the bus waveguide and the racetrack resonator. The coupling coefficient decreases exponentially (the transmission coefficient increases exponentially) when the gap increases. Finite Difference Time Domain (FDTD) simulations can be used to estimate the coupling. This method involves dividing the space into small cells (lower than $\frac{\lambda_0}{10n}$, where n is the material refractive index) and solving the discretized time-dependent Maxwell equations [212,213] at the price of quite long simulation time.

Our design was optimized using FDTD numerical simulations by Lumerical, using the same waveguide cross-section (400 nm by 300 nm). A mode source coupled to the bus waveguide is placed far enough from the coupling region to consider negligible coupling with the racetrack as shown in Figure 40. Then, the first field monitor is set on the waveguide after the coupling region at the same distance as the source and the second one is placed in the racetrack. The power collected by the two monitors allows determining the coupled and transmitted powers.

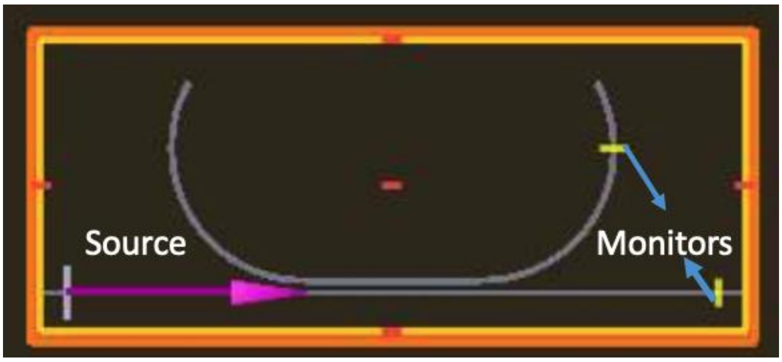

Figure 40 : *Schematic of the structure to be simulated in Lumerical. The FDTD region is represented in orange and includes the coupling region, the source, and the monitors of the field*

To proceed, the gap is randomly set to a value, and the simulation is run to obtain the corresponding transmission. The gap is then adjusted to reproduce the transmission values shown in Table 6, Table 7, Table 8 and Table 9. These simulations were performed for the two distinct racetrack configurations, and the results are shown in Figure 41. As can be seen in Figure 41, depending on the gap between the bus waveguide and the racetrack, the transmission can be tuned between nearly 0 and 1.

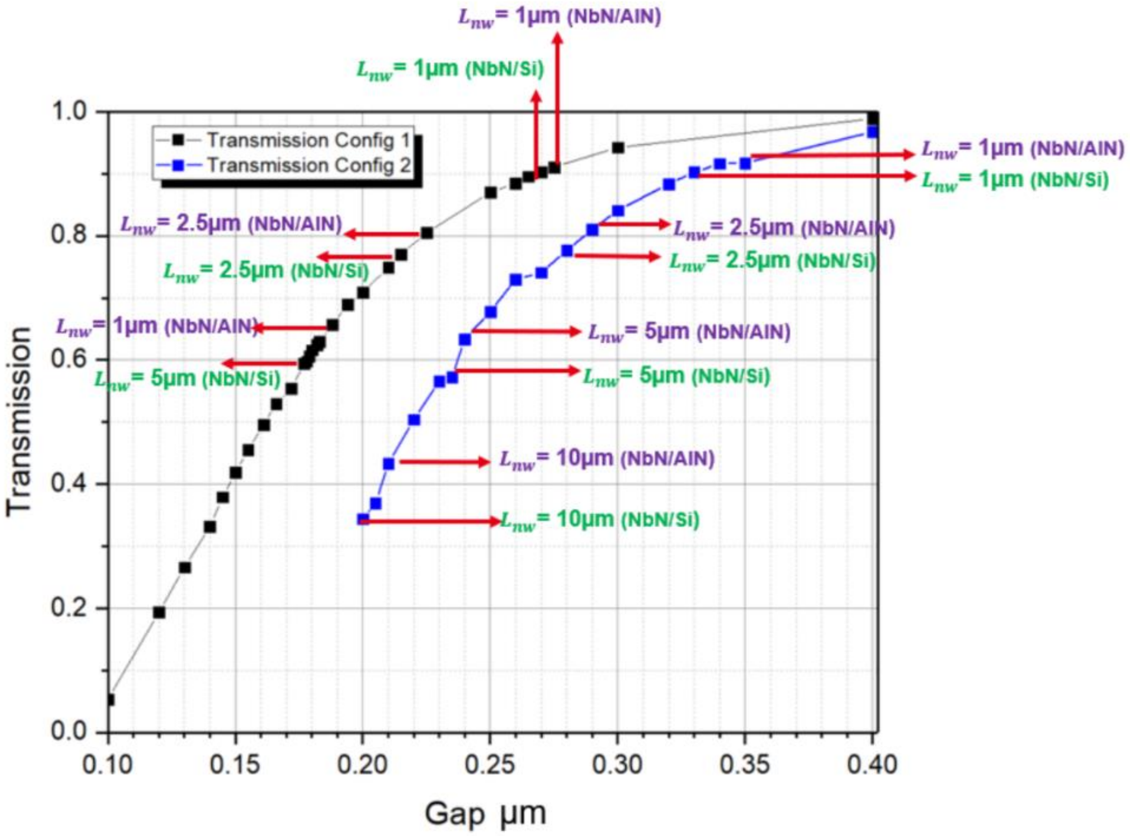

Figure 41 : *FDTD simulated transmission coefficient of the racetrack resonator. The black squares show the results of the simulations for a racetrack length of 57 µm, while the blue squares are associated to a racetrack length of 67 µm. Each point corresponds to a different simulation. The simulations results corresponding to the critical coupling condition for each stack and each nanowire length are highlighted.*

By matching the analytically calculated transmission values and the numerically calculated one, we can define a gap corresponding to the critical coupling condition for each racetrack configuration associated to each nanowire length. The gap values are summarized in Table 10 and Table 11.

NbN stack / L_{nw}	1 µm NbN	2.5 µm NbN	5 µm NbN
5nm on Si	270 nm	215 nm	180 nm
5nm on 10nm AlN	275 nm	225 nm	190 nm

Table 10 *The corresponding gap values to racetrack configuration 1*

NbN stack / L_{nw}	1 µm NbN	2.5 µm NbN	5 µm NbN	10 µm NbN

5nm on Si	330 nm	280 nm	235 nm	205 nm
5nm on 10nm AlN	335 nm	290 nm	245 nm	210 nm

Table 11 *The corresponding gap values to racetrack configuration 2*

4.2.2.3 Conclusion

To conclude, this approach presents a single-photon detection system that could provide near-unity detection efficiency using waveguide integrated SNSPDs with nanowire lengths between 1 and 10 µm. Furthermore, this approach is compatible with large-scale CMOS fabrication processes.

However, some points need to be highlighted, in particular the length of the cavity outside the nanowire region. Light trapped within the cavity can degrade the detector's temporal resolution. If the nanowire is too short, the photon will stay in the cavity longer before being absorbed. On the other hand, longer nanowires will require fewer round trips to achieve the same absorption level. Therefore, the effect of the cavity on jitter may be questioned. Tyler et al. [191]demonstrated through simulations that extrinsic jitter (due to the cavity) increases in cavities with shorter nanowires as photons would take more laps before absorption. Specifically, jitter ranges from 0.2 ps for nanowires of 10 µm to up to 10 ps for nanowires of about 1 µm in length. As a result, the cavity does not add significant extrinsic jitter for longer nanowires of 10 µm. In contrast, this contribution increases for very short nanowires. These statements will be verified when measuring the jitter of these structures. In addition, the length of the racetrack should be chosen as short as possible in order to minimize scattering of light outside the region of the nanowire. Best performances are then expected when the nanowire length is equal to the length of the straight section, i.e., 5 µm for racetrack 1 and 10 µm for racetrack 2. Finally, in real devices, possible losses associated to the electrical connections should be taken into account. However, they are expected to be negligible under proper design.

4.2.3 Beyond the single detector: SNSPDs in series for PNR

Detectors with photon number resolution (PNR) are essential for advanced protocols in quantum communication and overall, for optical quantum computing to minimize errors. PNR functionality allows for the quantification of the photons number after an absorption event. The best performing single photon detector type to date in almost all metrics is the SNSPD. Nevertheless, it lacks photon number resolution (PNR), as it is a binary threshold detector (either on or off).

Previous works proposing pseudo-PNR with fiber-coupled SNSPDs consider a detection system consisting of many detectors [214–217]. Regarding waveguide integrated detectors, Sahin et al. [215] proposed the detection scheme presented in Figure 42. In such system, the photons are distributed over N paralleled slots and are detected by end detectors, all of efficiency η. A metric like fidelity is appropriate for evaluating such configuration. Fidelity is the probability P(p|p) of outputting p detection events when a number state $|p>$— made of exactly p photons — enters the detection system. For the above-mentioned systems, for which the photons are fanned out in parallel, the fidelity is

$$P_{parallel}(N,\{\eta\},p|p)=\frac{N!}{N^{p}(N-p)!}\eta^{p} \qquad \textbf{(10)}$$

In order to get a high fidelity, η has to be as close to 1 as possible for parallel detection schemes. However, today, it is unachievable from a fabrication point of view.

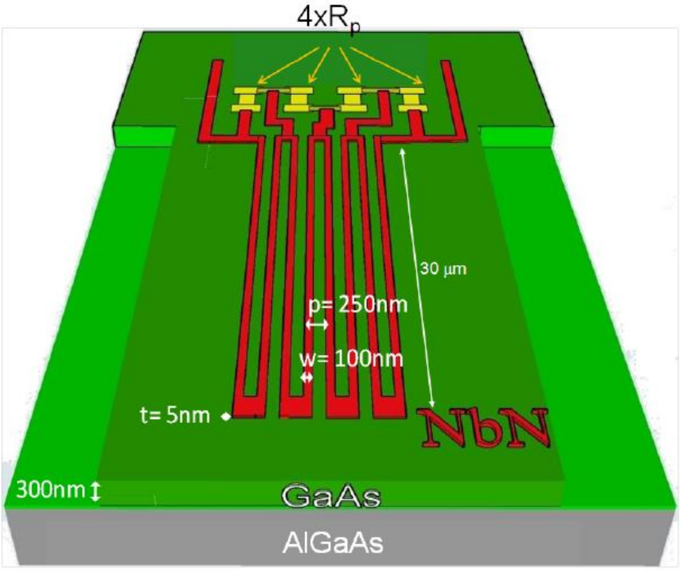

***Figure 42**: Schematic of a waveguide photon-number-resolving detector consisting of four nanowires in parallel*

Instead, Joël Bleuse and coworkers at CEA-IRIG propose a detection scheme, illustrated in Figure 43, where integrated SNSPDs are in series [218].The fidelity is expressed by:

$$P_{series}\left(N,\left\{\eta_1,\eta_i=\frac{1}{i}\right\}_{1<i\leq N;p|p)}\right)=\frac{N!}{N^{P}(N-p)!}\left(1-p\frac{1-\eta_1}{N}\right) \qquad \textbf{(11)}$$

In this configuration, the detectors are numbered from N at the entrance of the waveguide down to 1 at the end of it, their efficiencies being $\eta_i = 1/i$. Unlike the parallel scheme, only the last detector should show $\eta_1 = 1$ to maximize the fidelity. Therefore, the unavailability of unitary efficiency detectors is of small concern.

This result is obtained assuming that: i) the detectors are all the “on/off” type; ii) they all exhibit unitary internal efficiency i.e., if one photon or more are absorbed, it will be recorded as a detection event with probability 1; iii) their dark count is negligible.

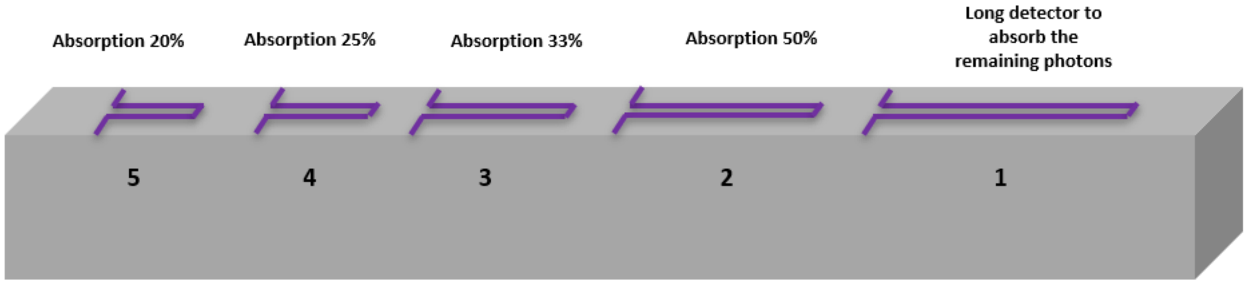

***Figure 43**: Schematic of a waveguide photon-number-resolving detector consisting of five nanowires in series*

4.3 Overview of the mask layout

This section describes the design of a maskset, called layout, including waveguide-integrated SNSPDs in various configurations, as well as a number of test structures required for proper calibration of SNSPD performances. The dimensions of the designed structures were determined by the simulations performed in section 4.2.

4.3.1 Mask levels

The maskset contains different layers associated to the lithography levels used in the fabrication process defined in collaboration with clean room experts. Here we present in Figure 44 only the sequence of the five lithography and patterning steps, while the details of the development of all fabrication steps are reported in Chapter 5. The first two lithography levels called WG and PROT correspond to standard layers for the definition of the silicon layer. The next three levels called SUPRA, CONTACT and MET1 correspond to specific layers associated to the NbN nanowire process including patterning and metallization.

- WG - Waveguide patterning

The first layer WG is used to define the silicon strip optical waveguides and racetrack resonators with DUV lithography at 193 nm wavelength. The minimum pattern dimension (line or trench) is 120 nm, defined by the resolution of the lithography tool.

- PROT - Protection of fiber grating couplers

In order to determine rib waveguides, an intermediate level of etching is defined by the second level PROT. It is used to define fiber grating couplers, alignment waveguides, reference arms, MMI as well as for the Mach Zehnder.

- SUPRA - Nanowire patterning

The third layer SUPRA is used to pattern the NbN layer into nanowires using electron beam lithography to achieve nanowire width and spacing in the range 70-100 nm.

- CONTACT - Contact patterning

The fourth layer is used to pattern vias of 8 µm x 8 µm in the encapsulating silica layer using DUV lithography at 248 nm wavelength. These vias are then filled with metal connecting the NbN nanowires with the upper metal pad layer MET1.

- MET1 - Metal pad patterning

Finally, the fifth layer allows to pattern metal pads of 80 µm x 80 µm using 248 nm DUV lithography.

These pads are used for electrical biasing and readout of the nanowires.

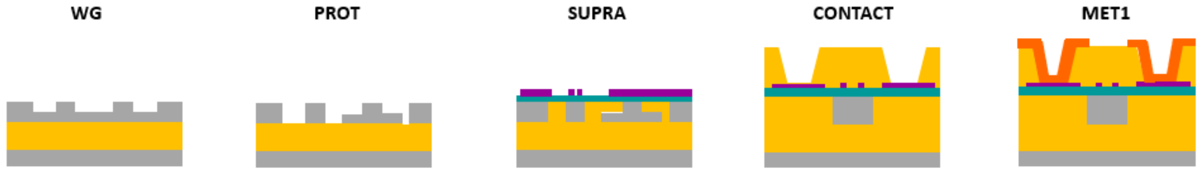

Figure 44 : *Process flow of the 5 litho-etch steps: WG, PROT, SUPRA, CONTACT and MET1*

4.3.2 Mapping of the layout field on 200 mm wafers

The total exposure field of a maskset used in 200 mm SOI technology is is 22 x 22 mm^2. It is used to write a large number of dies (45) to cover the whole surface of a 200 mm SOI wafer. The maskset was shared between different projects, among which my PhD project. The first two layers corresponding to the patterning of Si waveguides are shared with other projects while the last three layers corresponding to the NbN patterning and metallization are used specifically for my project. In order to save place on the mask and yet explore a broader range of parameters, we developed three series of layers labelled R, S and T for the nanowire patterning and metallization that are mapped over the full surface of a 200 mm SOI wafer, as illustrated in Figure 45.

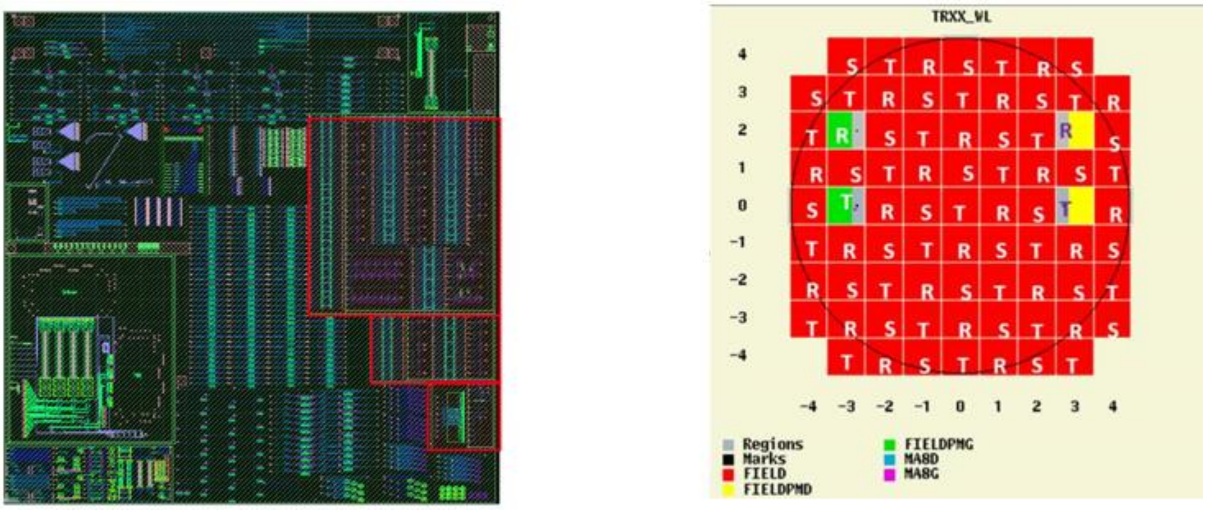
TRXX_WL

	-4	-3	-2	-1	0	1	2	3	4
4		S	T	R	S	T	R	S	
3	S	T	R	S	T	R	S	T	R
2	T	R	S	T	R	S	T	R	S
1	R	S	T	R	S	T	R	S	T
0	S	T	R	S	T	R	S	T	R
-1	T	R	S	T	R	S	T	R	S
-2	R	S	T	R	S	T	R	S	T
-3	T	R	S	T	R	S	T	R	S
-4		T	R	S	T	R	S	T	

▨ Regions
■ Marks
🟥 FIELD
🟨 FIELDPMD
🟩 FIELDPMG
🟦 MA8D
🟪 MA8G

(a) (b)

Figure 45: *(a) Maskset scheme in which my contribution is outlined in red. (b)Mapping of the 45 dies illustrating the three series of layers R, S and T for the nanowire patterning and metallization. The grey areas are not exposed, because of the presence of the primary markers PM.*

4.3.3 Design rules

The designs are drawn or scripted into a GDS file. Numerous tools are available to generate a GDS file, for this work I have used Virtuoso from Cadence. Each layer of the maskset has specific design rules (typically minimum feature size), taking into account typical required pattern dimensions and technological capabilities. There are also design rules between layers, for example inclusion rules depending on the alignment tolerance between two lithographic levels. All these rules are listed in the Design Rule Manual (DRM) accessible for each designer. The compatibility of the layout with these design rules is checked by a specific algorithm called DRC (Design Rule Check).

4.3.4 Overview of SNSPD layout

The detail of the SNSPD layout contribution is presented in Figure 46. It has an overall size of 100 mm^2 (20% of the maskset). It is divided into 6 blocks in order to take into account the optical packaging (also called pigtailing) constraints in addition to the design rules.

Each mask layer is represented by a different color:

WG : pink / PROT : yellow / SUPRA :green / CONTACT : red / MET1 : blue

Each block has its own set of features and functionalities. There are three different versions of blocks 1, 2 and 5, according to the mapping of Figure 45 while blocks 3, 4, and 6 remain identical. We will describe them in detail in the following.

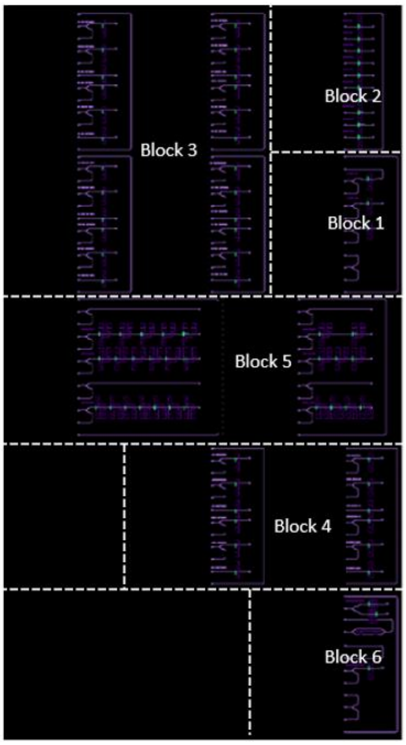

***Figure 46**: Schematic an overview of the layout*

4.3.4.1 Optical Inputs/outputs and pigtailing constraints

In contrast to other photonic individual components, SNSPDs cannot be measured at wafer level due to cryogenic constraints. After fabrication, the wafers need to be diced into small dies that will be optically and electrically packaged for cryogenic measurement.

Due to the high index contrast between silicon and silicon dioxide, silicon photonics waveguides have typical dimensions much smaller than standard monomode fibers (400 nm vs 8 µm). This dimension difference makes the design of fiber-to-chip interfaces challenging. Here, we use grating couplers that are mature components of the silicon photonics library. We have chosen to use fiber arrays of 12 fibers with 250 µm pitch, each block thus contains 12 input or output fiber grating couplers and a large empty space on the left which corresponds to the footprint of the fiber block for good mechanical stability. Among the 12 fiber ports, the first and last ones are dedicated to the active alignment of the fiber array, the other 10 in-between can be used for functional devices. Figure 47 illustrates the arrangement of fiber grating couplers for each block.

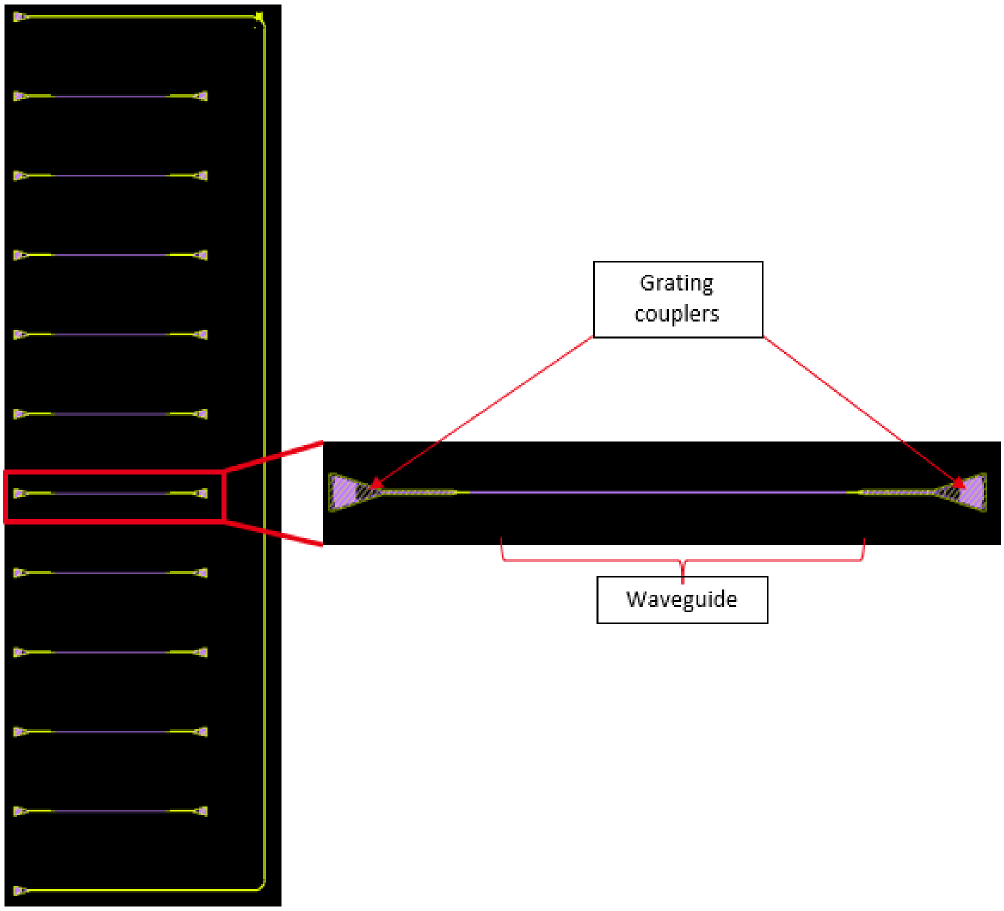

Figure 47: *An example of a block featuring 12 input ports. To achieve alignment, the first and last ports are connected. There is a grating coupler at the input and the output of each waveguide. The input grating couplers will be used for test. The output ones just serve as waveguide termination.*

4.3.4.2 Electrical contacts

The measurement of timing performances of SNSPDs (jitter and recovery time) requires high-speed electrical connections. We have thus chosen to design RF ground-signal-ground (GSG) transmission lines for high timing resolution of the readout. In order to prevent unwanted RF reflections which could degrade the timing performances, the NbN nanowires were gradually enlarged to a wide area dedicated to the electrical connection with the AlCu contact pad.

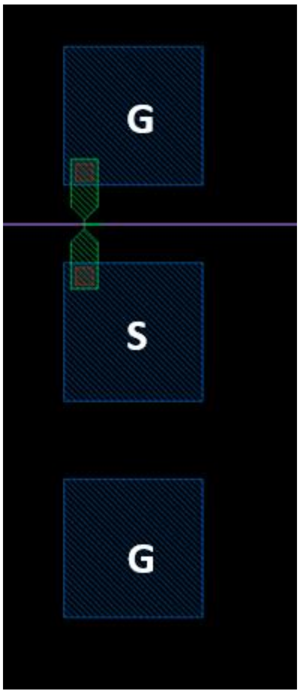

Figure 48: *Illustration of the electrical connection ground-signal-ground (GSG) used to connect the nanowires*

4.3.5 Detailed description of the layout blocks

4.3.5.1 Block 1: SNSPDs with calibration structures

Block 1, illustrated in Figure 49, is dedicated to the measurement of three U-shape detector devices. It includes the required calibration structures in order to obtain an accurate measurement of the detection efficiency. It is split into four sub-blocks for this purpose. In the first sub-block, the input laser power is split by a MMI (Multimode Interferometer) into two arms. The top arm comprises a U-shape detector whereas the bottom arm will serve as a reference to measure the power sent to the detector. This first sub-block also includes an output port to measure the residual transmission of the detector device. The fourth block is the MMI test structure to measure the splitting ratio between the two output arms for proper calibration of the power received by the detector. The intermediate second and third sub-blocks include two other detectors with their reference arm to measure the received power. R and S versions include U-shape detectors with length ranging from 10 to 110 µm while version T includes straight nanowires with length ranging from 10 to 80 µm.

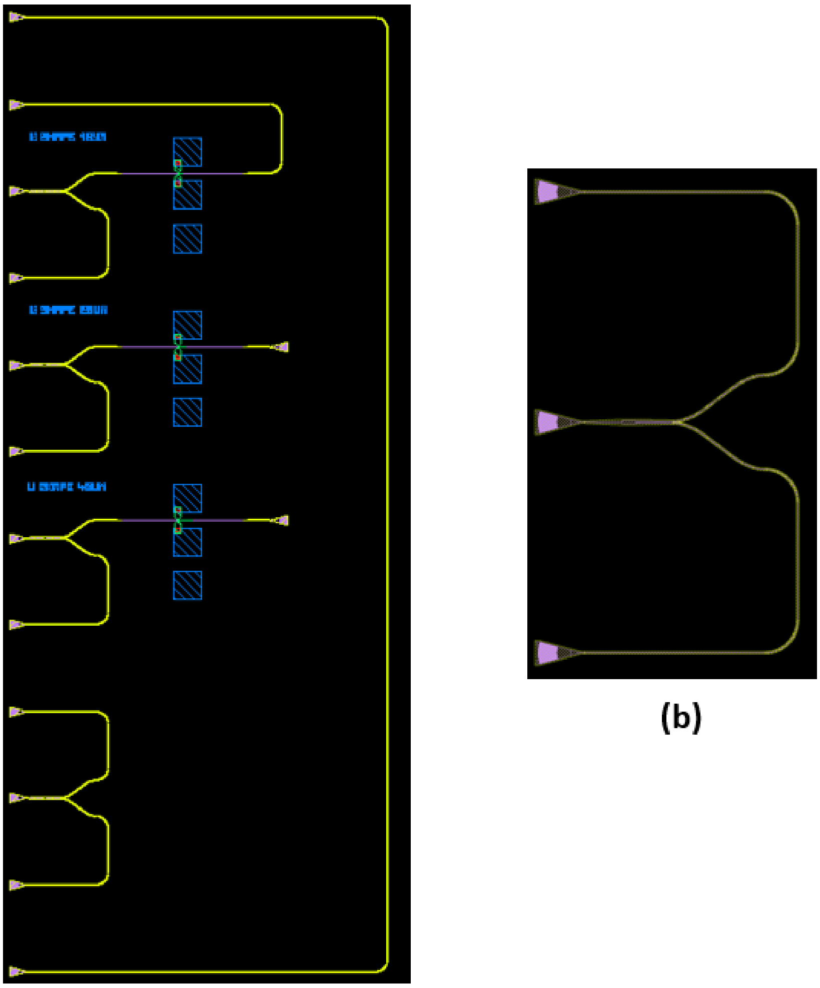
(a)

(b)

Figure 49: *(a) layout of block 1, version R (b) MMI structure*

4.3.5.2 Block 2: Geometric variation of U-shape and straight SNSPDs

Block 2 aims at studying SNSPD detection efficiency as a function of length and nanowire geometry. Version R includes 10 U-shape SNSPDs of different lengths while version S includes 10 straight SNSPDs. They are displayed in Figure 50 and Figure 51 respectively.

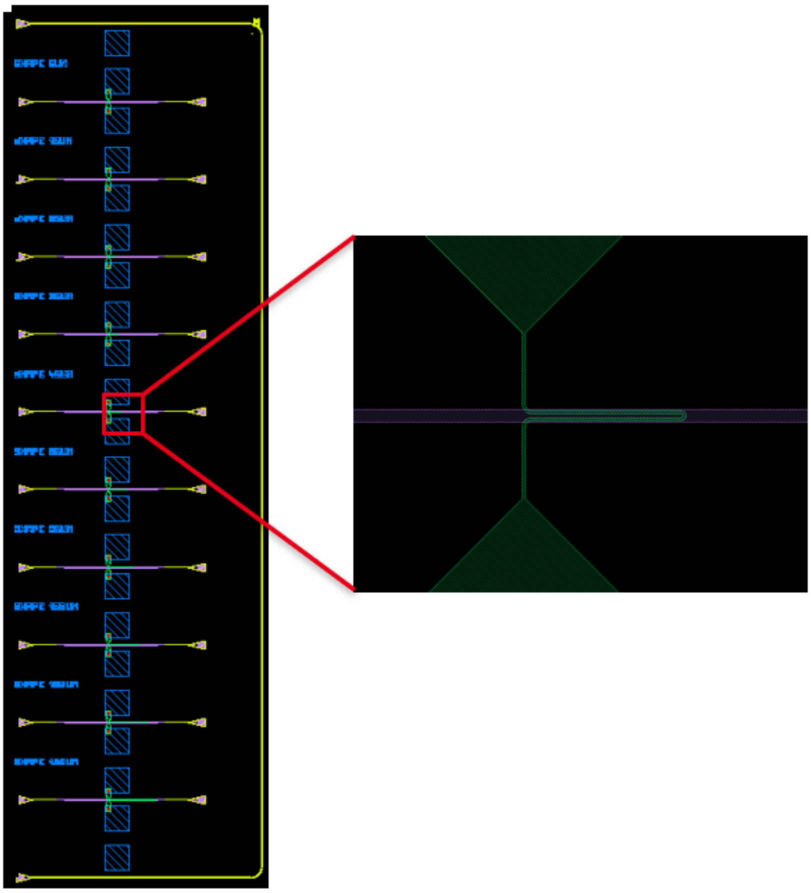

Figure 50: *layout of block 2, version R (U-shape nanowires)*

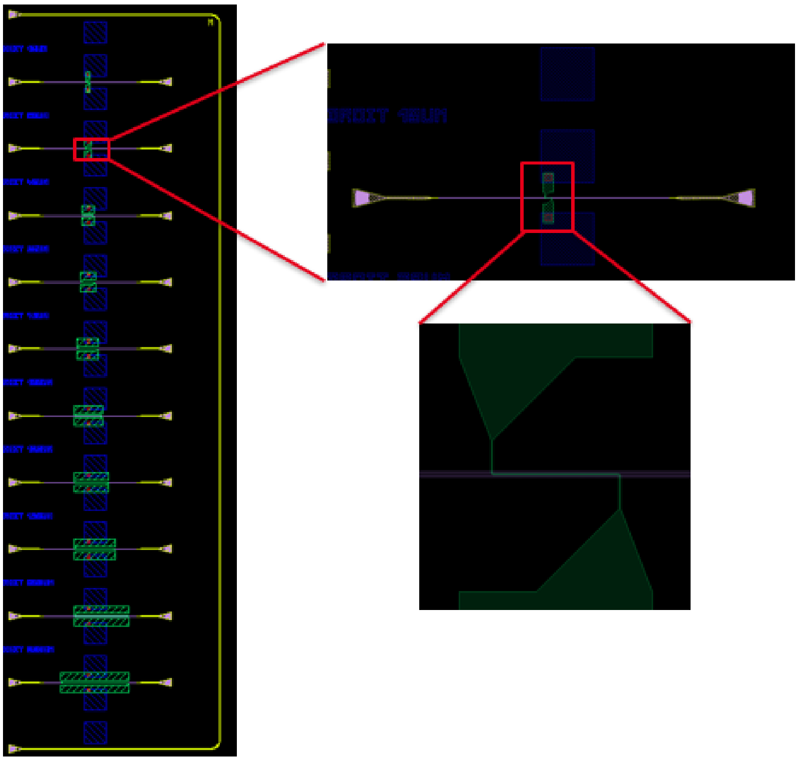

Figure 51: *layout of block 2, version S (straight nanowire)*

The nanowire lengths are reported in Table 12 together with the associated residual transmission calculated from mode simulation performed in section 4.2.1.3. Straight nanowires require longer nanowire length to achieve the same absorption as their U-shape counterparts. They range between 5 and 150 µm for U-shape nanowires and between 10 and 250 µm for straight nanowires. We expect a residual transmission in the range of 10^{-3} for 60 µm long U-shape nanowires and for 100 µm long straight nanowires.

5 nm NbN U-shape nanowire

Length µm	Transmission
5	$5.98\ 10^{-1}$
10	$3.58\ 10^{-1}$
20	$1.28\ 10^{-1}$
30	$4.59\ 10^{-2}$
40	$1.64\ 10^{-2}$
60	$2.11\ 10^{-3}$
80	$2.70\ 10^{-4}$
100	$3.47\ 10^{-5}$
125	$2.66\ 10^{-6}$
150	$2.04\ 10^{-7}$

5 nm NbN straight nanowire

Length µm	Transmission
10	$5.48\ 10^{-1}$
20	$3.00\ 10^{-1}$
30	$1.64\ 10^{-1}$
50	$4.94\ 10^{-2}$
75	$1.10\ 10^{-2}$
100	$2.44\ 10^{-3}$
125	$5.42\ 10^{-4}$
150	$1.20\ 10^{-4}$
200	$5.94\ 10^{-6}$
250	$2.93\ 10^{-7}$

Table 12 *Transmission rate of SNSPDs according to their length for a 6nm NbN thick. On left, the simulation results a U-shaped nanowire and on the right for a straight nanowire*

Version T includes U-shape SNSPDs of fixed length but with variations of the nanowire width between 70 and 100 nm in order to study its impact on operating conditions (temperature and biasing current), and detector performances (detection efficiency and dark counts). This version also includes some devices where we varied the tip of the U-shape nanowire width between 100 and 200 nm in order to investigate possible current crowding effects that might degrade the detector performances.

4.3.5.3 Block 3&4: SNSPDs integrated in ring resonators

Both blocks feature 12 U-shaped nanowires embedded in ring resonators, distributed into 6 SNSPDs in block 3 and 6 SNSPDs in block 4. The version R, S and T are the same of both blocks.

The various designs correspond to the gap values and nanowire length reported in Table 10 and Table 11. The nanowire length varies from 1 to 10 µm, and the gap values range from 180 to 335 nm. In addition to these values, we have included additional structures within ±5nm of the gap value to account for fabrication variation.

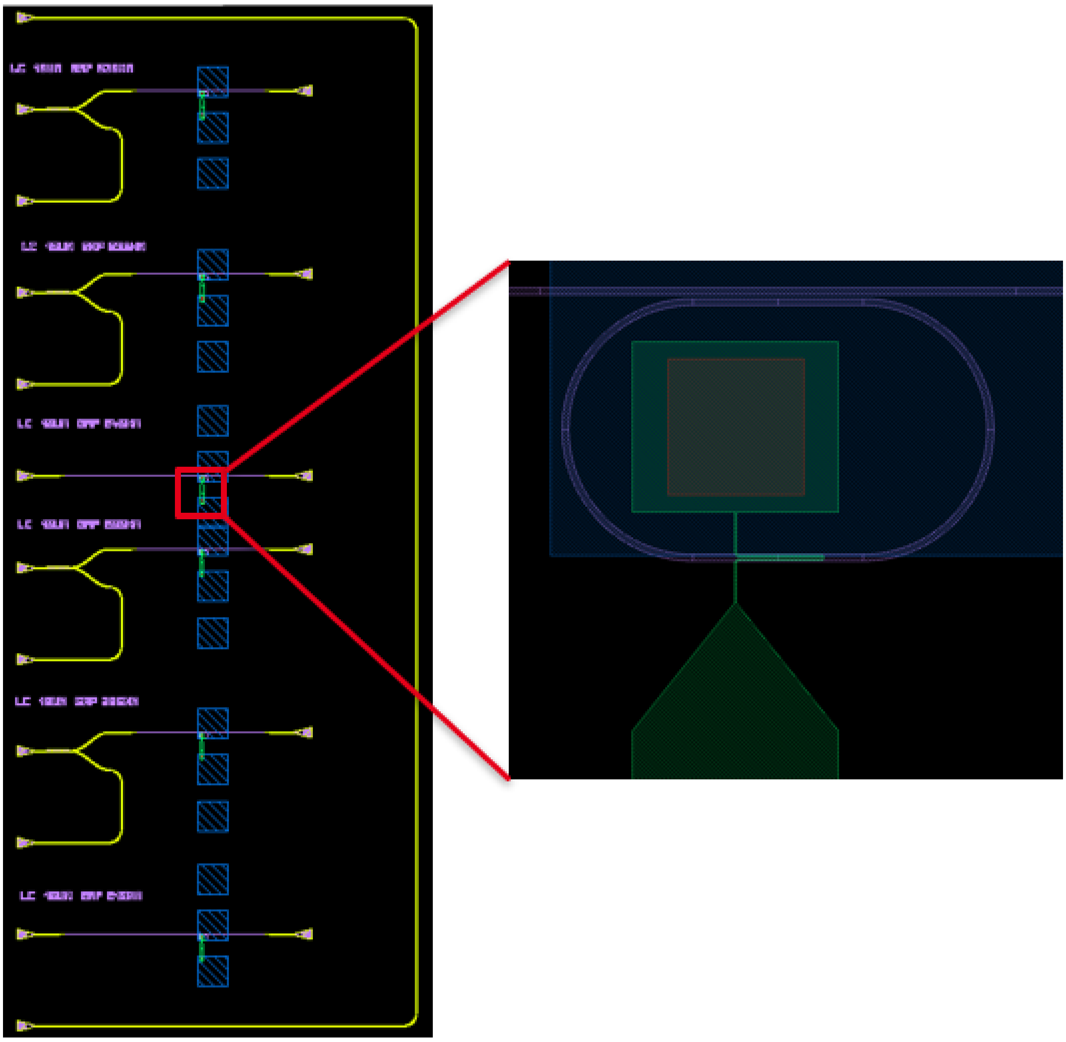

Figure 52: *example of the layout of block 3&4 (SNSPD embedded in resonator)*

4.3.5.4 Block 5: Photon number resolution architectures

This block includes SNSPD architectures providing photon number resolution (PNR). As described in section 4.2.3 of this chapter, the PNR architectures consist of several detectors in series with a specific length adjusted to achieve an equal repartition of photons over all detectors. We designed architectures integrating up to 7 SNSPDs in series. R and S versions include PNR architectures based on U-shaped nanowires (1, 2, 3, 4, 5, 6, 7 detectors in series), whereas the T version is based on straight nanowires (1, 2, 3, 4, 5, 6, 7 detectors in series).

The detectors are numbered from N at the entrance of the waveguide down to 1 at the end of it, their efficiencies being $\eta_i = 1/i$. Equation (13) is used to calculate the length of the different nanowires as a function of their absorption and their number in the serie. We calculate the required length and efficiency of each detector η_i for the two U-shape and straight nanowire configurations using the modal absorption calculated in section 4.2.1. The results are reported in Table 13 for a series of 7 detectors. We note that the final detector can be as long as possible in order to absorb the remaining photons. We have chosen a length of 100 µm for the last detector, corresponding to an expected residual transmission of 3.5×10^{-5} for U-shaped nanowire and 150 µm for straight nanowire, corresponding to an expected residual transmission of 1.2×10^{-4}.

$$L_i = -\frac{1}{\alpha_i} ln\left(1 - \frac{1}{i}\right) \quad \textbf{(13)}$$

5 nm NbN U-shape nanowire

Detector number	Efficiency η %	Length µm
1		100
2	0.50	6.75
3	0.33	3.95
4	0.25	2.80
5	0.20	2.17
6	0.17	1.78
7	0.14	1.50

5 nm NbN straight nanowire

Detector number	Efficiency η %	Length µm
1		150
2	0.50	11.52
3	0.33	6.74
4	0.25	4.78
5	0.20	3.71
6	0.17	3.03
7	0.14	2.56

Table 13 *Length and efficiency of each detector in series (up to 7)*

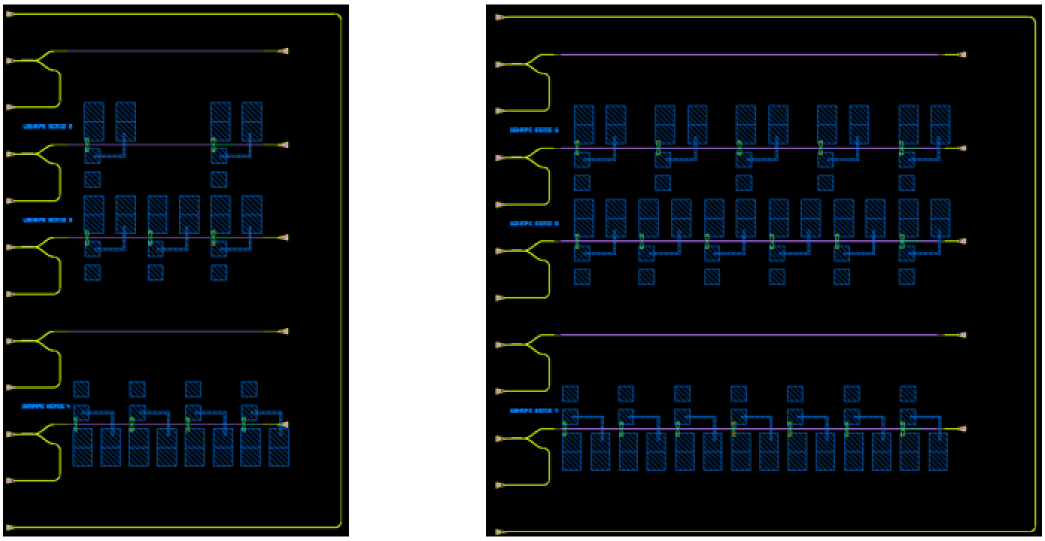

Figure 53: *layout of block 4(version R) embedding PNR detection architectures*

4.3.5.5 Block 6: Miscellaneous

The last block contains designs for a variety of purposes. The first sub-block aims to conduct the well-known Hanburry Brown and Twiss (HBT) experiment with an external source of single photons using an on-chip power splitter integrated with two SNSPDs. The SNSPD consists in a U-shape nanowire of length 60 µm with an expected residual transmission of 2.11×10^{-3}.

The second sub-block is a classical Mach-Zehnder interferometer with thermo-optical phase shifting in one arm to investigate the effect of thermal dissipation on the SNSPD operation. The third sub-block is designed to evaluate the impact of a classical channel propagating nearby the SNSPD of a quantum channel. The last two sub-blocks are similar to the designs of block 1, including the reference individual SNSPD chosen for the HBT configuration, with a reference branch to calibrate the received power after prior calibration of the splitting ratio of the MMI individual structure.

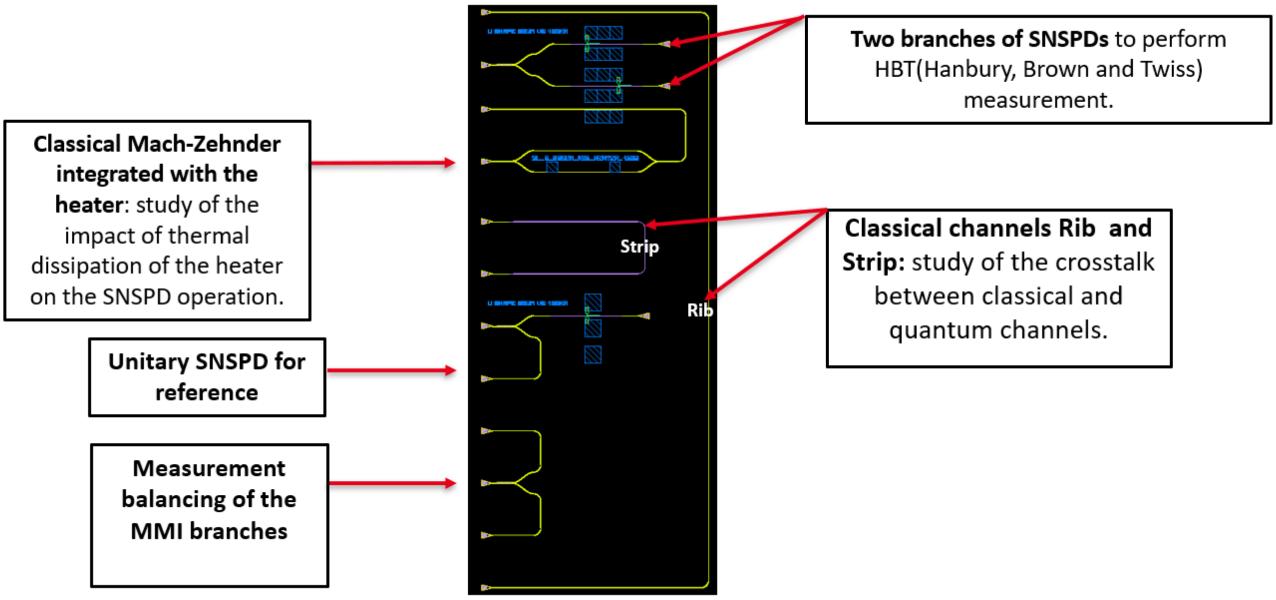

Two branches of SNSPDs to perform HBT(Hanbury, Brown and Twiss) measurement.

Classical Mach-Zehnder integrated with the heater: study of the impact of thermal dissipation of the heater on the SNSPD operation.

Classical channels Rib and Strip: study of the crosstalk between classical and quantum channels.

Unitary SNSPD for reference

Measurement balancing of the MMI branches

Figure 54: *layout of the block 6*

4.4 Conclusion

Throughout chapter 4, we presented the optimized design to obtain waveguide integrated SNSPDs with high efficiencies. We demonstrated that with the incorporation of the AlN buffer layer used to enhance the superconducting properties of the NbN layer, high absorption could be achieved for a U-shaped SNSPD configuration with nanowires less than 100 µm in length. Therefore, compared to the meander structure (vertically coupled detectors), which has nanowires with a length of several hundred microns (>200 µm), waveguide integrated SNSPDs are designed with much shorter nanowires. We have also shown the potential of cavity-coupled SNSPDs, in particular with silicon ring resonators. Thereby, we demonstrated near-unity detection efficiency using waveguide integrated SNSPDs with nanowire lengths between 1 and 10 µm. In addition, we proposed a detection scheme where integrated SNSPDs are placed in series to achieve photon number resolution PNR. The detectors in this configuration are numbered from N at the waveguide's entrance to 1 at its end, with their efficiencies being $\eta_i = 1/i.$ In contrast to parallel schemes already proposed in literature for PNR, only the last detector should show η_1 close to unitary to maximize the fidelity. Consequently, the lack of unitary efficiency detectors is of small concern. Finally, we have described the layout, various proposed designs, and a variety of test structures required for accurate calibration of SNSPD performances.

Chapter 5- Waveguide-integrated Superconducting Nanowire Single-Photon Detectors: development of fabrication process and preliminary characterization

5.1 Introduction

After design and layout of SNSPDs, I conducted the fabrication process development of waveguide-integrated SNSPDs on the 200 mm silicon photonics platform of CEA-LETI. The fabrication process of integrated SNSPDs can be split into three major parts. The first part consists in the fabrication of SOI waveguides and all other necessary passive elements. The second part consists in the deposition of the superconducting material NbN, while the last part consists in the structuration of the NbN nanowires and of metallic contact pads.

For this integrated SNSPD process development, I collaborated with process engineers specialized in lithography, etching, dielectric materials, metallic materials, chemical polishing, mechanical (CMP) and metrology. Together, we improved and adapted existing processes and developed new ones for the fabrication of SNSPDs. I took in charge most of the morphological and material characterization steps and ensured that the developed processes were stable and reproducible.

I will present the various technological steps, as well as the fabrication methods used. In section 2, I will briefly describe the first set of standard fabrication steps carried out to fabricate waveguides and other passive structures. In section 3, I will describe in detail the following of the process dedicated to the fabrication and metallization of NbN nanowires, as I developed those steps specifically in my PhD work. We used non-functional wafers (called dummy wafers) for the development and validation of new process steps, before implementing them to the functional SNSPD wafers. Finally, I will present preliminary electrical and optical characterizations carried out at room temperature after the full fabrications process of waveguide-integrated SNSPDs.

5.2 Fabrication process of SOI waveguides: patterning, encapsulation and CMP

5.2.1 SOI stack

The starting point for the realization of photonic circuits is silicon-on-insulator (SOI) wafers. These wafers consist of a crystalline silicon substrate, a silica layer BOX (Buried Oxide Layer), and a second thin crystalline silicon layer, which will be patterned to obtain the photonic circuits. We use SOI wafers from Soitec, manufactured using the SmartCut technology [219], a patented industrial bonding and cutting process from the company. This approach relies on a combination of light ion implantation and wafer bonding to transfer ultra-thin single crystal layers from one substrate to another. It acts like a scalpel on an atomic scale, allowing the active layers to be manipulated independently of the substrate. More specifically, different steps are combined to produce an SOI wafer, as summarized in Figure 55

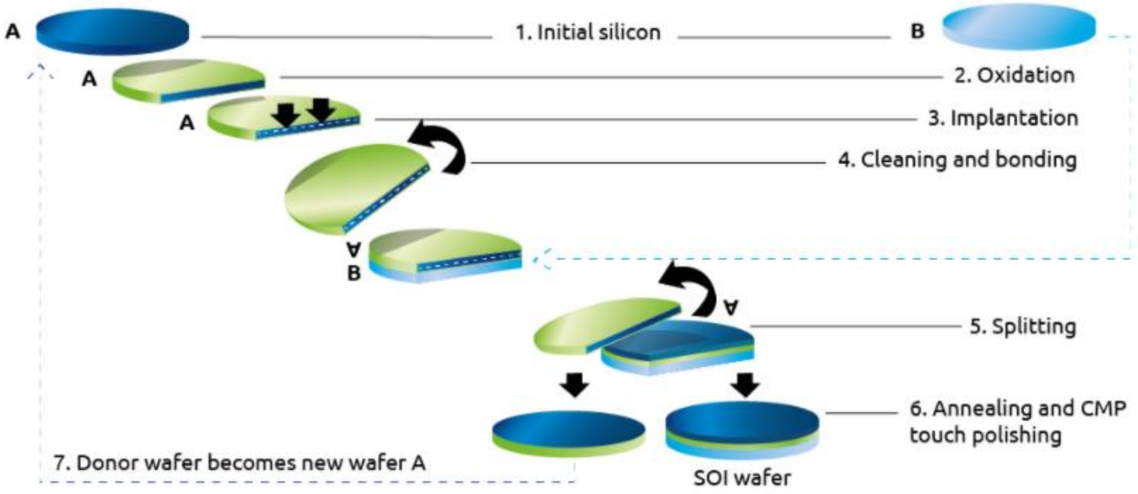

Figure 55 *: principle of the Smart-Cut process* [219]

For this work, we use SOI primary wafers of 200 mm diameter with a 340 nm Si thin layer, standardly used in the silicon photonics platform of CEA-LETI. To obtain a 300 nm thick Si layer which corresponds to the nominal thickness of Si waveguides, a thermal oxidation of 60 nm with a mixture of O_2 and HCl at 950°C (2h15min) is first performed, followed by an HF deoxidation to obtain a 310 nm thick Si. A second oxidation is realized according to the same recipe during 54min. The resulting stack is a 300 nm thick Si layer covered by 20 nm of thermal oxide.

5.2.2 Silicon waveguide patterning

The structuration process of the 300 nm Si layer into waveguides and other passive structures is performed by a succession of lithography and etching steps. I will first explain the principle of lithography and etching before describing the full patterning sequence used in this work.

5.2.2.1 Lithography

Lithography is one of the main steps in semiconductor technology since it allows to transfer the structures designed on the mask to the wafer. The patterning of the resist can be performed by irradiating the wafer with a source of electromagnetic radiation (UV, extreme UV or X-ray) or a beam of electrons. The choice of the lithographic process depends on the desired resolution which corresponds to the smallest feature size that can be written and to industrial cycle time constraints.

The silicon photonics platform makes use of the collective optical lithography process at UV and deep UV wavelengths of 248 and 193 nm respectively to define passive SOI structures. The resolution is determined by the wavelength of the light source, the exposition technique, and the resist [220]. The resolution limit can be expressed using Rayleigh's criterion:

$$W_{min} = k_1 \frac{\lambda}{NA} \qquad \textbf{(12)}$$

where k_1 is the resist's ability to distinguish between small changes in intensity, λ the wavelength of the projective lithography system, and NA the numerical aperture.

The reaction of the photoresist to UV light depends on its intensity. The dose, expressed in mJ/cm^2, must be optimized to achieve the desired dimensions. The width of the developed pattern changes as the dose changes. In the case of a positive tone photoresist, the width of the developed photoresist is smaller when the dose is higher, and the space between two neighboring patterns is wider. Furthermore, the dose value can vary depending on the mask's opening area (density) and the dimensions of the structures.

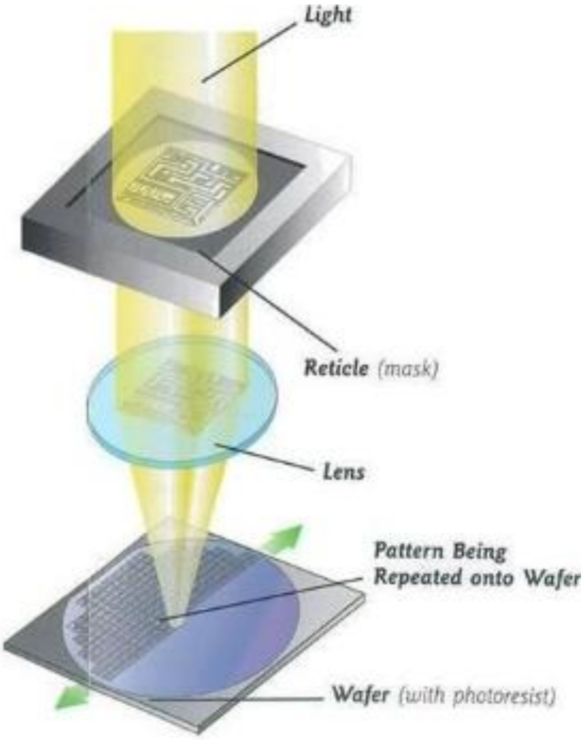

Figure 56 : *Principle diagram of lithography machine (From* [221]*)*

For the waveguide patterning, the exposure was realized with an ASM1100 stepper, using a 193-nm deep ultraviolet (DUV) lithography. This system is one of the most widely used in semiconductor technology because it enables high resolution (down to 120 nm) while maintaining a reasonable level of productivity and cost. The actual features contained on the chromium mask are bigger than the designed features on the GDS mask file. A converging lens is used to get the desired dimensions on the wafer (Figure 56). Furthermore, the wafer is not exposed as a whole simultaneously, but each 2.2 cm x 2.2 cm field area is exposed individually, leading to 45 full dies (see the schematics in Figure 57). However, due to the positioning of the primary marks (PM), some dies were truncated (PM, Figure 58). These marks are patterned before all the other lithographic steps since the stepper must use them to realize a general alignment [222], which tolerance is ± 125 nm (3σ) [223].

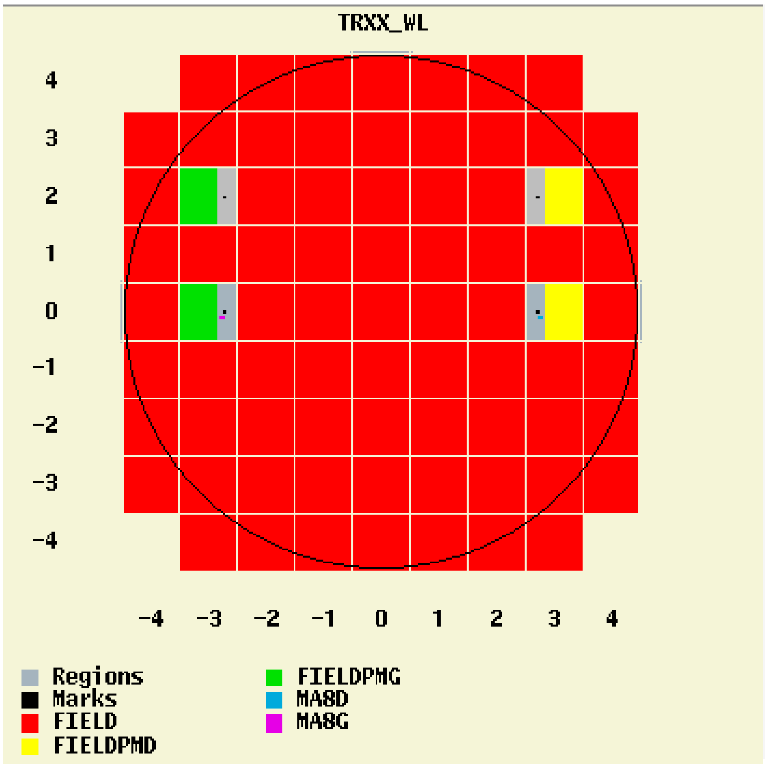

Figure 57 : *Wafer division into 45 full dies. The grey areas are not exposed, because of the presence of the PM markers (Figure 58)*

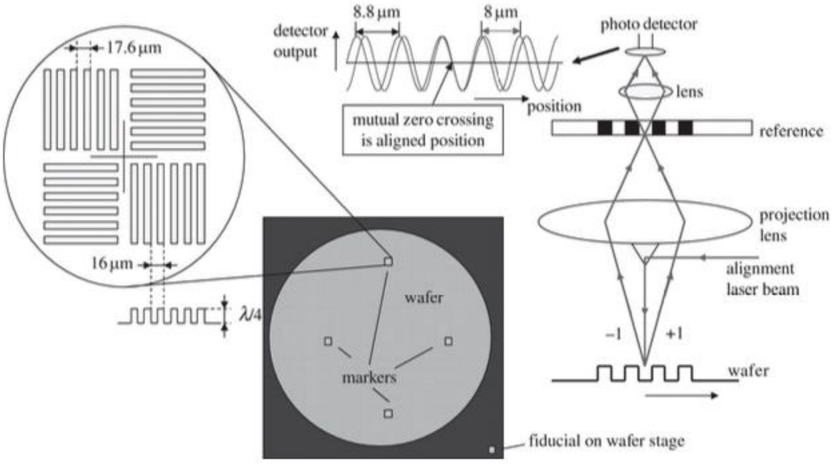

Figure 58 *: The alignment marks are diffraction gratings with a different periodicity to increase the capture range. One way to measure the markers is shown at the right, where both first orders are imaged on a reference grating and their interference is detected by a sensor. This configuration allows one to align the mask with an error lower than ± 125 nm (3σ). (Image from* [222]*)*

5.2.2.2 Etching

Concerning the etching, it involves the chemical and/or physical removal of layers from the wafer, involving only those areas of the wafer that are not covered by resist. The ratio of etch rates in different directions determines whether an etching process is isotropic or anisotropic. An inductively coupled plasma (ICP) reactor (Centura 5200) was used to etch silicon waveguides, allowing for anisotropic etching and vertical sidewalls. When the opening area is large enough, the etching process can be monitored using Optical Emission Spectroscopy (OES) or Interferometric Endpoint (IEP) detection systems [224,225]. During the etching process, the plasma composition changes. The different compounds can be detected by analyzing the emitted electromagnetic radiation with a spectrometer (OES). Alternatively, the reflectivity of the wafer abruptly changes when a layer is totally etched, which is detected by measuring the interferometric pattern of a laser beam passing through the chamber (IEP). Sometimes, depending on the etching thickness, certain patterns require the use of a hard mask, which also helps to have the most vertical sidewalls as possible. The hard mask is a material that is sufficiently selective to act as an etch mask for the silicon. Typically, in microelectronics, silica or silicon nitride materials are used as a hard mask.

5.2.3 Full patterning sequence

The SOI patterning follows a precise sequence as presented in Figure 59. First, a 145 nm silicon nitride hard mask is deposited by Low Pressure Chemical Vapor Deposition LPCVD. Then, an ultraviolet-sensitive resist is coated on the wafer. The wafer is then exposed to deep UV light through a mask carrying the pattern to be transferred. Then comes a step called development, during which the soluble resist is chemically removed. The non-soluble resist defines the desired pattern. A first etching step is performed to etch both the hard mask and the 20 nm oxide layers, followed by wet stripping to remove the resist as well as the polymers produced by the etching. Then, a second etching sequence is performed to partially etch the Si layer down to 165 nm in order to define the fiber grating couplers. As endpoint detection is not possible in the case of partial etching, the etching time was carefully calibrated during development of this etching step. A second lithography step is performed in order to protect the partially etched structures before the third etching sequence, in which etching of the Si layer is continued down to the BOX with endpoint detection.

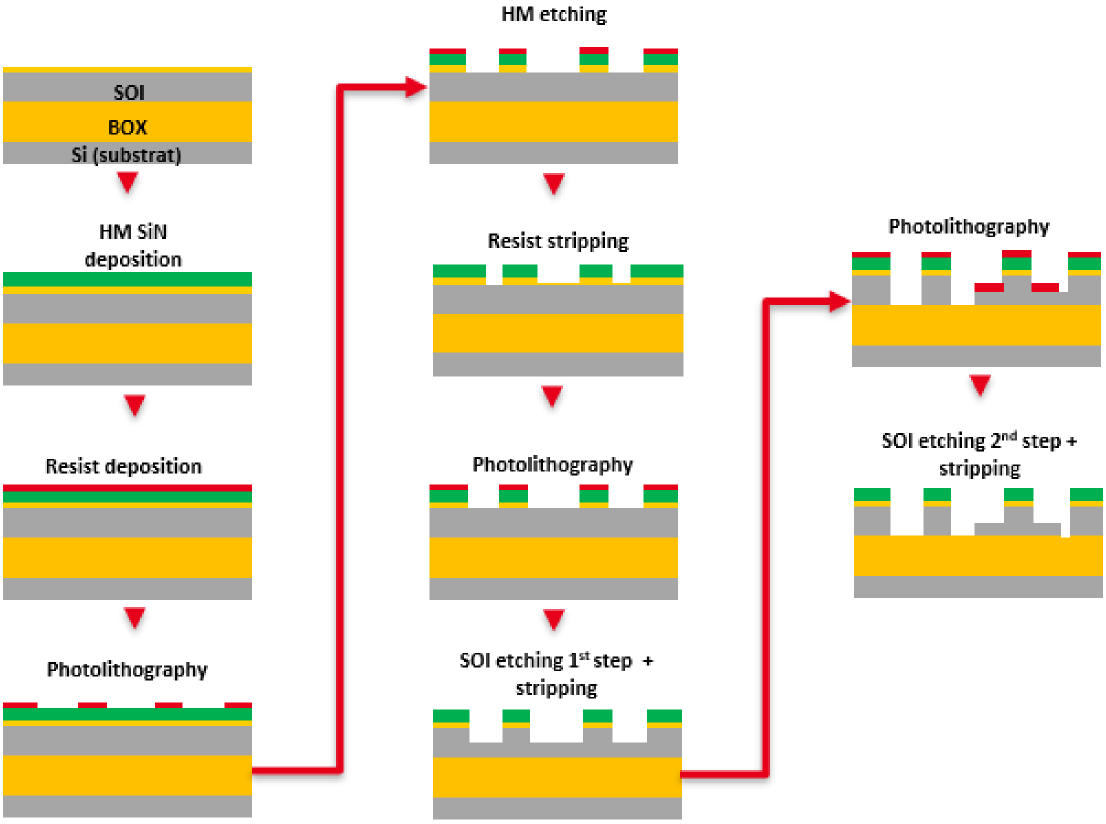

Figure 59 *: Process flow diagrams of the technological steps used for the SOI structuring*

5.2.3.1 Encapsulation and planarization

Following the patterning of the silicon waveguides, a series of silica encapsulation and planarization steps are then performed to prepare the wafer for subsequent superconducting material deposition. The objective of the whole process is to encapsulate the silicon waveguide and to remove the nitride hard mask in order to leave the top surface of Si waveguides ready for subsequent superconducting material deposition. We decided to remove only the silicon nitride hard mask and to keep the 20 nm of oxide on top of the waveguide because removing it would alter the waveguide quality and lead to increased propagation losses. Here I note that this layer was originally not taken into account in the optical simulation. However additional simulations showed that the impact of this layer was not significant. The sequence of technological steps to achieve encapsulation and planarization is depicted in Figure 60.

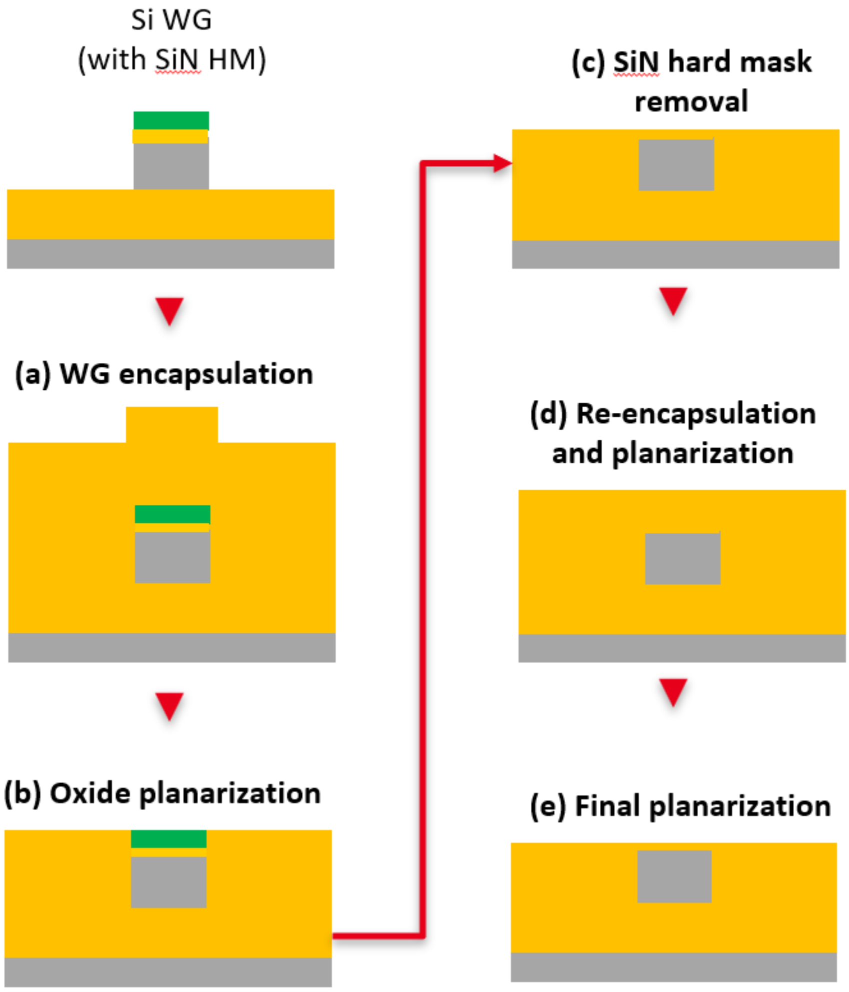

Figure 60 *: Process flow diagrams of the technological steps used for the encapsulation and planarization of the waveguides*

(a) <u>Waveguide encapsulation</u>

First, we deposited 700 nm of SiO_2 by high-density plasma (HDP) chemical vapor deposition at 400°C, using silane (SiH_4) as a precursor. This is a highly conformal oxide ensuring that air bubbles at the foot of the pattern are avoided. HDP deposition is therefore excellent for creating a compact encapsulation layer on top of waveguides.

(b) Oxide planarization

The oxide is then planarized using chemical mechanical polishing (CMP), which removes the oxide above the SiN, using SiN as a stop layer. The most challenging aspect of this step is to avoid polishing the SiN. Indeed, CMP is based on combining a chemical action (by the slurry or polishing solution) with a mechanical action (by the particles contained in the slurry and the rotating polishing disk). The slurry composition is critical, and it is determined by the purpose of the step. The chemical effect is even more important in the case of planarization of the oxide with a stop on SiN. The particles chosen should have a strong chemical affinity for the oxide and a weak affinity for the SiN. In this particular case, Cesium Cs particles were used. A chemical additive called surfactant protects the low zones (oxide around the waveguide), thus limiting its consumption and favoring the consumption of the high zones (SiN), where the pressure exerted by the polishing disk is so intense that the surfactant does not hold any role. Following planarization, spectroscopic ellipsometry is used to determine the remaining nitride thickness. This measurement revealed about 96nm of SiN, in excellent agreement with the 100 nm expected remaining SiN thickness after waveguide etching.

(c) SiN hard mask removal

In order to remove the hard mask, we opted for a non-selective dry etch based on (Cl_2/CHF_3/O_2He/Ar) that will etch both the oxide and the nitride. We tried a few different etching times and ended up etching for 59 seconds. After etching, the ellipsometry measurement reveals 5 nm of oxide on the waveguide. This etching step, however, leaves the surface very rough.

(d) Re-encapsulation and planarization

A second planarization and encapsulation are performed to overcome this. Plasma Enhanced Chemical Vapor Deposition (PECVD) was used to deposit 60 nm of SiO_2 at a low deposition rate (LDR) using tetraethyl orthosilicate [TEOS] as a precursor. Indeed, this method is softer and results in a protective layer on the surface for the waveguides. At this stage, the total thickness of the oxide is approximately 70 nm.

(e) Final planarization

A CMP touch is carried out to get 20 nm of oxide, leaving a smooth surface. The mechanical component of the CMP takes over in this case. To limit the irregularities on the wafer, the particles are chosen to be as smooth as possible. We used SiO_2 particles in an acidic medium to achieve this step. As a result, this sequence of steps provides a smooth, suitable topography and planarized surface without damaging the waveguide. Table 14 shows the thickness of the remaining oxide around. The results show a relatively high non-uniformity within wafers (4.2%) and also some non-uniformity (2%) between wafers. This is representative of a CMP process without etch stop layer but largely good enough to start the subsequent process brick associated to the superconducting nanowires.

	Min	Mean	Max
P01	12.6 nm	17.2 nm	22.5 nm
P02	7.9 nm	14.4 nm	18.1 nm
P03	10.1 nm	18.1 nm	21.8 nm
P04	12.7 nm	21.1 nm	26.4 nm
P05	9.5 nm	17.1 nm	21.4 nm
P06	7.9 nm	15.78nm	19.6 nm
P07	11.7 nm	19.8 nm	24.3 nm

Table 14: *Measurements of the remaining oxide on the waveguide after the CMP touch*

At this point, the fabrication of the waveguides is indeed completed. In the following, we move on to the definition of the superconducting nanowires.

5.3 Development of fabrication process of NbN nanowires

5.3.1 Deposition of the superconducting material

For the deposition of the superconducting material, which forms the core part of the detector, we use the optimized stack developed in chapter 3 consisting of ultrathin AlN and NbN films. We refer to chapter 3 for the detail of the deposition process.

We have demonstrated in chapter 3 that the integration of the AlN buffer layer results in an NbN thin film with superior superconducting properties. In order to further study the impact of the AlN layer on the performances of the detector itself, we split our 7 wafers into two groups, with and without AlN deposition, as illustrated in Figure 61 :

- P01, P02, P03 and P07: 6nm of NbN are deposited directly on the remaining oxide after the CMP touch.
- P04, P05 and P06: First, a pre-clean is performed to remove the remaining oxide on the waveguide, as described in chapter 3. The duration of the pre-clean was adapted for each

wafer due to the large dispersion of the residual oxide thickness from wafer to wafer. Then 10nm of AlN are deposited, followed by 6nm of NbN.

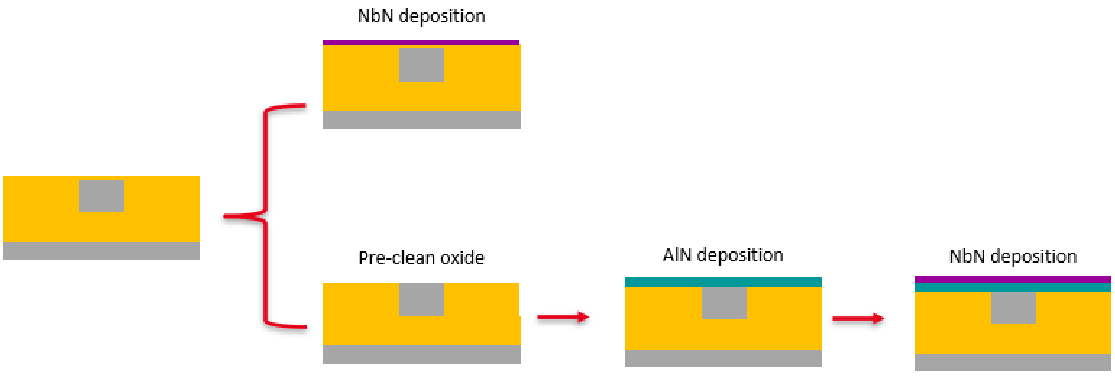

Figure 61 *: Deposition process of the superconducting stack*

5.3.2 Nanowire patterning

High-quality SNSPDs require nanowires with uniform width, free of undesirable constrictions. More specifically, for a stable device operation close to the critical current, resulting in high photon detection efficiencies, it is crucial that the current density J_c remains uniform along the nanowire [226].

The fabrication of SNSPDs therefore requires careful optimization of both lithography and etching of the 6 nm NbN thin film. Several fabrication batches were carried out to optimize process parameters for e-beam lithography and for etching.

5.3.2.1 Electron beam Lithography

The nanowire width designed on the masks range from 70 to 100 nm, which is too small for optical lithography. We therefore use e-beam lithography instead. The nanowire width is defined through the electron beam dose. The latter is highly dependent on several parameters, including resist thickness, electron beam lithography system alignment, and, most importantly, the electronic properties of the substrate. Moreover, the electronic properties of NbN thin films vary significantly depending on both NbN thickness and crystal quality. Therefore, in order to ensure a reliable fabrication process, a dose analysis was first carried out on dummy samples with the same structural and electronic properties as the samples used for the SNSPD fabrication. Specifically, the dose was optimized for all NbN thicknesses and underlying considered layers (AlN or SiO_2).

Because the density of the nanowires is relatively low on the mask, a negative resist, CAN038, is used in this development. For process window investigation, a focus exposure matrix FEM was carried out. A FEM wafer is a wafer with several patterns created using different resist exposure doses rom one die to another. As a result, the pattern shape and linewidth vary considerably within a single wafer, which allows for the rapid determination of the appropriate dose.

After the exposure, the resist is developed, revealing the nanowire patterns. The resist width is then measured using CD-SEM (Critical Dimension SEM).

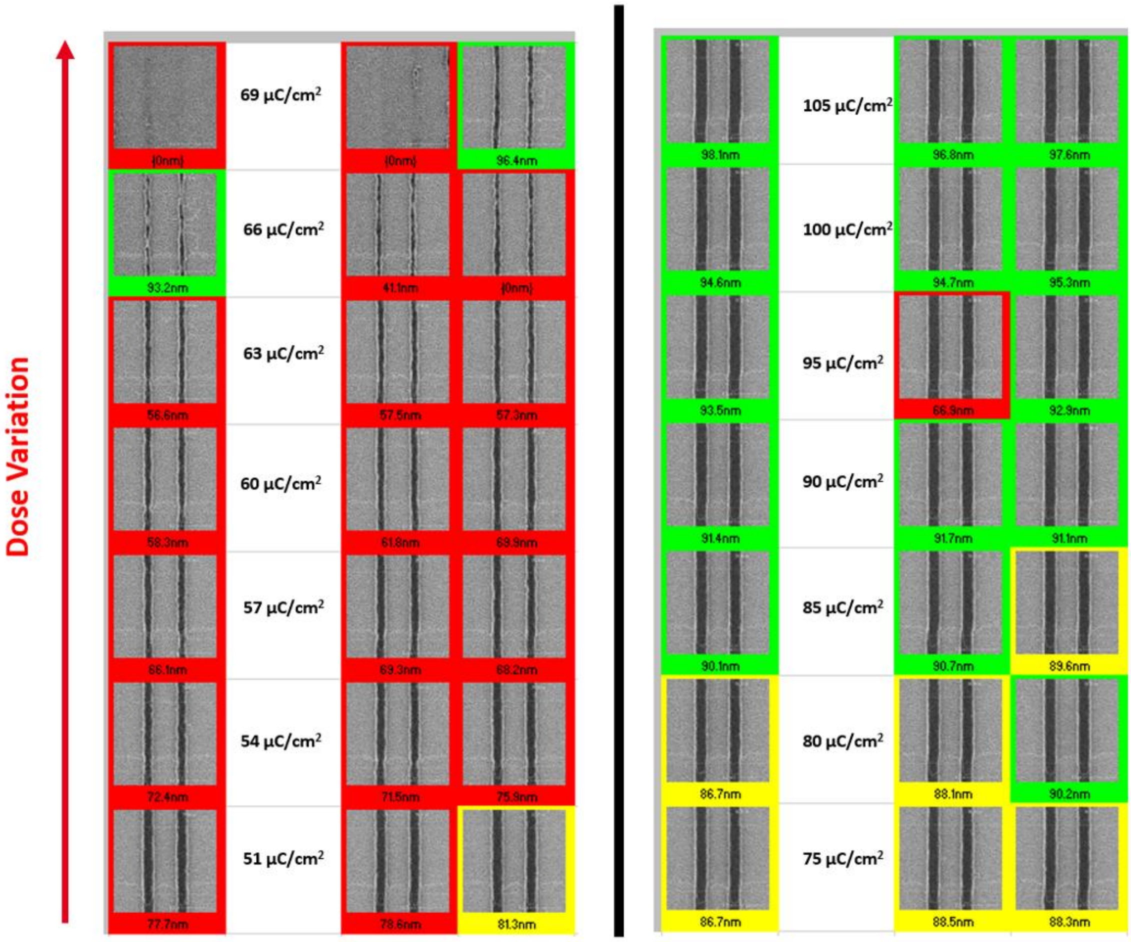

***Figure 62** : Results of CD-SEM measurements of FEMs performed on two dummy wafers to determine the optimal dose of the electron beam lithography to pattern nanowires of 100 nm width*

Figure 62 represents the CD-SEM measurements performed on the FEM sample. For the wafer on the left, the dose varied from 51 to 69 µC/cm^2, with a step of 3 µC/cm^{2}while for the wafer on the right, the dose varied from 75 to 105 µC/cm^2 with a step of 5 µC/cm^2 (increasing dose for dies from bottom to top). The matrix is divided into three color codes according to the dimension analysis.

The CD-SEM results below 80 nm width are represented in red, in yellow between 80 and 90nm, and in green between 90 nm and 100 nm. The SEM pictures highlighted in red show nanowire constrictions or even completely missing patterns. Following this analysis, we chose the most appropriate dose in green 105 µC/cm^2 resulting in a nanowire width of 100 nm (±5 nm), and exposed the whole wafer at a fixed dose, as shown in Figure 63. As expected, the resist patterns appear to be well defined, with a width around 97 nm, very close to the target of 100 nm, and free of constrictions over the entire wafer.

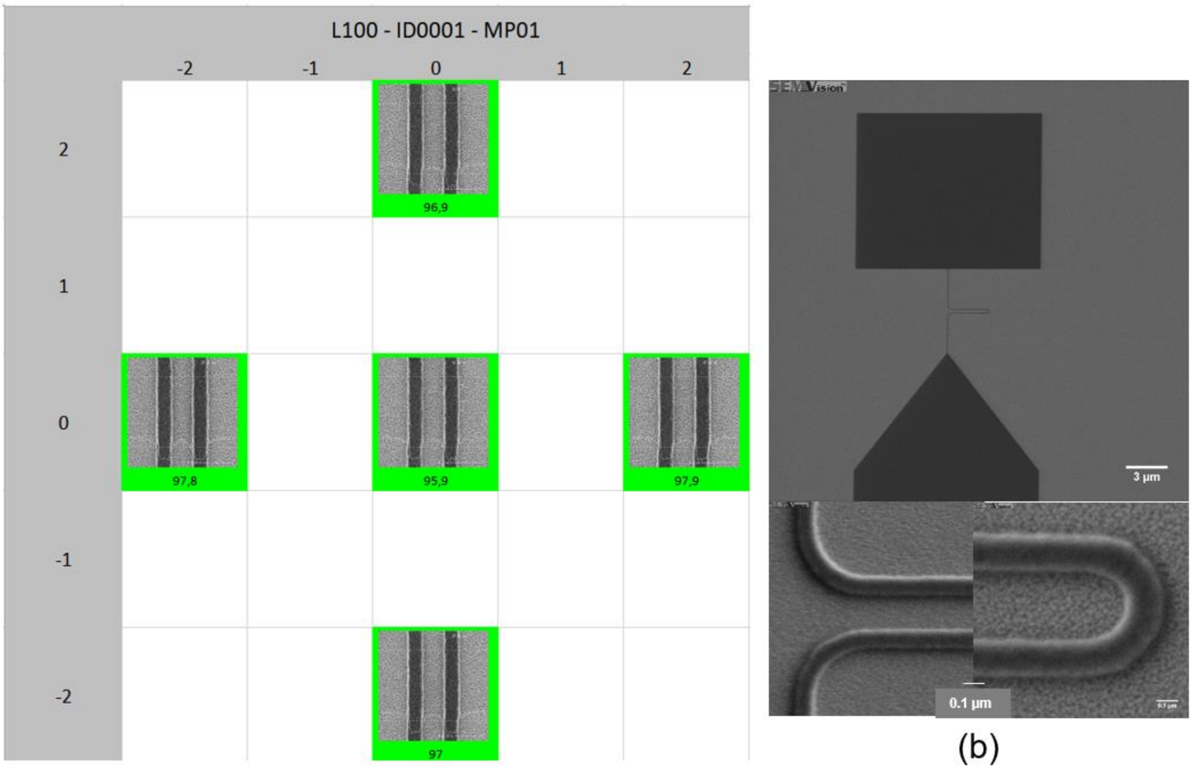

(a)

(b)

Figure 63 *: (a) CD-SEM of a wafer exposed at a fixed dose with 5 monitored dies. The nominal nanowire width is 100 nm on the mask (b) SEM image of a nanowire pattern in the wafer center.*

The exact resist thickness is then measured by AFM. Figure 64 shows an AFM image of the nanowire as well as a measurement of the resist height profile, which is approximately 47-49 nm, close to the target value of 50 nm. In view of these successful results, we can say that the development of nanowire e-beam lithography is completed.

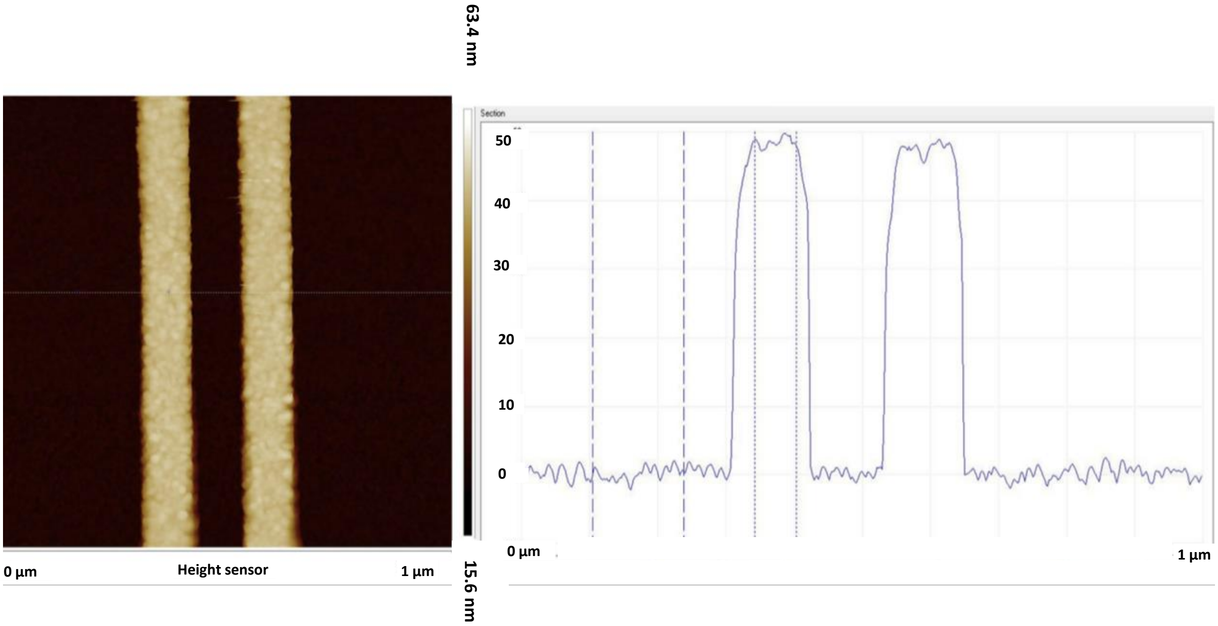

***Figure 64** : AFM height profile measurement of the resist*

5.3.2.2 Reactive ion etching of NbN nanowires

A high-density plasma etch tool (LAM Research 9400) was used for the development of nanowire etching. Our objective is to develop an etching recipe to define the NbN nanowires, compatible with the two different stacks, either NbN/AlN/Si or NbN/SiO_2/Si. The most challenging aspect of this development is the control of the etching process in the case of ultra-thin films of less than 10 nm thickness. The first challenge is the measurement of the etch rate. The conventional ellipsometry method to measure remaining thickness is too imprecise for the thickness range of our NbN films. We will use AFM profile measurements instead. The second challenge is the selectivity between NbN and the underlying layers. While partial etching of the AlN or of the oxide layer occurs after etching the NbN layer should not affect the operation of the device, we must however be cautious not to etch the underlying silicon layer, which could cause waveguide damage and degrade the propagation losses. As we had no prior experience with etching of NbN thin films, we decided to first develop the recipe for 25 nm NbN, which is less stringent regarding etching thickness control, then to optimize the recipe by moving to 12 nm NbN, and finally to fine-tune the process for the target thickness of 6 nm, performing all these studies on dummy wafers. All the dummy wafers under consideration had an AlN buffer layer of 10 nm.

- <u>Etching of 25nm NbN</u>

Our initial experiments were carried out on full sheet wafers with 25 nm NbN. Several gas combinations were tested, and the chosen etching recipe includes CF_4, O_2, and N_2 gases. The etch rate is approximately 38 nm/min. This value was obtained through interferometric endpoint detection and confirmed through weight measurements.

Then we moved to the etching of the dummy wafer already patterned with the resist. First, we performed a partial etch for 20 seconds to investigate the etch rate of the resist on patterned wafers. The height profile was measured using AFM and is approximately 35 nm. This height corresponds to the etched NbN and the remaining resist. The resist was then stripped, and the resulting height was measured again, which was 17 nm, meaning an etch rate of 68 nm/min, much faster than on unpatterned wafers. The stripping of the resist is carried out in two stages, the first one being a dry stripping in-situ and the second one a wet stripping ex-situ. The applied dry stripping was chosen to be purely chemical because isotropic etching of the resist is desired. Since the resist is primarily composed of carbon, resist stripping necessitates sending reactive oxygen (oxygen molecule broken by plasma) to form volatile compounds with carbon atoms of the resist such as CO or CO_2. In contrast, the wet stripping is intended to remove organic etching residues such as the polymers formed during dry etching. We use dimethyl sulfoxide (DMSO) for wet stripping.

As a result, we consumed around 18 nm of the 50 nm resist while etching a bit more than half of the NbN. Due to the limited resist budget, we decided not to etch the whole layer. Figure 65(a) and Figure 65(b) show SEM images of a typical nanowire of 100 nm nominal width and the Energy-Dispersive X-ray spectroscopy (EDX) results obtained to monitor the etching process, respectively. The SEM images reveal a clean partial etch: the nanowire is well defined, with width and gap values matching the target one. The bends have not narrowed and will therefore not be prone to any current crowding issues. Comparative EDX measurements are made on the nanowire and on the etched area. The presence of niobium in the etched area is confirmed, which is consistent with the presence of about 8 nm of remaining NbN after partial etching.

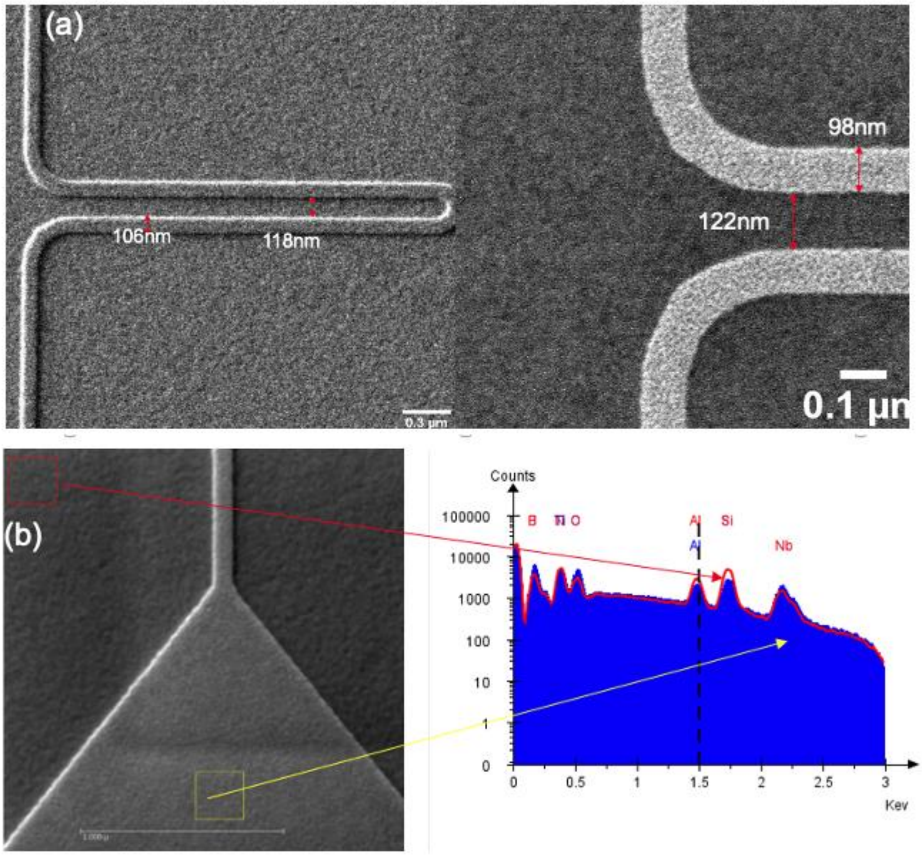

Figure 65 *: (a) SEM images of a partially etched nanowire. (b) EDX measurements, one measurement made on the nanowire (yellow square) and another on the etched area (red square).*

- <u>Etching of 12nm NbN</u>

Previously, we have shown that we have etched 17 nm during 20 s. To etch 12nm, we decide to make the first attempt at 17s. After etching, the resist is stripped (dry + wet) followed by an AFM measurement to measure the height profile as shown in Figure 66. The profile of the nanowires is spurious, they have a height of 12 nm as expected but there are grains or particles which height ranges between 10 and 15 nm (Figure 66b). The height distribution extracted from the entire AFM measurement area yields two peaks, a narrow peak at a value of 11.6 nm thickness which corresponds to the NbN thickness and a second broader peak around 8-10 nm corresponding to the spurious grains (Figure 66(c)).

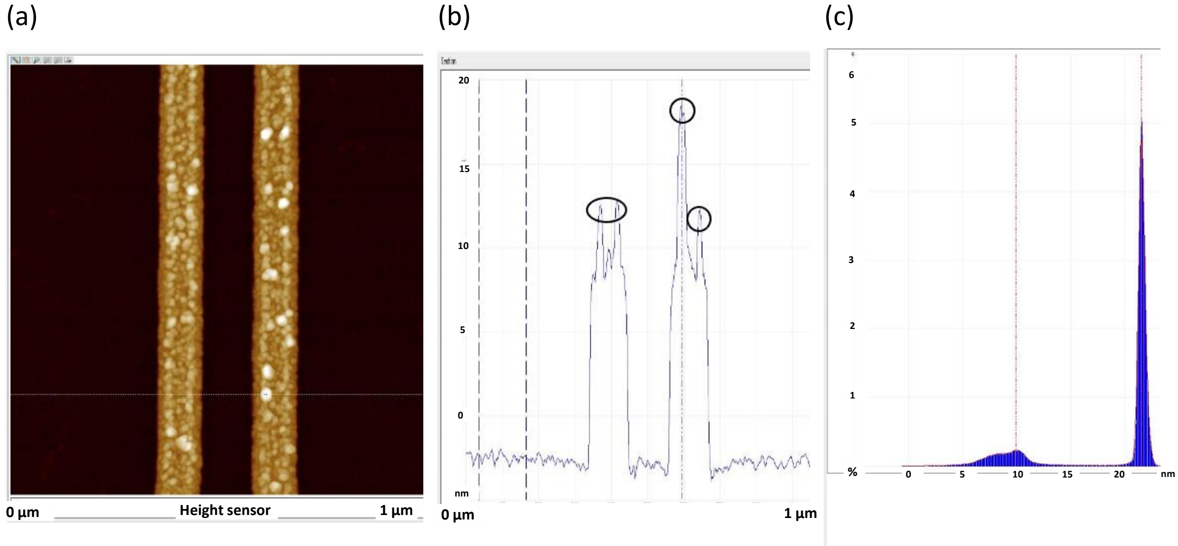

Figure 66 *: (a) AFM measurement of a totally etched NbN nanowire of 12 nm thickness; (b) height (c) height distribution*

SEM observations shown in Figure 67 confirm the presence of spurious particles. They are found both on the nanowires and on the etched area, and they tend to congregate on the edges of the NbN patterns. Similar observations were made on other wafers. EDX-SEM and EDX-STEM measurements were carried out in order to investigate the nature of these undesirable particles. The results are summarized in Figure 68 and Figure 69. Actually, EDX-STEM offers a better resolution than EDX-SEM and allows the selective analysis of the particles both in the etched area and on the nanowire. Thanks to the thin samples, this technique allows a chemical analysis of the layers and not only of the surface.

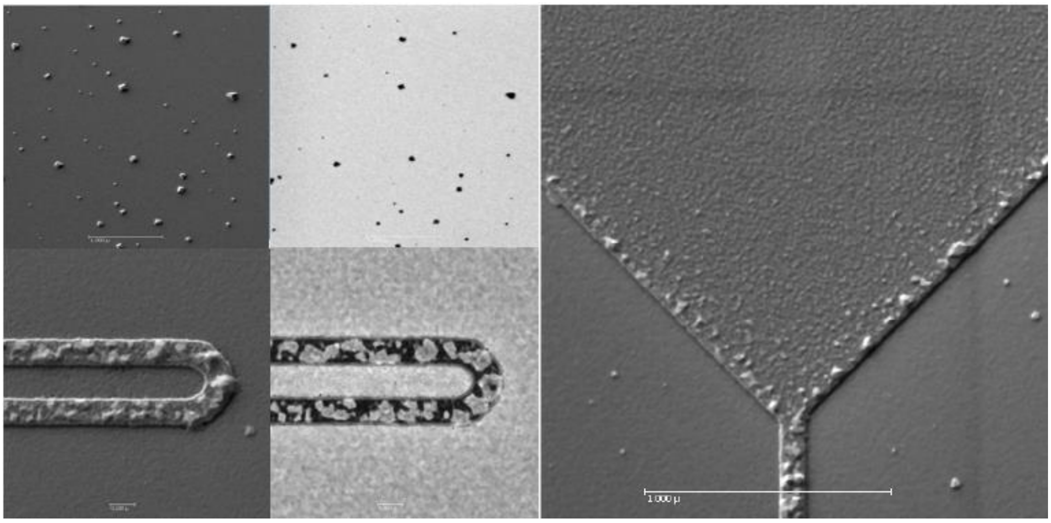

Figure 67 : *SEM images of a totally etched 12 nm NbN nanowire showing particles generated during the etching*

The EDX-SEM analysis of Figure 68 shows that there is no Nb signal in the etched area (red), indicating that the NbN layer has been completely etched as expected, whereas an Al pick is present, confirming the presence of the AlN layer. Nb, fluorine F, and oxygen O signals are present on the nanowire(blue) but not in the etched area (red). The EDX-STEM analysis of Figure 69 validates and complements the EDX-SEM measurements. The particles above the nanowires and in the etched area are of same nature, mainly composed of aluminum (blue), oxygen (red), and fluorine (green).

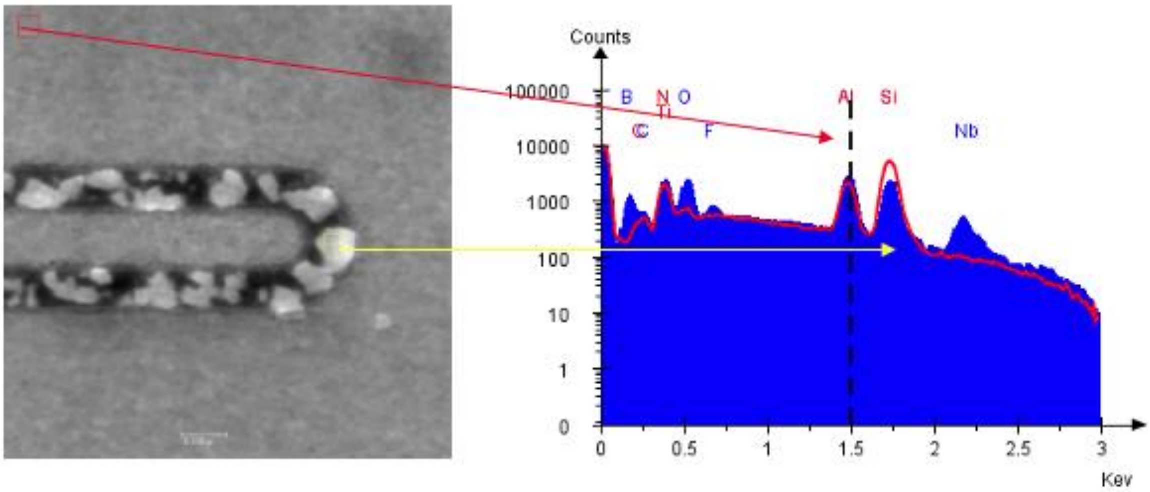

Figure 68 : *SEM-EDX results. comparison of EDX spectra of an etched area (red curve) and a particle on a nanowire (blue curve).*

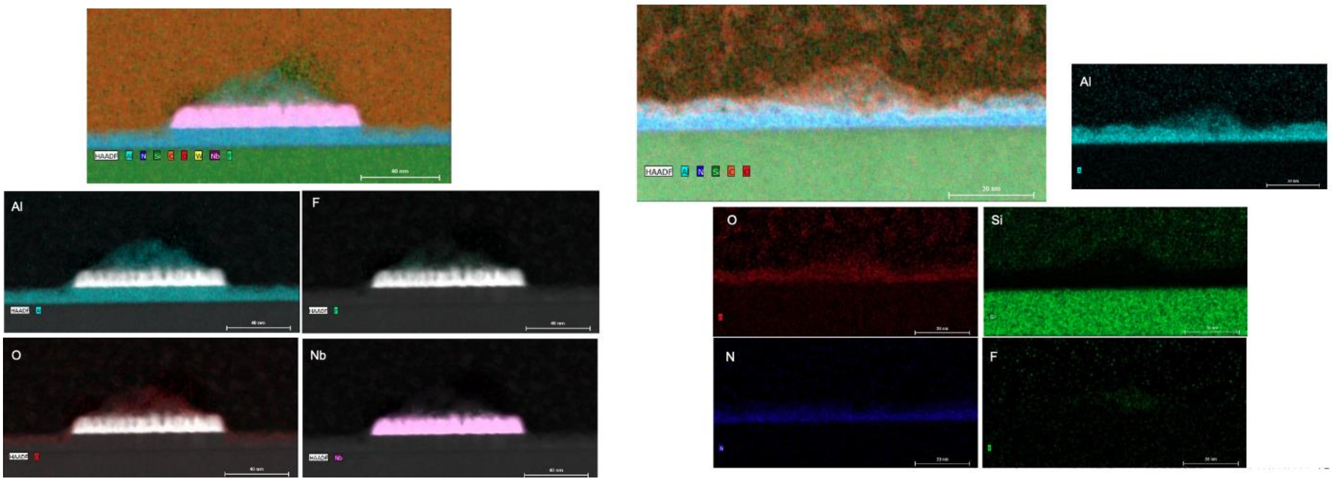

Figure 69 : *EDX-STEM analysis (Left) on the nanowire and (Right) on the etched zone*

Because of the presence of aluminum and oxygen, we initially thought that the problem might be linked to the oxidation of the AlN layer since it is not protected after etching and the SEM observations were made one day after the etching. Furthermore, due to the presence of fluorine, the particles may have resulted from the interaction of the etching gases (CF_4) with the AlN. These assumptions would explain why we saw no issues during partial etching, when the entire AlN layer was still covered by NbN. To investigate the oxidation hypothesis, we reduced the time between each process step and made observations immediately after the step was performed. The following protocol was adopted:

Etching → SEM → Dry strip in situ → SEM → Wet strip ex-situ → SEM.

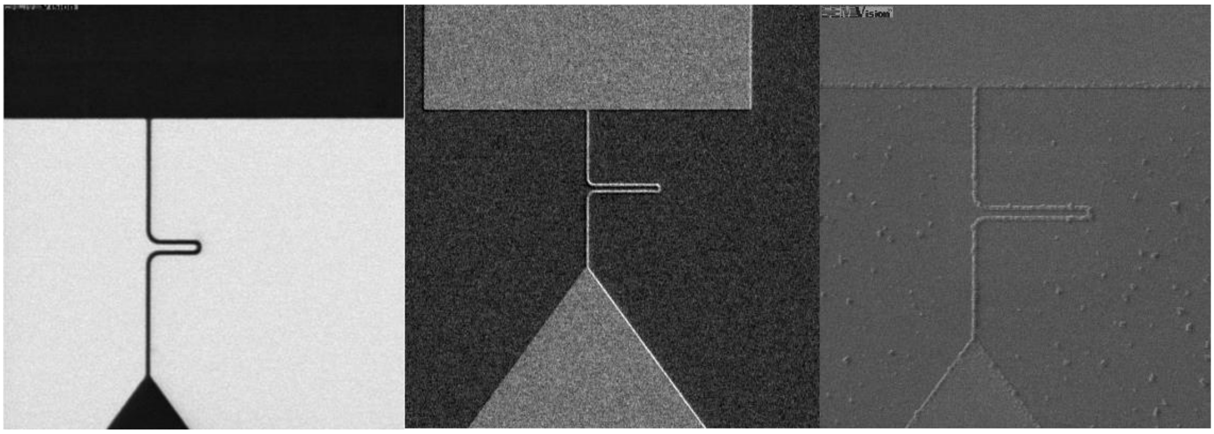

Figure 70 : *SEM images (Left) after NbN etching; (Center) after dry stripping; (Right) after wet stripping*

Figure 70 shows the observations after each step. The surface is clean after etching and in-situ stripping. However, particles appear after wet stripping, indicating that the DMSO-based chemistry of the WET stripping is responsible for the particle generation and should be replaced by another chemistry. We also learned from all this study that the etching recipe works well to selectively etch NbN with respect to AlN and that we can therefore rely on endpoint detection to stop the etching process.

- Etching of 6nm NbN

Based on this newly acquired knowledge, we applied the etching recipe to the 6 nm wafers and replaced the DMSO wet stripping chemistry with Dipropylene Glycol Monomethyl Ether and Oxalic acid Dihydrate that we referred to as CA25.

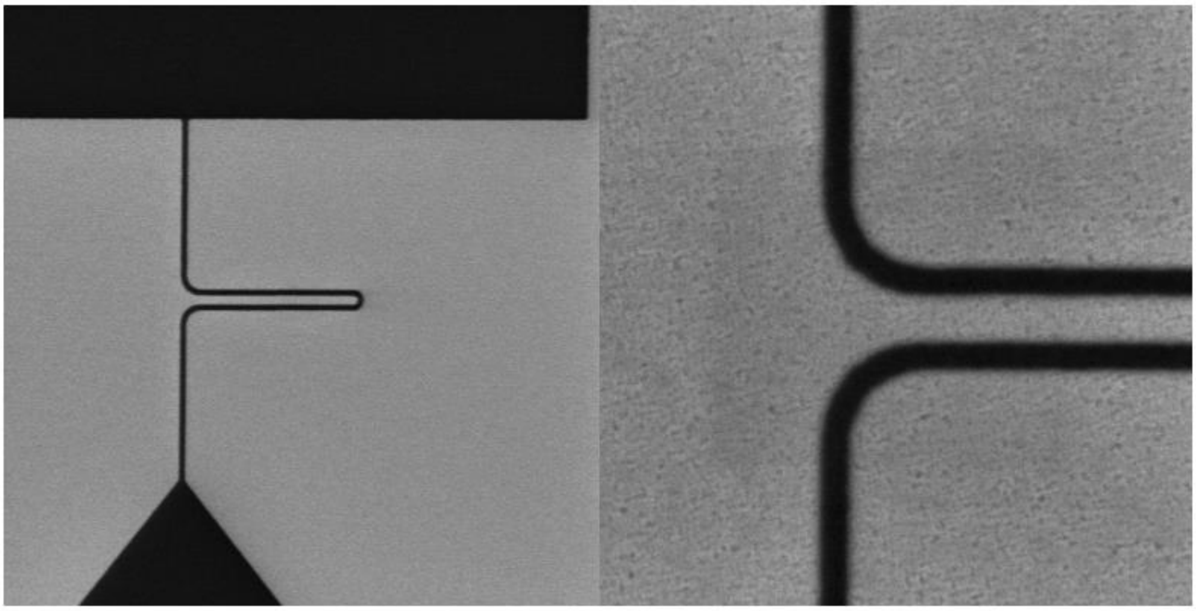

***Figure 71** : SEM images after etching, dry and CA25 wet stripping*

Figure 71 reveals the etching results with the new wet stripping chemistry. Observations were made immediately following the stripping, 24 hours later and four days later. In all cases, the nanowires remain intact, with no residual particles. After this successful development of the full NbN patterning sequence, AFM measurements were carried out, confirming the 6 nm nanowire thickness with a roughness of approximately 0.4 nm as illustrated in Figure 72. Two other wafers were prepared using the same process, showing the same nicely defined nanowires totally free of unwanted particles, thus confirming the good reproducibility of the process.

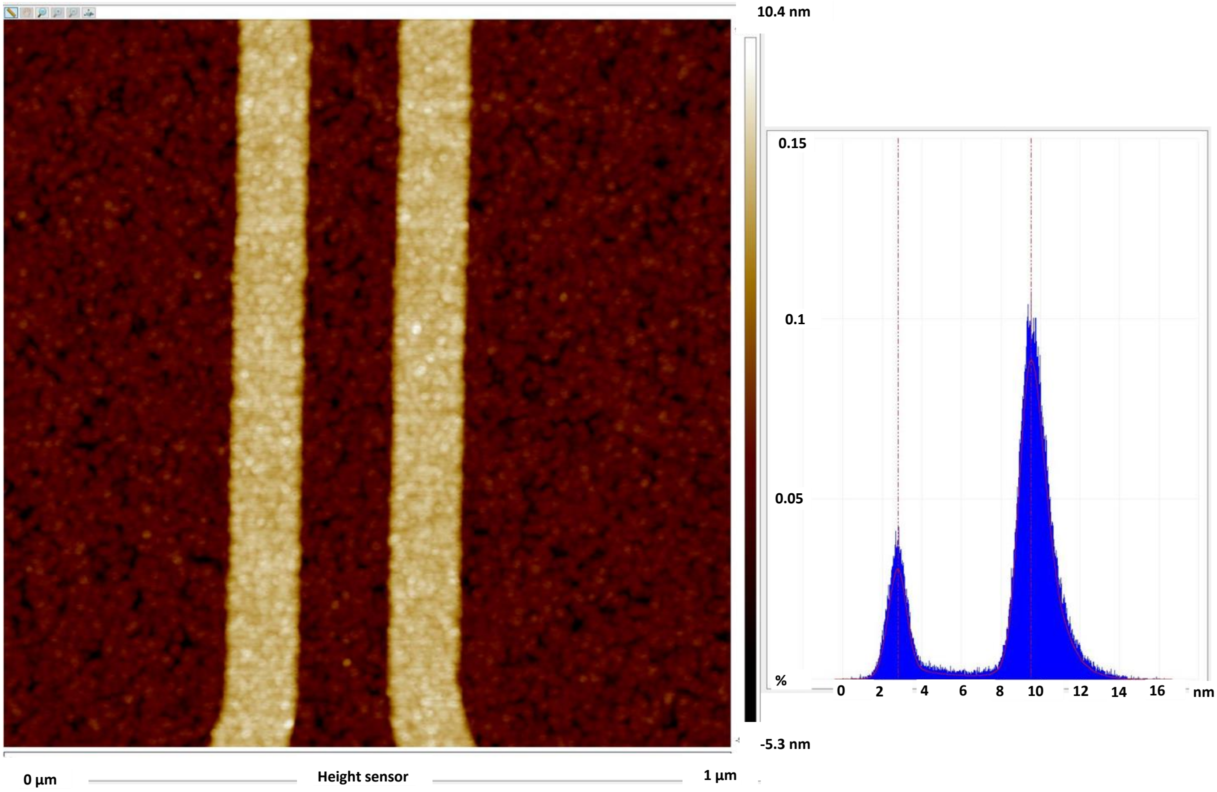

Figure 72 *: AFM height distribution measurement of a totally etched NbN nanowire of 6 nm thickness*

Finally, we want to examine the nanowire width after they have been etched. However, we could not perform automatic CD-SEM measurements because the program was unable to detect the etching flanks, possibly due to a slope in the etching profile. Therefore, TEM observations were made, and the height profile indeed shows a slight slope, as shown in Figure 73. Thus, to determine the width of the nanowire, we decided to make manual CD-SEM measurements. Figure 74 shows a nanowire with a width of approximately 90 nm. In order to obtain 100 nm nanowires after etching, the electron beam dose should be adjusted to target a value around 110 nm after lithography (rather than 100 nm).

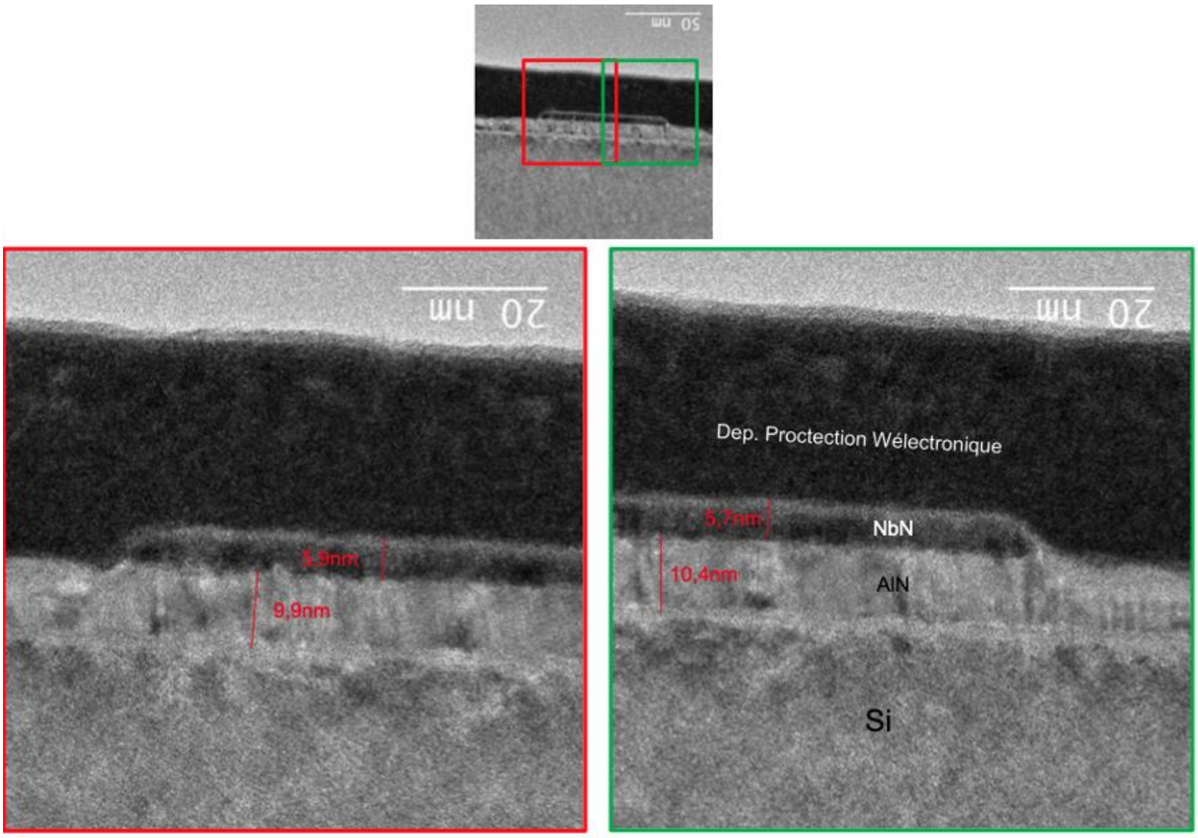

***Figure 73** : TEM images showing the various materials of the stack as well as the slope of the nanowires after etching*

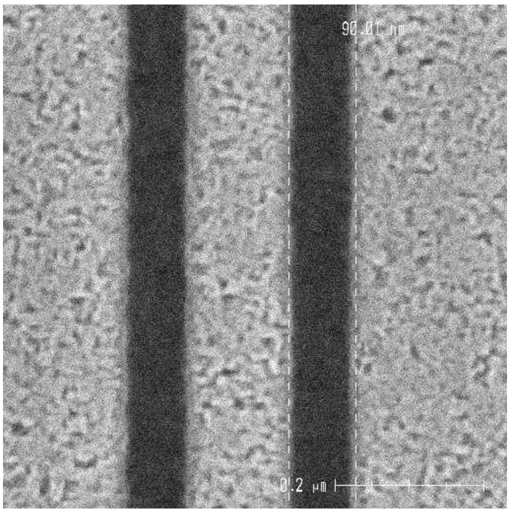

***Figure 74 :** CD-SEM measurement of a nanowire with a width of 90nm after etching*

Although we were unable to determine why the DMSO chemistry produced these undesirable particles (due to time constraints), **we can now claim to have developed a successful recipe for properly etching NbN ultrathin films deposited on an underlying AlN layer**. The full process sequence (e-beam lithography, etching and stripping) is now ready to be applied on functional wafers embedding silicon waveguides. The SEM picture of a U-shape nanowire atop a SOI waveguide is illustrated in Figure 75. The nanowire is well defined, free of constrictions, and is well centered with respect to the silicon waveguide.

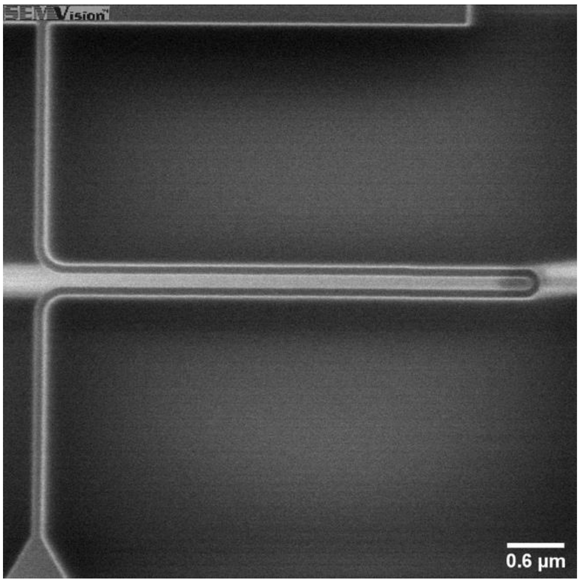

Figure 75 *: SEM image of a U-shape nanowire atop a silicon waveguide*

5.4 Development of metallic contacts on the NbN nanowires

Following the front-end fabrication of the waveguide-integrated nanowires, electrical contacts are required to obtain a fully functional SNSPD device. Figure 76 depicts the sequence of the main technological steps required to define the metallic contacts: encapsulation, opening of vias in the oxide down to the NbN, conformal metal deposition and patterning to define the contact pads.

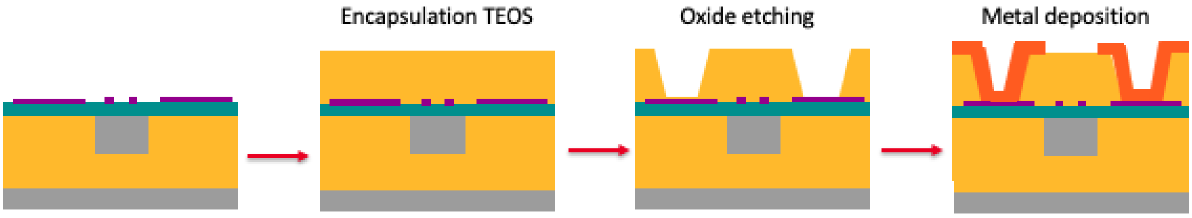

Figure 76 *: The sequence of the main technological steps necessary for the definition of metallic contacts*

5.4.1 Encapsulation

The first step consists in the deposition of an oxide layer to encapsulate the nanowires and protect them from oxidation and ageing. The oxide thickness will define the distance between the silicon waveguides/the NbN nanowires and the metal pads. This distance must be sufficient to ensure that there is no absorption of the guided mode due to the presence of the metal layer and to avoid heating of the nanowires due to energy dissipation when biasing them, which could unintentionally trigger their switching to a resistive state in the absence of photon absorption. 600 nm of TEOS oxide were deposited to this aim, verified using ellipsometry. We note that a CMP step is not necessary as the topology associated to the ultra-thin 6 nm nanowires is not significant.

5.4.2 Opening of the vias

The encapsulation oxide is then patterned using a sequence of lithography and etching steps. The lithography performed to open the vias was done with 248 nm wavelength DUV light in an ASM300 stepper and aligned with the previous levels using the PM markers. Since the minimum feature size of our vias is in the order of a few microns, no special development was undertaken for this step.

In contrast, the subsequent etching of the vias through the oxide down to the NbN was a much more challenging step, as the etching must stop on the NbN layer without damaging or etching it. For optimal control of this step, we decided to split the oxide etching into two steps: a first fast dry etching step to etch most of the oxide (around 500 nm) followed by a purely chemical wet etching step to remove the rest of the oxide with a good chemical selectivity with respect to NbN. The development of both etching steps has been carried out on a series of dummy wafers with the same stack of 6nm NbN/ 10nm AlN /Si.

5.4.2.1 Dry etching step

For the first dry etching step, the objective is to determine the etch rate, by measuring the remaining oxide thickness using ellipsometry. The determined etch rate is approximately 285 nm/min. Therefore, it would take 105 s to etch about 500nm. It has to be noted that the remaining oxide thickness is measured on special test structures called “thickness boxes” placed in the periphery of the chips to check the technological steps. However, these test structures are much larger than the via (103 μm x 72 μm vs 8 μm x 8 μm or 10 μm x 10 μm). Therefore, FIB-SEM observations shown in Figure 77 and Figure 78 are performed directly in the via and in the test structures after 105 s (45s + 65s) etching to determine the exact etched thickness in the via and calibrate the ellipsometry measurements in the test structures. Furthermore, observations were made both at the wafer edge and center to check for etch rate variation across the wafer.

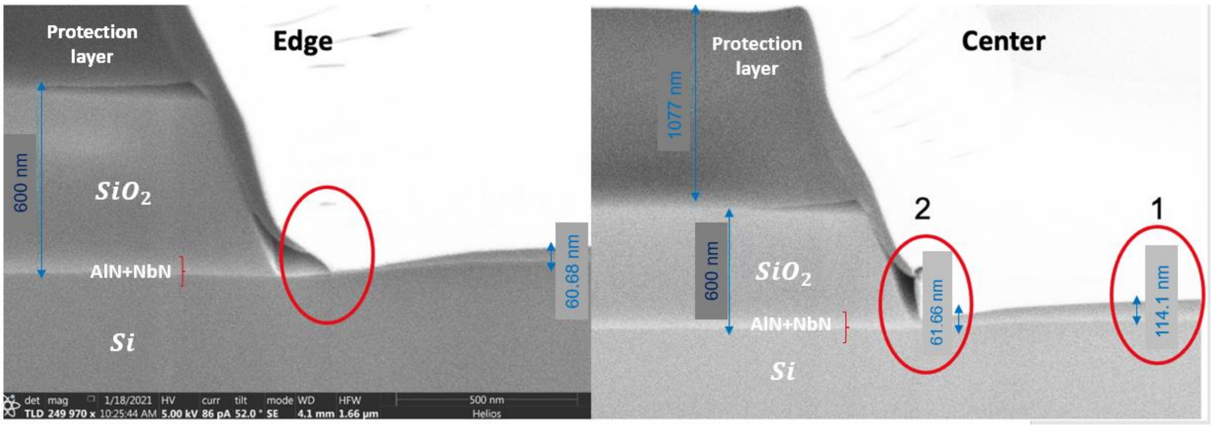

Figure 77 : *FIB-SEM image in the thickness test structures after partial dry etching*

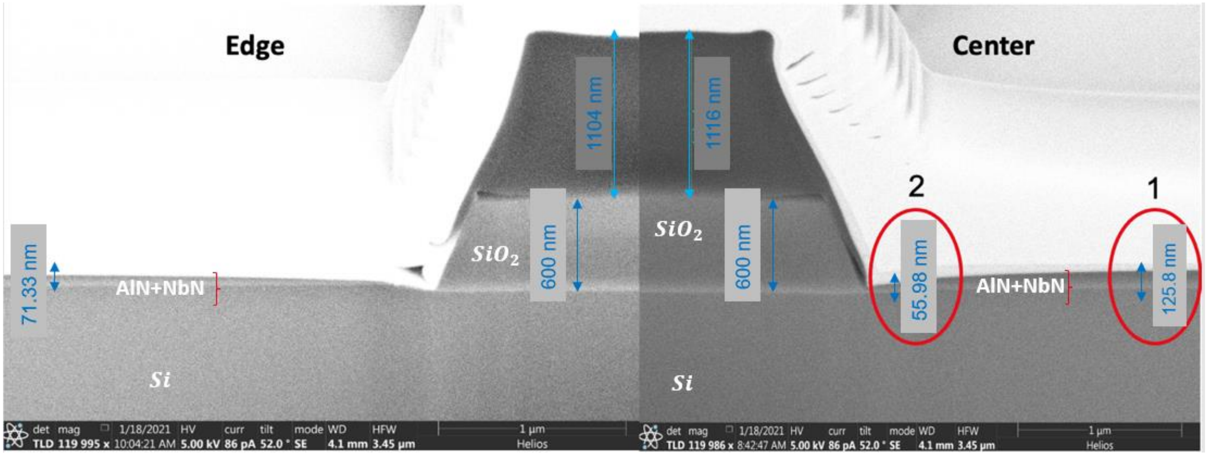

Figure 78 : *FIB-SEM images in via after partial dry etching*

The first point to mention is that the pictures do not allow to distinguish the contrast between AlN and NbN. According to FIB-SEM observations, the remaining oxide thickness in the via is 126 and 72 nm in the center and edge of the wafer, respectively. Whereas the remaining oxide thickness measured in the test structures is 114 and 61 nm at the center and edge of the wafer, respectively. We conclude that the etching rate in the thickness box is slightly higher than in the via and is higher in the edge than in the center. The phenomenon of etch trenching of the oxide is observed i.e., the etch rate at the trenches is higher. Because of the significant variation in etching between the center and the wafer edge, we decide to etch 5% less time for the following (95s instead of 105s) in order to eliminate the risk of damaging or etching the NbN. The remaining oxide, measured by ellipsometry, is found to be approximately 160 nm with these new conditions.

5.4.2.2 Wet etching step

The objective is now to remove the remaining oxide using wet etching. The chemistry must be selective, removing only the desired oxide layer and not the NbN layer. The wafer is placed in a wet bath of buffered oxide etch BOE (5/7/1) during 60 s, consisting of ammonium fluoride NH_4F as a buffer and hydrofluoric acid HF. Then, the residual resist is quickly removed by a combination of immersion in a heated solvent solution and high-pressure spraying. Finally, the wafer is immersed in a 0.1% HF bath to remove the generated polymers during the etching on the side and the bottom of the vias. The ellipsometry measurement shows zero oxide thickness as expected. The integrity of the NbN layer is then verified by EDX-STEM observations. EDX-STEM analysis shown in Figure 79 reveals the presence of two layers: a lower layer of NbN and an upper layer of NbO. The STEM pictures displayed in Figure 80 show an oxidized and amorphized top surface, as well as a crystalline interface between NbN and AlN. Furthermore, the top surface has a roughness of about 1 nm. These observations confirm the perfect integrity of the NbN layer covered by its native oxide NbO.

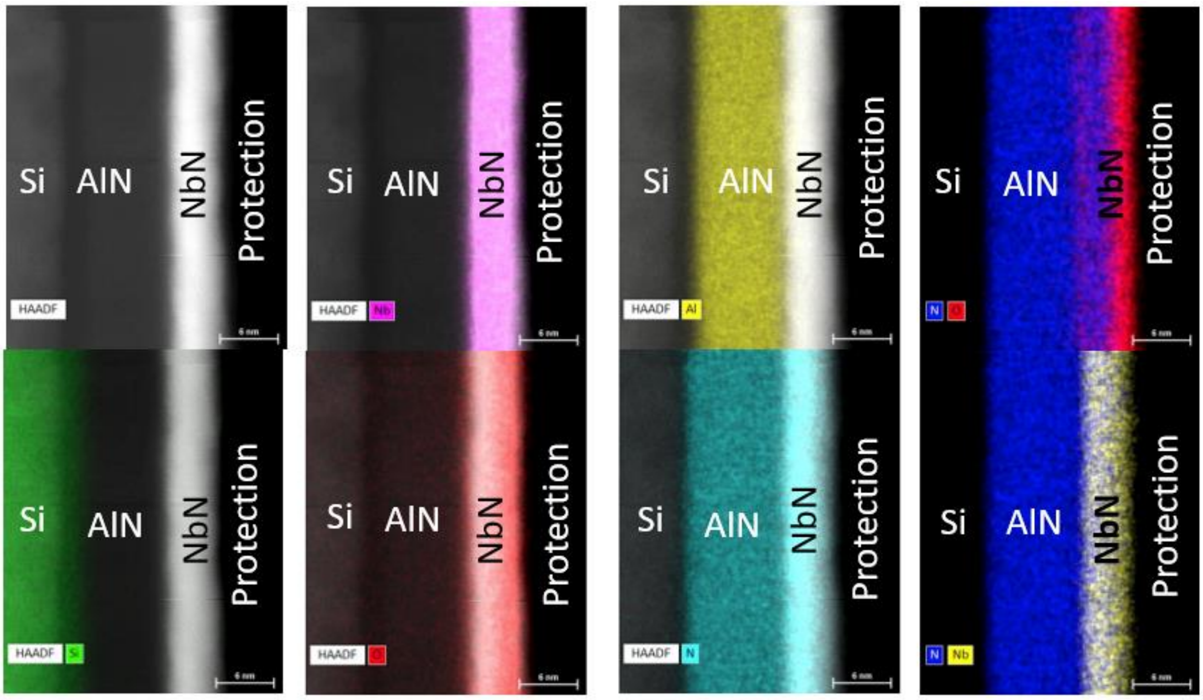

***Figure 79** : EDX-STEM analysis in the via revealing the presence and the integrity of the NbN layer*

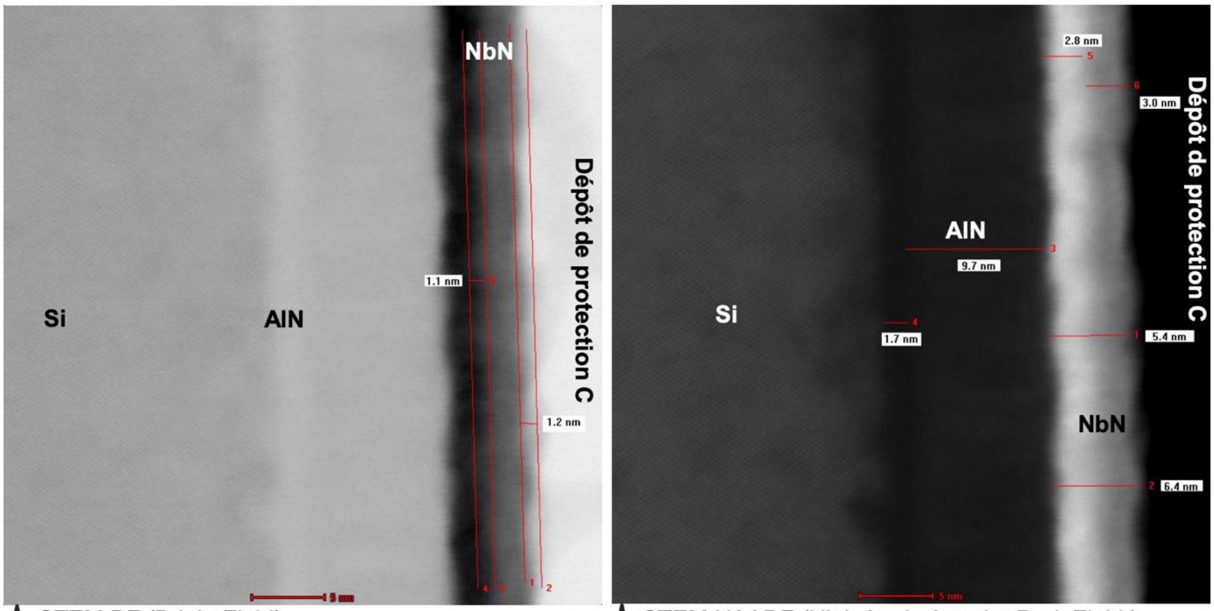

STEM BF (Bright Field)

STEM HAADF (High Angle Annular Dark Field)

***Figure 80** : STEM observations in the via after etching. STEM BF (Left) shows a difference in crystallinity within the NbN layer, whereas STEM HAADF (Right) illustrates a difference in chemical nature within the NbN layer.*

We can therefore conclude that we have successfully developed a process to open the via through the oxide without damaging the NbN layer.

5.4.3 Metal deposition and patterning

In order to develop the metal deposition and patterning process steps, we use the same dummy wafers that served to develop the etching process. The objective is to ensure electrical continuity of the metal and good contact with the NbN pads.

We choose aluminum-copper (AlCu) as the main metal because of its very low resistivity. The metallic stack comprises two adhesion layers of Ti and TiN of 10 nm and 40 nm thickness respectively, a 650 nm layer of AlCu with 0.5 % Cu and two protective layers of Ti and TiN of 10 nm and 40 nm thickness respectively to limit the oxidation and corrosion of copper. The deposition of this Ti/TiN/AlCu/Ti/TiN stack was performed by physical vapor deposition (PVD) in an Endura 5500 tool at 350°C for Ti/TiN and 450°C for AlCu. The three different material layers were deposited in the same tool without exposing the wafer to the outside environment in order to prevent from oxidation and ensure a low resistivity of the full metal stack. After the deposition, a cross-section SEM observation, displayed in Figure 81, was made to verify the continuity of the deposited metallic stack. Indeed, thanks to the slope of the sidewalls of the via, the metal features perfect continuity all over the topology of the via.

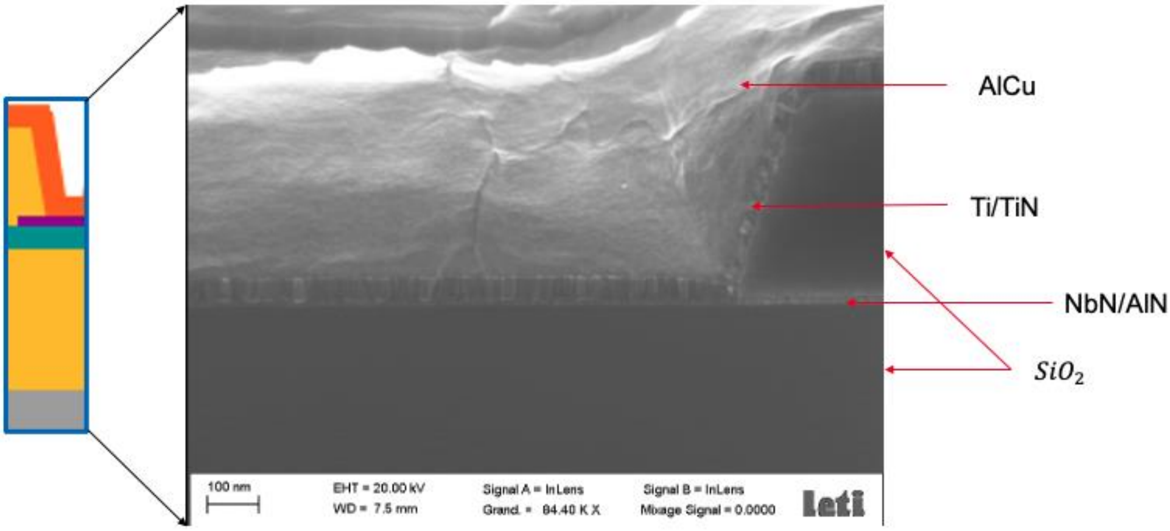

***Figure 81** : SEM image in the via after metal deposition distinguishing the layers of the stack*

After metal deposition, lithography and etching are performed to define the contact pads. However, an intermediate lithography and etching sequence followed by metal removal is performed first to unveil the PM alignment marks previously covered by the metal deposition, as they are necessary to align the metal pads with the underneath structures.

For contact pad lithography and etching on dummy wafers, the mask level designed in Chapter 4 was not yet available at the time of this back-end module development. We used another mask already available in the lab with same opening rate and pattern size instead, with the objective to later apply the optimized process with the appropriate mask on the functional wafers. We used already developed processes for both lithography and etching. The latter was carried out using a Cl_2/HBr plasma etching, and the endpoint was detected using OES as the high opening rate of the mask ensures a strong signal due to the high concentration of etching products in the chamber. The resist was then stripped with an O_2N_2 plasma followed by a hydroxylamine wet etch. Figure 82 displays the SEM pictures taken after the formation of the metallic pads.

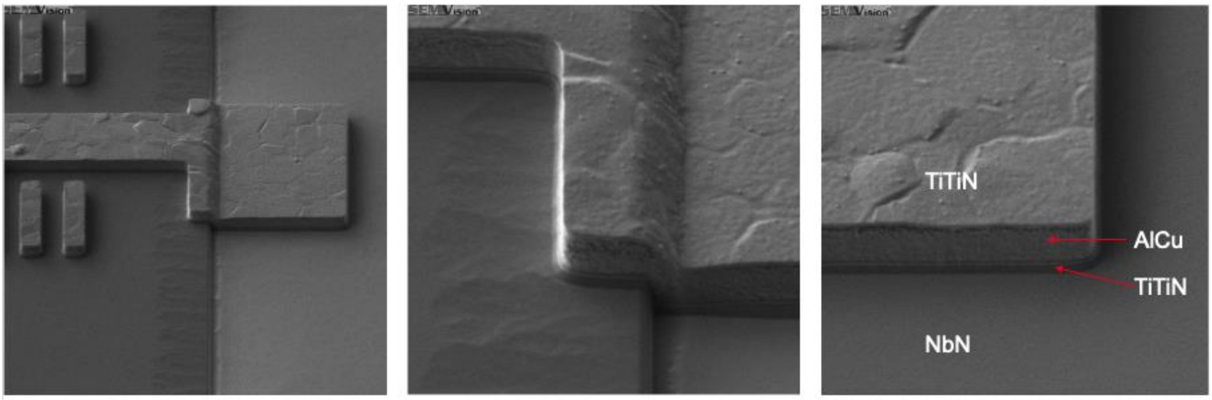

Figure 82 *: SEM images of the metal multi stack layer. It is possible to recognize the light gray parts (Ti/TiN) at the top and bottom of the AlCu alloy.*

Electrical tests

In order to validate the full back-end process, we need to perform electrical tests. For this purpose, we have included Transmission Line Measurement (TLM) structures in our layout. These structures, illustrated in Figure 83, allow the measurement of the contact resistance R_c between the metal and the NbN and R_s the sheet resistance of NbN.

The total resistance $R_T = 2R_c + R_s = \frac{V}{I}$ depends on the distance between metal pads and can be determined by measuring the slope of the V(I) characteristic. This measurement is performed between each set of two consecutive pads separated by distance L$_i$ in order to extract R_s and R_c , as shown in Figure 83.

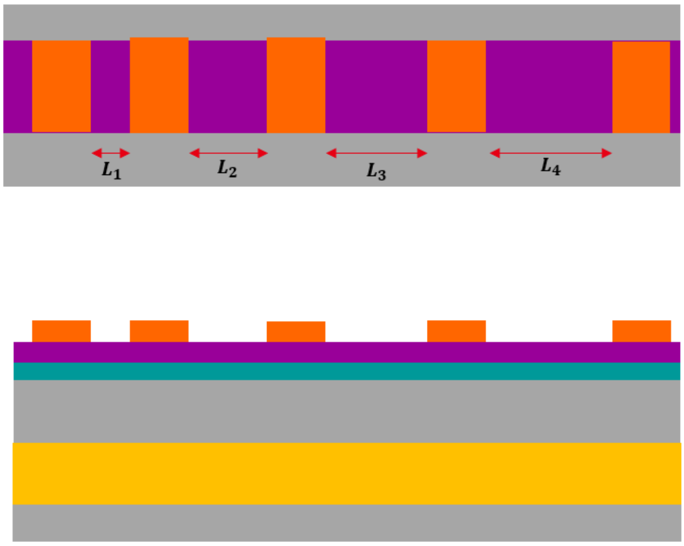

Figure 83*: Description of TLM structures*

The measurement is performed on the dummy wafer used for the metal and patterning development (6 nm NbN / 10 nm AlN) where 5 dies are tested according to the mapping shown in Figure 84. The I-V characteristics of the TLM structure on one of the measured dies are presented in Figure 84. The four curves correspond to the measurement between the 5 pads. They are all linear, which confirms the ohmic nature of the contact between AlCu and NbN. On average, the contact resistance is around $R_c \approx 350\ ohm$ and the sheet resistance is $R_s \approx 2.4\ 10^{-2}\ \Omega.\mathrm{cm}^2$. The five measured dies show a variation of 11% across the entire wafer for both the contact and sheet resistance. These values may seem relatively high, but they are explained by the very thin NbN layer of only a few nanometers.

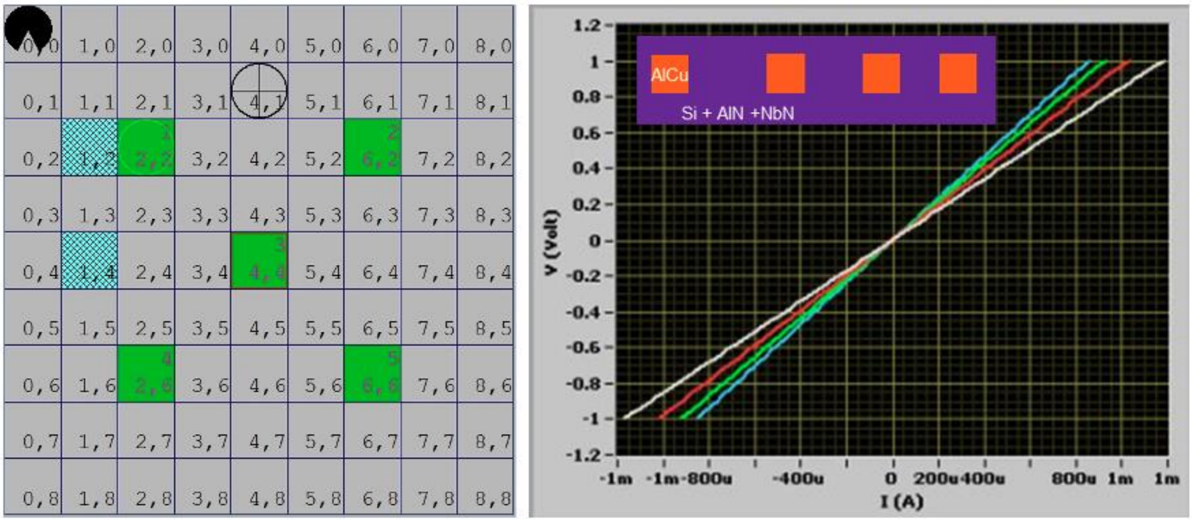

0,0	1,0	2,0	3,0	4,0	5,0	6,0	7,0	8,0
0,1	1,1	2,1	3,1	4,1	5,1	6,1	7,1	8,1
0,2	1,2	1 2,2	3,2	4,2	5,2	2 6,2	7,2	8,2
0,3	1,3	2,3	3,3	4,3	5,3	6,3	7,3	8,3
0,4	1,4	2,4	3,4	3 4,4	5,4	6,4	7,4	8,4
0,5	1,5	2,5	3,5	4,5	5,5	6,5	7,5	8,5
0,6	1,6	4 2,6	3,6	4,6	5,6	5 6,6	7,6	8,6
0,7	1,7	2,7	3,7	4,7	5,7	6,7	7,7	8,7
0,8	1,8	2,8	3,8	4,8	5,8	6,8	7,8	8,8

Figure 84 *: Mapping measurements are shown on the left, and the measured dies are highlighted in green. The I-V characteristics of TLM structures are shown on the right.*

Thanks to these good electrical results, we can conclude that the whole metallization process including the critical opening step of the vias has been successfully developed. It was then applied to functional wafers.

5.5 Optical and electrical characterization of SNSPD devices at room temperature

Following the fabrication of the integrated SNSPDs, preliminary optical and electrical characterizations were conducted at room temperature on the wafer-level photonic probers of CEA-LETI. These characterizations were performed by Valentin Brisson, the PhD student who followed up on my project. I could not perform these measurements myself due to time constraints, but I present them as they are the direct result of all the technological developments I have carried out. The cryogenic optical and electrical characterizations of the SNSPDs that I designed and fabricated will be part of Valentin Brisson's PhD thesis.

5.5.1 Electrical characterization

We performed room temperature resistance measurements of the straight and U-shape SNSPDs across the whole wafer. This represents a hundred of devices. Figure 85 displays the resistance of the devices as a function of their length. The curves are remarkably linear, showing that the resistance of the nanowire is proportional to their length with a value of 11 kΩ/µm and an excellent reproducibility all over the wafer. As expected, the resistance of the SNSPD devices per unit length is doubled for straight SNSPDs with respect to their U-shape counterparts. **The observed uniformity of the nanowire resistance at room temperature over 200 mm SOI wafers is a major result, as it validates the good quality of the developed technology process, namely the uniformity of the NbN deposit, of the nanowire lithography and patterning and of the metallization.** The observed yield seems to be much higher than the yield obtained in the fabrication of commercial SNSPDs operating at normal incidence. These results are very encouraging for the future measurements of the devices at cryogenic temperature.

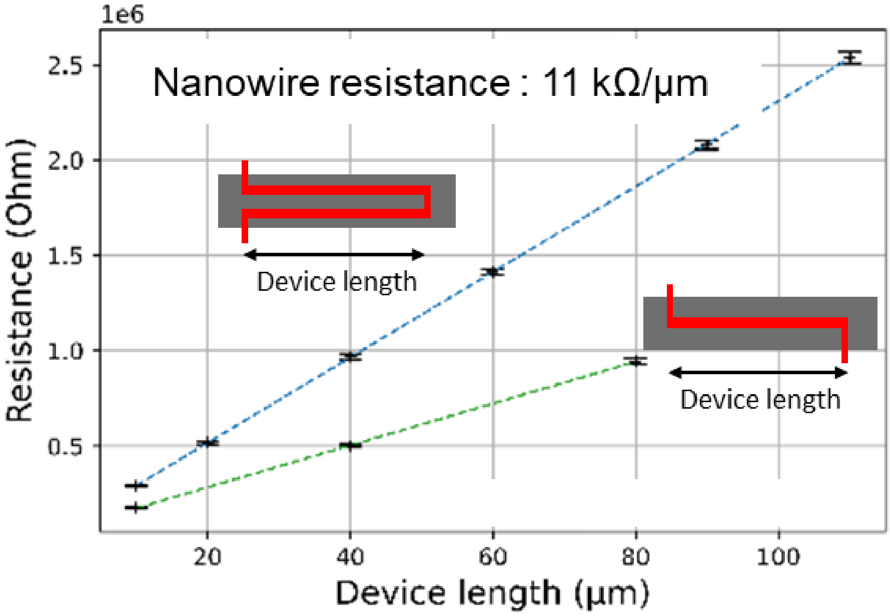

***Figure 85**: Resistance of the nanowires (straight and U-shape) as a function of their length*

5.5.2 Impact of the SNSPD fabrication process on passive waveguides

In order to fully validate the process steps associated to nanowire fabrication and metallization, an important point is to verify that these additional process steps did not degrade the passive structures fabricated prior to the SNSPD process. For this purpose, we carried out optical characterization of passive spiraled waveguide structures as well as fiber grating couplers and power splitters based on multimode interferometers in order to compare their losses before and after the SNSPD process.

Optical measurements are performed by coupling light from a fibered tunable laser to the structures under test through a grating coupler and by measuring the transmitted power out-coupled by a similar grating coupler as a function of wavelength between 1500 and 1600 nm every 25 pm. A polarization controller was used to select TE polarization.

5.5.2.1 Grating couplers

The grating couplers were designed to be used with an 8° incidence angle for maximum transmission at 1550 nm. The measurements were performed on two different wafers. For the first one, the fabrication process was stopped after the waveguide patterning, encapsulation, and CMP, while the complete fabrication process including the SNSPDs was carried out on the second wafer. The grating coupler transmission spectra measured on 11 dies per wafer are presented in Figure 86.

For all the dies on both wafers, the grating couplers losses are the lowest at 1550nm, as expected from design. The average value of the losses is 2.5 dB per grating coupler for the reference wafer without the SNSPD process and is increased to 4.5 dB per grating coupler for the wafer with the SNSPD process.

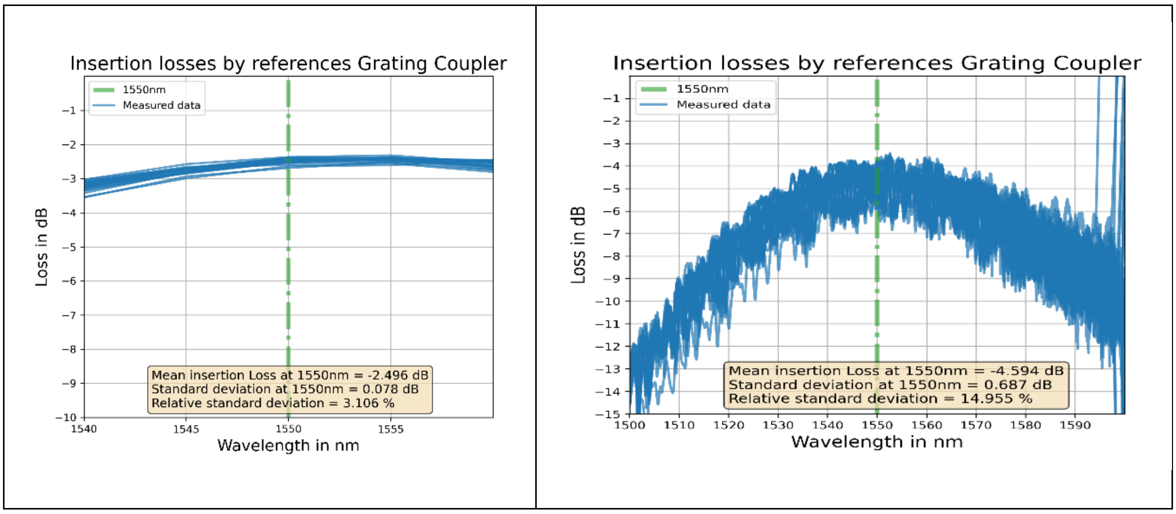

Figure 86: *Grating coupler transmission spectrum for all the measured dies (left) without the SNSPD fabrication process; (right) with the SNSPD fabrication process.*

5.5.2.2 Passive waveguides

As a reminder, we have designed strip waveguides with a cross-section of 400 nm in width and 300 nm in height. To evaluate the waveguide losses at 1550 nm and subtract the contribution of grating couplers, we measured the transmission through spiraled waveguides of different lengths (2, 4, and 6 cm), illustrated in Figure 87.

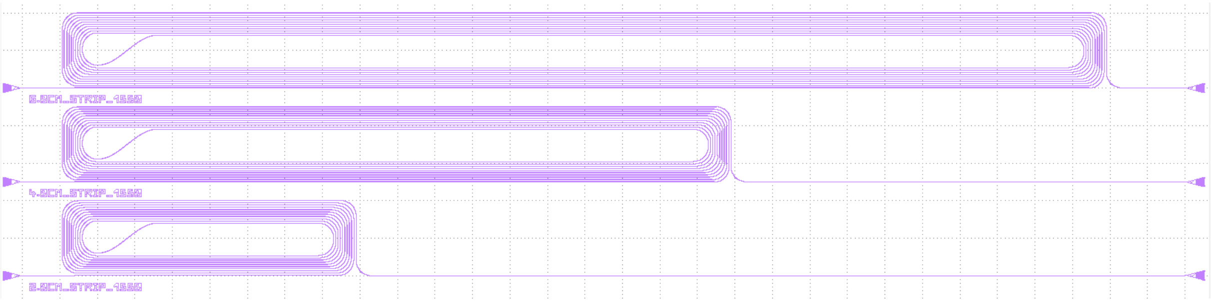

Figure 87: *layout of spiraled waveguides of different lengths (2, 4, and 6 cm)*

Figure 88 displays the transmitted power for a typical die as a function of spiral length. We calculate the linear loss per unit length for each die by performing a linear fit of the data points. The measured losses for all the measured dies are shown in Table 15 and Table 16 for the reference wafer without the SNSPD process and the wafer with the SNSPD process respectively. The results show that losses are increased from 2.4 dB/cm with a standard deviation of 0.11 dB/cm before the SNSPD process to 7.3 dB/cm with a standard deviation of 2.7 dB/cm afterwards.

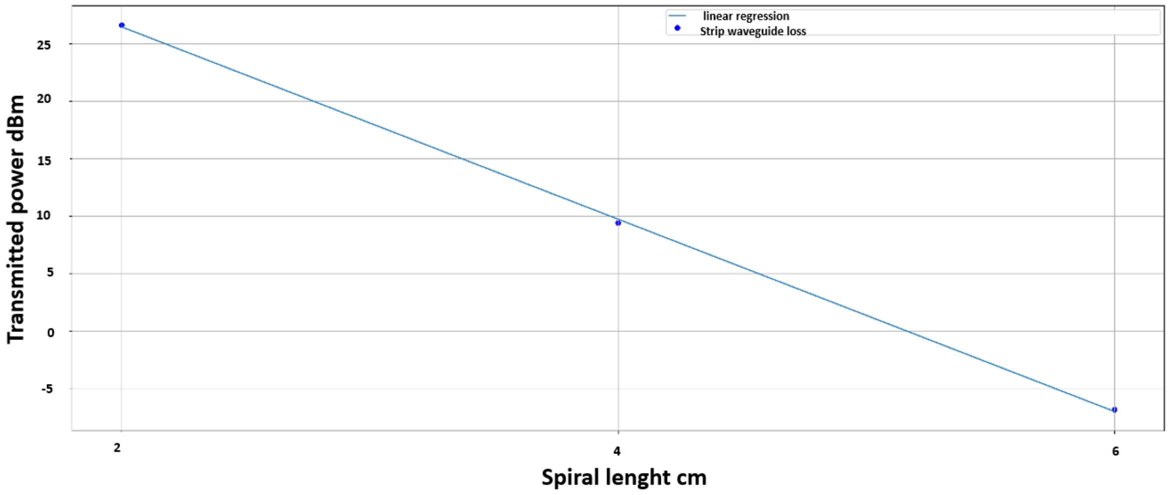

Figure 88: *Transmitted power for a given die as function of the spiral length for strip waveguides*

Die number	Waveguide losses (dB/cm)
1	-2.5
2	-2.5
3	-2.3
4	-2.3
5	-2.1
7	-2.4
8	-2.4
9	-2.5
10	-2.3

Table 15 *: Measured waveguide losses expressed in dB/cm for 9 measured dies on the wafer without the SNSPD process*

Die number	Waveguide losses (dB/cm)
2	-7.3
4	-6.1
6	-7.2
7	-6.6
8	-7.9
10	-5.3
12	-5.2
13	-9.3
17	-4.8
19	-8.9
20	-9.7

Table 16 : *Measured waveguide losses expressed in dB/cm for 11 measured dies on the wafer with the SNSPD process*

The results observed on the waveguides confirm those observed on the fiber grating couplers: the SNSPD process is responsible for an increase of the losses of the passive structures. We suspect the preclean step performed before the AlN deposition to remove the 10-20 nm of remaining oxide above the waveguides to be at the origin of the degradation of the top surface of the passive structures. This step should be investigated and optimized in future work in order to preserve the transmission properties of the passive structures. For the first generation of SNSPDs under study, the increase of the passive structure losses should have limited impact on the on-chip performances of the SNSPDs.

5.6 Conclusion

In this chapter, I have described the whole methodology and process flow for the accurate and reliable fabrication of waveguide-integrated SNPDs on a 200 mm SOI platform. The process flow requires five mask levels and about eighty technological steps. While some of them were previously developed (SOI passive structures including waveguides and fiber grating couplers, their encapsulation and hard mask removal), I focused on the development of specific steps such as nanowire lithography and patterning, as well as via opening through the encapsulation oxide. These steps were developed on separate wafer batches before being applied for the functional wafer batch embedding the SOI waveguides and passive structures. In contrast to most of the technological step developments in the clean room, these steps were particularly challenging and time-consuming, mainly due to the ultra-thin NbN thickness. Therefore, I had to use advanced characterization techniques such as AFM, FIB-SEM, TEM and STEM combined with EDX.

A first level of validation of the developed processes was obtained on dummy wafer batches, mainly through various microscopy morphological observations up to electrical test for the metallization module. After these successful results, the newly developed and optimized process steps were applied to the batch of functional wafers embedding the full waveguide-integrated SNSPD devices. Unfortunately, all along the technological developments, I experienced several equipment failures that caused considerable delays in my project, in addition to longer fabrication time in the cleanroom due to the pandemic.

However, room temperature optical and electrical characterization were conducted a few weeks after the end of my PhD by another PhD student. They show very encouraging results, offering a strong validation of the technological developments I carried out for more than one year. In particular, the waveguide-integrated NbN nanowires feature excellent electrical properties with remarkable uniformity across 200 mm wafers, indicating a very high fabrication yield. This is a significant improvement with respect to previous reports in the literature pointing to limited fabrication yield of less than 50%, mainly due to constrictions in the nanowires. Regarding optical properties, the process steps associated to nanowire fabrication seem to induce additional propagation losses of the SOI waveguides of a few dB/cm. This indicates that there is probably still some room for improvement regarding the surface preparation before AlN/NbN deposition. However, given the short length of the waveguide-integrated SNSPDs, in the range of 100 µm or less, this slight degradation of the SOI propagation losses should have limited impact on the performances of the SNSPDs. In contrast, the excellent electrical properties are very encouraging for the operation of the waveguide-integrated SNSPDs at cryogenic temperature.

Conclusion and perspectives

6.1 Conclusion

The motivation behind developing waveguide-integrated SNSPDs is to build an integrated quantum photonics platform with key components to generate, manipulate and detect single photons. In this work, we have developed high-quality polycrystalline NbN thin (5-11 nm) films on 200 mm silicon substrates thanks to the introduction of a thin (10-20 nm) AlN layer, both materials being deposited with CMOS-compatible sputtering processes. Whereas NbN directly deposited on silicon presents randomly oriented grains, NbN deposited on AlN is textured along the <111> axis, which translates into an improvement of its critical temperature up to 10 K for 9 nm thick NbN. This is important for practical applications to reduce the energy consumption, cost and footprint of cryogenic systems. In addition, we have fabricated simple fiber-coupled SNSPDs based on NbN/AlN and operating under normal incidence illumination. The SNSPDs feature a system detection efficiency of 6-8% for NbN thickness in the range of 5-9 nm, in good agreement with simulated values. These results validate the single-photon detection properties of the NbN/AlN stack.

Moreover, we performed numerical simulations to design high efficiency waveguide-integrated SNSPDs and presented two different architectures: broad-band SNSPDs integrated on straight SOI waveguide and narrow-band SNSPDs integrated in microring resonator cavities optimized for better timing accuracy. Regarding SNSPDs integrated on straight waveguide designs, their numerical absorption efficiency was investigated for various SOI waveguide and NbN nanowire dimensions. We demonstrated that with the incorporation of the AlN buffer layer used to enhance the superconducting properties of the NbN layer, high absorption could be achieved for a U-shaped SNSPD configuration with nanowires of less than 100 µm in length. Therefore, compared to the meander structure of fiber-coupled detectors operating at normal incidence, which have nanowires of several hundred micrometers length (> 200 µm), we have designed waveguide-integrated SNSPDs with much shorter nanowires. Indeed, there is a strong interest to shorten the nanowire length in order to decrease the jitter of the device and the reset time, while decreasing the detector footprint and reducing the impact of possible fabrication imperfections. A further decrease of the nanowire length was addressed by increasing the nanowire absorption efficiency by the means of a silicon ring resonator. If the incident photon is critically coupled with the cavity, such a device extends the interaction time between the SNSPD and the photon. This paves the way for highly efficient detection while keeping nanowire lengths short. Simulated detection efficiencies of up to near unity for lengths between 1 and 10 µm were obtained. In addition, we proposed a detection scheme where integrated SNSPDs are placed in series to achieve photon number resolution (PNR).

Then, we have used the NbN/AlN stack on SOI wafers to fabricate waveguide-integrated detectors and described the process flow developed to fabricate integrated SNSPDs in a 200 mm silicon photonics platform. Patterning nanowires free of constrictions over the entire wafer on one side, opening of the via while maintaining the integrity of the NbN layer on the other side, were the most challenging technological developments.

Finally, we have presented room temperature optical and electrical characterization of SNSPDs. They show very encouraging results, bringing a strong validation of the technological developments. In particular, the waveguide-integrated NbN nanowires feature excellent electrical properties with remarkable uniformity across 200 mm wafers, indicating a very high fabrication yield. This is a significant improvement with respect to previous reports in the literature pointing to limited fabrication yield of less than 50%, mainly due to constrictions in the nanowires. Regarding optical properties, the process steps associated to nanowire fabrication seem to induce additional propagation losses of the SOI waveguides of a few dB/cm. This indicates that there is probably still some room for improvement regarding the surface preparation before AlN/NbN deposition. However, given the short length of the waveguide-integrated SNSPDs, in the range of 100 µm or less, this slight degradation of the SOI propagation losses should have limited impact on the performances of the SNSPDs. In contrast, the excellent electrical properties are very encouraging for the operation of the waveguide-integrated SNSPDs at cryogenic temperature.

The results presented in this thesis have highlighted the possibility of achieving scalable and reproducible SNSPDs. We are optimistic that the properties of SNSPDs, such as critical current, on-chip detection efficiency, and temporal resolution, will match theoretical expectations and will also be reproducible from device to device.

6.2 Perspectives

6.2.1 At the individual detector level

Readout electronics

The development of custom electronics to optimally exploit the superior performance metrics of SNSPDs is of high importance, including counting electronics and low-temperature electronics for device readout, in particular, for achieving a further reduction of the timing jitter and dark count rates of these detectors and a higher maximum count rate.

Coupling efficiency to optical fibers

Waveguide-integrated SNSPDs are limited to low system detection efficiencies due to interface losses when coupling to optical fibers. Optimized fiber grating couplers in silicon still feature 2-2.5

dB coupling loss (coupling efficiency around 60%). More efficient coupling between optical fibers and waveguide-SNSPDs nanowire detectors has been achieved using a complex 3D interface produced by direct laser writing that relies on total internal reflection, reaching system detection efficiencies of up to 70% over a wide spectral range in the near-infrared [149]. Significant efforts should be further invested in finding more efficient practical 2D approaches for interfacing these detectors with optical fibers, thus allowing more efficient chip-to-chip communication.

Integration on other photonics platform

Beyond integration on SOI waveguides, the integration of SNSPDs on other photonic platforms such as silicon nitride, which is also CMOS-compatible, is of strong interest. Indeed, recent improved fabrication techniques allow obtaining extremely low surface roughness and ultra-low-loss Si_3N_4 waveguides with typically 0.05 dB/cm, one order of magnitude lower than in silicon waveguides [104]. Using this platform would also enable a wider range of detection wavelengths not provided by silicon, e.g for the compatibility with high-brightness single photon sources made of InAs quantum dots in GaAs micropillar cavities

SNSPD material with high critical temperature (longer term)

As one of the weak points for SNSPDs applications is the need for relatively low cryogenic temperatures, high critical temperature T_c superconducting materials, which can be easily integrated into photonics circuit, would allow using more compact and affordable cryogenic equipment. Copper oxides have demonstrated very high critical temperature up to 93K for YBaCuO in bulk material, but it is yet very challenging to maintain high critical temperature in thin films and to process them.

6.2.2 At multiple detector level

Photon number resolution

Photon number resolution (PNR) is an important capability required for quantum communication protocols and more generally for optical quantum computing to minimize errors. Unfortunately, this functionality is not offered by SNSPDs. Several works proposing pseudo-PNR with waveguide integrated SNSPDs consider a detection system consisting of many detectors [214–217]. In such system, the photons are distributed over N paralleled slots and are detected by end detectors, all of efficiency close to unity. In this work, we propose a detection scheme where integrated SNSPDs are in series [218] . This configuration is less demanding because it does not require all the detectors to have an efficiency close to the unit. Therefore, the unavailability of unitary efficiency detectors is of small concern.

Scalability

Building up-scaled systems with numerous individually addressed waveguide-integrated detectors can face readout issues. The demonstration of such systems would require advanced interfaces and multiplexing solutions. Recently several studies have been carried out on the engineering of microwave signal propagation in SNSPDs. In 2018, Zhu et al. [156] showed multi-photon coincidence detectors based on two-terminal devices consisting of sixteen detector elements. This was achieved through time-domain multiplexing via signal delays. However, several considerations, such as chip footprint, noise, electrical and optical crosstalk, cryostat heat loads via cabling and optical fibers, effective optical coupling, and interfaces with electronic circuits, must be considered for further large-scale deployment.

6.2.3 Integration with other key components on the same chip

Development of cryo-compatible photon manipulation on-chip

In a classical photonic integrated circuit, the photonic circuit reconfigurability is achieved through a phase shifter. However, since SNSPDs are used as single photons detectors, cryo-compatible phase shifters, offering low dissipation are required. In order to reconfigure photons at low temperatures, different materials platforms or more sophisticated devices such as photonics MEMS can be used. Lomonte et al. [227] demonstrated the first realization of single-photon detection and high-speed (up to 1 GHz) cryogenic reconfigurability in Lithium Niobate on insulator LNOI platform. They showed the combined operation of an electrically tunable Mach-Zehnder interferometer and two waveguide-integrated SNSPDs at its outputs, as represented in Figure 89. This integration paves the way for the realization of scalable photonic devices for active light manipulation and detection.

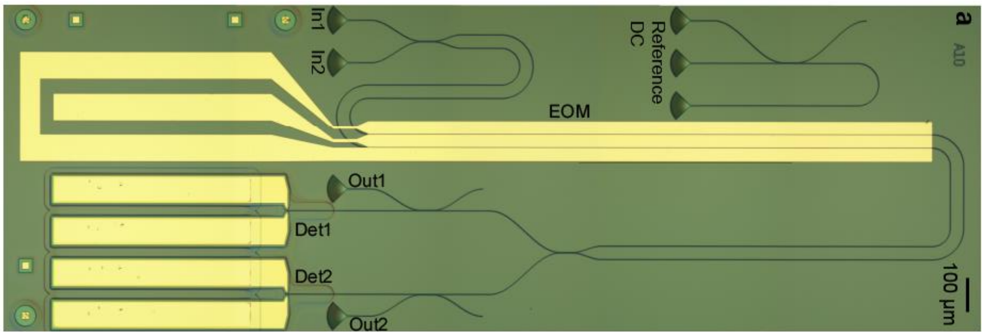

Figure 89 *: Microscope image of the integrated device employed for demonstrating the joint cryogenic operation of SNSPDs and an electro-optical modulator (EOM)[227]*

MEMS phase shifters combined with SNSPDs have been experimentally demonstrated by Gyger et al. [228] and Grottke [229]. The phase shift is induced by electrostatic displacement of mechanical structures, which results in a change in the effective refractive index. This approach is interesting; however, the devices operate in the MHz range.

Integration with single photon sources

Single photon sources are also key for quantum photonic technologies scaling. Integrated single photon sources on silicon exploiting a non-linear effect are being developed in parallel to SNSPDs in order to integrate both on the same chip. Recently, Sabattoli et al. demonstrated a high-Q micro-ring silicon resonators (loaded Q factor around 4.10^5) generating heralded single photons at MHz rate [230]. However, to improve photon generation quality, efficiency, and rates, further technological developments are required. Likewise, as these sources currently rely on off-chip optical pumping, improvement in their efficiency will facilitate the integration of precision and tunable pump lasers, filters, and control electronics on the same chip.

French summary

Absract

Ce travail vise à développer des détecteurs de photons uniques à nanofils supraconducteurs (dit SNSPDs) intégrés sur une plateforme SOI de 200 mm. Ces détecteurs constituent une brique fondamentale pour le développement de puces photoniques en silicium à grande échelle avec une efficacité de détection proche de 100% pour des applications en communication et calcul quantique. Dans cette thèse, nous étudions la conception, la fabrication et de la caractérisation à température ambiante de SNSPDs intégrés aux guides d'ondes en silicium.

Dans une première phase, nous avons développé des films minces de NbN polycristallin de haute qualité (5-11 nm) sur des substrats de silicium de 200 mm grâce à l'introduction d'une couche mince tampon (10-20 nm) d'AlN, les deux matériaux étant déposés avec des procédés de pulvérisation CMOS compatibles. Une amélioration de la température critique jusqu'à 10 K pour du NbN de 9 nm d'épaisseur a été observée avec l'introduction de la couche d'AlN. Ensuite, nous avons fabriqué des SNSPDs avec une architecture simple, en utilisant l'empilement de matériaux NbN/AlN et fonctionnant sous une illumination à incidence normale. Les SNSPDs ont présenté une efficacité de détection du système en bon accord avec les valeurs simulées, validant ainsi les propriétés de détection de photons uniques de l'empilement NbN/AlN.

Dans un deuxième temps, nous avons conçu des SNSPDs intégrés aux guides d'ondes afin d'obtenir des efficacités de détection élevées. Nous avons démontré qu'avec l'incorporation de la couche tampon AlN utilisée pour améliorer les propriétés supraconductrices de la couche NbN, une absorption élevée pouvait être obtenue pour une configuration SNSPD en forme de U de moins de 100 µm de longueur. Nous avons également montré le potentiel des SNSPDs couplés à une cavité, en particulier avec des résonateurs en anneau de silicium, pour réduire la longueur du détecteur et améliorer les propriétés temporelles. Plus précisément, nous avons démontré une efficacité de détection simulée proche de l'unité en utilisant des SNSPDs intégrés avec des nanofils d'une longueur comprise entre 1 et 10 µm. De plus, nous avons proposé un schéma de détection dans lequel les SNSPDs intégrés sont placés en série pour obtenir une résolution du nombre de photons, une caractéristique importante pour les applications du calcul quantique.

Dans une troisième phase, nous avons développé des procédés CMOS compatible pour la fabrication de SNSPDs intégrés aux guides d'ondes sur la plateforme photonique en silicium de 200 mm, en utilisant l'empilement NbN/AlN optimisé.

Enfin, nous avons effectué des caractérisations électriques et optiques à température ambiante, fournissant ainsi un premier niveau de validation des designs et des procédés développés, avec notamment une excellente uniformité de la résistance des nanofils sur les wafers SOI de 200 mm. Ces résultats sont très prometteurs pour la caractérisation des performances du détecteur en termes d'efficacité et propriétés temporelles.

Chapitre 1 : Introduction

L'information quantique avec des photons nécessite des dispositifs qui fonctionnent au niveau du photon unique, et les détecteurs de photons uniques sont un élément clé des systèmes photoniques quantiques. Parmi les différentes approches de détection de photons uniques, on trouve les détecteurs à photons uniques à nanofils supraconducteurs (SNSPDs). Ces détecteurs surpassent les autres technologies de détection de photons uniques dans le proche infrarouge (NIR) en raison de leur efficacité élevée et de leur grande précision temporelle. Leurs propriétés remarquables et leur compatibilité avec l'intégration de sources à photons uniques et d'éléments photoniques passifs font des SNSPDs d'excellents candidats pour l’intégration sur puce. En outre, la plateforme silicium offre un niveau d'intégration élevée, une grande stabilité fonctionnelle et la perspective d'une production de masse abordable, ce qui en fait une plateforme appropriée pour ce développement. Alors que des SNSPDs efficaces ont déjà été démontrés par plusieurs groupes dans le monde au niveau du dispositif unique, le passage à l'échelle des puces photoniques quantiques nécessite des procédés de fabrication à grande échelle, entièrement CMOS compatibles. Dès 2018, le CEA LETI, l'un des acteurs européens dans le domaine de la photonique intégrée sur silicium, a décidé de tirer parti de cette technologie pour développer des puces photoniques quantiques.

Dans ce contexte, l'objectif de mon doctorat était de démontrer pour la première fois des SNSPDs intégrés produits à l'aide d'un procédé entièrement compatible CMOS sur des plaquettes de 200mm. Pour atteindre cet objectif, j'ai d'abord étudié et optimisé, en collaboration avec les chercheurs du CEA-IRIG, les propriétés supraconductrices des couches minces de NbN déposées dans notre salle blanche. La qualité des propriétés quantiques de nos films a été confirmée par la fabrication et l'étude d'un SNSPD intégré à une cavité verticale. Une partie importante de mon travail a consisté à concevoir des SNSPDs intégrés aux guides d'ondes afin d'optimiser leurs performances. Plusieurs configurations de SNSPDs ont été proposées. Les dimensions des structures conçues ont été déterminées par des simulations optiques. Nous avons ainsi démontré une efficacité de détection proche de l'unité en utilisant des SNSPDs intégrés aux anneaux raisonnants. En collaboration avec les chercheurs de l'IRIG, nous avons également proposé un schéma de détection permettant d'atteindre une résolution du nombre de photons PNR. Pour la fabrication des SNSPDs intégrés aux guides d'ondes, j'ai collaboré avec les ingénieurs des procédés du LETI. Ensemble, nous avons amélioré et adapté les procédés existants et en avons développé de nouveaux pour la fabrication des SNSPDs. Après la fabrication, des caractérisations optiques et électriques préliminaires ont été réalisées à température ambiante sur les testeurs photoniques du CEA-LETI. Ces caractérisations montrent des résultats très encourageants, offrant une première validation des développements technologiques. Actuellement, Valentin Brisson, le doctorant qui a poursuivi mon projet, travaille sur des caractérisations à basse température dans les laboratoires de l'IRIG, afin de démontrer la maturité des procédés de fabrication à grande échelle qui ont été développé au cours de ce travail. Ainsi, les SNSPDs sur guides d'ondes entrent dans la boîte à outils des technologies de photonique quantique intégrée, et seront probablement utilisés dans un large éventail de domaines, englobant le calcul et les simulations quantiques photoniques et les communications quantiques.

Dans ce manuscrit, le premier chapitre vise à donner un aperçu de l'information quantique avec des photons. Le deuxième chapitre fait le point sur l'état de l'art des détecteurs de photons uniques. Puis, je donne quelques bases du phénomène de la supraconductivité. Les principaux concepts physiques sont détaillés afin d'affiner la compréhension de ce travail. Les mécanismes de détection et les caractéristiques fondamentales des détecteurs de photons uniques supraconducteurs sont ensuite décrits et développés. Ensuite, l'état de l'art des SNSPDs est discuté. Le chapitre 3 présente l'optimisation de la croissance critique d'un film ultrafin de NbN sur un substrat Nitrure d’aluminium/silicium par la technique de pulvérisation est présentée. La fabrication d'un SNSPD intégré à une cavité verticale pour valider les propriétés de détection du NbN développé est également abordée dans le chapitre 3. Les chapitres 4 et 5 sont consacrés au développement de SNSPDs CMOS compatibles intégrés aux guides d'onde photonique en silicium. Le chapitre 4 traite la conception des SNSPDs intégrés aux guides d’ondes ainsi que le jeu de masques dédié. Le design optimisé pour obtenir des SNSPDs intégrés à haute efficacité est présenté, et le potentiel des SNSPDs couplés à une cavité, en particulier avec un anneau résonnant de silicium, est également discuté. Enfin, le chapitre 5 présente la fabrication des premiers SNSPDs intégrés dans une plateforme silicium de 200 mm ainsi que les caractérisations optiques et électriques préliminaires des SNSPD à température ambiante.

Chapitre 2 : Détection de photons uniques

Les détecteurs de photons uniques sont l'un des éléments fondamentaux des systèmes photoniques quantiques. Dans ce chapitre, nous présentons l'état de l'art des détecteurs de photons uniques. Ensuite, nous donnons un aperçu de base du phénomène de la supraconductivité. Les principaux concepts physiques sont détaillés afin d'affiner la compréhension de ce travail. Les mécanismes de détection et les caractéristiques fondamentales des détecteurs de photons uniques supraconducteurs sont ensuite décrits et développés. Enfin, l'état de l'art des SNSPDs est présenté.

Du point de vue de la fabrication, les technologies à base de semiconducteurs pour la détection de photons uniques sont très avancées d'un point de vue de fabrication et les détecteurs ne nécessitent pas de températures cryogéniques pour fonctionner. Cependant, en particulier aux longueurs d'onde des télécommunications, ils présentent une faible efficacité, des coups d'obscurité élevés et de longs temps de latence. Par conséquent, ces détecteurs ne sont pas adaptés aux applications d'information quantique où ces figures de mérite sont des paramètres clés.

D'autre part, les détecteurs supraconducteurs ont également progressé rapidement au cours de la dernière décennie. Les détecteurs TES résolvent intrinsèquement le nombre de photons tout en exigeant une température de fonctionnement très basse (< 100 mK) et en étant extrêmement lents pour les applications à grande vitesse.

Les détecteurs SNSPDs, le sujet de cette thèse, sont une technologie très prometteuse grâce à leur haute efficacité, leur haut débit, leur faible gigue et leur faible taux d'obscurité. De plus, les performances exceptionnelles des SNSPDs combinées à la possibilité d'intégration sur des substrats semiconducteurs nous ont motivés à choisir les SNSPDs comme détecteur de photons uniques.

SNSPDs à cavité verticale :

Le premier dispositif a été proposé par Gol'tsman et al. en 2001 [106] et était éclairé avec une incidence normale. Il consistait en un fil droit de NbN de 1,3 µm de long, 225 nm de large et 5 nm d'épaisseur. Gol'tsman et al. [106] ont démontré que ce dispositif pouvait détecter des photons uniques dans le visible et le proche infrarouge. En plus, l'efficacité quantique du dispositif a été estimée à environ 20%.

Afin d'augmenter le couplage optique sous incidence normale, il a été rapidement proposé et mis en œuvre de plier le nanofil en un méandre pour correspondre à la taille du spot optique [59]. L'un des principaux défis du couplage normal est la courte longueur d'interaction entre la lumière et les détecteurs, qui ont généralement une épaisseur de 4 à 10 nm. Les SNSPDs sont donc intégrés dans des microcavités optiques pour augmenter la probabilité d'absorption optique en permettant au photon d'être réfléchi plusieurs fois [81].

Un exemple de cavité est constitué de deux couches ayant une différence d'indice de réfraction, généralement du silicium oxydé thermiquement sur des plaquettes de silicium. Habituellement, le détecteur se trouve au-dessus de la couche d'oxyde, qui est conçue de manière que son épaisseur soit égale à un quart de la longueur d'onde de la lumière à détecter. Un miroir en or peut être déposé sous la couche d'oxyde pour augmenter encore l'absorption. À l'aide d'une simple cavité optique telle que décrite à la Figure 18.A, Redaelli et al [122] ont montré un détecteur à base de NbTiN ayant une efficacité de détection globale de 85 % à 1310 nm. Alors que pour un détecteur à base de MoSi, un record de 98 % a été atteint à 1550 nm [108].

L'un des principaux défis du couplage normal est la longueur d'interaction courte entre la lumière et les détecteurs, qui ont généralement une épaisseur de 4 à 10 nm. Par ailleurs, le méandre doit être relativement long et dense pour obtenir une efficacité de détection élevée. Cela compromet la vitesse du détecteur et rend les dispositifs plus sensibles aux imperfections de fabrication.

D'un point de vue commercial et stratégique, les SNSPDs couplés à une cavité sont aujourd'hui produits par plusieurs entreprises. Six startups, à savoir ID Quantique (Suisse), PHOTEC (Chine), Photon Spot (États-Unis), Quantum Opus (États-Unis), SCONTEL (Russie) et Single Quantum (Pays-Bas), travaillent à la commercialisation de la technologie SNSPD ; la plus ancienne de ces sociétés est SCONTEL, fondée par Gol'tsman en 2004.

SNSPDs intégrés aux guides d’ondes :

Les progrès de la fabrication ont permis le développement de circuits intégrés photoniques compacts et à faibles pertes qui surpassent de nombreux systèmes optiques en espace libre en termes de complexité et de stabilité. Le développement d'une plateforme intégrée de photonique quantique avec des composants clés pour générer, manipuler et détecter des photons uniques est nécessaire pour le progrès de l'optique quantique. En particulier, l'intégration de détecteurs de photons uniques est une étape technologique clé qui permettra la mise en œuvre d'un large éventail de technologies classiques et quantiques.

En 2009, Hu et al. [126] ont introduit le concept de détecteurs intégrés. Deux ans plus tard, en 2011, Sprengers et al. [127] ont présenté la première réalisation expérimentale d'un détecteur photonique à nanofils supraconducteurs constitué d'un nanofil de NbN fabriqué au-dessus d'un guide d'ondes en GaAs. Pernice et al. [85] ont poursuivi en démontrant à leur tour détecteur à nanofils supraconducteurs en NbN intégré aux guides d'ondes silicium, présentant une efficacité de détection sur puce allant jusqu'à 91 % aux longueurs d'onde des télécommunications. Ils ont observé des coups d'obscurité remarquablement bas et une gigue temporelle ultra-courte de 18ps. Pour le détecteur le plus court, d'une longueur de 10 µm, ils ont mesuré un temps de reset de 455 ps. En utilisant des géométries de détecteur courtes, ils ont pu travailler dans un régime d'impulsion inférieur à la nanoseconde. Une largeur d'impulsion inférieure à la nanoseconde implique un taux de détection supérieur à 2 GHz. Dans le même groupe, Schuck et al. [128] ont démontré un SNSPD NbTiN à faible bruit intégré à un guide d'onde SiN, présentant des coups d'obscurité dans la gamme des milli-Hz.

Pour cette configuration, le SNSPD est placé au-dessus du guide d'ondes. Le champ du mode du guide d'ondes se couple de manière évanescente au nanofil supraconducteur, ce qui permet l'absorption des photons dans la direction de leur propagation. L'absorption de photons avec une efficacité proche de l'unité est obtenue avec des longueurs de quelques dizaines de micromètres [85]. Cette longueur ne correspond qu'à une fraction de la structure du méandre, dans les architectures verticales, qui est de l'ordre de plusieurs centaines de microns (>200µm) [86] pour couvrir le diamètre du champ de mode de la fibre. Comme les nanofils courts ont une inductance cinétique plus faible, ils devraient présenter des temps de restauration plus courts [101], ce qui se traduira par des taux de comptage de photons plus élevés. Bien que la diminution de la longueur du dispositif réduise l'inductance cinétique et puisse entraîner des taux de détection de GHz, cette approche affecte l'efficacité de la détection en raison de la réduction de la longueur d'interaction entre le guide d'ondes et le détecteur. Pour réduire davantage le temps de récupération et augmenter le taux de détection, des cavités photoniques ou des circuits résonnants peuvent être utilisés pour réduire la longueur du nanofil tout en conservant la même efficacité de détection. Cependant, cela se fait au détriment d'une gamme de fréquences optiques limitée [102,129,130].

Chapitre 3 : Étude des films supraconducteurs en NbN sur une plate-forme de silicium de 200 mm

Dans ce chapitre, nous établissons le module de départ nécessaire à la fabrication des SNSPDs. Pour le développement de nos SNSPDs, nous avons choisi le NbN pour ses excellentes propriétés supraconductrices, sa qualité cristalline, et le retour d'expérience sur ce matériau, car il a été le plus étudié [158-162]. Le NbN est un matériau électriquement conducteur avec un aspect métallique qui est opaque aux longueurs d'onde visibles, même à des épaisseurs de quelques dizaines de nanomètres [163].

Le nitrure de niobium (Nb_xN_y) est un matériau non stœchiométrique et polymorphe qui existe en neuf phases hexagonales ou cubiques. Seule sa phase cubique à faces centrées cfc présente d'excellentes propriétés supraconductrices, avec une température critique T_C pour le bulk comprise entre 14 et 17 K [158]. Par conséquent, NbN cfc est la phase cristallographique souhaitée en raison de ses propriétés supraconductrices.

Le NbN est un bon candidat pour les SNSPDs grâce à sa température critique relativement élevée et à ses bonnes propriétés électriques et temporelles. Cependant, le choix du substrat est crucial pour obtenir un matériau NbN de haute qualité. Le NbN est généralement déposé sur des substrats amorphes ou un paramètre de maille différent, ce qui conduit à une structure polycristalline avec une température critique dégradée et des inhomogénéités de film qui limitent le rendement de fabrication et la reproductibilité des SNSPDs. Le décalage entre le paramètre de maille du substrat et de la couche déposée doit être choisi le plus petit possible car il joue un rôle dans la déformation résiduelle du film et la structure cristalline du matériau. Afin d'améliorer la qualité cristalline du NbN, des substrats à faible mésappariement tels que le saphir, le TiN, le MgO, le SiC, le GaN ou l'AlN [164-169] ont été proposés mais ils ne sont pas tous bien adaptés à une mise en œuvre à grande échelle.

Le choix du substrat dépend également de l'intégration visée du détecteur. Selon l'application et la longueur d'onde de fonctionnement souhaitée, les propriétés optiques du substrat sont essentielles pour la conception des guides d'ondes. De plus, la maturité technologique de la plateforme choisie doit également être considérée.

Dans ce travail, nous souhaitons développer des SNSPDs qui fonctionneront à des longueurs d'onde de télécommunications. Dans ce but, nous avons choisi la plateforme en silicium de 200 mm, malgré l'important décalage de réseau avec le NbN. Afin d'obtenir un matériau supraconducteur de meilleure qualité, nous avons choisi de l'AlN comme couche tampon.

Nous avons développé des films minces (5-11 nm) de NbN polycristallin de haute qualité sur des substrats de silicium de 200 mm grâce à l'introduction d'une couche mince (10-20 nm) d'AlN, les deux matériaux étant déposés avec des procédés de pulvérisation compatibles CMOS. Alors que le NbN déposé directement sur le silicium présente des grains orientés de manière aléatoire, le NbN déposé sur l'AlN est texturé le long de l'axe <111>, ce qui se traduit par une amélioration de sa température critique jusqu'à 10 K pour du NbN de 9 nm d'épaisseur. Ceci est important pour les applications pratiques afin de réduire la consommation énergétique, le coût et l'encombrement des systèmes cryogéniques. De plus, nous avons fabriqué des SNSPDs sans cavité, utilisant l'empilement NbN/AlN et fonctionnant sous une illumination à incidence normale. Les SNSPDs présentent une efficacité de détection du système de 6-8% pour une épaisseur de NbN dans la gamme 5-9 nm, en bon accord avec les valeurs simulées. Ces résultats valident les propriétés de détection de l'empilement NbN/AlN.

Le dépôt d'un tel empilement de NbN/AlN sur des plaquettes de SOI peut en outre être utilisé pour fabriquer des détecteurs intégrés aux guides d'ondes, qui constituent un élément clé de plateforme de photonique quantique intégrée, capable de générer, de manipuler et de détecter un grand nombre de qubits photoniques pour les communications sécurisées et l'informatique quantique. Ce sujet est l'objet du chapitre 4 et 5.

Chapitre 4 : Conception des détecteurs de photons uniques intégrés aux guides d'ondes

Ce chapitre est consacré au développement de SNSPDs intégrés à un guide d'onde photonique. L'objectif final est de les combiner avec des sources de photons uniques et des composants passifs ou actifs afin de développer des circuits entièrement intégrés pour des applications quantiques. Nous visons à développer des détecteurs compatibles CMOS en tirant parti des plateformes microélectroniques et photoniques avancées pour un déploiement à grande échelle, un faible coût et une fabrication de masse des circuits intégrés photoniques quantiques.

Tout au long du chapitre 4, nous avons présenté la conception optimisée pour obtenir des SNSPDs intégrés avec des efficacités élevées.

Nous avons démontré qu'avec l'incorporation de la couche tampon d'AlN utilisée pour améliorer les propriétés supraconductrices de la couche de NbN, une absorption élevée pouvait être obtenue pour une configuration en forme de U avec des nanofils de moins de 100 µm de longueur. Par conséquent, par rapport à la structure en méandre (détecteurs à couplage vertical), qui comporte des nanofils d'une longueur de plusieurs centaines de microns (>200 µm), les SNSPD intégrés aux guides d’ondes sont conçus avec des nanofils beaucoup plus courts. Nous avons également montré le potentiel des SNSPDs couplés à une cavité, en particulier avec des anneaux résonants en silicium. Nous avons ainsi démontré une efficacité de détection proche de l'unité avec des nanofils d'une longueur comprise entre 1 et 10 µm.

De plus, nous avons proposé un schéma de détection où les SNSPD sont placés en série pour obtenir une résolution du nombre de photons. Les détecteurs de cette configuration sont numérotés de N à l'entrée du guide d'ondes à 1 à son extrémité, leurs efficacités étant $\eta_i = 1/i$. Contrairement aux schémas parallèles déjà proposés dans la littérature pour la résolution du nombre de photon unique, seul le dernier détecteur doit présenter une efficacité proche de l'unité

η_1 pour maximiser la fidélité. Par conséquent, le manque de détecteurs à efficacité proche de l'unité est peu préoccupant.

Enfin, nous avons décrit le layout, les différentes conceptions proposées, et une variété de structures de test nécessaires pour une calibration précise des performances du SNSPDs.

Le détail de la contribution du layout SNSPD est présenté à la Figure 46. Il a une taille globale de 100 mm2 (20% du maskset). Il est divisé en 6 blocs afin de prendre en compte les contraintes de packaging optique en plus des règles de design. Chaque bloc possède son propre ensemble de caractéristiques et de fonctionnalités. Il existe trois versions différentes des blocs 1, 2 et 5, selon la cartographie de la Figure 45 tandis que les blocs 3, 4 et 6 restent identiques.

Chapitre 5 : Détecteurs de photons uniques à nanofils supraconducteurs intégrés aux guides d'ondes : développement des procédés de fabrication et caractérisation préliminaire

Après la conception et le layout des SNSPDs, j'ai mené le développement des procédés de fabrication des SNSPDs intégrés aux guides d'ondes sur la plateforme photonique silicium de 200 mm du CEA-LETI. Pour ce développement, j'ai collaboré avec des ingénieurs spécialisés en lithographie, gravure, matériaux diélectriques, matériaux métalliques, polissage chimique, mécanique (CMP) et métrologie. Ensemble, nous avons amélioré et adapté les procédés existants et en avons développé de nouveaux pour la fabrication des SNSPDs. J'ai pris en charge la plupart des étapes de caractérisation morphologique et des matériaux et j'ai veillé à ce que les procédés développés soient stables et reproductibles.

Dans ce chapitre, j'ai décrit l'ensemble de la méthodologie et des procédés pour la fabrication précise et fiable de SNSPDs intégrés aux guides d'ondes dans une plateforme SOI de 200 mm. Le flow de fabrication nécessite cinq niveaux de masques et environ quatre-vingts étapes technologiques. Bien que certaines d'entre elles aient déjà été développées (structures passives SOI comprenant des guides d'ondes et des coupleurs à réseau de fibres, leur encapsulation et l'élimination des masques durs), je me suis concentré sur le développement d'étapes spécifiques telles que la lithographie et le modelage de nanofils, ainsi que l'ouverture de via à travers l'oxyde d'encapsulation.

Dans un premier temps, ces étapes ont été développées sur des lots témoins. À la différence de la plupart des développements d'étapes technologiques en salle blanche, ces étapes étaient particulièrement difficiles et longues, principalement en raison de l'épaisseur ultra-mince du NbN. J'ai donc dû utiliser des techniques de caractérisation avancées telles que l'AFM, le FIB-SEM, le TEM et le STEM combinés à l'EDX.

Un premier niveau de validation des procédés développés a été obtenu sur les lots témoins, principalement à travers diverses observations morphologiques par microscopie jusqu'au test électrique pour le module de métallisation. Après ces résultats positifs, les procédés développés et optimisés ont été appliqués au lot fonctionnel contenant les dispositifs SNSPDs intégrés aux guides d'ondes.

Les caractérisations optiques et électriques à température ambiante montrent des résultats très encourageants, offrant une forte validation des développements technologiques que j'ai menés pendant plus d'un an. En particulier, les nanofils de NbN présentent d'excellentes propriétés électriques et une uniformité remarquable sur des plaquettes de 200 mm, ce qui indique un rendement de fabrication très élevé. Il s'agit d'une amélioration significative par rapport à la littérature indiquant un rendement de fabrication limité à moins de 50 %, principalement en raison de constrictions dans les nanofils. En ce qui concerne les propriétés optiques, les étapes du procédés associées à la fabrication des nanofils semblent induire des pertes de propagation supplémentaires de quelques dB/cm dans les guides d'ondes SOI. Cela indique qu'il y a probablement encore une marge d'amélioration concernant la préparation de la surface avant le dépôt d'AlN/NbN. Cependant, étant donné la faible longueur des nanofils, de l'ordre de 100 µm ou moins, cette légère dégradation des pertes de propagation devrait avoir un impact limité sur les performances des SNSPD. En revanche, les excellentes propriétés électriques sont très encourageantes pour le fonctionnement des SNSPDs intégrés aux guides d'ondes à une température cryogénique

Conclusion :

La motivation derrière le développement de SNSPDs intégrés aux guides d'ondes est de construire une plateforme intégrée de photonique quantique avec des composants clés pour générer, manipuler et détecter des photons uniques.

Les résultats présentés dans cette thèse ont mis en évidence la possibilité de réaliser des SNSPDs à grande échelle et reproductibles. Nous sommes optimistes quant aux propriétés des SNSPDs, telles que le courant critique, l'efficacité de détection sur puce et la résolution temporelle, qui correspondront aux attentes théoriques et seront également reproductibles d'un dispositif à l'autre.

Heureusement, les performances et les fonctionnalités de cette étude passionnante peuvent encore être améliorées. Les développements importants qui pourraient améliorer les SNSPDs intégrés dans les guides d'ondes et plus largement les circuits intégrés photoniques quantiques sont également décrits dans ce manuscrit.

References

[1] Werner R F and Farrelly T 2019 Uncertainty from Heisenberg to Today *Found. Phys.* **49** 460–91

[2] Wootters W K and Zurek W H 1982 A single quantum cannot be cloned *Nature* **299** 802–3

[3] Aspect A, Grangier P and Roger G 1981 Experimental Tests of Realistic Local Theories via Bell's Theorem *Phys. Rev. Lett.* **47** 460–3

[4] Gisin N, Ribordy G, Tittel W and Zbinden H 2002 Quantum cryptography *Rev. Mod. Phys.* **74** 145–95

[5] Bennett C H and Brassard G 2014 Quantum cryptography: Public key distribution and coin tossing *Theor. Comput. Sci.* **560** 7–11

[6] Ekert A K 1991 Quantum cryptography based on Bell's theorem *Phys. Rev. Lett.* **67** 661–3

[7] Bennett C H, Brassard G and Mermin N D 1992 Quantum cryptography without Bell's theorem *Phys. Rev. Lett.* **68** 557–9

[8] Gottesman D, Lo H-K, Lütkenhaus N and Preskill J 2004 Security of quantum key distribution with imperfect devices *ArXivquant-Ph0212066*

[9] Chau H F 2002 Practical scheme to share a secret key through a quantum channel with a 27.6% bit error rate *Phys. Rev. A* **66** 060302

[10] You L 2020 Superconducting nanowire single-photon detectors for quantum information *Nanophotonics* **9** 2673–92

[11] Scheidl T, Ursin R, Fedrizzi A, Ramelow S, Ma X-S, Herbst T, Prevedel R, Ratschbacher L, Kofler J, Jennewein T and Zeilinger A 2009 Feasibility of 300 km Quantum Key Distribution with Entangled States *New J. Phys.* **11** 085002

[12] Avesani M, Calderaro L, Schiavon M, Stanco A, Agnesi C, Santamato A, Zahidy M, Scriminich A, Foletto G, Contestabile G, Chiesa M, Rotta D, Artiglia M, Montanaro A, Romagnoli M, Sorianello V, Vedovato F, Vallone G and Villoresi P 2021 Full daylight quantum-key-distribution at 1550 nm enabled by integrated silicon photonics *Npj Quantum Inf.* **7** 93

[13] Bennett C H, Bessette F, Brassard G, Salvail L and Smolin J 1992 Experimental quantum cryptography *J. Cryptol.* **5** 3–28

[14] Breguet J, Muller A and Gisin N 1994 Quantum Cryptography with Polarized Photons in Optical Fibres: Experiment and Practical Limits *J. Mod. Opt.* **41** 2405–12

[15] Muller A, Zbinden H and Gisin N 1996 Quantum cryptography over 23 km in installed under-lake telecom fibre *Europhys. Lett. EPL* **33** 335–40

[16] Chen J-P, Zhang C, Liu Y, Jiang C, Zhang W, Hu X-L, Guan J-Y, Yu Z-W, Xu H, Lin J, Li M-J, Chen H, Li H, You L, Wang Z, Wang X-B, Zhang Q and Pan J-W 2020 Sending-or-Not-Sending with Independent Lasers: Secure Twin-Field Quantum Key Distribution over 509 km *Phys. Rev. Lett.* **124** 070501

[17] Chen Y-A, Zhang Q, Chen T-Y, Cai W-Q, Liao S-K, Zhang J, Chen K, Yin J, Ren J-G, Chen Z, Han S-L, Yu Q, Liang K, Zhou F, Yuan X, Zhao M-S, Wang T-Y, Jiang X, Zhang L, Liu W-Y, Li Y, Shen Q, Cao Y, Lu C-Y, Shu R, Wang J-Y, Li L, Liu N-L, Xu F, Wang X-B, Peng C-Z and Pan J-W 2021 An integrated space-to-ground quantum communication network over 4,600 kilometres *Nature* **589** 214–9

[18] Anon Home *ID Quantique*

[19] Martinis J M, Boixo S, Neven H, Arute F, Arya K, Babbush R, Bacon D, Bardin J C, Barends R, Biswas R, Brandao F G S L, Buell D A, Burkett B, Chen Y, Chen Z, Chiaro B, Collins R, Courtney W, Dunsworth A, Farhi E, Foxen B, Fowler A, Gidney C, Giustina M, Graff R, Guerin K, Habegger S, Harrigan M P, Hartmann M J, Ho A, Hoffmann M, Huang T, Humble T S, Isakov S V, Jeffrey E, Jiang Z, Kafri D, Kechedzhi K, Kelly J, Klimov P V, Knysh S, Korotkov A, Kostritsa F, Landhuis D, Lindmark M, Lucero E, Lyakh D, Mandrà S, McClean J R, McEwen M, Megrant A, Mi X, Michielsen K, Mohseni M, Mutus J, Naaman O, Neeley M, Neill C, Niu M Y, Ostby E, Petukhov A, Platt J C, Quintana C, Rieffel E G, Roushan P, Rubin N C, Sank D, Satzinger K J, Smelyanskiy V, Sung K J, Trevithick M D, Vainsencher A, Villalonga B, White T, Yao Z J, Yeh P and Zalcman A 2019 Quantum supremacy using a programmable superconducting processor

[20] Zhang E J, Srinivasan S, Sundaresan N, Bogorin D F, Martin Y, Hertzberg J B, Timmerwilke J, Pritchett E J, Yau J-B, Wang C, Landers W, Lewandowski E P, Narasgond A, Rosenblatt S, Keefe G A, Lauer I, Rothwell M B, McClure D T, Dial O E, Orcutt J S, Brink M and Chow J M 2020 High-fidelity superconducting quantum processors via laser-annealing of transmon qubits *ArXiv201208475 Quant-Ph*

[21] Zhong H-S, Wang H, Deng Y-H, Chen M-C, Peng L-C, Luo Y-H, Qin J, Wu D, Ding X, Hu Y, Hu P, Yang X-Y, Zhang W-J, Li H, Li Y, Jiang X, Gan L, Yang G, You L, Wang Z, Li L, Liu N-L, Lu C-Y and Pan J-W 2020 Quantum computational advantage using photons *Science* **370** 1460–3

[22] Aaronson S and Arkhipov A 2010 The Computational Complexity of Linear Optics *ArXiv10113245 Quant-Ph*

[23] Xia H, Shentu G, Shangguan M, Xia X, Jia X, Wang C, Zhang J, Pelc J S, Fejer M M, Zhang Q, Dou X and Pan J-W 2015 Long-range micro-pulse aerosol lidar at 15 µm with an upconversion single-photon detector *Opt. Lett.* **40** 1579

[24] Yu C, Shangguan M, Xia H, Zhang J, Dou X and Pan J-W 2017 Fully integrated free-running InGaAs/InP single-photon detector for accurate lidar applications *Opt. Express* **25** 14611

[25] Tsang J C, Kash J A and Vallett D P 2000 Picosecond imaging circuit analysis *IBM J. Res. Dev.* **44** 583–603

[26] Song P, Stellari F, Eckhardt J P, McNamara T and Tong C-L 2004 Timing Analysis of a Microprocessor PLL Using High Quantum Efficiency Superconducting Single Photon Detector (SSPD) (Worcester, Massachusetts, USA) pp 197–202

[27] Rezus Y L A, Walt S G, Lettow R, Renn A, Zumofen G, Götzinger S and Sandoghdar V 2012 Single-Photon Spectroscopy of a Single Molecule *Phys. Rev. Lett.* **108** 093601

[28] Li L and Davis L M 1993 Single photon avalanche diode for single molecule detection *Rev. Sci. Instrum.* **64** 1524–9

[29] Becker W, Bergmann A, Hink M A, König K, Benndorf K and Biskup C 2004 Fluorescence lifetime imaging by time-correlated single-photon counting: Fluorescence Lifetime Imaging by TCPSC *Microsc. Res. Tech.* **63** 58–66

[30] Homulle H A R, Powolny F, Stegehuis P L, Dijkstra J, Li D-U, Homicsko K, Rimoldi D, Muehlethaler K, Prior J O, Sinisi R, Dubikovskaya E, Charbon E and Bruschini C 2016 Compact solid-state CMOS single-photon detector array for in vivo NIR fluorescence lifetime oncology measurements *Biomed. Opt. Express* **7** 1797

[31] Puszka A, Di Sieno L, Dalla Mora A, Pifferi A, Contini D, Boso G, Tosi A, Hervé L, Planat-Chrétien A, Koenig A and Dinten J-M 2013 Time-resolved diffuse optical tomography using fast-gated single-photon avalanche diodes *Biomed. Opt. Express* **4** 1351

[32] Matthews J C, Zhou X-Q, Cable H, Shadbolt P J, Saunders D J, Durkin G A, Pryde G J and O'Brien J L 2016 Towards practical quantum metrology with photon counting *Npj Quantum Inf.* **2** 16023

[33] von Helversen M, Böhm J, Schmidt M, Gschrey M, Schulze J-H, Strittmatter A, Rodt S, Beyer J, Heindel T and Reitzenstein S 2019 Quantum metrology of solid-state single-photon sources using photon-number-resolving detectors *New J. Phys.* **21** 035007

[34] Wang J, Paesani S, Ding Y, Santagati R, Skrzypczyk P, Salavrakos A, Tura J, Augusiak R, Mančinska L, Bacco D, Bonneau D, Silverstone J W, Gong Q, Acín A, Rottwitt K, Oxenløwe L K, O'Brien J L, Laing A and Thompson M G 2018 Multidimensional quantum entanglement with large-scale integrated optics *Science* **360** 285–91

[35] Knill E, Laflamme R and Milburn G J 2001 A scheme for efficient quantum computation with linear optics *Nature* **409** 46–52

[36] Anon THORLABS Photomultiplier (PMTs)

[37] HAMAMATSU Photomultiplier Tubes: Basic and applications

[38] Melchior H, Goetzberger A, Nicollian E H and Lynch W T 1969 Electrical suppression of avalanche currents in semiconductor junctions *Solid-State Electron.* **12** 449–62

[39] Haecker W, Groezinger O and Pilkuhn M H 1971 Infrared Photon Counting by Ge Avalanche Diodes *Appl. Phys. Lett.* **19** 113–5

[40] Zang K, Jiang X, Huo Y, Ding X, Morea M, Chen X, Lu C-Y, Ma J, Zhou M, Xia Z, Yu Z, Kamins T I, Zhang Q and Harris J S 2017 Silicon single-photon avalanche diodes with nano-structured light trapping *Nat. Commun.* **8** 628

[41] Kittel C 1986 *Introduction to Solid State Physics*

[42] Lacaita A, Zappa F, Cova S and Lovati P 1996 Single-photon detection beyond 1 µm: performance of commercially available InGaAs/InP detectors *Appl. Opt.* **35** 2986

[43] Zhou M, Wang W, Qu H, Han H, Zhu Y, Guo Z, Gui L, Wang X and Lu W 2020 InGaAsP/InP single photon avalanche diodes with ultra-high photon detection efficiency *Opt. Quantum Electron.* **52** 299

[44] Hiskett P A, Buller G S, Loudon A Y, Smith J M, Gontijo I, Walker A C, Townsend P D and Robertson M J 2000 Performance and design of InGaAs/InP photodiodes for single-photon counting at 155 µm *Appl. Opt.* **39** 6818

[45] Carroll M S, Childs K, Jarecki R, Bauer T and Saiz K 2008 Ge–Si separate absorption and multiplication avalanche photodiode for Geiger mode single photon detection *Appl. Phys. Lett.* **93** 183511

[46] Rothman J, Pes S, Bleuet P, Abergel J, Gout S, Nicolas J-A, Rostaing J-P, Renet S, Mathieu L and Le Perchec J 2020 Meso-photonic Detection with HgCdTe APDs at High Count Rates *J. Electron. Mater.* **49** 6881–92

[47] Sun X, Abshire J B, Krainak M A, Lu W, Beck J D, Sullivan W W, Mitra P, Rawlings D M, Fields R A, Hinkley D A and Hirasuna B S 2019 HgCdTe avalanche photodiode array detectors with single photon sensitivity and integrated detector cooler assemblies for space lidar applications *Opt. Eng.* **58** 1

[48] Singh A, Srivastav V and Pal R 2011 HgCdTe avalanche photodiodes: A review *Opt. Laser Technol.* **43** 1358–70

[49] Lita A E, Miller A J and Nam S W 2008 Counting near-infrared single-photons with 95% efficiency *Opt. Express* **16** 3032

[50] Fukuda D, Fujii G, Numata T, Yoshizawa A, Tsuchida H, Fujino H, Ishii H, Itatani T, Inoue S and Zama T 2009 Photon number resolving detection with high speed and high quantum efficiency *Metrologia* **46** S288–92

[51] Snider E, Dasenbrock-Gammon N, McBride R, Debessai M, Vindana H, Vencatasamy K, Lawler K V, Salamat A and Dias R P 2020 Publisher Correction: Room-temperature superconductivity in a carbonaceous sulfur hydride *Nature* **588** E18–E18

[52] Bardeen J, Cooper L N and Schrieffer J R 1957 Theory of Superconductivity *Phys. Rev.* **108** 1175–204

[53] Hazra D, Tsavdaris N, Jebari S, Grimm A, Blanchet F, Mercier F, Blanquet E, Chapelier C and Hofheinz M 2016 Superconducting properties of very high quality NbN thin films grown by high temperature chemical vapor deposition *Supercond. Sci. Technol.* **29** 105011

[54] Guo Y, Zhang Y-F, Bao X-Y, Han T-Z, Tang Z, Zhang L-X, Zhu W-G, Wang E G, Niu Q, Qiu Z Q, Jia J-F, Zhao Z-X and Xue Q-K 2004 Superconductivity Modulated by Quantum Size Effects *Science* **306** 1915–7

[55] Anon About BCS-Theory

[56] Ginzburg V L and Landau L D 2009 On the Theory of Superconductivity *On Superconductivity and Superfluidity* (Berlin, Heidelberg: Springer Berlin Heidelberg) pp 113–37

[57] Dew-Hughes D 1975 Superconducting A-15 compounds: A review *Cryogenics* **15** 435–54

[58] Cava R J 1990 Superconductors Beyond 1-2-3 *Sci. Am.* **263** 42–9

[59] Cava R J 2000 Oxide Superconductors *J. Am. Ceram. Soc.* **83** 5–28

[60] Chockalingam S P, Chand M, Jesudasan J, Tripathi V and Raychaudhuri P 2008 Superconducting properties and Hall effect of epitaxial NbN thin films *Phys. Rev. B* **77** 214503

[61] Oates D E, Anderson A C, Chin C C, Derov J S, Dresselhaus G and Dresselhaus M S 1991 Surface-impedance measurements of superconducting NbN films *Phys. Rev. B* **43** 7655–63

[62] Gurevich A 2015 Maximum screening fields of superconducting multilayer structures *AIP Adv.* **5** 017112

[63] Nikolić P and Sachdev S 2006 Effective action for vortex dynamics in clean d -wave superconductors *Phys. Rev. B* **73** 134511

[64] Renema J J, Gaudio R, Wang Q, Zhou Z, Gaggero A, Mattioli F, Leoni R, Sahin D, de Dood M J A, Fiore A and van Exter M P 2014 Experimental Test of Theories of the Detection Mechanism in a Nanowire Superconducting Single Photon Detector *Phys. Rev. Lett.* **112** 117604

[65] Maxwell E 1950 Isotope Effect in the Superconductivity of Mercury *Phys. Rev.* **78** 477–477

[66] Matthias B T 1953 Transition Temperatures of Superconductors *Phys. Rev.* **92** 874–6

[67] Gomersall I R and Gyorffy B L 1973 On the connection between high superconducting transition temperature, T_c, and lattice instability in transition metal compounds: NbN *J. Phys. F Met. Phys.* **3** L138–44

[68] Holzman I and Ivry Y 2019 Superconducting Nanowires for Single-Photon Detection: Progress, Challenges, and Opportunities *Adv. Quantum Technol.* 1800058

[69] Gol'tsman G N, Korneev A, Rubtsova I, Milostnaya I, Chulkova G, Minaeva O, Smirnov K, Voronov B, S?ysz W, Pearlman A, Verevkin A and Sobolewski R 2005 Ultrafast superconducting single-photon detectors for near-infrared-wavelength quantum communications *Phys. Status Solidi C* **2** 1480–8

[70] Esmaeil Zadeh I, Los J W N, Gourgues R B M, Steinmetz V, Bulgarini G, Dobrovolskiy S M, Zwiller V and Dorenbos S N 2017 Single-photon detectors combining high efficiency, high detection rates, and ultra-high timing resolution *APL Photonics* **2** 111301

[71] Il'in K S, Milostnaya I I, Verevkin A A, Gol'tsman G N, Gershenzon E M and Sobolewski R 1998 Ultimate quantum efficiency of a superconducting hot-electron photodetector *Appl. Phys. Lett.* **73** 3938–40

[72] Kadin A M and Johnson M W 1996 Nonequilibrium photon-induced hotspot: A new mechanism for photodetection in ultrathin metallic films *Appl. Phys. Lett.* **69** 3938–40

[73] Semenov A D, Gol'tsman G N and Korneev A A 2001 Quantum detection by current carrying superconducting film *Phys. C Supercond.* **351** 349–56

[74] Semenov A, Engel A, Hübers H-W, Il'in K and Siegel M 2005 Spectral cut-off in the efficiency of the resistive state formation caused by absorption of a single-photon in current-carrying superconducting nano-strips *Eur. Phys. J. B* **47** 495–501

[75] Bulgadaev S A 1999 Berezinskii-Kosterlitz-Thouless phase transitions in two-dimensional systems with internal symmetries *J. Exp. Theor. Phys.* **89** 1107–13

[76] Halperin B I and Nelson D R 1979 Resistive transition in superconducting films *J. Low Temp. Phys.* **36** 599–616

[77] Bulaevskii L N, Graf M J, Batista C D and Kogan V G 2011 Vortex-induced dissipation in narrow current-biased thin-film superconducting strips *Phys. Rev. B* **83** 144526

[78] Zotova A N and Vodolazov D Y 2012 Photon detection by current-carrying superconducting film: A time-dependent Ginzburg-Landau approach *Phys. Rev. B* **85** 024509

[79] Engel A, Renema J J, Il'in K and Semenov A 2015 Detection mechanism of superconducting nanowire single-photon detectors *Supercond. Sci. Technol.* **28** 114003

[80] Guo Q, Li H, You L, Zhang W, Zhang L, Wang Z, Xie X and Qi M 2015 Single photon detector with high polarization sensitivity *Sci. Rep.* **5** 9616

[81] Rosfjord K M, Yang J K W, Dauler E A, Kerman A J, Anant V, Voronov B M, Gol'tsman G N and Berggren K K 2006 Nanowire single-photon detector with an integrated optical cavity and anti-reflection coating *Opt. Express* **14** 527

[82] Verevkin A, Zhang J, Sobolewski R, Lipatov A, Okunev O, Chulkova G, Korneev A, Smirnov K, Gol'tsman G N and Semenov A 2002 Detection efficiency of large-active-area NbN single-photon superconducting detectors in the ultraviolet to near-infrared range *Appl. Phys. Lett.* **80** 4687–9

[83] Gol'tsman G N, Smirnov K, Kouminov P, Voronov B, Kaurova N, Drakinsky V, Zhang J, Verevkin A and Sobolewski R 2003 Fabrication of nanostructured superconducting single-photon detectors *IEEE Trans. Appiled Supercond.* **13** 192–5

[84] Miki S, Fujiwara M, Sasaki M, Baek B, Miller A J, Hadfield R H, Nam S W and Wang Z 2008 Large sensitive-area NbN nanowire superconducting single-photon detectors fabricated on single-crystal MgO substrates *Appl. Phys. Lett.* **92** 061116

[85] Pernice W H P, Schuck C, Minaeva O, Li M, Goltsman G N, Sergienko A V and Tang H X 2012 High-speed and high-efficiency travelling wave single-photon detectors embedded in nanophotonic circuits *Nat. Commun.* **3** 1325

[86] Marsili F, Verma V B, Stern J A, Harrington S, Lita A E, Gerrits T, Vayshenker I, Baek B, Shaw M D, Mirin R P and Nam S W 2013 Detecting single infrared photons with 93% system efficiency *Nat. Photonics* **7** 210–4

[87] Smirnov K, Divochiy A, Vakhtomin Y, Morozov P, Zolotov P, Antipov A and Seleznev V 2018 NbN single-photon detectors with saturated dependence of quantum efficiency *Supercond. Sci. Technol.* **31** 035011

[88] Ferrari S, Schuck C and Pernice W 2018 Waveguide-integrated superconducting nanowire single-photon detectors *Nanophotonics* **7** 1725–58

[89] Engel A and Schilling A 2013 Numerical analysis of detection-mechanism models of superconducting nanowire single-photon detector *J. Appl. Phys.* **114** 214501

[90] Brassard G, Lütkenhaus N, Mor T and Sanders B C 2000 Limitations on Practical Quantum Cryptography *Phys. Rev. Lett.* **85** 1330–3

[91] Lütkenhaus N and Jahma M 2002 Quantum key distribution with realistic states: photon-number statistics in the photon-number splitting attack *New J. Phys.* **4** 44–44

[92] Dušek M, Haderka O and Hendrych M 1999 Generalized beam-splitting attack in quantum cryptography with dim coherent states *Opt. Commun.* **169** 103–8

[93] Shibata H, Shimizu K, Takesue H and Tokura Y 2015 Ultimate low system dark-count rate for superconducting nanowire single-photon detector *Opt. Lett.* **40** 3428

[94] Calandri N, Zhao Q-Y, Zhu D, Dane A and Berggren K K 2016 Superconducting nanowire detector jitter limited by detector geometry *Appl. Phys. Lett.* **109** 152601

[95] Wu H, Gu C, Cheng Y and Hu X 2017 Vortex-crossing-induced timing jitter of superconducting nanowire single-photon detectors *Appl. Phys. Lett.* **111** 062603

[96] Cheng Y, Gu C and Hu X 2017 Inhomogeneity-induced timing jitter of superconducting nanowire single-photon detectors *Appl. Phys. Lett.* **111** 062604

[97] Zhao Q, Zhang L, Jia T, Kang L, Xu W, Chen J and Wu P 2011 Intrinsic timing jitter of superconducting nanowire single-photon detectors *Appl. Phys. B* **104** 673–8

[98] Korzh B, Zhao Q-Y, Allmaras J P, Frasca S, Autry T M, Bersin E A, Beyer A D, Briggs R M, Bumble B, Colangelo M, Crouch G M, Dane A E, Gerrits T, Lita A E, Marsili F, Moody G, Peña C, Ramirez E, Rezac J D, Sinclair N, Stevens M J, Velasco A E, Verma V B, Wollman E E, Xie S, Zhu D, Hale P D, Spiropulu M, Silverman K L, Mirin R P, Nam S W, Kozorezov A G, Shaw M D and Berggren K K 2020 Demonstration of sub-3 ps temporal resolution with a superconducting nanowire single-photon detector *Nat. Photonics* **14** 250–5

[99] Korzh B, Zhao Q-Y, Frasca S, Zhu D, Ramirez E, Bersin E, Colangelo M, Dane A E, Beyer A D, Allmaras J, Wollman E E, Berggren K K and Shaw M D 2018 WSi superconducting nanowire single photon detector with a temporal resolution below 5 ps *Conference on Lasers and Electro-Optics* (San Jose, California: OSA) p FW3F.3

[100] Annunziata A J, Quaranta O, Santavicca D F, Casaburi A, Frunzio L, Ejrnaes M, Rooks M J, Cristiano R, Pagano S, Frydman A and Prober D E 2010 Reset dynamics and latching in niobium superconducting nanowire single-photon detectors *J. Appl. Phys.* **108** 084507

[101] Kerman A J, Dauler E A, Keicher W E, Yang J K W, Berggren K K, Gol'tsman G and Voronov B 2006 Kinetic-inductance-limited reset time of superconducting nanowire photon counters *Appl. Phys. Lett.* **88** 111116

[102] Vetter A, Ferrari S, Rath P, Alaee R, Kahl O, Kovalyuk V, Diewald S, Goltsman G N, Korneev A, Rockstuhl C and Pernice W H P 2016 Cavity-Enhanced and Ultrafast Superconducting Single-Photon Detectors *Nano Lett.* **16** 7085–92

[103] Ejrnaes M, Cristiano R, Quaranta O, Pagano S, Gaggero A, Mattioli F, Leoni R, Voronov B and Gol'tsman G 2007 A cascade switching superconducting single photon detector *Appl. Phys. Lett.* **91** 262509

[104] Zhang C, Zhang W, Huang J, You L, Li H, lv C, Sugihara T, Watanabe M, Zhou H, Wang Z and Xie X 2019 NbN superconducting nanowire single-photon detector with an active area of 300 µm-in-diameter *AIP Adv.* **9** 075214

[105] Cheng R, Poot M, Guo X, Fan L and Tang H X 2017 Large-Area Superconducting Nanowire Single-Photon Detector With Double-Stage Avalanche Structure *IEEE Trans. Appl. Supercond.* **27** 1–5

[106] Gol'tsman G N, Okunev O, Chulkova G, Lipatov A, Semenov A, Smirnov K, Voronov B, Dzardanov A, Williams C and Sobolewski R 2001 Picosecond superconducting single-photon optical detector *Appl. Phys. Lett.* **79** 705–7

[107] Miki S, Yabuno M, Yamashita T and Terai H 2017 Stable, high-performance operation of a fiber-coupled superconducting nanowire avalanche photon detector *Opt. Express* **25** 6796

[108] Reddy D V, Nerem R R, Nam S W, Mirin R P and Verma V B 2020 Superconducting nanowire single-photon detectors with 98% system detection efficiency at 1550 nm *Optica* **7** 1649

[109] Zhang W, You L, Li H, Huang J, Lv C, Zhang L, Liu X, Wu J, Wang Z and Xie X 2017 NbN superconducting nanowire single photon detector with efficiency over 90% at 1550 nm wavelength operational at compact cryocooler temperature *Sci. China Phys. Mech. Astron.* **60** 120314

[110] Hu P, Li H, You L, Wang H, Xiao Y, Huang J, Yang X, Zhang W, Wang Z and Xie X 2020 Detecting single infrared photons toward optimal system detection efficiency *Opt. Express* **28** 36884

[111] Chang J, Los J W N, Tenorio-Pearl J O, Noordzij N, Gourgues R, Guardiani A, Zichi J R, Pereira S F, Urbach H P, Zwiller V, Dorenbos S N and Esmaeil Zadeh I 2021 Detecting telecom single photons with 99.5−2.07+0.5% system detection efficiency and high time resolution *APL Photonics* **6** 036114

[112] Korneeva Y P, Mikhailov M Y, Pershin Y P, Manova N N, Divochiy A V, Vakhtomin Y B, Korneev A A, Smirnov K V, Sivakov A G, Devizenko A Y and Goltsman G N 2014 Superconducting single-photon detector made of MoSi film *Supercond. Sci. Technol.* **27** 095012

[113] Caloz M, Perrenoud M, Autebert C, Korzh B, Weiss M, Schönenberger C, Warburton R J, Zbinden H and Bussières F 2018 High-detection efficiency and low-timing jitter with amorphous superconducting nanowire single-photon detectors *Appl. Phys. Lett.* **112** 061103

[114] Amari P, Feuillet-Palma C, Jouan A, Couëdo F, Bourlet N, Géron E, Malnou M, Méchin L, Sharafiev A, Lesueur J and Bergeal N 2018 High-temperature superconducting nano-meanders made by ion irradiation *Supercond. Sci. Technol.* **31** 015019

[115] Arpaia R, Ejrnaes M, Parlato L, Tafuri F, Cristiano R, Golubev D, Sobolewski R, Bauch T, Lombardi F and Pepe G P 2015 High-temperature superconducting nanowires for photon detection *Phys. C Supercond. Its Appl.* **509** 16–21

[116] Santavicca D F 2018 Prospects for faster, higher-temperature superconducting nanowire single-photon detectors *Supercond. Sci. Technol.* **31** 040502

[117] Curtz N, Koller E, Zbinden H, Decroux M, Antognazza L, Fischer Ø and Gisin N 2010 Patterning of ultrathin YBCO nanowires using a new focused-ion-beam process *Supercond. Sci. Technol.* **23** 045015

[118] Xing X, Balasubramanian K, Bouscher S, Zohar O, Nitzav Y, Kanigel A and Hayat A 2020 Photoresponse above 85 K of selective epitaxy grown high-T $_c$ superconducting microwires *Appl. Phys. Lett.* **117** 032602

[119] Lyatti M, Savenko A and Poppe U 2016 Ultra-thin YBa $_2$ Cu $_3$ O $_{7-x}$ films with high critical current density *Supercond. Sci. Technol.* **29** 065017

[120] Ejrnaes M, Parlato L, Arpaia R, Bauch T, Lombardi F, Cristiano R, Tafuri F and Pepe G P 2017 Observation of dark pulses in 10 nm thick YBCO nanostrips presenting hysteretic current voltage characteristics *Supercond. Sci. Technol.* **30** 12LT02

[121] Mukhtarova A, Redaelli L, Hazra D, Machhadani H, Lequien S, Hofheinz M, Thomassin J-L, Gustavo F, Zichi J, Zwiller V, Monroy E and Gérard J-M 2018 Polarization-insensitive fiber-coupled superconducting-nanowire single photon detector using a high-index dielectric capping layer *Opt. Express* **26** 17697

[122] Redaelli L, Bulgarini G, Dobrovolskiy S, Dorenbos S N, Zwiller V, Monroy E and Gérard J M 2016 Design of broadband high-efficiency superconducting-nanowire single photon detectors *Supercond. Sci. Technol.* **29** 065016

[123] Miller A J, Lita A E, Calkins B, Vayshenker I, Gruber S M and Nam S W 2011 Compact cryogenic self-aligning fiber-to-detector coupling with losses below one percent *Opt. Express* **19** 9102

[124] Redaelli L, Zwiller V, Monroy E and Gérard J M 2017 Design of polarization-insensitive superconducting single photon detectors with high-index dielectrics *Supercond. Sci. Technol.* **30** 035005

[125] Mukhtarova A, Redaelli L, Hazra D, Machhadani H, Lequien S, Hofheinz M, Thomassin J-L, Gustavo F, Zichi J, Zwiller V, Monroy E and Gérard J-M 2018 Polarization-insensitive fiber-coupled superconducting-nanowire single photon detector using a high-index dielectric capping layer *Opt. Express* **26** 17697

[126] Xiaolong Hu, Holzwarth C W, Masciarelli D, Dauler E A and Berggren K K 2009 Efficiently Coupling Light to Superconducting Nanowire Single-Photon Detectors *IEEE Trans. Appl. Supercond.* **19** 336–40

[127] Sprengers J P, Gaggero A, Sahin D, Jahanmirinejad S, Frucci G, Mattioli F, Leoni R, Beetz J, Lermer M, Kamp M, Höfling S, Sanjines R and Fiore A 2011 Waveguide superconducting single-photon detectors for integrated quantum photonic circuits *Appl. Phys. Lett.* **99** 181110

[128] Schuck C, Pernice W H P and Tang H X 2013 Waveguide integrated low noise NbTiN nanowire single-photon detectors with milli-Hz dark count rate *Sci. Rep.* **3** 1893

[129] Tyler N A, Barreto J, Villarreal-Garcia G E, Bonneau D, Sahin D, O’Brien J L and Thompson M G 2016 Modelling superconducting nanowire single photon detectors in a waveguide cavity *Opt. Express* **24** 8797

[130] Akhlaghi M K, Schelew E and Young J F 2015 Waveguide integrated superconducting single-photon detectors implemented as near-perfect absorbers of coherent radiation *Nat. Commun.* **6** 8233

[131] Shibata H, Hiraki T, Tsuchizawa T, Yamada K, Tokura Y and Matsuo S 2019 A waveguide-integrated superconducting nanowire single-photon detector with a spot-size converter on a Si photonics platform *Supercond. Sci. Technol.* **32** 034001

[132] Li Y, Tao L, Zhao Y, Huang H, She X, Liao H, Zhu J, Zhu Z, Huang R, Liu X and Gan F 2021 Design of Fabrication-Tolerant and Compact Waveguide Superconducting Single-Photon Detector Based on TM $_0$ Mode Absorption *IEEE Photonics J.* **13** 1–9

[133] Kahl O, Ferrari S, Kovalyuk V, Goltsman G N, Korneev A and Pernice W H P 2015 Waveguide integrated superconducting single-photon detectors with high internal quantum efficiency at telecom wavelengths *Sci. Rep.* **5** 10941

[134] Kovalyuk V, Hartmann W, Kahl O, Kaurova N, Korneev A, Goltsman G and Pernice W H P 2013 Absorption engineering of NbN nanowires deposited on silicon nitride nanophotonic circuits *Opt. Express* **21** 22683

[135] Lobanov Y, Shcherbatenko M, Semenov A, Kovalyuk V, Kahl O, Ferrari S, Korneev A, Ozhegov R, Kaurova N, Voronov B M, Pernice W H P and Gol’tsman G N 2017 Superconducting Nanowire Single Photon Detector for Coherent Detection of Weak Signals *IEEE Trans. Appl. Supercond.* **27** 1–5

[136] Sahin D, Gaggero A, Zhou Z, Jahanmirinejad S, Mattioli F, Leoni R, Beetz J, Lermer M, Kamp M, Höfling S and Fiore A 2013 Waveguide photon-number-resolving detectors for quantum photonic integrated circuits *Appl. Phys. Lett.* **103** 111116

[137] Sprengers J P, Gaggero A, Sahin D, Jahanmirinejad S, Frucci G, Mattioli F, Leoni R, Beetz J, Lermer M, Kamp M, Höfling S, Sanjines R and Fiore A 2011 Waveguide superconducting single-photon detectors for integrated quantum photonic circuits *Appl. Phys. Lett.* **99** 181110

[138] Sayem A A, Cheng R, Wang S and Tang H X 2020 Lithium-niobate-on-insulator waveguide-integrated superconducting nanowire single-photon detectors *Appl. Phys. Lett.* **116** 151102

[139] Lomonte E, Wolff M A, Beutel F, Ferrari S, Schuck C, Pernice W H P and Lenzini F 2021 Single-photon detection and cryogenic reconfigurability in Lithium Niobate nanophotonic circuits *ArXiv210310973 Phys. Physicsquant-Ph*

[140] El Dirani H, Bajoni D, Sciancalepore C, Sabattoli F A, Garrisi F, Petit-Etienne C, Hartmann J M, Pargon E, Monat C, Liscidini M and Galli M 2019 Low-Loss Silicon Technology for High-Q Bright Quantum Sources *2019 IEEE 16th International Conference on Group IV Photonics (GFP)* (Singapore, Singapore: IEEE) pp 1–2

[141] Silverstone J W, Bonneau D, O’Brien J L and Thompson M G 2016 Silicon Quantum Photonics *IEEE J. Sel. Top. Quantum Electron.* **22** 390–402

[142] El Dirani H, Youssef L, Petit-Etienne C, Kerdiles S, Grosse P, Monat C, Pargon E and Sciancalepore C 2019 Ultralow-loss tightly confining Si $_3$ N $_4$ waveguides and high-Q microresonators *Opt. Express* **27** 30726

[143] Shadmani A, Thomas R, Liu Z, Volet N, Heck M J R, Scholz S, Wieck A D, Ludwig A, Lodahl P and Midolo L 2022 Integration of GaAs waveguides with quantum dots on Silicon substrates for quantum photonic circuits *Conference on Lasers and Electro-Optics* CLEO: QELS_Fundamental Science (San Jose, California: Optica Publishing Group) p FF4J.6

[144] Cheng R, Wang S and Tang H X 2019 Superconducting nanowire single-photon detectors fabricated from atomic-layer-deposited NbN *Appl. Phys. Lett.* **115** 241101

[145] Mu X, Wu S, Cheng L and Fu H Y 2020 Edge Couplers in Silicon Photonic Integrated Circuits: A Review *Appl. Sci.* **10** 1538

[146] Nambiar S, Sethi P and Selvaraja S 2018 Grating-Assisted Fiber to Chip Coupling for SOI Photonic Circuits *Appl. Sci.* **8** 1142

[147] Marchetti R, Lacava C, Carroll L, Gradkowski K and Minzioni P 2019 Coupling strategies for silicon photonics integrated chips [Invited] *Photonics Res.* **7** 201

[148] Wilmart Q, Brision S, Hartmann J-M, Myko A, Ribaud K, Petit-Etienne C, Youssef L, Fowler D, Charbonnier B, Sciancalepore C, Pargon E, Bernabe S and Szelag B 2021 A Complete Si Photonics Platform Embedding Ultra-Low Loss Waveguides for O- and C-Band *J. Light. Technol.* **39** 532–8

[149] Wolff M A, Beutel F, Schütte J, Gehring H, Häußler M, Pernice W and Schuck C 2021 Broadband waveguide-integrated superconducting single-photon detectors with high system detection efficiency *Appl. Phys. Lett.* **118** 154004

[150] Slussarenko S and Pryde G J 2019 Photonic quantum information processing: A concise review *Appl. Phys. Rev.* **6** 041303

[151] Gerrits T, Thomas-Peter N, Gates J C, Lita A E, Metcalf B J, Calkins B, Tomlin N A, Fox A E, Linares A L, Spring J B, Langford N K, Mirin R P, Smith P G R, Walmsley I A and Nam S W 2011 On-chip, photon-number-resolving, telecommunication-band detectors for scalable photonic information processing *Phys. Rev. A* **84** 060301

[152] Divochiy A, Marsili F, Bitauld D, Gaggero A, Leoni R, Mattioli F, Korneev A, Seleznev V, Kaurova N, Minaeva O, Gol'tsman G, Lagoudakis K G, Benkhaoul M, Lévy F and Fiore A 2008 Superconducting nanowire photon-number-resolving detector at telecommunication wavelengths *Nat. Photonics* **2** 302–6

[153] Jahanmirinejad S, Frucci G, Mattioli F, Sahin D, Gaggero A, Leoni R and Fiore A 2012 Photon-number resolving detector based on a series array of superconducting nanowires *Appl. Phys. Lett.* **101** 072602

[154] Sahin D, Gaggero A, Zhou Z, Jahanmirinejad S, Mattioli F, Leoni R, Beetz J, Lermer M, Kamp M, Höfling S and Fiore A 2013 Waveguide photon-number-resolving detectors for quantum photonic integrated circuits *Appl. Phys. Lett.* **103** 111116

[155] Lusardi N, Los J W N, Gourgues R B M, Bulgarini G and Geraci A 2017 Photon counting with photon number resolution through superconducting nanowires coupled to a multi-channel TDC in FPGA *Rev. Sci. Instrum.* **88** 035003

[156] Zhu D, Zhao Q-Y, Choi H, Lu T-J, Dane A E, Englund D and Berggren K K 2018 A scalable multi-photon coincidence detector based on superconducting nanowires *Nat. Nanotechnol.* **13** 596–601

[157] Gaggero A, Martini F, Mattioli F, Chiarello F, Cernansky R, Politi A and Leoni R 2019 Amplitude-multiplexed readout of single photon detectors based on superconducting nanowires *Optica* **6** 823

[158] Hazra D, Tsavdaris N, Jebari S, Grimm A, Blanchet F, Mercier F, Blanquet E, Chapelier C and Hofheinz M 2016 Superconducting properties of very high quality NbN thin films grown by high temperature chemical vapor deposition *Supercond. Sci. Technol.* **29** 105011

[159] Shcherbatenko M, Tretyakov I, Lobanov Yu, Maslennikov S N, Kaurova N, Finkel M, Voronov B, Goltsman G and Klapwijk T M 2016 Nonequilibrium interpretation of DC properties of NbN superconducting hot electron bolometers *Appl. Phys. Lett.* **109** 132602

[160] Kitaygorsky J, Komissarov I, Jukna A, Pan D, Minaeva O, Kaurova N, Divochiy A, Korneev A, Tarkhov M, Voronov B, Milostnaya I, Gol'tsman G and Sobolewski R R 2007 Dark Counts in Nanostructured NbN Superconducting Single-Photon Detectors and Bridges *IEEE Trans. Appl. Supercond.* **17** 275–8

[161] Ferrari S, Kovalyuk V, Hartmann W, Vetter A, Kahl O, Lee C, Korneev A, Rockstuhl C, Gol'tsman G and Pernice W 2017 Hot-spot relaxation time current dependence in niobium nitride waveguide-integrated superconducting nanowire single-photon detectors *Opt. Express* **25** 8739

[162] Vetter A, Ferrari S, Rath P, Alaee R, Kahl O, Kovalyuk V, Diewald S, Goltsman G N, Korneev A, Rockstuhl C and Pernice W H P 2016 Cavity-Enhanced and Ultrafast Superconducting Single-Photon Detectors *Nano Lett.* **16** 7085–92

[163] Hiltunen L, Leskelä M, Mäkelä M, Niinistö L, Nykänen E and Soininen P 1988 Nitrides of titanium, niobium, tantalum and molybdenum grown as thin films by the atomic layer epitaxy method *Thin Solid Films* **166** 149–54

[164] Zhang J J, Su X, Zhang L, Zheng L, Wang X F and You L 2013 Improvement of the superconducting properties of NbN thin film on single-crystal silicon substrate by using a TiN buffer layer *Supercond. Sci. Technol.* **26** 045010

[165] Zhang Q, Wang H, Tang X, Peng W and Wang Z 2019 Superconductivity Dependence on Epitaxial NbN Film Thickness *IEEE Trans. Appl. Supercond.* **29** 1–5

[166] Martini F, Gaggero A, Mattioli F and Leoni R 2019 Single photon detection with superconducting nanowires on crystalline silicon carbide *Opt. Express* **27** 29669

[167] Sam-Giao D, Pouget S, Bougerol C, Monroy E, Grimm A, Jebari S, Hofheinz M, Gérard J-M and Zwiller V 2014 High-quality NbN nanofilms on a GaN/AlN heterostructure *AIP Adv.* **4** 107123

[168] Machhadani H, Zichi J, Bougerol C, Lequien S, Thomassin J-L, Mollard N, Mukhtarova A, Zwiller V, Gérard J-M and Monroy E 2019 Improvement of the critical temperature of NbTiN films on III-nitride substrates *Supercond. Sci. Technol.* **32** 035008

[169] Cheng R, Wright J, Xing H G, Jena D and Tang H X 2020 Epitaxial niobium nitride superconducting nanowire single-photon detectors *Appl. Phys. Lett.* **117** 132601

[170] Villégier J-C, Delaet B, Feautrier P, Frey L, Delacour C and Bouchiat V 2006 Fabrication of High-Speed Single Photon Detectors in NbN for Quantum Information Processing *J. Phys. Conf. Ser.* **43** 1373–6

[171] Zhang L, You L, Yang X, Wu J, Lv C, Guo Q, Zhang W, Li H, Peng W, Wang Z and Xie X 2018 Hotspot relaxation time of NbN superconducting nanowire single-photon detectors on various substrates *Sci. Rep.* **8** 1486

[172] Miki S, Grein M E, Kerman A J, Marsili F, Dauler E A, Nam S W, Shaw M D, Terai H, Verma V B and Yamashita T 2014 Review of superconducting nanowire single-photon detector system design options and demonstrated performance *Opt. Eng.* **53** 081907

[173] Wright J, Chang C, Waters D, Lüpke F, Feenstra R, Raymond L, Koscica R, Khalsa G, Muller D, Xing H G and Jena D 2021 Unexplored MBE growth mode reveals new properties of superconducting NbN *Phys. Rev. Mater.* **5** 024802

[174] Jouve G, Séverac C and Cantacuzène S 1996 XPS study of NbN and (NbTi)N superconducting coatings *Thin Solid Films* **287** 146–53

[175] Chang H W, Wang C L, Huang Y R, Chen T J and Wang M J 2017 Growth and characterization of few unit-cell NbN superconducting films on 3C-SiC/Si substrate *Supercond. Sci. Technol.* **30** 115010

[176] Schmidt E, Ilin K and Siegel M 2017 AlN-Buffered Superconducting NbN Nanowire Single-Photon Detector on GaAs *IEEE Trans. Appl. Supercond.* **27** 1–5

[177] Shiino T, Shiba S, Sakai N, Yamakura T, Jiang L, Uzawa Y, Maezawa H and Yamamoto S 2010 Improvement of the critical temperature of superconducting NbTiN and NbN thin films using the AlN buffer layer *Supercond. Sci. Technol.* **23** 045004

[178] Jellison G E and Modine F A 1996 Parameterization of the optical functions of amorphous materials in the interband region *Appl. Phys. Lett.* **69** 371–3

[179] Drude P 1900 Zur Elektronentheorie der Metalle *Ann. Phys.* **306** 566–613

[180] Mukhtarova A, Redaelli L, Hazra D, Machhadani H, Lequien S, Hofheinz M, Thomassin J-L, Gustavo F, Zichi J, Zwiller V, Monroy E and Gérard J-M 2018 Polarization-insensitive fiber-coupled superconducting-nanowire single photon detector using a high-index dielectric capping layer *Opt. Express* **26** 17697

[181] Miller A J, Lita A E, Calkins B, Vayshenker I, Gruber S M and Nam S W 2011 Compact cryogenic self-aligning fiber-to-detector coupling with losses below one percent *Opt. Express* **19** 9102

[182] Redaelli L, Bulgarini G, Dobrovolskiy S, Dorenbos S N, Zwiller V, Monroy E and Gérard J M 2016 Design of broadband high-efficiency superconducting-nanowire single photon detectors *Supercond. Sci. Technol.* **29** 065016

[183] Amnon Yariv, Pochi Yeh, and Amnon Yariv 2007 *Photonics: optical electronics in modern communications* vol 6 (Oxford University Press New York)

[184] Zhu Z and Brown T 2002 Full-vectorial finite-difference analysis of microstructured optical fibers *Opt. Express* **10** 853

[185] Pernice W H P, Schuck C, Minaeva O, Li M, Goltsman G N, Sergienko A V and Tang H X 2012 High-speed and high-efficiency travelling wave single-photon detectors embedded in nanophotonic circuits *Nat. Commun.* **3** 1325

[186] Goell J E 1973 Rib Waveguide for Integrated Optical Circuits *Appl. Opt.* **12** 2797

[187] Dai D and He S 2004 Analysis of characteristics of bent rib waveguides *J. Opt. Soc. Am. A* **21** 113

[188] Ogusu K 1983 Optical strip waveguide: a detailed analysis including leaky modes *J. Opt. Soc. Am.* **73** 353

[189] Ogusu K, Kawakami S and Nishida S 1979 Optical strip waveguide: an analysis *Appl. Opt.* **18** 908

[190] Kahl O, Ferrari S, Rath P, Vetter A, Nebel C and Pernice W H P 2016 High Efficiency On-Chip Single-Photon Detection for Diamond Nanophotonic Circuits *J. Light. Technol.* **34** 249–55

[191] Tyler N A, Barreto J, Villarreal-Garcia G E, Bonneau D, Sahin D, O'Brien J L and Thompson M G 2016 Modelling superconducting nanowire single photon detectors in a waveguide cavity *Opt. Express* **24** 8797

[192] Gol'tsman G N, Smirnov K, Kouminov P, Voronov B, Kaurova N, Drakinsky V, Zhang J, Verevkin A and Sobolewski R 2003 Fabrication of nanostructured superconducting single-photon detectors *IEEE Trans. Appiled Supercond.* **13** 192–5

[193] Kovalyuk V, Hartmann W, Kahl O, Kaurova N, Korneev A, Goltsman G and Pernice W H P 2013 Absorption engineering of NbN nanowires deposited on silicon nitride nanophotonic circuits *Opt. Express* **21** 22683

[194] Annunziata A J, Quaranta O, Santavicca D F, Casaburi A, Frunzio L, Ejrnaes M, Rooks M J, Cristiano R, Pagano S, Frydman A and Prober D E 2010 Reset dynamics and latching in niobium superconducting nanowire single-photon detectors *J. Appl. Phys.* **108** 084507

[195] Charaev I, Semenov A, Doerner S, Gomard G, Ilin K and Siegel M 2017 Current dependence of the hot-spot response spectrum of superconducting single-photon detectors with different layouts *Supercond. Sci. Technol.* **30** 025016

[196] Gerrits T, Verma V B, Stern J A, Harrington S, Lita A E, Marsili F, Vayshenker I, Baek B, Shaw M D, Mirin R P and Nam S W 2013 Detecting single infrared photons with 93% system efficiency *Nat. Photonics* **7** 210–4

[197] Rosfjord K M, Yang J K W, Dauler E A, Kerman A J, Anant V, Voronov B M, Gol'tsman G N and Berggren K K 2006 Nanowire single-photon detector with an integrated optical cavity and anti-reflection coating *Opt. Express* **14** 527

[198] Akhlaghi M K, Schelew E and Young J F 2015 Waveguide integrated superconducting single-photon detectors implemented as near-perfect absorbers of coherent radiation *Nat. Commun.* **6** 8233

[199] Münzberg J, Vetter A, Beutel F, Hartmann W, Ferrari S, Pernice W H P and Rockstuhl C 2018 Superconducting nanowire single-photon detector implemented in a 2D photonic crystal cavity *Optica* **5** 658

[200] Vetter A, Ferrari S, Rath P, Alaee R, Kahl O, Kovalyuk V, Diewald S, Goltsman G N, Korneev A, Rockstuhl C and Pernice W H P 2016 Cavity-Enhanced and Ultrafast Superconducting Single-Photon Detectors *Nano Lett.* **16** 7085–92

[201] Abaeiani G, Ahmadi V and Saghafi K 2006 Design and analysis of resonant cavity enhanced-waveguide photodetectors for microwave photonics applications *IEEE Photonics Technol. Lett.* **18** 1597–9

[202] Song J, Eu-Jin A L, Luo X, Huang Y, Tu X, Jia L, Fang Q, Liow T-Y, Yu M and Lo G-Q 2014 A microring resonator photodetector for enhancement in L-band performance *Opt. Express* **22** 26976

[203] Bogaerts W, Selvaraja S K, Dumon P, Brouckaert J, De Vos K, Van Thourhout D and Baets R 2010 Silicon-on-Insulator Spectral Filters Fabricated With CMOS Technology *IEEE J. Sel. Top. Quantum Electron.* **16** 33–44

[204] Absil P P, Hryniewicz J V, Little B E, Cho P S, Wilson R A, Joneckis L G and Ho P-T 2000 Wavelength conversion in GaAs micro-ring resonators *Opt. Lett.* **25** 554

[205] Melloni A, Morichetti F and Martinelli M 2008 Four-wave mixing and wavelength conversion in coupled-resonator optical waveguides *J. Opt. Soc. Am. B* **25** C87

[206] Pasquazi A, Ahmad R, Rochette M, Lamont M, Little B E, Chu S T, Morandotti R and Moss D J 2010 All-optical wavelength conversion in an integrated ring resonator *Opt. Express* **18** 3858

[207] Davanço M, Ong J R, Shehata A B, Tosi A, Agha I, Assefa S, Xia F, Green W M J, Mookherjea S and Srinivasan K 2012 Telecommunications-band heralded single photons from a silicon nanophotonic chip *Appl. Phys. Lett.* **100** 261104

[208] Sabattoli F A, Sciancalepore C, Galli M, Bajoni D, Dirani H E, Garrisi F, Sam S, Petit-Etienne C, Hartmann J M, Pargon E, Monat C and Liscidini M 2019 A Source of Heralded Single Photon Using High Quality Factor Silicon Ring Resonators *2019 21st International Conference on Transparent Optical Networks (ICTON)* (Angers, France: IEEE) pp 1–4

[209] Garrisi F, Sabattoli F A, Sam S, Barone A, Massara M P, Pirzio F, Morichetti F, Melloni A, Liscidini M, Galli M and Bajoni D 2020 Electrically driven source of time-energy entangled photons based on a self-pumped silicon microring resonator *Opt. Lett.* **45** 2768

[210] Rodney Loudon 2000 *The quantum theory of light*

[211] Bogaerts W, De Heyn P, Van Vaerenbergh T, De Vos K, Kumar Selvaraja S, Claes T, Dumon P, Bienstman P, Van Thourhout D and Baets R 2012 Silicon microring resonators *Laser Photonics Rev.* **6** 47–73

[212] Sadiku M N O 2015 *Numerical Techniques in Electromagnetics with MATLAB®* (CRC Press)

[213] Kane Yee 1966 Numerical solution of initial boundary value problems involving maxwell's equations in isotropic media *IEEE Trans. Antennas Propag.* **14** 302–7

[214] Divochiy A, Marsili F, Bitauld D, Gaggero A, Leoni R, Mattioli F, Korneev A, Seleznev V, Kaurova N, Minaeva O, Gol'tsman G, Lagoudakis K G, Benkhaoul M, Lévy F and Fiore A 2008 Superconducting nanowire photon-number-resolving detector at telecommunication wavelengths *Nat. Photonics* **2** 302–6

[215] Jahanmirinejad S, Frucci G, Mattioli F, Sahin D, Gaggero A, Leoni R and Fiore A 2012 Photon-number resolving detector based on a series array of superconducting nanowires *Appl. Phys. Lett.* **101** 072602

[216] Sahin D, Gaggero A, Zhou Z, Jahanmirinejad S, Mattioli F, Leoni R, Beetz J, Lermer M, Kamp M, Höfling S and Fiore A 2013 Waveguide photon-number-resolving detectors for quantum photonic integrated circuits *Appl. Phys. Lett.* **103** 111116

[217] Zhu D, Colangelo M, Chen C, Korzh B A, Wong F N C, Shaw M D and Berggren K K 2020 Resolving Photon Numbers Using a Superconducting Nanowire with Impedance-Matching Taper *Nano Lett.* **20** 3858–63

[218] Bleuse J, Bruno G and Gérard J M An optimal multi-detector configuration for photon-number resolving measurements

[219] Bruel M 1999 Separation of silicon wafers by the smart-cut method *Mater. Res. Innov.* **3** 9–13

[220] Stephen A Campbell 2001 *The science, and engineering of microelectronic fabrication* (Oxford University Press New York)

[221] Anon 2019 What's the difference between an etcher and a lithography machine for making chips?

[222] Schmidt R-H M 2012 Ultra-precision engineering in lithographic exposure equipment for the semiconductor industry *Philos. Trans. R. Soc. Math. Phys. Eng. Sci.* **370** 3950–72

[223] Laudon M and Romanowicz B F 2007 *NSTI Nanotech 2007: May 20-24, 2007, Santa Clara, California, USA* (Boca Raton, Fla: CRC Press)

[224] Layadi N, Molloy S J, Esry T C, Lill T, Trevor J, Grimbergen M N and Chinn J 1999 Interferometry for end point prediction during plasma etching of various structures in complementary metal–oxide–semiconductor device fabrication *J. Vac. Sci. Technol. B Microelectron. Nanometer Struct.* **17** 2630

[225] Roland J P, Marcoux Paul J, Ray G W and Rankin G H 1985 Endpoint detection in plasma etching *J. Vac. Sci. Technol. Vac. Surf. Films* **3** 631–6

[226] Kerman A J, Dauler E A, Yang J K W, Rosfjord K M, Anant V, Berggren K K, Gol'tsman G N and Voronov B M 2007 Constriction-limited detection efficiency of superconducting nanowire single-photon detectors *Appl. Phys. Lett.* **90** 101110

[227] Lomonte E, Wolff M A, Beutel F, Ferrari S, Schuck C, Pernice W H P and Lenzini F 2021 Single-photon detection and cryogenic reconfigurability in Lithium Niobate nanophotonic circuits *ArXiv210310973 Phys. Physicsquant-Ph*

[228] Gyger S, Zichi J, Schweickert L, Elshaari A W, Steinhauer S, Covre da Silva S F, Rastelli A, Zwiller V, Jöns K D and Errando-Herranz C 2021 Reconfigurable photonics with on-chip single-photon detectors *Nat. Commun.* **12** 1408

[229] Grottke T, Hartmann W, Schuck C and Pernice W H P 2021 Optoelectromechanical phase shifter with low insertion loss and a 13π tuning range *Opt. Express* **29** 5525

[230] Sabattoli F A, Sciancalepore C, Galli M, Bajoni D, Dirani H E, Garrisi F, Sam S, Petit-Etienne C, Hartmann J M, Pargon E, Monat C and Liscidini M 2019 A Source of Heralded Single Photon Using High Quality Factor Silicon Ring Resonators *2019 21st International Conference on Transparent Optical Networks (ICTON)* (Angers, France: IEEE) pp 1–4